SLAC-R-550
UC-414

Measurement of the b Quark Fragmentation Function in Z^0 Decays

Danning Dong

Stanford Linear Accelerator Center
Stanford University
Stanford, CA 94309

SLAC-Report-550
December 1999

Prepared for the Department of Energy
under contract number DE-AC03-76SF00515

Printed in the United States of America. Available from the National Technical Information Service, U.S. Department of Commerce, 5285 Port Royal Road, Springfield, VA 22161.

Measurement of the b Quark Fragmentation Function in Z^0 Decays

by

Danning Dong

Submitted to the Department of Physics
on September 21, 1999, in partial fulfillment of the
requirements for the degree of
Doctor of Philosophy

Abstract

We present results of a new measurement of the inclusive b quark fragmentation function in Z^0 decays using a novel kinematic B hadron energy reconstruction technique. The measurement is performed using 150,000 hadronic Z^0 events recorded in the SLD experiment at SLAC between 1996 and 1997. The small and stable SLC beam spot and the CCD-based vertex detector are used to reconstruct topological B-decay vertices with high efficiency and purity, and to provide precise measurements of the kinematic quantities used in this technique. We measure the B energy with good efficiency and resolution over the full kinematic range. While comparing the scaled B energy distribution with predictions of several models of b quark fragmentation, we also test several functional forms of the B energy distribution. Several fragmentation models and functional forms are excluded by the data. The mean of the scaled energy distribution of the weakly decaying B hadron is measured to be $x_B = 0.714 \pm 0.005$ (stat) $\pm$ 0.007 (syst) $\pm$ 0.002 (model).

Thesis Supervisor: Frank E. Taylor
Title: Senior Research Scientist

Acknowledgments

To all the people who have helped me during these years, I say Thank You. But I feel compelled to first thank my advisor, Frank Taylor. If I have succeeded in taking a few right turns and have found a good direction to go, Frank has certainly been the one who is guiding me right by my side. I thank Frank for suggesting me to take my eventual thesis topic which I had lots of fun working on. I also thank Louis Osborne for his generous support and care. Without Frank and Lou, I would not be writing this thesis. My heartfelt thanks go to both of them.

I cannot find a better opportunity to thank Charlie Baltay and Marty Breidenbach, whose leadership has made SLD a world class high energy physics experiment. What I have learned working on SLD will benefit my career tremendously.

I thank all who helped me adjust to the new research environment after I came to SLAC in 1996. I thank Phil Burrows for his help and for introducing me to Richard Dubois. It was fun to work with Richard, Gary Bower, Peter Rowson, and others in the Calorimeter Group.

I thank John Jaros and Su Dong for their encouragements and support in and outside the SLD Tracking Group. I also thank Toshi Abe, Aaron Chou, David Jackson, Vincenzo Lia, Thomas Markiewicz, Leon Rochester, Nick Sinev, Tracy Usher, and others.

Many thanks go to Phil Burrows, Dave Jackson and Dave Muller for their constant interests in and support for my thesis topic from very early on. I thank Phil for explaining to me, among many other things, how to plan and work on the physics analysis and for his many insightful suggestions. I thank Dave Jackson for being a very supportive colleague and a close friend. With his strong vertexing background, Dave steadfastly stood by my side and helped me when I was taking a slightly untraditional approach to my thesis analysis. I thank Dave Muller for his help throughout the entire course of this analysis. Dave essentially guided me on a daily basis. Our numerous discussions proved to be fruitful. Dave's most favorite phrase is " ...This can be quickly looked at, which requires almost no work at all." Still, I never really managed to live up to such high expectations. I also thank Gary Bower, Jim Brau, Mohan Kalelkar, Takashi Maruyama, Morris Swartz, Stephane Willocq, and Charlie Young for their help. What I have done cannot be separated from the help of these wonderful colleagues and friends. I am indebted to all of them.

I would like to thank Bob Jaffe and Dick Yamamoto for serving on my Thesis Committee and for their careful reading of this thesis. I thank Dave Muller for reading part of this thesis. In spite of his own very busy schedule, Frank Taylor has put in numerous hours reading the draft thesis time and again and has given me many helpful suggestions. I deeply thank him for his unfailing support.

I thank members of the MIT-Yale VXD3 survey group: Henry Kendall, Louis Osborne, Robin Verdier, Erwin Lee, Dale Ross, and my fellow graduate student Vincenzo Lia; I also thank Ming Liu, Thomas Moore, Steve Manly, Jeff Snyder, and Will Emmett at Yale.

I thank Mike Huffer, Jim Johnson, Terry Schalk, and the SLD software group for their kindness.

I thank Sandy Fowler, Larry Rosenson, and Peggy Berkovitz at MIT for all the help they extended to me during these years. I thank everyone who attended my thesis defense at MIT, which was an experience I will never forget.

I thank fellow graduate students Kenji Abe, Aaron Chou and Haejoo Kang, Vance Eschenburg, Kazu and Yumi Hasuko, Xinh Huynh, Matt Langston, Herman Staengle, Liying Sun, Julia Thom, Eric Torrence, Sean Walston, and Tom Wright. Even though we occasionally had intense debate sessions, Cheng-Ju Lin has always been a close friend and colleague, with whom I shared many good memories. His skill in Chinese cooking makes him an even better friend to be with! I thank John Coller. John, I still owe you an SLD shift! I thank resident postdocs Hidemi Akimoto, Ken Baird VIII, Glen Crawford, Mourad Daoudi, Nicolo de Groot, Sal Fahey, Masako Iwasaki, and Victor Serbo for their help or discussions. I thank theorists Stan Brodsky and Lance Dixon for answering my questions and making suggestions to my physics analysis. I thank Nina Stolar, Pauline Wethington at the SLAC Public Affair Office for giving me the opportunity to enjoy the exciting experience as a SLAC tour guide.

I thank Tom Zuwei Feng and Jeff Zhaohui Zhang for being good friends since undergraduate years. I thank Jeff for attending my thesis defense, bringing a bottle of Champagne, and taking those memorable photographs. I thank Zhifeng An, Zhengting Chang, Jiang Chen and Qinqin Wang, Shanhui Fan, Hairong and Xiaobin Song, Jian Tang, Eric Neng Wang, and Quan Yuan and Shi Yuan. I thank Amy Cai and her family, Baihe Xiao and Wenjie Xie, and Lily Jinzhi Zhang and Yiaohua Zhu for being so kind. I thank Hongjiang Sun and Liuping Wang, Hongqiao Sun and Weiping Li, and their families for their hospitality and kind help.

A simple thank you is not enough when it comes to my former Cambridge roommate Matthew Carpenter, who saved my life in January 1995. I am grateful to him for what he did.

I thank my parent-in-law for taking good care of my daughter. I thank aunt Bin-Yuan Lee for her years of love and support, and grand-uncle Rong Sheng for his generous help. I am indebted to my older brother Chenning Tong and sister-in-law Yi Wu for their love and support during these years. I owe a lot to them.

Due to my status as a US permanent resident, my wife Elsa Chan has not been able to come to the US because she needed to wait outside the US to apply for an immigration visa, which takes a few years to obtain. We have been separated by the Pacific Ocean for the past two years. My lovely daughter Allysa was a new born baby when she had to leave me and go back to Hong Kong. During these times, I always try to recall what the Judge told us on the day when we got married: "Share the sweet moments and be prepared to go through the hard times." Elsa, I thank you for all you have done for me. I feel very fortunate to have you as my wife. I will love you forever.

Finally, I thank the two most important people for me, my father Han-Chuan Dong and my mother Shu-Yiao Lee, whom I have only seen for two weeks during the past ten years since I stepped onto the US soil. Their life-long commitment to each other and their sacrifices for me and my brother continue to generate from inside the deepest passion I have ever felt. My gratitude and love for them cannot be expressed in words. To them, I dedicate this thesis.

Contents

List of Figures

List of Tables

Chapter 1

Introduction

This thesis will mainly present a measurement of the bottom (b) quark fragmentation function in Z^0 decays. The measurement is performed based on excellent tracking, vertexing, and a novel energy reconstruction technique. The data analyzed in this measurement include 150,000 hadronic Z^0 decays recorded at the Stanford Linear Accelerator Center (SLAC) with the SLAC Large Detector (SLD) measuring electron-positron collisions and annihilations produced by the SLAC Linear Collider (SLC) during the 1996-1997 runs.

We measure the heavy quark (b and c) fragmentation functions not only because we need to improve our understanding of the non-perturbative aspect of the theory of strong interaction, Quantum Chromodynamics (QCD), but also because heavy quark fragmentations are important for a number of other heavy flavor physics measurements. Heavy quark fragmentation is a sizable systematic uncertainty in several measurements. In addition, B mixing and B lifetime measurements can surely benefit from an improved B hadron energy reconstruction technique.

Prior to this measurement, the b quark fragmentation function had recently been studied both at LEP at CERN and at SLD. Since LEP experiments possess a total of roughly 16 million hadronic Z^0 decays compared to the 560 thousand events that SLD has, a much improved technique must be used if we intend to make this new

SLD measurement competitive or better than those at LEP experiments.

Based on this consideration, at an early stage we focused on developing a technique that would reconstruct B hadron energy with good resolution and meanwhile was hoping to produce a much higher efficiency for selecting B hadrons than those of LEP measurements in order to compensate for the disparity in the number of raw hadronic Z^0 decay events between LEP experiments and SLD. Fortunately, by taking full advantage of tracking and vertexing capabilities present at SLD and SLC, such a technique was indeed found, and subsequently developed to produce this currently most precise measurement of the b fragmentation function. The upgraded SLD vertex detector (VXD3), which provides excellent spatial resolutions, and the small SLC Interaction Point (IP) are central to the successful application of this technique at SLD.

The thesis is organized as follows. In Chapter 2 we introduce the Standard Model briefly. Since this analysis is mainly concerned with the strong interaction, electroweak interactions are described in Appendix A. General aspects of the theory of strong interaction (QCD) are only briefly discussed. In Chapter 3, we focus on hadron productions in $e^+e^- \to Z^0 \to q\bar{q}$ and their treatments in the context of QCD. The main theme of this thesis, the fragmentation function, is introduced. Some details are provided or discussed, including various hadronization models and heavy quark fragmentation functions. In Chapter 4 we introduce the experimental apparatus: the SLAC Linear Collider and SLAC Large Detector. In Chapter 5 we discuss SLD's upgraded vertex detector (VXD3) which is inseparable from this analysis and my own research experience as a graduate student. Topics include the optical survey, the global alignment, and the performance of VXD3. Chapter 6 contains a description of the fairly standard SLD hadronic event selection and B tagging. In Chapter 7 we present the new energy reconstruction technique for this analysis in detail. In Chapter 8 various heavy quark fragmentation models are tested using our data. In Chapter 9 we unfold the B energy distribution and discuss the model-dependence of our method. In Chapter 10 we investigate various systematic effects. We conclude in Chapter 11. In Appendix B we derive the formula used in our energy reconstruction technique to solve for the missing longitudinal momentum. Some questions about this technique are raised and discussed. Appendix C gives a detailed mathematical account of how we have treated error propagation in the unfolding procedure.

Chapter 2

The Standard Model

The goal of this thesis is to improve our understanding of a fundamental question: how does an energetic quark turn into a jet of hadrons? In particular, how does a bottom quark *hadronize* into a bottom hadron?

In this chapter, we will first review some basics of the Standard Model of the electroweak and strong interactions. Then we will describe the fragmentation of quarks and gluons.

2.1 Overview

Tremendous progress has been made in our understanding of the universe, and in particular, fundamental particles and their interactions. Not only has our understanding improved over time, the very notion of what constitutes fundamental particles has been also subject to change[1].

Among the four fundamental interactions in nature, gravitation remains not unified with the other three. The electromagnetic and the weak interactions have been successfully unified by an effective field theory called electroweak theory. The strong

[1]The Superstring theory assumes that the most fundamental objects are not point particles, but very small string-like objects.

interaction has been successfully described by Quantum Chromodynamics (QCD). Electroweak theory and QCD combined are called the Standard Model.

The Standard Model is based on quantum gauge field theories in which fundamental interactions are the consequences of the local gauge invariance principle. More specifically, the Standard Model is based on the $\mathrm{SU}(3)_{color}\otimes$ $\mathrm{SU}(2)_L\otimes$ $\mathrm{U}(1)_Y$ gauge group. The $\mathrm{SU}(3)_{color}$ is the color gauge symmetry group which generates the strong interaction, the $\mathrm{SU}(2)_L$ is the "weak isospin" gauge symmetry group, and the $\mathrm{U}(1)_Y$ is the "weak hypercharge" gauge symmetry group. $\mathrm{SU}(2)_L\otimes$ $\mathrm{U}(1)_Y$ generates the unified electroweak interaction.

The most fundamental fermions that have been discovered are divided into two categories: those not subject to the strong interaction which are called leptons and those which also interact by the strong force which are called quarks. Quarks are the only fundamental particles known today that interact via all four interactions. In the Standard Model, there are three generations of leptons and quarks, each containing a pair of leptons and a pair of quarks. Left-handed leptons and their associated neutrinos (e and ν_e, μ and ν_μ, and τ and ν_τ) form the three lepton generations, and left-handed quarks (u and d, c and s, and t and b) form the three quark generations. Right-handed fermions are weak isospin singlets[2]. Quarks, but not leptons, carry color charge which enables them to interact via strong interaction. Each quark can carry one of three different color charges: blue, green, or red. Every particle has its own antiparticle. The fermions of the Standard Model are summarized in Table 2.1. The spectrum of leptons and quarks are shown in Table 2.2 and Table 2.3.

The interactions between fundamental particles are mediated by the gauge bosons, the types of which depend on the type of interaction involved: the photon (γ), the W^+, W^-, or the Z^0 for the electroweak interaction and the gluon for the strong interaction. Table 2.4 shows the Standard Model gauge bosons.

[2]Right-handed neutrinos have not been experimentally observed, nor has the third generation neutrino called ν_τ.

$$
\begin{array}{ccc}
\begin{pmatrix} \nu_e \\ e \end{pmatrix}_L & \begin{pmatrix} \nu_\mu \\ \mu \end{pmatrix}_L & \begin{pmatrix} \nu_\tau \\ \tau \end{pmatrix}_L \\
\begin{pmatrix} u \\ d \end{pmatrix}_L & \begin{pmatrix} c \\ s \end{pmatrix}_L & \begin{pmatrix} t \\ b \end{pmatrix}_L \\
e_R & \mu_R & \tau_R \\
u_R & c_R & t_R \\
d_R & s_R & b_R
\end{array}
$$

Table 2.1: Fermion constituents of the Standard Model.

Lepton	Charge (e)	Mass (MeV/c^2)	Lifetime (s)
ν_e	0	< 0.020	$> m_{\nu_e}$ (eV) $\times$ 300 (s/eV)
e	-1	$0.51099907 \pm 0.00000015$	$> 4.3 \times 10^{23}$ yr (68% C.L.)
ν_μ	0	< 0.17	$> m_{\nu_e}$ (eV) $\times$ 15.4 (s/eV)
μ	-1	105.658389 ± 0.000034	$(2.19703 \pm 0.00004) \times 10^{-6}$
ν_τ (?)	0	< 1	unknown
τ	-1	$1777.05^{+0.29}_{-0.26}$	$(290.0 \pm 1.2) \times 10^{-15}$

Table 2.2: The Standard Model spectrum of leptons. (?) indicates the discovery is not firmly established.

2.2 Electroweak Interaction

Appendix A contains a more detailed description the electroweak theory. Here we only briefly mention the part that is relevant to the SLD experiment and this thesis analysis.

2.2.1 Weak Neutral Currents

In $e^+e^- \rightarrow f\bar{f}$, two neutral vector gauge bosons may be exchanged: the massless photon and the massive Z^0. The Born or tree-level Feynman diagram for these processes are shown in Figure 2-1. The cross-section, σ, is proportional to the modulo square of the sum of the matrix elements represented by the two diagrams, $|\mathcal{M}_\gamma +$

Quark	Charge (e)	Mass (GeV/c^2)	$I(J^P)$	Other
u	$+\frac{2}{3}$	$0.0015 - 0.005$	$\frac{1}{2}(\frac{1}{2}^+)$	$I_z = +\frac{1}{2}$
d	$-\frac{1}{3}$	$0.003 - 0.009$	$\frac{1}{2}(\frac{1}{2}^+)$	$I_z = -\frac{1}{2}$
s	$-\frac{1}{3}$	$0.060 - 0.170$	$0(\frac{1}{2}^+)$	strangeness=-1
c	$+\frac{2}{3}$	$1.1 - 1.4$	$0(\frac{1}{2}^+)$	charm=$+1$
b	$-\frac{1}{3}$	$4.1 - 4.4$	$0(\frac{1}{2}^+)$	bottom=-1
t	$+\frac{2}{3}$	(173.8 ± 5.2)	$0(\frac{1}{2}^+)$	top=$+1$

Table 2.3: The Standard Model spectrum of Quarks

Name	Charge (e)	Mass (GeV/c^2)	$I(J^{PC})$	Other
γ	0	$< 2 \times 10^{-25}$	$0,1(1^{--})$	Stable
g	0	0	$0(1^-)$	SU(3) color octet
$W^\pm$	± 1	80.41 ± 0.10	$J = 1$	$\Gamma = 2.06 \pm 0.06$ GeV
Z	0	91.187 ± 0.007	$J = 1$	$\Gamma = 2.940 \pm 0.007$ GeV

Table 2.4: The Standard Model spectrum of gauge bosons

$\mathcal{M}_{Z^0}|^2$. Three terms are present in the cross section: the purely electromagnetic, the interference, and the purely weak. The existence of the interference term has been demonstrated by experiments.

One striking feature of the theory is that left-handed and right-handed fermions

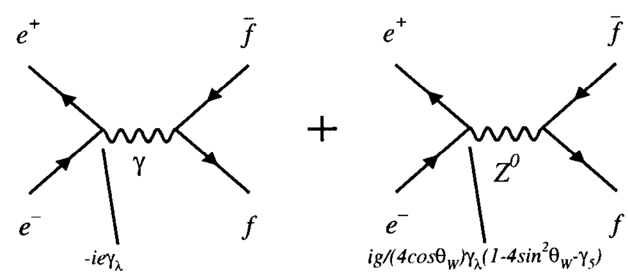

Figure 2-1: Tree level Feynman diagrams representing $e^+e^- \to f\bar{f}$. Vertex factors for $e^+e^- \to \gamma$ and $e^+e^- \to Z^0$ are indicated.

have different couplings to Z^0:

$$\begin{aligned} g_L &= 2I_3 - 2Q\sin^2\theta_W, \\ g_R &= -2Q\sin^2\theta_W. \end{aligned} \tag{2.1}$$

Decomposing the interaction into V–A form, we have

$$\sqrt{2}\left(\frac{G_F M_Z^2}{\sqrt{2}}\right)^{1/2} \bar{f}\gamma^\mu(c_V^f - c_A^f\gamma_5) f Z_\mu, \tag{2.2}$$

where the vector (V) and axial-vector (A) coupling coefficients are

$$\begin{aligned} c_V^f = (g_L + g_R)/2 = &\quad I_3 - 2Q\sin^2\theta_W, \\ c_A^f = (g_L - g_R)/2 = &\quad I_3. \end{aligned} \tag{2.3}$$

c_V and c_A for all Standard Model fermions are listed in Table 2.5. These V- and A-coefficients are used for determining vertex factors for $Z^0 f\bar{f}$ vertices (see Figure 2-1).

Fermion	Charge (e)	c_V	c_A
ν_e,ν_ν,ν_τ	0	$\frac{1}{2}$	$\frac{1}{2}$
e, μ, τ	$-\frac{1}{2}$	$-\frac{1}{2} + 2\sin^2\theta_W$	$-\frac{1}{2}$
u, c, t	$+\frac{2}{3}$	$+\frac{1}{2} - \frac{4}{3}\sin^2\theta_W$	$\frac{1}{2}$
d, s, b	$-\frac{1}{3}$	$-\frac{1}{2} + \frac{2}{3}\sin^2\theta_W$	$-\frac{1}{2}$

Table 2.5: c_V and c_A for Standard Model fermions.

2.2.2 Polarized Cross Section of $e^+e^- \to Z^0 \to f\bar{f}$

At SLC, the polarized electron beam allows precision measurements of electroweak parameters by probing the characteristics of polarized $e^+e^- \to Z^0$ production.

The electron polarization is defined as

$$\mathcal{P}_e = \frac{N_{eL} - N_{eR}}{N_{eL} + N_{eR}}, \tag{2.4}$$

where N_{eL} and N_{eR} are the number of left-handed and right-handed electrons, respectively.

At the Z-pole, ignoring the γ-exchange and $\gamma - Z^0$ interference terms and the transverse polarization, the polarization dependence of the differential cross-section is

$$\frac{d\sigma}{d\cos\theta} \propto (1 + \mathcal{P}_e A_e)(1 + \cos^2\theta) - 2A_f(\mathcal{P}_e + A_e)\cos\theta, \tag{2.5}$$

where θ is the angle of the final fermion with respect to the electron beam direction, and A_e is the electron left-right asymmetry which, for any fermion f, is defined as

$$A_f = \frac{(c_V^f + c_A^f)^2 - (c_V^f - c_A^f)^2}{(c_V^f + c_A^f)^2 + (c_V^f - c_A^f)^2}. \tag{2.6}$$

The A_{LR}^f at the Z^0 vertex is defined as

$$A_{LR}^f \equiv \frac{\sigma(e_R^+ e_L^- \to Z^0 \to f\bar{f}) - \sigma(e_L^+ e_R^- \to Z^0 \to f\bar{f})}{\sigma(e_R^+ e_L^- \to Z^0 \to f\bar{f}) + \sigma(e_L^+ e_R^- \to Z^0 \to f\bar{f})}. \tag{2.7}$$

In this analysis, we measure the energy spectrum of bottom (B) hadrons in $Z^0 \to b\bar{b}$ decays[3]. Most relevant here is R_b, which is defined as the ratio of the cross section of $Z^0 \to b\bar{b}$ to the total hadronic Z^0 cross-section ($Z^0 \to q\bar{q}$)

$$R_b = \frac{\sigma(Z^0 \to b\bar{b})}{\sum_q \sigma(Z^0 \to q\bar{q})}, \tag{2.8}$$

where $q\bar{q}$ is a quark-antiquark pair and the sum is over quark flavors. At the Z-pole,

[3]The rate for gluon splitting into $b\bar{b}$ is only about 0.3% so a very small number of $b\bar{b}$ come from gluon splittings.

five flavors, u, d, s, c, and b, are produced. The current measured value is $R_b \simeq 21.7\%$.

We use the 150,000 hadronic Z^0 events collected by the SLD detector during the 1996-1997 run. The number of $Z^0 \to b\bar{b}$ events is approximately 32,500. Although we do not use in this analysis the fact that most b quarks produced are left-handed, we do plan to take advantage of this property in our future b fragmentation studies.

2.3 Strong Interaction

The modern theory of the strong interaction is Quantum Chromodynamics (QCD) [1], which is a Yang-Mills theory based on a local non-Abelian color gauge symmetry group SU(3)$_{color}$. *Quarks* are the spin $\frac{1}{2}$ fermions in the theory and color triplets, which transform as the fundamental representation of the SU(3) group. *Gluons* are the vector gauge bosons that mediate the strong force and 'glue' quarks and anti-quarks together to form mesons and baryons which form a color-anticolor octet. For SU(3), there are eight such gauge fields, $A^a_\mu(x)$ $(a = 1, 2, ..., 8)$, which transform according to the Adjoint representation. Because the SU(3) color symmetry is exact and unbroken, the gluons are massless. This seems to imply that the strong force is a long-range force, in analogy to QED where photon is massless and electromagnetic force is long-range. However, the strong force as we have observed is a short-range force that tightly binds colored quarks together to form color non-singlet hadrons. Therefore, if QCD is to be a correct theory of the strong interaction, it has to satisfy the requirement that it is a *confining* theory. So far this has not yet been proved as a theorem.

The choice of the SU(3) gauge group arises from the hypothesis, based on much evidence, that quarks form color triplets. The SU(3) color transformations are generated by the 3×3 matrices $T^a = \lambda^a/2$, where λ^a are the Gell-Mann matrices [2] which obey the commutation relations:

$$[T^a, T^b] = if^{abc}T^c, \tag{2.9}$$

where f^{abc} are the structure constants of SU(3). The QCD Lagrangian can be written as

$$\mathcal{L} = -\frac{1}{4}F^a_{\mu\nu}F^{\mu\nu a} + \overline{q}(i\gamma_\mu D^\mu - m)q, \tag{2.10}$$

where m is the bare mass of the quark field and $F^{\mu\nu}$ is the non-Abelian field strength tensor,

$$F^a_{\mu\nu} = \partial_\mu A^a_\nu - \partial_\nu A^a_\mu + g f^{abc} A^b_\mu A^c_\nu, \tag{2.11}$$

and D_μ is the covariant derivative:

$$D_\mu = \partial_\mu - i g_s T^a A^a_\mu(x), \tag{2.12}$$

where g is the bare coupling constant of the theory.

Figure 2-2 shows the three types of interaction vertex allowed in QCD: $gq\bar{q}$, ggg, and $gggg$. The second and third types of vertices is a consequence of the last term in (2.11), which implies self-interactions between the gluons. Gluons themselves carry color-anticolor charge (such as red-antiblue). Self-interaction between the vector gauge bosons is a distinct feature of non-Abelian local gauge theory. In Quantum Electrodynamics (QED), the local gauge symmetry group U(1) is Abelian and as a result the photon does not carry electric charge and there is no interactions between the photons. However, in the Electroweak theory, the SU(2) part of the gauge group is non-Abelian, which results in self-interaction between the vector gauge bosons, for example, $W^+W^+Z^0$, $W^+W^+Z^0Z^0$ or $W^+W^+W^-W^-$ interactions. Self-interaction between gluons does not mean a red-antiblue gluon will interact with another red-antiblue gluon. A gluon can only interact with gluons with color-anticolor charges different from those carried by itself.

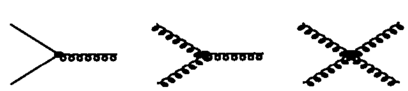

Figure 2-2: Three types of interaction vertices in QCD: $gq\bar{q}$, ggg, and $gggg$.

2.3.1 Asymptotic Freedom and Perturbative QCD

The Running Strong Coupling Constant

QCD has the unique characteristics of asymptotic freedom. In QED, the fermion loop contribution in charge renormalization causes the effective coupling constant $\alpha_{EM}(Q^2)$ to *increase* with increasing Q^2, the 4-momentum transfer. In the Thomson limit of $Q^2 = 0$, $\alpha_{EM} \simeq 1/137$, which is much smaller than 1 so that perturbative expansions work very well. Even at the Z^0 mass scale, α_{EM} is still only $\sim 1/128$. However, higher and higher orders in α_{EM} must be included as Q^2 increases. In QCD, the presence of the self-interactions between the gluons, in contrast, results in a negative contribution to the effective strong coupling $\alpha_s(Q^2)$. The net effect of these contributions to the strong coupling constant $\alpha_s \equiv \frac{g_s^2}{4\pi}$, at Leading Logarithm Approximation (LLA), is given by

$$\alpha_s(Q^2) = \frac{\alpha_s(\mu^2)}{1 + \frac{\alpha_s(\mu^2)}{12\pi}(11N - 2n_f)\log(\frac{Q^2}{\mu^2})}, \tag{2.13}$$

where $\alpha_s(\mu^2)$ is the "experimental" strong coupling constant at an arbitrary renormalization scale μ^2, $N = 3$ is the number of colors, and n_f is the number of quark flavors that can be produced, which includes all flavors with mass less than $Q/2$. For example, for $Q^2 \sim 1$ GeV, only *uds* quarks can be produced so $n_f = 3$; but at the Z^0 mass, $n_f = 5$ because charm and bottom but not top quarks can be produced. As long as $n_f \leq 16$, the $\alpha_s(Q^2)$ will decrease with increasing Q^2 and will approach zero as $Q^2 \to \infty$. This property in field theory is called *asymptotic freedom.*

Asymptotic freedom allows the application of perturbative techniques to calculate high energy QCD processes when $\alpha_s(Q^2) \ll 1$. But even at the Z^0 mass scale ($\sim$ 91 GeV), the strong coupling constant $\alpha_s(M_{Z^0}^2) \simeq 0.12$, which is still not very small and higher orders in the perturbative expansion series may in some instances have a sizable effect in the result. At next-to-leading order ($\mathcal{O}(\alpha_s^2)$) there is still about $(5-10)\%$ uncertainty in the perturbative results. At the low energy scale of about 0.5 GeV, which is the scale of a typical hadron mass, $\alpha_s(Q^2) \geq 1$ and therefore perturbative QCD is totally inapplicable. This is typically referred to as the non-perturbative regime. Processes such as hadron production is non-perturbative and has not been well-understood. This thesis will measure one aspect of hadron production, namely the b quark fragmentation function, in order to probe into this non-perturbative process.

The Effective Perturbative QCD Parameter Λ_{QCD}

Since the renormalization scale μ^2 in (2.13) is arbitrary, the coupling at a different renormalization scale $Q^2 = \bar{\mu}^2$ is related to $\alpha_s(\mu^2)$, in the leading logarithm approximation (LLA),

$$\frac{1}{\alpha_s(\bar{\mu}^2)} = \frac{1}{\alpha_s(\mu^2)} + \frac{\beta_0}{4\pi}\log(\frac{\bar{\mu}^2}{\mu^2}), \tag{2.14}$$

where $\beta_0 = 11 - \frac{2}{3}n_f$, or

$$-\frac{4\pi}{\beta_0\alpha_s(\bar{\mu}^2)} + \log(\bar{\mu}^2) = -\frac{4\pi}{\beta_0\alpha_s(\mu^2)} + \log(\mu^2). \tag{2.15}$$

This suggests that we can define a new mass scale Λ_{QCD},

$$\log\Lambda^2_{QCD} = -\frac{4\pi}{\beta_0\alpha_s(\mu^2)} + \log(\mu^2), \tag{2.16}$$

which is independent of the specific choice of the renormalization scale μ^2. Instead of expressing $\alpha_s(Q^2)$ as a function of $\alpha(\mu^2)$, μ^2, and Q^2, we can express it as a function of only Λ^2_{QCD} and Q^2,

$$\alpha_s(Q^2) = \frac{4\pi}{\beta_0\log(Q^2/\Lambda^2_{QCD})}. \tag{2.17}$$

Λ_{QCD} can be regarded as *the* fundamental parameter of perturbative QCD, instead of the strong coupling constant α_s. Generally speaking, in any renormalization scheme, a physical observable should be independent of the renormalization scale μ if the calculation is carried out to all orders in perturbation theory, which leads to the renormalization group equation [3].

Λ_{QCD} is determined experimentally to be $\sim$ 200 MeV. At a scale where $Q^2 \gg \Lambda^2_{QCD}$, the strong coupling α_s is small and perturbative calculations of observable by means of expansion in a series of α_s are meaningful. Thus, predictions of perturbative QCD are subject to experimental tests, sometimes even precision tests. The prediction that partons appear as distinct jets in the final state at high energies is a consequence of this high energy perturbative regime. α_s has been measured to a precision of only about 5%, but its flavor-independence has been tested to a much higher precision of about 0.5%.

Due to the self-interaction of the gluons, a large number of Feynman diagrams must be taken into account in calculations at even moderately small (third or higher) orders of α_s. The high multiplicity of jets in the final state complicates perturbative calculations. These factors make perturbative QCD calculations much more difficult than their QED analog. In addition, higher-order calculations depend on the renormalization scheme chosen, which can to some degree obscure the meaningful tests of perturbative QCD predictions. Nevertheless, in a variety of processes, especially hard processes, perturbative QCD predictions are fruitful and have been tested to good precision. More detailed description of perturbative QCD related to this thesis is covered in the next Chapter.

2.3.2 Non-perturbative QCD and Fragmentation

The most serious challenge to QCD, however, lies in the low energy regime where the strong interaction processes are essentially non-perturbative.

It has been a well-established fact that quarks and gluons are not directly observed as final state particles in experimental apparatus. This characteristics of the strong interaction has led to the *color confinement* postulate

All hadron states and physical observables must be color singlets.

Color non-singlet objects cannot be observables. This may be viewed from a different perspective: physical phenomena are invariant under the color transformation. The color SU(3) is therefore an exact symmetry. However, the origin of confinement itself is unknown and is still an open question. Confinement may eventually be found to be a dynamical consequence of QCD.

A naive analysis of single gluon exchange between quarks shows that the color singlet two- or three-body states $q\bar{q}$ or qqq have negative color factors and are strongly attractive. This gives us a hint that color singlet states are probably the only states stable enough to exist.

The fact that partons must form hadron states, as required by color confinement, indicate that the strong interaction between partons is very strong when hadronization actually occurs, presumably at a low energy scale of a few hundred MeV. Thus hadronization is a non-perturbative phenomenon and perturbative calculations are inapplicable in this regime, making hadronization probably the most uncertain part of the theory of strong interaction. Had it not been the case, that is, if partons can be observed in the final states just like electrons and photons in QED, we would not have had to battle this problem of hadronization. QCD predictions as well as their experimental tests would have been more precise, and also more transparent, than they are today.

At present we really do not know the correct way to fragment a collection of partons into hadrons, other than the perturbative evolution of partons. An integrated solution to this problem requires a much improved experimental probe and theoretical understanding of the confinement mechanism. This is the most profound motivation for the analysis of this thesis. By measuring the b quark fragmentation function, we expect to gain a more precise knowledge of hadronization for the b. Further information are described in the next Chapter.

It has been one of the key problems in theoretical physics to find a solution to calculate strongly coupled, non-perturbative QCD processes[4]. Lattice QCD is one way to go. Once this problem is solved, we should be able to calculate and predict from first principles QCD phenomena such as hadron productions, hadron masses, and hadron decays.

[4]Recently, a conjecture was proposed [4] that compactification of M/string theory on various Anti-deSitter spacetimes, which includes weakly coupled supergravity, is dual to various conformal field theories, including strongly coupled super-Yang-Mills theory which is intimately related to QCD, thereby achieving a mapping between strongly- and weakly-coupled theories.

Chapter 3

Hadron Production in $e^+e^- \to q\bar{q}$

Electron-positron annihilation provides an excellent probe of the QCD vacuum and allows the study of theory both in the asymptotically free regime and the non-perturbative regime. Lowest order perturbative QCD can be applied at early times, when the strong coupling is relatively small at high Q^2, to calculate processes such as hard gluon radiation. In this high Q^2 regime the evolution of the hard partons can be described perturbatively. Eventually the hard partons turn into jets of hadrons in a process called *hadronization* or *fragmentation*. This long-distance process cannot be described by perturbative QCD and has not been calculated precisely. Rather, many phenomenological models are used to describe this low Q^2 process.

Among the six quark flavors, up, down and strange (u, d, and s) quarks have a mass (much) smaller than Λ_{QCD}. These light quarks suffer the most from the soft and collinear gluon radiation, which takes place at a scale where the strong coupling constant is of order *one*, eliminating the hope to apply perturbation theory to calculate light quark fragmentation functions. Only phenomenological models have been used to describe light quark fragmentation. Charm, bottom and top (c, b, and t) quarks are heavy quarks with a mass much greater than Λ_{QCD}. This mass difference between heavy and light quarks has a significant impact on their fragmentation. The top quark has a very large mass which would have been ideal for studying the behavior of fragmentation function in the heavy quark mass limit. Unfortunately top quark does not fragment because it has a much larger width, Γ, than the QCD scale Λ. It weakly decays before non-perturbative effects become important and therefore does not hadronize into a jet containing a t hadron. Charm and bottom quarks are the only heavy quarks that fragment into heavy hadrons. Their heavy masses allow a partial description of their fragmentation based purely on perturbative calculations, but such descriptions are not good enough. The heavier b mass allows b quark fragmentation to be better described by perturbative calculations. In addition, heavy quark effective theory (HQET) can be applied to study heavy quark fragmentation. In sum, heavy quark fragmentation provides the best probes for non-perturbative effects in quark fragmentation and the best testing ground for predictions of both perturbative calculations and phenomenological models. We return to this subject in the heavy quark fragmentation section later.

Let us consider the $e^+e^- \to Z^0 \to q\bar{q}$ process first. We learn about the original final state quark-antiquark pair and how they dynamically evolve and finally hadronize by studying the detected hadrons. The production of hadrons in $e^+e^- \to Z^0 \to q\bar{q}$, where the quark-antiquark pair must have opposite color charges, can be split into several stages (a schematic is shown in Figure 3-1):

Stage 1 Production of a $q\bar{q}$ pair in $e^+e^- \to q\bar{q}$

This is a hard electroweak (EW) process in which the primary quark and antiquark are produced. This EW process can be calculated perturbatively to high precision.

Stage 2 Perturbative evolution of the $q\bar{q}$ pair

At early times and high Q^2, the quark-antiquark pair interact with a small coupling constant α_s due to asymptotic freedom. Consequently, their evolution may be described perturbatively via parton Bremsstrahlung, including the following possible splittings: $q \to qg$, $\bar{q} \to \bar{q}g$, $g \to gg$, $g \to ggg$, and $g \to q\bar{q}$. Although in a perturbative regime, the calculation is nevertheless complicated by gluon radiation, vertex corrections and self-energy corrections. Perturbative QCD calculations for 2, 3, 4, and

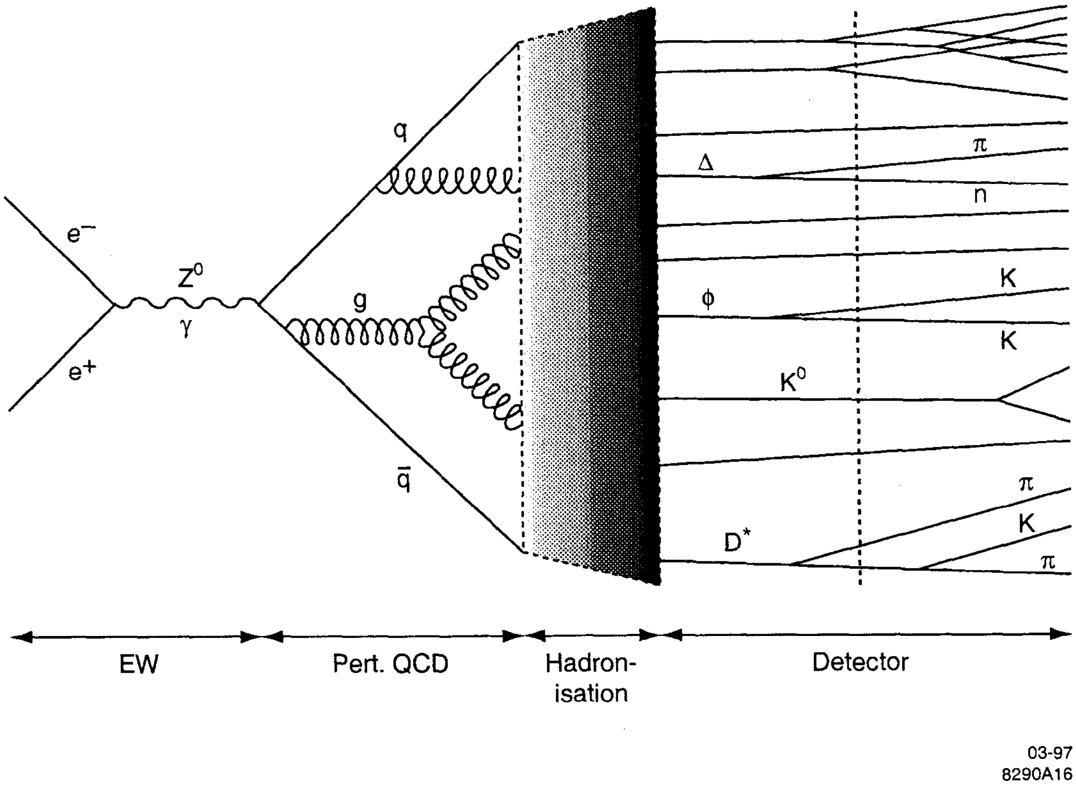

Figure 3-1: Schematic of hadron production in e^+e^- annihilation.

even 5 parton final states have been carried out. Leading logarithm approximation (LLA) gives inclusive properties of multi-g "final" states.

Stage 3 Hadronization: partons $\to$ final state hadrons

These final state partons including the original quark-antiquark pair which have lost some energy combine with other quarks and antiquarks to form primary hadrons resonances.

Stage 4 Decays of the primary resonances into 'stable' particles

For example, $B, K_s^0, \phi, \Delta, \rho, ... \to \pi^{\pm}, K^{\pm}, p, \overline{p}, ...$(leptons)

We first consider how stage 1 and 2 are treated in perturbative QCD.

3.1 Fixed Order Matrix Elements

The Born or tree level cross section for $e^+e^- \to q\bar{q}$ is given by the electroweak theory. Equation (A.42) gives the tree level formula in the limit $s = M_Z^2$ where the γ-exchange and interference terms are neglected. QCD contributes only the color factor $N_c = 3$ for final state $q\bar{q}$ pairs. In the three-jet process $e^+e^- \to q\bar{q}g$, effects proportional to α_s will appear in the cross section formula. To leading order, the cross section for three-jet production in the massless quark limit is given by [5]:

$$\frac{d\sigma}{dx_1 dx_2} = \sigma_0 \frac{\alpha_s}{2\pi} C_F \frac{x_1^2 + x_2^2}{(1-x_1)(1-x_2)}, \tag{3.1}$$

where σ_0 is the Born cross section, $C_F = 4/3$ is the quark color factor, and x_1 and x_2 are the scaled quark energies ($x_i = 2E_i/\sqrt{s}$). This cross section diverges in the collinear limit where $x_1 \to 1$ or $x_2 \to 1$, but in this regime three-jet final states are indistinguishable from two-jet states, and corresponding divergences in the one-loop propagator and vertex corrections cancel the collinear divergences.

Leading order calculations have been carried out for production of up to five jets [5, 6, 7, 8, 9]. Two- or three-jet cross sections have been calculated to $\mathcal{O}(\alpha_s^2)$ [8, 10, 7, 11]. Next-to-leading order [$\mathcal{O}(\alpha_s^3)$] QCD predictions for $e^+e^- \to 4$ jets, suppressing $\mathcal{O}(1/N_c^2)$ where $N_c = 3$ for QCD, is also available [12]. The precision in calculations of matrix elements has improved, however, due to limited orders in α_s considered, one should not expect these predictions to be sufficient to describe the detailed structure of e^+e^- annihilations where multiple gluon emissions play an important role even up to orders of α_s.

3.2 Parton Shower QCD Calculations

A practical approach to predicting the soft structure of jets, other than direct matrix element calculations, is the *parton shower* technique, which is based on the Leading

Logarithm Approximation (LLA) to perturbative QCD, where leading logarithmic term $\alpha_s^n(Q^2)\log^n(Q^2/\Lambda_{QCD}^2)$ are summed to all orders n[1]. This approach approximates the calculation of the soft structure of jets down to scales $\sim \Lambda_{QCD}$. Refinements that include sub-leading terms are possible. In the parton shower approach, individual events are generated by quarks produced in $e^+e^- \rightarrow q\bar{q}$ which radiate off-shell gluons ($q \rightarrow qg$), which in turn can branch into parton pairs ($g \rightarrow gg$ and $g \rightarrow q\bar{q}$). Hence a *parton shower* or cascade is produced, as is shown in Figure 3-2. In

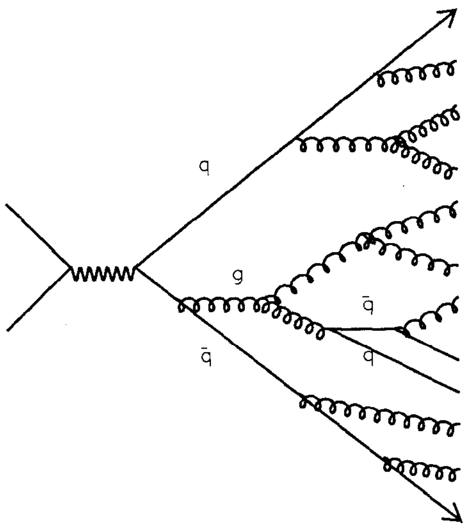

Figure 3-2: Schematic representation of a parton shower.

LLA, by neglecting the interference terms [13], it is possible to treat these branchings as classical probabilities.

Consider the branching of a quark a turning into a quark b and a gluon c. Let z be the fraction of 4-momentum of the initial quark a retained by the resulting quark b after the branching, hence c has a momentum fraction of $(1-z)$. Since the probability for an initial quark to radiate a gluon is proportional to the strong coupling constant, we have $\mathcal{P}_a \propto \alpha_s(Q^2)$. As a quark evolves by repeatedly splitting into a quark and

[1]Equation (2.17) indicates that $\alpha_s(Q^2)\log(Q^2) \sim 1$.

a gluon, its momentum Q^2 decreases so that the strong coupling constant $\alpha_s(Q^2)$ increases. To take this change of mass scale and therefore coupling strength into account, we define a dimensionless parameter, $\tau = \log(Q^2/\Lambda^2)$, commonly referred to as the virtuality scale. So $\alpha_s(Q^2)$ is now represented as $\alpha_s(\tau)$. The meaning of τ is clearly seen as follows. τ is at its maximum value initially when the quark is most energetic, and it decreases as Q^2 decreases. When non-perturbative effects set in at $Q^2 \sim \Lambda^2$, τ becomes ~ 0. Therefore, τ can be considered as a measure of the 'time' it will take for the quark to enter the non-perturbative regime or the hadronization stage.

The probability for a quark to radiate a gluon also depends on the fraction energy of the radiated gluon. Therefore, apart from $\alpha_s(\tau)$, the probability $\mathcal{P}_a$ must also depend on the 4-momentum fraction, z, defined above. The specific functional form of this dependence of the branching probability on z is given by the process-dependent parton *splitting function* $P_{a\to bc}(z)$ (often denoted by $P_{ba}(z)$, where b is the result of the splitting of a).

Since the virtually ('time') is measured by τ, the differential probability for the branching of a parton, $a \to bc$, to take place within a small interval $d\tau$, and within a given fraction-momentum interval dz, is given by [14, 15]

$$d\mathcal{P}_a(z,\tau) = \sum_{b,c} \frac{\alpha_s(\tau)}{2\pi} P_{a\to bc}(z) d\tau dz, \tag{3.2}$$

where we sum over all parton flavors for b and c into which a is allowed to split. Integrating both sides of (3.2) over z, we obtain the probability for a parton a to branch into any flavored b and c within a small virtuality interval, and with *any* momentum fraction,

$$\mathcal{I}_a(\tau)d\tau = \int_z d\mathcal{P}_a(z,\tau) = \int_z \sum_{b,c} \frac{\alpha_s(\tau)}{2\pi} d\tau P_{a\to bc}(z) dz. \tag{3.3}$$

The scale-independent (Q^2- or τ-independent) parton splitting function $P_{a\to bc}(z)$ is process-dependent and is given by

$$P_{q\to qg}(z) = \frac{4}{3}\left(\frac{1+z^2}{1-z}\right), \tag{3.4}$$

$$P_{q\to gq}(z) = P_{q\to gq}(1-z), \tag{3.5}$$

$$P_{g\to gg}(z) = 6\left(\frac{1-z}{z} + \frac{z}{1-z} + z(1-z)\right), \tag{3.6}$$

$$P_{g\to q\bar{q}}(z) = \frac{1}{2}(z^2 + (1-z)^2). \tag{3.7}$$

Apart from the color factor $\frac{4}{3}$, the splitting function for $q \to qg$ is the same as the splitting function for an electron to radiate a virtual photon, derived independently by Weizsacker and Williams in 1934.

The probability that a parton starting with virtuality τ_{max} will reach τ without undergoing any splitting is given by the Sudakov factor $S_a(\tau)$

$$\mathcal{P}_{\text{no-emission}}(\tau_{max}, \tau) = exp\left(-\int_{\tau}^{\tau_{max}} \mathcal{I}_a(\tau')d\tau'\right) = \frac{S_a(\tau_{max})}{S_a(\tau)}, \tag{3.8}$$

$$S_a(\tau) = exp\left(-\int_{\tau_0}^{\tau} d\tau' \int_{z_{min}(\tau')}^{z_{max}(\tau')} dz \frac{\alpha_s(Q^2)}{2\pi} P_{b\to bc}(z)\right), \tag{3.9}$$

where $\tau_0 = \log(Q_0^2/\Lambda^2)$ and Q_0 is a shower virtuality cutoff, z_{max} and z_{min} are kinematic cutoffs based on the virtuality τ'. The Sudakov factor can be pre-tabulated in Monte Carlo programs, such as the Lund algorithm. The evolution of an individual parton is determined by finding τ such that

$$S_a(\tau) = \frac{S_a(\tau_{max})}{R}, \tag{3.10}$$

where R is a random number between 0 and 1. The main parameters of parton shower models are the virtuality cutoff Q_0 and the scale Λ^2. Various parton shower models differ in their choice of the virtuality parameter τ, in their choice of the scale Q^2 for the running of α_s, and in their definition of z, where z can be defined as the E_b/E_a, $p_{\|b}/p_{\|a}$, or the light-cone variable $(E_b + p_{\|b})/(E_a + p_{\|a})$.

In general, parton shower technique gives a poor prediction for the hard three-jet rate, but this can be improved by matching the first stage of the parton shower branching with a matrix element calculation. In addition, the inclusion of sub-leading logarithms may modify the splitting functions to an extra order in α_s in the case of Next-to-Leading order Logarithm Approximation (NLLA) [16], or it may impose the additional constraint of angular ordering on the gluon emission in the case of the Modified Leading Logarithmic Approximation (MLLA) [17]. MLLA extends the resummation to terms of order $\alpha_s^n(Q^2)\log^{2n}(Q^2/\Lambda^2)$ and is only useful quantitatively for calculations of the evolution of hadron multiplicities.

Partons present at the end of parton showering stage combine to generate primary hadrons, a process called hadronization. Hadronization is typically characterized by the fragmentation functions (see Section 3.4). Let us first discuss the $e^+e^- \to$ hadron cross section which is closed related to the fragmentation functions.

3.3 $e^+e^- \to$ Hadron Cross Section

The naive parton model prediction for the ratio, R, of the cross section of the inclusive process $e^+e^- \to$ hadrons to that of the process $e^+e^- \to \mu^+\mu^-$ is

$$R = \frac{\sigma(e^+e^- \to hadrons)}{\sigma(e^+e^- \to \mu^+\mu^-)} = N_c \sum_{i=1}^{n_f} e_{q_i}^2, \tag{3.11}$$

[2]Since the parton shower calculation is incomplete at any fixed order in α_s, it is not possible to relate the parton shower scale Λ to the standard $\Lambda_{\overline{MS}}$ or any other Λ_{QCD}.

where i is the flavor index, e_{q_i} is the electric charge of the quark q_i of flavor i, and the n_f is *not* the total number of flavors in the theory, but the number of flavors that are allowed to be produced at the given center-of-mass energy of Q. $N_c = 3$ is the number of colors in QCD.

Real gluon emission ($q \to qg$), virtual gluon corrections at the vertex, and quark self-energy in the final state modify the total hadronic cross-section by order $\alpha_s(Q^2)$ (to lowest order). The cross-section for real gluon emission diverges in the soft gluon limit, which is called infrared (IR) divergence, or in the limit when the q and g become collinear, which is referred to as the mass singularity. Virtual gluon correction and quark self-energy are in general both infrared and ultraviolet (UV) divergent. Regularization schemes were introduced to cancel these divergences [18, 19, 20, 21]. Dimensional Regularization [20, 21] removes both IR and UV divergences.

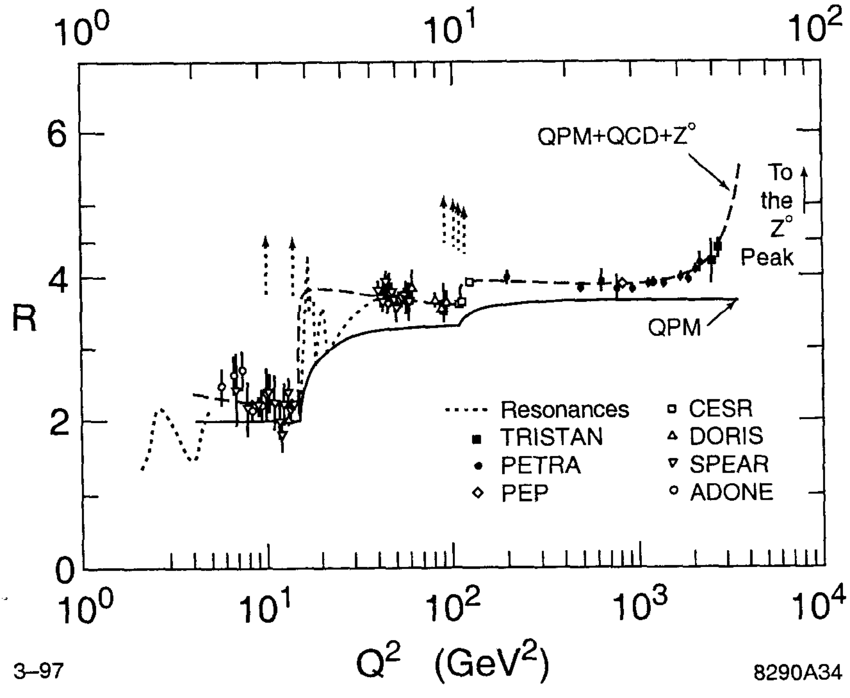

Figure 3-3: The R ratio as a function of c.m. energy. The expectation for $N_c = 3$ is shown as a solid line, the dashed line shows the predicted value of $N_c = 3$ when the effects of QCD and the Z^0 are included. The top axis is Q. At the Z-pole, $R = 20.78 \pm 0.03$.

The Block-Nordsieck theorem [22], which states that transition rate summed over the final states is free of infrared divergence (soft), generally breaks down in QCD. Instead, the transition rate summed over the initial and final degenerate states is still free of infrared (soft and collinear) divergence at any order of perturbation theory, which is the KLN theorem [23]. This insures that the final result is finite. At the lowest order, the correction to the Born cross section is

$$\sigma(e^+e^- \to hadrons) = \sigma_{Born}(1 + \frac{\alpha_s}{\pi}). \tag{3.12}$$

Shown in Figure 3-3 is a summary of measurements of R which were made up to 1988, as a function of c.m. energy [24]. The increase in R just above $Q^2 = 10$ and 100 GeV^2 represent the $c\bar{c}$ and $b\bar{b}$ thresholds. Moreover, the QPM+QCD+Z^0 prediction comes very close to data if the quarks are assigned fractional charges and the number of colors $N_c = 3$.

3.4 Fragmentation Functions

Hadronization can be characterized by the quark or gluon fragmentation function which is the distribution the fraction of the energy (or momentum) of the fragmenting parton i carried by the produced primary hadron h. The fragmentation function is often written as $D_i^h(z, \mu^2)$. Here, $z = E_h/E_i$ where E_i and E_h are the energies (or momenta) of the fragmenting parton i and the produced primary hadron h, respectively. μ^2 is an arbitrary factorization scale (see below).

Since the number of hadrons of type h with energy fraction $z = E_h/E_i$ per dz is $D_i^h(z, \mu^2)dz$, conservation of energy requires that

$$\sum_{\text{All } h} \int_{z_{min}^h}^1 z D_i^h(z, \mu^2) dz = 1, \tag{3.13}$$

where $z_{min}^h = 2m_h/E_i$ is the kinematic threshold (m_h is the mass of the hadron), and the summation is over the available hadron types h. The mean multiplicity of hadron of type h emerging from a parton i is

$$\langle n_h^i \rangle = \int_{z_{min}^h}^1 D_i^h(z, \mu^2) dz. \tag{3.14}$$

3.4.1 Symmetries of Fragmentation Functions

Due to CP or isospin symmetry, we expect a set of symmetry relations given below, for example

$$D_i^h(z, \mu^2) = D_{\bar{i}}^{\bar{h}}(z, \mu^2), \tag{3.15}$$

$$D_u^{\pi^+}(z, \mu^2) = D_{\bar{d}}^{\pi^+}(z, \mu^2), \tag{3.16}$$

$$D_u^{\pi^+}(z, \mu^2) = D_{\bar{d}}^{\pi^-}(z, \mu^2). \tag{3.17}$$

3.4.2 Factorization of Single Hadron Cross Section

According to the factorization theorem, the measured fragmentation function can be written as a convolution of a short-distance, perturbative term (coefficient function) and a long-distance, non-perturbative term (operator matrix element). We can therefore express the single hadron inclusive cross section in terms of the perturbative parton differential cross sections and their respective fragmentation functions.

To produce a hadron of type h with a scaled energy $x = 2E_h/Q = 2E_h/\sqrt{s}$, where $Q = \sqrt{s}$ is the center of mass energy, we first produce a parton i with a scaled energy $y = 2E_i/Q = 2E_i/\sqrt{s}$ and then allow this parton i to fragment into the hadron h. Since the energy of the parton i must be larger than that of the hadron h, we have $y > x$. In fact, using the z variable defined above, we have $x = yz$ or $z = x/y$. Therefore the probability of producing h with an energy fraction between x and $x + dx$ is

$$d\sigma^h(x, Q^2) = \sum_i \int_x^1 dy \frac{d\sigma^i(y, Q^2, \mu^2)}{dy} D_i^h(z = \frac{x}{y}, \mu^2) dz, \tag{3.18}$$

where $(d\sigma^i/dy)dy$ is the differential probability of producing a parton i ($i = q, \bar{q}$, or g)

with energy fraction between y and $y+dy$, and $D_i^h(z)dz$ is the differential probability that the parton i fragments into the hadron h carrying an energy fraction between $z = E_h/E_i$ and $z+dz$. The integration over y is to sum over all possible intermediate parton fraction momentum y. Finally, all parton flavors that can produce h are summed over. The variables y and z are *not* experimental observables, but $x = yz$, which is $E_h/(Q/2) = E_h/(\sqrt{s}/2)$, *is* an experimental observable. Since $0 \le z \le 1$, we have $x \le y = x/z \le 1$. $D_i^h(z)$, which does not depend on scale Q^2, is the fragmentation function containing non-perturbative information about hadronization and is not calculable using perturbation methods. In the case of only one quark flavor (q and $\bar{q}$), (3.18) can simply be written as

$$\begin{aligned} d\sigma^h(x,Q^2) &= \int_x^1 dy \frac{d\sigma^q(y,Q^2)}{dy} D_q^h(\frac{x}{y})\frac{dx}{y} \\ &+ \int_x^1 dy \frac{d\sigma^{\bar{q}}(y,Q^2)}{dy} D_{\bar{q}}^h(\frac{x}{y})\frac{dx}{y} \\ &+ \int_x^1 dy \frac{d\sigma^g(y,Q^2)}{dy} D_g^h(\frac{x}{y})\frac{dx}{y}. \end{aligned} \tag{3.19}$$

3.4.3 Single Hadron Inclusive Cross Section

The single hadron inclusive cross section is given by

$$\frac{d\sigma}{dx}(e^+e^- \to hX) \equiv \frac{d\sigma^h}{dx}(x,Q^2), \tag{3.20}$$

where the r.h.s is given by (3.18) or (3.19). Using (3.13) and normalization properties of quark splitting functions $P_{q\to qg}$ and $P_{q\to gq}$, it can be shown that the cross section is normalized according to

$$\sum_{\text{All } h} \int_0^1 \frac{x}{2}\frac{d\sigma^h}{dx}(x,Q^2)dx = \sigma_{tot}^{e^+e^-}, \tag{3.21}$$

where $\sigma_{tot}^{e^+e^-}$ is the total cross section for $e^+e^- \to$ hadrons [25, 26]. In general the inclusive cross section is a function of the center of mass energy Q^2.

Using the above defined fragmentation function, the distribution $f^h(x, Q^2)$ of the scaled hadron energy x is

$$
\begin{aligned}
f^h(x, Q^2) &\equiv \frac{1}{\sigma_{tot}^{e^+e^-}} \frac{d\sigma}{dx}(e^+e^- \to hX) \\
&= \frac{1}{\sigma_{tot}^{e^+e^-}} \sum_i \int_x^1 \frac{dy}{y} \frac{d\sigma^i(y, Q^2, \mu^2)}{dy} D_i^h(\frac{x}{y}, \mu^2),
\end{aligned}
\tag{3.22}
$$

where we have used (3.18). Equation (3.22) is sometimes used to define the fragmentation function. At the lowest order (tree-level), no gluon Bremsstrahlung occurs, so the parton differential cross section $d\sigma/dy$ is reduced to

$$
\begin{aligned}
f^h(x, Q^2) &= \frac{1}{\sigma_{tot}^{e^+e^-}} \sum_i \int_x^1 \frac{dy}{y} \sigma_0^i \delta(y-1) D_i^h(\frac{x}{y}, \mu^2) \\
&= \frac{1}{\sigma_{tot}^{e^+e^-}} \sum_i \sigma_0^i D_i^h(x, \mu^2),
\end{aligned}
\tag{3.23}
$$

where $\sigma_0^i\ \delta(y-1)$ is the tree-level quark differential cross section, and

$$
\begin{aligned}
\sigma_0^i &= \sigma(e^+e^- \to q_i \bar{q}_i) \\
&= N_c \frac{4\pi\alpha_{EM}^2}{3} e_{q_i}^2
\end{aligned}
\tag{3.24}
$$

is the tree level $e^+e^- \to q\bar{q}$ cross section. e_{q_i} is the electric charge of the quark q_i. $N_c = 3$ is the number of colors.

3.4.4 Evolution Equation for Fragmentation Function

The fragmentation function $D_i^h(z, \mu^2)$ obeys an evolution equation [26] similar to the parton density DGLAP evolution equation [13, 27, 14]

$$
\begin{aligned}
\mu^2 \frac{\partial}{\partial \mu^2} D_i^h(z, \mu^2) &= \frac{\alpha_s(\mu^2)}{2\pi} \sum_j \int_z^1 \frac{dy}{y} P_{i\to j}(y, \mu^2) D_j^h(\frac{z}{y}, \mu^2) \\
&= \frac{\alpha_s(\mu^2)}{2\pi} \sum_j \int_z^1 \frac{dy}{y} P_{i\to j}(\frac{z}{y}, \mu^2) D_j^h(y, \mu^2),
\end{aligned}
\tag{3.25}
$$

where the summation over j runs over all available parton flavors, and $P_{i\to j}$ is, as described earlier, the splitting function of parton i into j. Note that the result of the integration remains the same if the variables z/y and y are interchanged between the two functions $P_{i\to j}$ and D_j^h.

The evolution equation (3.25) produces the scaling violation in the x-dependence of the inclusive cross section (3.22). For example, $f^h(x = 0.5, Q = 90\ \text{GeV})$ is generally not the same as $f^h(x = 0.5, Q = 10\ \text{GeV})$. Rather, experimental data on the hadron spectra at one center-of-mass energy scale Q_1^2 can be compared with the fragmentation function in (3.22), which can then be evolved to another energy scale ${Q_2}^2$ using (3.25). From the viewpoint of scaling violation, the experimental determination of the b fragmentation function in $e^+e^- \to Z^0$ at SLD will contribute one data point to join other data points to demonstrate the scaling violation in fragmentation. Since uncertainty in the measured fragmentation function at one scale, when evolved to another scale, can lead to a larger uncertainty, the measurement precision at M_Z^2 is likely to influence the precision of the evolved b fragmentation at higher Q^2. Very precise measurement at the Z^0 mass scale can provide solid predictions for jets at high energies in e^+e^- or $p\bar{p}$ collisions, for example, for $W^\pm$, t, or even the Higgs decays.

3.4.5 Experimental Issue

Since it is impossible to experimentally identify the individual partons that fragment, there is no way to directly measure the fragmentation function $D_i^h(z, \mu^2)$. Fortunately, the inclusive scaled-energy spectra $f^h(x)$ are experimental observables. By using various proposed fragmentation models, we can compare the measured hadron energy spectra with model predictions. Fragmentation models that describe the data well not only can provide insights into the underlying dynamics, but also can be very important for improving Monte Carlo simulations of fragmentation.

Heavy quark tagging techniques allow high purity separation of events from light quarks (uds) and those from heavy quarks (b or c). Therefore we can study fragmentation in light quark events and heavy quark events separately. Using the polarization of the SLC electron beam, together with the electroweak forward-backward asymmetry of quarks, we can further separate quark jets from antiquark jets. This can provide constraints on the non-singlet fragmentation defined as $D_i^h(z,\mu^2) - D_{\bar{i}}^h(z,\mu^2)$. In particular, this thesis describes a new experimental measurement of the b quark fragmentation function, which will be described later.

3.5 Fragmentation Models

In e^+e^- annihilation experiments, Monte Carlo simulation of the fragmentation process is essential. Fragmentation models, usually phenomenological, are often used in such simulations to allow for the study of background and efficiency in physics analyses, and for comparison with experimental data to test input models themselves. Improving fragmentation models is thus an important step toward improving the quality of physics analyses. Testing existing models, therefore, is the starting point. This thesis tests various models for b quark fragmentation using a much improved B hadron energy data spectrum.

Currently, there are three major types of fragmentation models

- The independent fragmentation model
- The string fragmentation model
- The cluster fragmentation model

Note that in discussing fragmentation models, the fragmentation function is usually denoted as $f(z)$ instead of the more complicated $D_i^h(z)$. $f(z)$ should not be confused with the inclusive hadron spectrum $f^h(x)$ mentioned earlier.

3.5.1 Independent Fragmentation

In this type of Independent Fragmentation (IF) model, each energetic parton in the event fragments in isolation and corresponds to a well separated "jet". An initial quark q with energy W pairs up with an antiquark $\bar{q}_1$ and forms a hadron $q\bar{q}_1$ carrying energy fraction $W \cdot z_1$, leaving behind a remnant q_1 with energy $(1 - z_1)W$. This q_1 in turn produces another hadron $q_1\bar{q}_2$ carrying an energy $z_2(1 - z_1)W$, leaving behind a remnant q_2. This process continues until the energy left with the quark q_n is too low to form the lightest hadron. The fraction of energy of the parent quark shared by the daughter products is characterized by a fragmentation function, $f(z)$, which is assumed to be the same at each step of the fragmentation process.

One problem with the IF is that it does not conserve 4-momentum in each jet or flavor in each event. To fix these problems, an additional *ad hoc* rescaling prescription is introduced. The IF models reproduce global properties of high energy, isolated jet well. They do not reproduce energy flow between jets of an event. Data from e^+e^- annihilation have excluded this fragmentation scheme. However, IF models are still used in $p\bar{p}$ Monte Carlo simulations, where details of the soft structure of jets are of little importance, but will not be considered in this thesis.

The Field and Feynman model [28] was one of the first versions of the scheme to be implemented by a Monte Carlo calculation. Various other independent fragmentation schemes were later developed. One of the most commonly used in hadron-hadron collider is the ISAJET Monte Carlo [29].

3.5.2 String Fragmentation

String Fragmentation: The Lund Model

The string fragmentation scheme was first introduced in 1974 by Artru and Mennessier [30]. Subsequently, the Lund group developed the Lund model of string fragmentation. Their Monte Carlo simulation, JETSET 7.4 [15], is a powerful and popular tool for physics Monte Carlo simulations, and is used for the analysis in this thesis.

The string model is motivated by the idea that the partons are connected by a color flux tube, or string. The transverse size of the string is small compared to its length, due to the couplings between gluons. The string has a constant energy density per unit length, or string constant, of order ~ 1 GeV/fm. As the partons move apart the energy of the string rises linearly. When the potential energy has grown high enough to produce a $q\bar{q}$ pair, the string breaks to form two separate string objects.

Figure 3-4 shows a schematic of the process. Horizontal axis x is the spatial-x

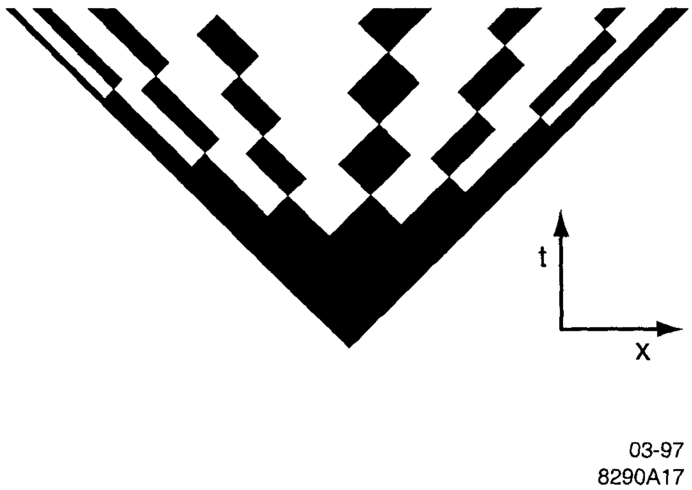

Figure 3-4: Schematic of hadronization in JETSET.

axis, and vertical axis denotes the time. When a $q_0\bar{q}_0$ pair is produced at the (x, t) origin $(x_0 = 0, t_0 = 0)$, shown in the figure as the bottom tip of the large dark angle, the q_0 and $\bar{q}_0$ start moving out back-to-back in the center-of-mass frame. In the $x - t$ plane, since the partons are highly relativistic, their world-lines are at an angle of $\simeq 45°$ (or $135°$) relative to the x axis. In between the $q\bar{q}$ pair there exists the color flux tube or string which is represented by the line that connects the pair. This line sweeps out a area on the $x - t$ plane which is the dark area. The string is stretched and a new pair, $q_1\bar{q}_1$ can be produced at a new point, (x_1, t_1), which is the point where white area starts to emerge at the earliest time in the figure, when the string breaks into two parts. Now there are two strings, one connecting q_0 and $\bar{q}_1$, the other connecting $\bar{q}_0$ and q_1. In between q_1 and $\bar{q}_1$, there is no string and therefore no dark area. This breaking process continues. When a quark q_i meets an antiquark $\bar{q}_j$, they form a hadron $q_i\bar{q}_j$. This bounded quark-antiquark pair oscillates in a "yo-yo" mode, which, in a highly boosted Lorenz frame, looks like a rectangle tilted by $\simeq 45°$ (or $135°$). The string breakup continues until there exists only hadrons in the system.

The Lund Monte Carlo reflects the fact that all $q\bar{q}$ production vertices are causally disconnected and the process must be symmetric from either end of the string. This symmetry is implemented by breaking the string into hadrons from either end, much like in IF models, but using a specific probability for a quark to hadronize into a hadron. The Lund symmetric fragmentation function is

$$f(z) = \frac{1}{z}(1-z)^a \exp\left(-\frac{bm_\perp^2}{z}\right), \tag{3.26}$$

where z is the fraction of the light-cone momentum, $E+p_{||}$, of a parent string taken by the daughter, $m_\perp = \sqrt{m^2+p_\perp^2}$, m is the quark mass, and a and b are parameters of the model, which must be tuned to best fit the data [31]. The symbols $\perp$ and $||$ refer to the string axis. a and b are free parameters that may be flavor dependent. A large number of additional parameters are used to tune the relative production of particles [32]. The splitting of the string is done in such a way that energy, momentum and all the quantum numbers are conserved.

Massive quarks must be produced some distance apart so that the field energy between them can be transformed into mass and transverse momentum. This is done by producing them at a point and allowing them to quantum-mechanically "tunnel" out to the allowed region. This tunneling process occurs with a probability [33]:

$$P = \exp\left(-\frac{\pi m_\perp^2}{\kappa}\right), \tag{3.27}$$

where κ is the string constant. The mass term in the exponent suppresses strange and heavy quark (c, b) production, yielding the following relative production rates for quark flavors $u : d : s : c \sim 1 : 1 : 0.3 : 10^{-11}$. Heavier quarks are not produced in the string break up, but are allowed to be produced in the parton shower process.

String fragmentation must be combined with some perturbative calculation of the underlying hard process, typically either a second-order matrix element calculation [34] or an LLA parton shower [35]. The JETSET parton shower model has been tuned to reproduce well most experimental observables in e^+e^- data [36]. However, the tuning of large number of parameters make it hard to constrain the underlying dynamics of the model.

String Fragmentation: The Bowler Model

Bowler has shown [37], within the framework of the Artru-Mennessier model, that a massive endpoint quark with mass M_Q leads to a modification of the symmetric fragmentation function, due to the fact that the string area swept out is reduced for massive endpoint quarks compared with massless quarks. The resulting function is similar to the one in the Lund model, but with a new parameter r_Q, which is in principle predicted to be one [15]:

$$f(z) = \frac{1}{z^{1+r_Q bm_Q^2}}(1-z)^a \exp\left(-\frac{bm_\perp^2}{z}\right). \tag{3.28}$$

See (3.26) for comparison.

String Fragmentation: The UCLA Model

The UCLA model [38, 39] is an extension of the Lund string model with the hadron species parameters determined by the phase space, spin counting, and isospin counting. In the JETSET scheme, M_h and p_T are chosen first, and then z is drawn from $f(z)$, where $\int f(z)dz = 1$ for each hadronic species. In the UCLA model, $f(z)$ is a universal function with $\sum_h \int f^h(z)dz = 1$. Thus a and b remain free parameters, yet all of the suppression of vector and strange hadrons is done through the increased masses of those particles and the Clebsch-Gordon coefficients for the couplings between neighboring spins. The UCLA model has seen remarkable success in fitting a wide range of data.

3.5.3 Cluster Fragmentation

In the cluster fragmentation model the partons present at the end of a parton shower are used to form colorless clusters, each is split into a $q\bar{q}$ pair; quarks and antiquarks with opposite color are paired up locally to form clusters, which are the primary fragmentation products. Heavy clusters decay into lighter ones, and these ultimately decay into the final state hadrons. Figure 3-5 shows a diagram of the cluster fragmentation. The first widely successful model of this type was developed by Marchesini

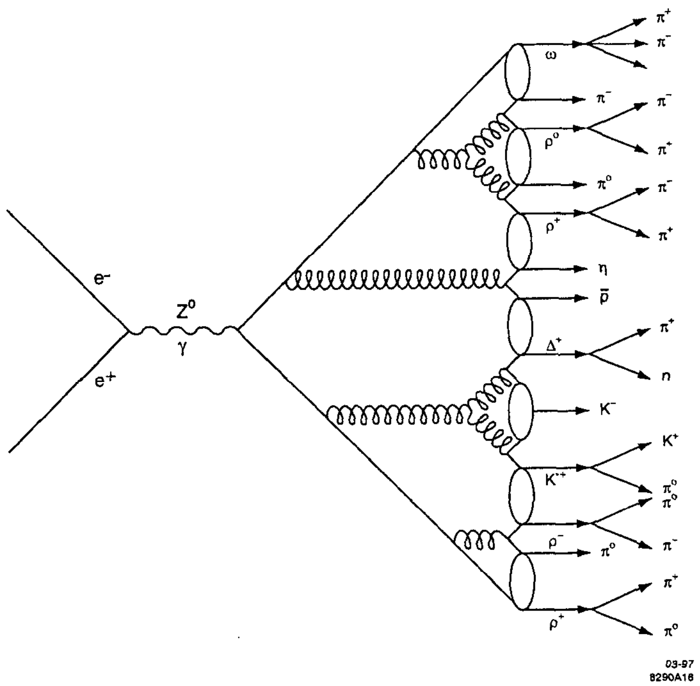

Figure 3-5: Schematic of hadronization in HERWIG.

and Webber [40]. The present version of the program is known as HERWIG [41]. HERWIG does a good job of evolving the partons but the resulting cluster fragmentation does not describe data very well, which is partly because Local Parton Hadron

Duality (LPHD) [42] does not work very well for producing heavy quark energy spectra.

3.6 Heavy Quark Fragmentation Function

Because of the large mass of a heavy quark, the behavior of heavy quark fragmentation is very different from that of light quarks. Suzuki, Bjorken, and others pointed out long ago that heavy hadrons carry most of the energy of the fragmenting heavy quarks [43, 44, 45, 46]. Within the parton-model, when a heavy quark with a mass $M > 5$ GeV hadronizes into a primary heavy hadron containing the heavy quark and a light quark, the average scaled momentum of the heavy hadron is expected to be [43, 44]

$$\langle z \rangle \sim 1 - 1/M_Q, \tag{3.29}$$

where z is the scaled momentum of the heavy hadron, and M_Q is the mass of the heavy quark (Q), expressed in GeV. For the bottom (b) quark with a mass of about 5 GeV, $\langle z \rangle \sim 0.80$. This is reasonably close to the current measured value of about 0.72. It turns out that this leading nature of heavy hadron can also be understood from a purely perturbative point of view [47]. Hard gluon radiation can only occur at very early times and is highly suppressed due to the small coupling α_s. Only (soft) gluons with an energy fraction of order $\frac{\Lambda}{M_Q} \ll 1$ may be radiated with high probability. Λ is the effective QCD scale which determines when the non-perturbative effect takes over and is approximately 200 MeV. The predominant emission of soft gluons from heavy quarks leads to a heavy hadron energy spectrum peaked near $z \sim 1 - \Lambda/M_Q$ or $1 - M_q/M_Q$ where M_q and M_Q are the mass of light and heavy quarks, respectively, and $M_Q \gg \Lambda > M_q$.

Due to the unknown non-perturbative aspect of fragmentation, so far there has been no theoretical prediction of the complete fragmentation function that is derived from first principles and can be readily compared with experimental data. Instead, non-perturbative contribution are theoretically treated in two different approaches: phenomenological models and perturbative QCD calculations. In both cases the non-perturbative parameters are to be extracted from experimental data.

3.6.1 Phenomenological Approach

In a phenomenological approach, the fragmentation function is not derived from first principles or QCD, but is to a large extent based on some phenomenological assumptions. A model usually contains one or more parameters which can only be determined from experimental data. Models whose predictions agree with data could provide insights into the underlying non-perturbative dynamics and are useful for accurate Monte Carlo simulations.

The Peterson Model

The Peterson model has been widely used in e^+e^- annihilation Monte Carlo simulation. The model is based on the following ansatz [48]: the fragmentation function of a heavy quark Q is proportional to the quantum-mechanical transition probability (amplitude squared), in the parton-model picture, of the process $Q \to H + q$, where $H = (Q\bar{q})$,

$$M(Q \to H + q) \propto \frac{1}{\Delta E}. \tag{3.30}$$

Let z be the fraction of the longitudinal momentum P of Q carried by H, then

$$\begin{aligned} \Delta E &= \sqrt{m_{Q\perp}^2 + z^2P^2} + \sqrt{m_{q\perp}^2 + (1-z)^2P^2} \\ &\quad -\sqrt{m_Q{}^2 + P^2} \\ &\propto 1 - \tfrac{1}{z} - \tfrac{\epsilon_Q}{1-z}, \end{aligned} \tag{3.31}$$

where the single parameter $\epsilon_Q \sim m_{q\perp}^2/m_{Q\perp}^2$, and $m_\perp^2 = m^2 + P_\perp^2$ is the transverse mass. Taking a factor of z^{-1} for longitudinal phase space, we arrive at the fragmentation function

$$D_Q^H(z) = \frac{N}{z(1 - \frac{1}{z} - \frac{\epsilon_Q}{1-z})^2}, \tag{3.32}$$

where N is a normalization factor and ϵ_Q must be determined from experiments.

Since the Peterson model contains only one free parameter and it was consistent with early heavy quark fragmentation data, it has been used as the standard in Monte Carlo simulations of b and c fragmentation functions by many experiments, including both the LEP and SLD experiments. It is important to test the Peterson model at a higher precision. Recent measurements of the b fragmentation function suggested that the shape of the Peterson functional form is too wide to reproduce the data.

Figure 3-6 shows the Peterson fragmentation function $f(z)$ using parameters in the default SLD Monte Carlo simulation: $\epsilon_b = 0.006$ for b quarks and $\epsilon_c = 0.06$ for c quarks. The much larger value of ϵ_c compared with ϵ_b is due to the mass-scaling of the ϵ_Q parameter: $\epsilon_c/\epsilon_b \simeq (m_{b\perp}/m_{c\perp})^2$. Table 3.1 lists some relevant z parameters

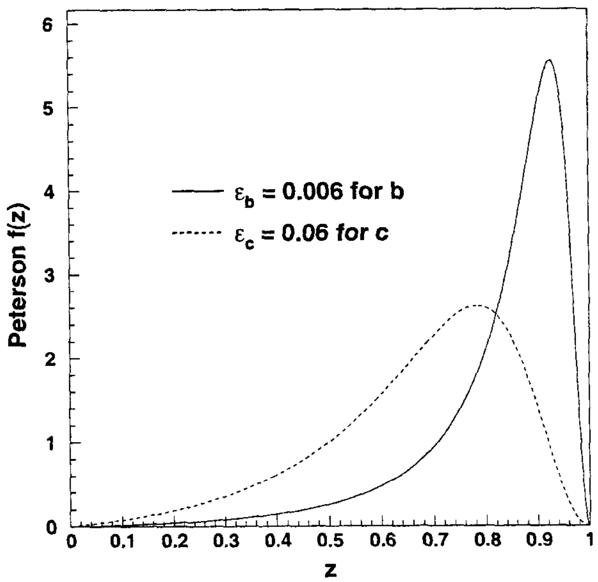

Figure 3-6: Peterson functions $f(z)$ for b quark using $\epsilon_b = 0.006$ and for c quark using $\epsilon_c = 0.06$ where $z = P_{H\|}/P_{Q\|}$ ($Q = b$ or c).

associated with the two Peterson functions for b and c quarks.

Quark	Peak z_{peak}	Average $\langle z \rangle$	Width Δz
b	0.93	0.83	0.14
c	0.78	0.67	0.18

Table 3.1: Peak, average and width of the default SLD Peterson functions for b and c.

The Kartvelishvili (or KLP) Model

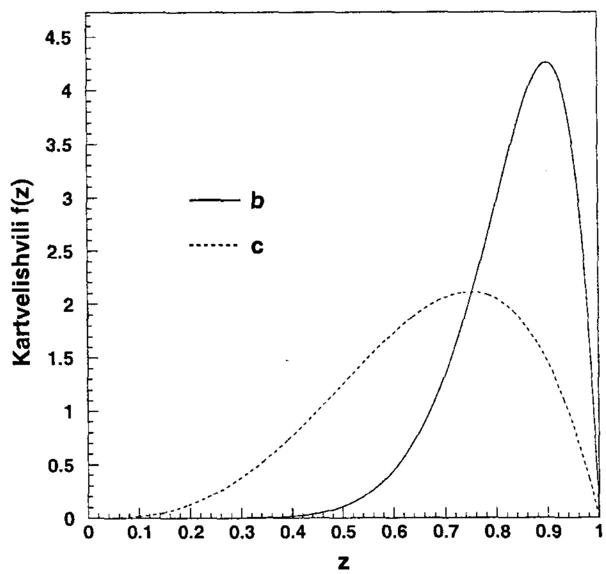

Figure 3-7: Kartvelishvili functions $f(z)$ for b and c quark where $z = P_{H\|}/P_{Q\|}$ ($Q = b$ or c).

Kartvelishvili, Likhoded, and Petrov analyzed the inclusive charm spectra in Ref. [49]. Assuming the validity of the reciprocity relation [50] at $z \sim 1$,

$$f(z) = D_c^D(z) = F_D^c(z), \tag{3.33}$$

where $f(z) = D_c^D(z)$ is the c fragmentation into a charm hadron D, and $F_D^c(z)$ is the c quark density in the charm hadron D, they proposed a new charm fragmentation function

$$f(z) = \frac{\Gamma(2+\gamma-\alpha_c-\alpha_q)}{\Gamma(1-\alpha_c)\Gamma(1+\gamma-\alpha_q)} z^{-\alpha_c}(1-z)^{\gamma-\alpha_q}, \tag{3.34}$$

Further, assuming that (3.33) holds for all z, the charm fragmentation function becomes

$$f(z) = 20z^3(1-z), \tag{3.35}$$

which peaks at $z \sim 0.75$. Generalizing this result to the case of b quark, the fragmentation function is

$$f(z) = 110z^9(1-z), \tag{3.36}$$

which peaks at $z \sim 0.90$. The functional forms of the two fragmentation functions in this model are shown in Figure 3-7. As in the Peterson model, both c and b fragmentation functions peak at large z, with the c fragmentation function softer than the b fragmentation function. Table 3.2 lists some relevant z parameters associated with the Kartvelishvili functions for b and c quarks. Compared with the Peterson b quark fragmentation function, the Kartvelishvili function is significantly narrower ($\Delta z = 0.10$), peaks at a lower z value, and almost vanishes for $z < 0.4$. For charm, the Kartvelishvili function is not dramatically different from the Peterson function.

Quark	Peak z_{peak}	Average $\langle z \rangle$	Width Δz
b	0.90	0.89	0.10
c	0.75	0.67	0.18

Table 3.2: Peak, average and width of the Kartvelishvili functions for b and c.

The Collins and Spiller Model

Collins and Spiller pointed out [51] that the large z behavior of the Peterson model, $f(z) \sim (1-z)^2$ as $z \rightarrow 1$, is in conflict with the dimensional counting rules [52, 53] and reciprocity which lead one to expect that $f(z) \sim (1-z)$ in the limit $z \to 1$[3]. This motivated them to propose a new heavy quark fragmentation model which is consistent with reciprocity,

$$f(z) \simeq N\left(\frac{1-z}{z} + \frac{2-z}{1-z}\tilde{\epsilon}_Q\right)(1+z^2)\left(1 - \frac{1}{z} - \frac{\tilde{\epsilon}_Q}{1-z}\right)^{-2}, \tag{3.37}$$

with $\tilde{\epsilon}_Q$ defined as

$$\tilde{\epsilon}_Q \equiv \langle k_T^2 \rangle / M_Q^2 \sim (0.45/M_Q)^2, \tag{3.38}$$

where unit is in GeV. For $M_c \simeq 1.5$ GeV/c^2 and $M_b \simeq 4.5$ GeV/c^2, we have $\tilde{\epsilon}_c \sim 0.09$ and $\tilde{\epsilon}_b \sim 0.010$. The corresponding c and b fragmentation functions are shown in Figure 3-8.

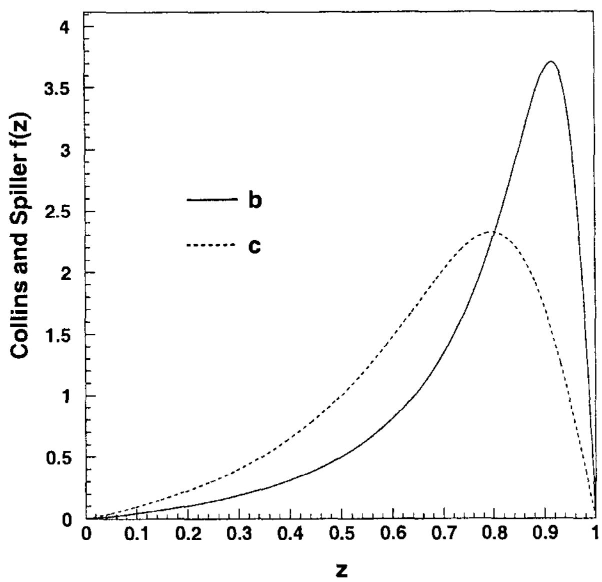

Figure 3-8: Collins and Spiller functions $f(z)$ for b quark using $\tilde{\epsilon}_b \sim 0.010$ and for c quark using $\tilde{\epsilon}_c \sim 0.09$ where $z = P_{H\|}/P_{Q\|}$ ($Q = b$ or c).

Table 3.3 lists some relevant z parameters associated with the Collins and Spiller

[3]The authors of Ref. [58] pointed out that the correct dimensional counting rules for QCD do in fact give a limiting behavior of $(1-z)^2$ for the fragmentation function. The Kartvelishvili model discussed below also behaves like $(1-z)$ as $z \to 1$.

functions for b and c quarks for the same values of the parameters $\tilde{\epsilon}_b$ and $\tilde{\epsilon}_c$ mentioned above. The width of the z distribution for b quark, $\Delta z = 0.18$, is larger than that of the Peterson function used at SLD. The average z is smaller than the Peterson function.

Quark	Peak z_{peak}	Avearge $\langle z \rangle$	Width Δz
b	0.92	0.78	0.18
c	0.80	0.67	0.19

Table 3.3: Peak, average and width of the Collins and Spiller functions for b and c.

3.6.2 Perturbative QCD Approach

As the fragmentation process is intrinsically non-perturbative, it may seem strange that heavy quark fragmentation function can be studied based on perturbative QCD. In fact, in the limit of large heavy quark mass M_Q, there is a cutoff on the minimum allowed opening angle of gluon emission relative to the heavy quark momentum [45]. The opening angle, θ_g, grows with the quark mass: $\theta_g \sim M_Q/E_Q$ which is significantly larger than Λ/E_Q. The fragmentation of a very heavy quark will therefore be calculable to arbitrary order of $\alpha_s(m_Q^2)$ in perturbation theory [54]. M_Q must be much larger than Λ because effects which are in powers of Λ/M_Q are neglected altogether in a perturbative calculation.

In these perturbative QCD calculations, all terms of the form $[\alpha_s \log(Q^2/M_H^2)]^n$ ($n = 1, 2, ...$) are summed in the leading-order (LO) [45], while all $\alpha_s[\alpha_s \log(Q^2/M_H^2)]^n$ terms are summed in the next-to-leading order (NLO) [54]. In a full perturbative analysis, results depend on the choice of the scale Λ_{QCD}, since the perturbative and the non-perturbative contributions do not scale with the mass in the same way. This is a major theoretical uncertainty that cannot be eliminated unless one were to sum results at all orders of α_s, where the result would not depend on Λ_{QCD} [55].

Unfortunately, the known heavy quarks (c and b) are not heavy enough for the purely perturbative description to be sufficient to describe the data well, although this approach has helped us understand many interesting features of heavy quark production. In the case of large, but limited, heavy quark mass, one expects non-perturbative effects to be important. It was pointed out long ago that non-perturbative effects should obey linear scaling in the mass of the heavy quark and should not depend on the mass scale Q^2 [43, 44, 45]. In addition, the distinction between perturbative and non-perturbative regime is no longer possible as $x \to 1$, where x is the energy of the heavy hadron scaled by the beam energy. Unfortunately, these effects must be taken into account in order to describe the experimental data to good precision. Most phenomenological fragmentation models were built to parameterize the non-perturbative contributions. However, model-dependent parameterizations are only as good as their phenomenological assumptions.

For a large, but limited, heavy quark mass, non-perturbative contributions effectively shift the peak of the fragmentation function $f(z)$ to a lower z value. For the b quark, for example, the measured B hadron energy spectrum, $f^B(x)$ peaks near 0.82, but the perturbative analysis shows that z always peaks above 0.92 even when QCD parameters such as Λ_{QCD} and the quark mass are varied in a wide range [54].

3.6.3 Heavy Quark Effective Theory Approach

A model-independent analysis [56] was proposed by Jaffe and Randall, within the framework of heavy quark effective theory (HQET), to extract the non-perturbative contribution. This analysis keeps the distinction between perturbative and non-perturbative physics explicitly. The matrix elements of the heavy quark operators, where the non-perturbative features originate, is evaluated at low renormalization mass scale (at the M_Q scale). *Heavy quark symmetry* is exploited to expand the moments of the fragmentation function in powers of Λ/M_Q, where Λ is some QCD scale. One can then evolve these moments via perturbative QCD to the high Q^2 at which they are measured. The mass expansion coefficients are independent of M_Q and are therefore the same for both c and b quarks. This provides a test of the heavy quark symmetry. Randall and Rius analyzed the low moments of the c and b fragmentation functions [57]. In this approach, moments rather than the shape of the fragmentation function are of most interest, based on the understanding that the shape of the heavy quark energy distributions are generally less well-measured than their means.

The advantage of this approach, as opposed to the full perturbative approach, is addressed in Ref. [56]. In a full perturbative calculation, it seems justified to perturbatively evolve the fragmentation function between the two mass scales M_Q^2 and Q^2, since both Q and M_Q are much greater than the QCD scale Λ. However, this is not always possible. As $x \to 1$, the QCD coupling α_s is magnified by Sudakov log-factors which are of order $\log(1-x)$, making the effect essentially non-perturbative. Further analyses show that non-perturbative effects cannot be neglected for x such as $(1-x)Q^2 \sim \Lambda^2$.

In Ref. [58], the perturbative QCD fragmentation function for a heavy quark to fragment into heavy-light mesons are calculated explicitly within the context of HQET and using the heavy quark mass expansion in the heavy quark limit of $M_Q \to \infty$. The fragmentation functions for S-wave pseudoscalar and vector mesons are calculated to NLO in the $1/M_Q$ expansion. The method breaks down when $1 - z < M_q^2/M_Q^2$. The problem with this model is that it becomes unphysical (negative) at z near 1 unless one of the phenomenological parameters C_3 is set to 1, leaving this model less attractive as a phenomenological fragmentation model. In fact, when $C_3 = 1$, there is essentially no need for $1/M_Q$ expansion at all, and the model can be replaced by the complete perturbative QCD fragmentation functions (still in the context of HQET). We refer to this as the BCFY model later in this thesis.

3.6.4 Summary

In sum, perturbative calculations have been successful in explaining several important features of heavy quark fragmentation using field-theoretic rather than phenomenological terms. However, the heavy quark mass is not large enough and hence puts a limit on the kinematic range in which perturbative treatments are valid. In spite of our good understanding of perturbative QCD, the difficulty in carrying out higher order perturbative QCD calculations somewhat affects the precision of perturbative predictions. But this is not the greatest problem we are facing. Non-perturbative effects are the problem. They are not negligible. They have been parameterized, but not calculated, in various model-dependent or model-independent approaches. We simply do not know how to calculate non-perturbative contributions, but we do know certain features of these contributions. The success of some widely used phenomenological models indicate that there is still some distance between where we are now and where we hope to be: a complete field-theoretic understanding of the non-perturbative aspects of fragmentation, without invoking any additional, usually phenomenological, assumptions about the process. Until then, we probably will not fully understand why certain phenomenological models work well but others do not.

In this thesis, we do not resolve any of the great problems we are facing. Instead, we try to make an important experimental contribution to this subject. We make a precise measurement of the shape of the bottom quark fragmentation function at the Z^0 mass scale and test various existing fragmentation models using our data.

Chapter 4

Experimental Apparatus

The data of this analysis were collected by the SLC Large Detector (SLD) experiment of the Stanford Linear Collider (SLC) at the Stanford Accelerator Center (SLAC) in Stanford, California. The SLAC Linear Collider [59] is a unique single-pass electron-positron ($e^+ - e^-$) collider that produces longitudinally-polarized Z^0's in the collisions of electrons and positrons, taking advantage of SLAC's 50 GeV electron accelerator. The SLC Large Detector (SLD) is a state-of-the-art full coverage multipurpose detector placed at the interaction region. The e^+e^- collisions take place at the geometrical center of the SLD. This chapter presents an overview of the main features of the SLC and the SLD.

4.1 The SLAC Linear Collider

The SLC is the world's only linear e^+e^- collider [60]. The design of the SLC is shaped by the physics goal to produce polarized Z^0 bosons in e^+e^- collisions at the center of the SLD detector. The SLC is designed to

- generate polarized electron beam
- generate positron beam

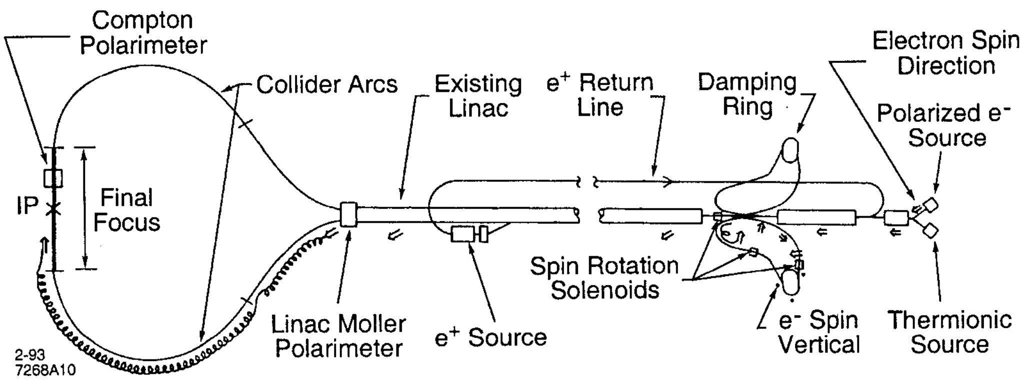

Figure 4-1: The SLC layout.

- focus the electron and positron bunches to small sizes
- accelerate the electron and positron beams (up to $\sim$ 50 GeV).
- focus the electron and positron bunches to very small sizes
- make electron and position collide

The layout of the SLC is shown in Figure 4-1. The SLC consists mainly of the polarized electron source, the damping rings, the linear accelerator (Linac), the positron source, the collider arcs and the final focus.

4.1.1 The Polarized Electron Source

The rate at which new pulses of electrons are injected into the SLC is limited to 120 Hz because the pulses have to be stored in a damping ring for 8 msec to reduce their phase space volume and packing more pulses into the damping ring introduces bunch lengthening instabilities [61]. The electrical power required for generating the needed RF pulses scales linearly with the repetition rate. In typical operation of the SLC, two longitudinally polarized electron bunches are generated at the start of each of the 120 cycles, each containing as many as 6×10^{10} electrons. The polarized electron source is shown in Figure 4-2. The electron beam is generated by an electron

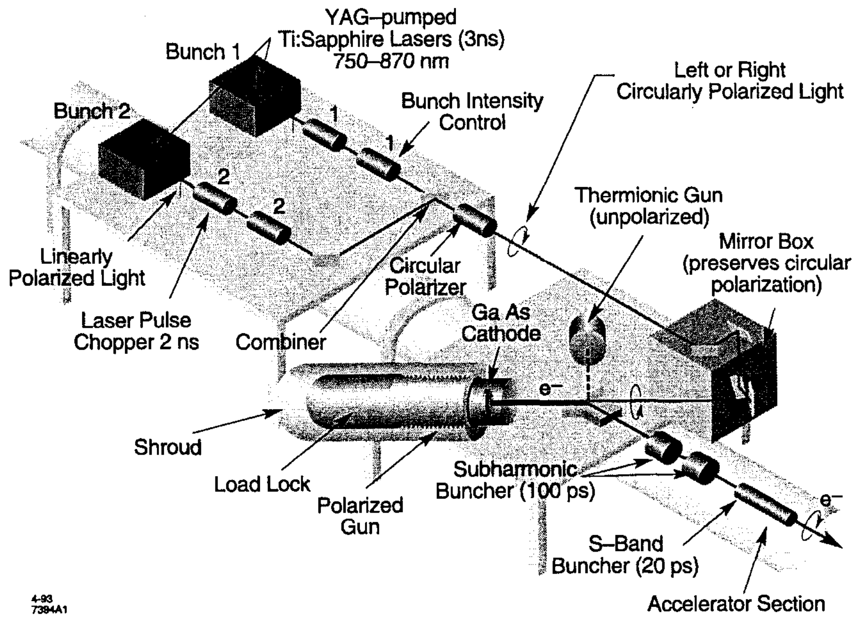

Figure 4-2: The Polarized Light Source.

gun containing a strained-lattice gallium-arsenide (GaAs) cathode [62], which photo-emits longitudinally polarized electrons when illuminated by circularly polarized laser beam. The helicity of the photons in the circularly polarized of the laser beam is determined on a pulse-by-pulse basis by the sign of the voltage applied to a Pockels cell through which the linearly polarized beam passes. The orientation of the electron polarization is determined by the helicity of the incident photons, which in practice is selected by a pseudo-random sequence on each machine cycle in an effort to cancel out any periodicities in the accelerator performance between the two polarization states.

Electron Gun and Photo Cathode

A unique capability of SLC is to produce polarized Z^0 at the Interaction Point (IP). This is made possible by the use of Gallium-Arsenide (GaAs) photo-cathodes [62] in the electron gun at the electron injector. Circularly polarized laser-light (from a Nd:YAG-pumped Ti:sapphire laser) is used to selectively excite transitions of electrons into longitudinally-polarized states in the conduction band of the photo-cathode material. An energy state diagram is shown in Figure 4-3.

For the 1992 physics run, a bulk GaAs cathode was used. This cathode had a theoretical maximum polarization of 50%, and the average polarization achieved was about 22%. For 1993 and 1994/95 runs, a strained-lattice cathode of a thickness of only about 300 nm consisting of GaAs grown on a GaAsP (Gallium-Arsenide-Phosphide) substrate was used. The mismatch in the lattice spacings of these two materials puts a strain on the epitaxial GaAs. This strain serves to break the degeneracy of the $m_j = 3/2$ and $m_j = 1/2$ levels of the $P_{3/2}$ valence state and theoretically allows for 100% polarization. For the 1993 run an average of 63% polarization was achieved at the IP [63]. In the 1994-95 run, an even thinner epitaxial layer of 100 nm was used and this boosted the delivered polarization to 77%.

4.1.2 The Damping Rings

The North and South damping rings (NDR and SDR) are located near the electron source. The electrons coming out of the electron source enter the NDR and experience synchrotron radiation. This dissipative process reduces the phase space (emittance) and the spread of the beam. The reduced spread in both momentum and position space allows for fewer losses during acceleration, lower backgrounds near the interaction point within the SLD detector, and higher luminosity. The radiative losses are compensated by short accelerator sections. The particles settle in stable orbits determined by the damping ring parameters and the angular divergence and bunch length decreases.

The electron beam could not pass through the NDR and still be longitudinally polarized because the energy dependent horizontal spin precession about the vertical axis due to the bending fields would have effectively randomized the spins [64]. In order to preserve the electron polarization within the damping ring, the electron spin vector must be pointing parallel to the direction of the magnetic field of the bending magnets. This is achieved by passing the beam through a solenoid field as it passes

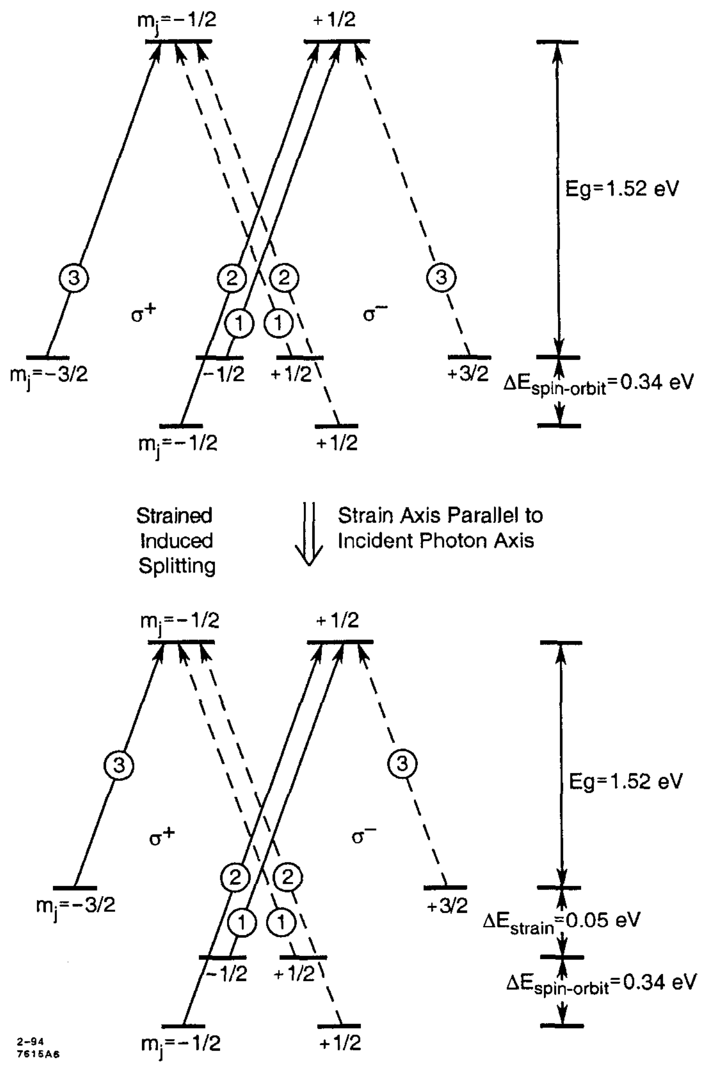

Figure 4-3: The energy state diagram for bulk GaAs (top) and the changes it undergoes when the lattice is strained (bottom). The polarization is due to the preference of certain excitation modes; the relative sizes of the matrix elements are shown in the circles. For the bulk GaAs, the maximum theoretical polarization is 50%. For the strained lattice, the maximum theoretical polarization is 100%.

through the Linac-To-Ring (LTR) transfer line to enter the damping ring. The spin vector is transformed from parallel to the direction of the motion into perpendicular to the plane of the damping ring by spin rotators.

Because the positrons have a larger energy spread as they are collected from photo-conversion at the positron source, they must be damped in the SDR for *two* machine cycles (about 16.6 msec) while the electrons are damped for only 1 machine cycle (about 8.3 msec). There are no spin rotators because the positrons are unpolarized. A transverse polarization builds up, but due to the very small storage time compared with the Sokolov-Ternov polarization buildup time [65] of about 960 seconds, the transverse polarization of the positron is negligible. Some parameters of the damping ring are listed in Table 4.1.

Energy	1.19 GeV
Circumference	35.270 m
Revolution Frequency	8500.411 kHz
RF Frequency	714.000 Mhz
Bending Radius	2.0372 m
Energy Loss/turn	93 keV
Damping Times τ_x	3.32 ± 0.28 msec (e^-)
	3.60 ± 0.15 msec (e^+)
Damping Times τ_y	4.11 ± 0.31 msec (e^-)
	4.17 ± 0.14 msec (e^+)

Table 4.1: Parameters of the SLC damping rings [66, 67].

After existing the Damping Rings, the beams had a flat profile (ϵ_x/ϵ_y). The flat beam profiles produced small spot sizes at the SLC IP resulting in a significant increase in luminosity over the 1992 SLC run, which employed the round beam profiles.

4.1.3 The Linac

The 2-mile long Linac is a linear copper pipe divided into about 244 40-feet-long sections. Each section is made of 480 one-inch thick copper plates. The required energy to accelerate the particles is supplied in form of microwave pulses by a 65 MW peak-power, 2,856 GHz klystron [68], which produces 120 5-μsec-long RF pulses every second. The microwaves produced by the klystrons are guided by copper waveguides to the beampipe which is 25 feet under ground. The microwaves create an alternating field in the cavities which is in phase with the passage of the electrons and the positrons such that these particles always experience an accelerating field. An accelerating gradient of 17 MeV/m is achieved in the copper structures, providing a possible single beam energy of 46.5 GeV.

4.1.4 Positron Production

During each machine cycle, three bunches of particles are accelerated down the Linac. The first two bunches are the positrons and the electrons which will be brought into collision at the IP. The third bunch, known as the "scavenger" electron bunch, is kicked off the main Linac about 2/3 the way down the Linac and is diverted into the positron source where collisions with a Tungsten positron production target take place. The resulting electromagnetic showers produce both the electrons and the positrons.

Positrons in the energy range of 2-20 MeV are captured and transported back to the front end of the Linac in a separate beam-line and injected into the South Damping Ring (SDR), where they are stored for 16.6 msec before the next machine cycle. The positron target typically yields one positron per incident electron.

4.1.5 The Arcs

The electrons and positrons are accelerated to an energy of about 46.5 GeV per particle when they reach the end of the Linac and enters the Beam Switch Yard (BSY), where they are diverted into two opposing arcs of 1 kilometers in length: the South and North collider arcs, respectively. The arcs contain a sequence of dipole and quadrupole magnets to keep the beam in circular orbits. The bending of the beams causes an energy loss of nearly 1 GeV per particle due to synchrotron radiation before they enter the final focus region of the SLC. Since the arcs do not lie in a horizontal plane, the beam transport is complicated by motion in both directions perpendicular to the arcs.

The use of flat beams starting in 1993 disallowed the use of Linac solenoids to orient the spin vector at the IP. The introduction of large amplitude betatron oscillations in the North Arc (so called *spin bumps*) was effective to orient the spin vector at the IP [69].

4.1.6 The Final Focus

To produce a reasonable luminosity and a stable IP the SLC must make up for low repetition rate of a linear collider due to its single-pass characteristics by significantly reducing the beam size and the overlapping cross section between the electron and positron beams. This is achieved by the final focus. In the final focus, the two beams are compressed to a transverse size of roughly 0.5 x 2.3 μm^2 by a pair of superconducting quadrupole triplets. The longitudinal size is about 700 μm. The final quadrupole is 1.5 meters from the IP. The collisions take place at the center of the SLD detector. The length of the bunch at the IP is approximately 1mm [60]. The small and stable IP is an important advantage of the SLC. The final focus was upgraded before the 1994-95 run to reduce the chromatic effects on the focal length [70].

4.1.7 The Compton Polarimeter

The Compton polarimeter provides a precise measurement of the electron beam polarization by measuring the asymmetry in polarized Compton scattering at the Compton IP located approximately 30 meters downstream of the SLC IP [71]. The spin vector does not precess between the SLC IP and the Compton IP because there is only quadrupole focusing magnets and no dipole bending magnets.

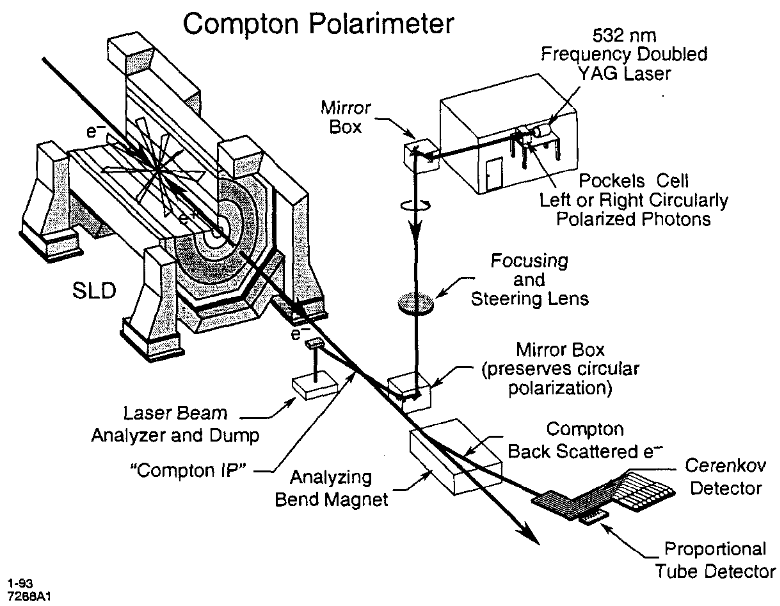

Figure 4-4: The Compton Polarimeter.

The layout of the Compton polarimeter is shown in Figure 4-4. The Compton polarimeter has two main components: a laser and an electron spectrometer. The laser produces circularly polarized photons with a wavelength of 532 nm, corresponding to a photon energy of only 2.33 eV. The electrons Compton scatter off the photons and then are bent by the analyzing dipole magnets before entering the electron spectrometer, the Compton Cerenkov Detector.

The Compton scattering between a circularly polarized photon and a polarized electron has a cross-section (σ_C) which depends on the spin-states of the electron and the photon. We can define an asymmetry function $A_C(E)$ such that

$$\frac{d\sigma_C}{dE} = \frac{d\sigma_C^u}{dE}[1 + P_\gamma P_e A_C(E')], \tag{4.1}$$

where $d\sigma_C^u/dE$ is the unpolarized Compton cross section, P_e is the electron polarization, and P_γ is the laser polarization. The asymmetry function $A_C(E')$ is only a function of the center-of-mass energy, E', of the scattered electron which can be calculated theoretically. The beam polarization, P_e, can be extracted from

$$A_m = \frac{N^{obs}(J_z = 3/2) - N^{obs}(J_z = 1/2)}{N^{obs}(J_z = 3/2) + N^{obs}(J_z = 1/2)} = a_d P_\gamma P_e A_C(E') \tag{4.2}$$

where A_m is the observed asymmetry, N^{obs} is the number of events observed in the two possible spin configurations, and a_d is the analyzing power of the detector used to measure the scattered electron energy. This analyzing power depends on the transport optics of the electron beam from the Compton IP to the Compton polarimeter detectors.

4.1.8 Energy Spectrometer

The beam energy at SLC is measured on a pulse-by-pulse basis by a pair of wire imaging synchrotron radiation detectors (WISRD) [72]. The WISRDs are located between the IP and the beam dumps. The incoming beam is deflected by two horizontal bending magnets. These magnets each produce a swath of synchrotron radiation which is imaged by a multi-wire proportional chamber (MWPC). The wire spacing is 100 μm which results in an energy resolution of 22 MeV. The energy spread is measured less accurately (typically 50-100 MeV). It is better to estimate it from wire scans in high-dispersion locations in the arcs. In between the two horizontal bending magnets is a precisely calibrated vertical bending magnet. This vertical magnet deflects the beam by an angle, which is proportional to its energy and can be determined by the distance between the two swathes imaged on the MWPC. The average center of mass collision energy measured for the 1993 run was 91.26 ± 0.02 GeV and the energy spread was 110 MeV [73]. The corresponding value for the 1994-95 run was 91.28 ± 0.02 GeV with a spread of only 60 MeV.

During the 1997-98 SLC run, an energy scan around the Z^0-pole was performed. It was found that the beam energy has been 46 MeV off the Z^0-pole. Systematic corrections to measurements such as the A_{LR} were performed.

4.2 The SLAC Large Detector

The SLC Large Detector (SLD) is the only detector that takes data at SLC because the SLC has only one Interaction Point (IP). Proposed in 1984, SLD was designed as a general purpose detector with nearly complete solid angle coverage around the IP. A state-of-the-art high energy physics detector, SLD is a second generation detector at SLC following the upgraded PEP detector MARK II. Figure 4-5 and Figure 4-6 show a cut-away and a quadrant view of SLD. The specification of the SLD detector is listed in Table 4.2.

To achieve almost full solid coverage, SLD contains two main geometric sections: the barrel and the end caps. The barrel is a cylinder of 4.5 m in radius and 10 m in length. The two end caps are mounted on the two large doors which close off the two sides of the barrel cylinder and can be opened during down times for access. SLD covers 98% of the solid angle.

SLD consists of several subsystems: a precision vertex detector (VXD) and a high resolution drift chamber (CDC) for tracking of charged particles, a detector for particle ID over a wide range of momentum (CRID), a calorimeter with hadron calorimetry (LAC) which provides good e/π and $\pi K p$ discrimination, a 0.6 Tesla conventional solenoid, and an instrumented flux return for muon identification (WIC). All subsystems have optical fiber transmission cable connection for readout to gain high bandwidth, low noise transmission of data. Since the barrel region of the detector has been used and understood very well, we will focus on the description of the barrel region.

The Standard SLD Coordinate System is defined as follows: the z-axis is along the positron direction (North). The x-axis is perpendicular to the incoming beams and lies in the horizontal plane facing West. The y-axis is in the vertical plane pointing upwards, and the (x, y) origin is on the beam axis. Sometimes we also refer to the cylindrical coordinates in which the plane perpendicular to the beam axis is called the $r\phi$ plane where r is the radius from the beam axis and ϕ is the azimuthal angle

Item	Specification
Drift Chamber System	
Spatial Resolution	$< 100\mu$m
Magnetic Field	0.6 Tesla
Momentum Resolution	
$\sigma(1/p)$ measurement limit	1.3×10^{-3} (GeV/c)$^{-1}$
$\sigma(p)/p$ Coulomb scattering limit	$1-2\times10^{-2}$
Two-Track Separation	1mm
Calorimetry	
Electromagnetic	
Energy Resolution σ_E/E	$8\%/\sqrt{E(\text{GeV})}$
Segmentation	~ 33 mrad $\times$ 36 mrad
Angular Resolution	~ 5 mrad
Hadronic	
Energy Resolution σ_E/E	$55\%/\sqrt{E(\text{GeV})}$
Segmentation	~ 66 mrad $\times$ 72 mrad
Angular Resolution	~ 10 mrad
Vertex Detector	
Segmentation	22 μm $\times$ 22 μm
Precision Transverse to Line of Flight	$4-20\mu$m
Two-Track Separation	40μm
Particle Identification	
e/π	1×10^{-3}
μ/π (above 1 GeV)	2×10^{-3}
K/π (up to 30 GeV)	1×10^{-3}
K/p (up to 50 GeV)	1×10^{-3}
Solid Angle Coverage	
Tracking	97%
Particle Identification	97%
EM Calorimeter	$\geq 99\%$
Hadron Calorimeter	97%

Table 4.2: SLD specification [74].

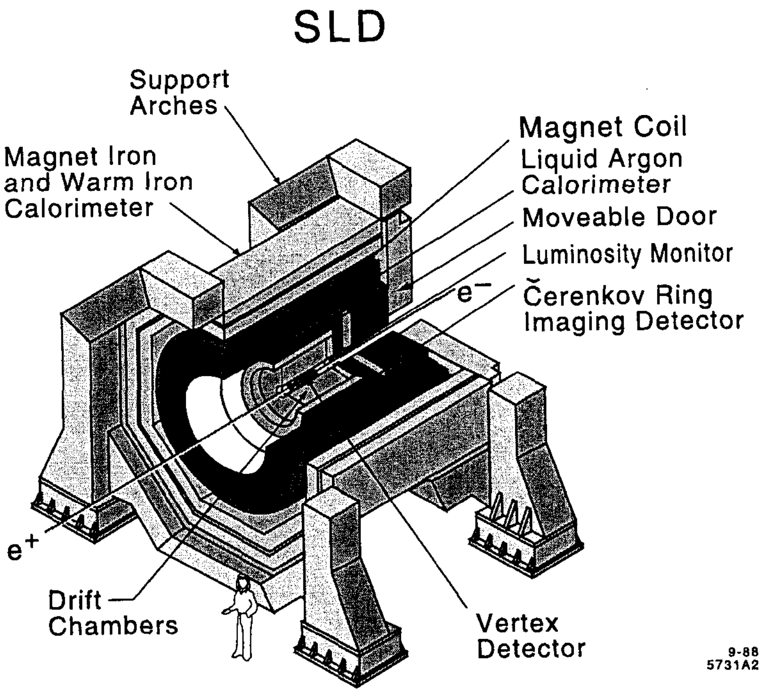

Figure 4-5: The SLD detector (isometric view). The end-caps have been removed for clarity.

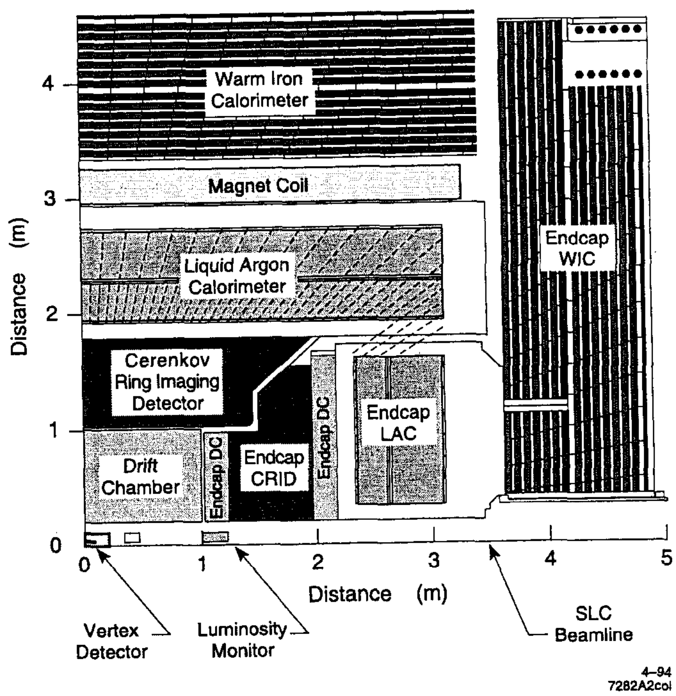

Figure 4-6: The SLD detector (quadrant view).

Layer Number	Radius (cm) from the beam line
1	2.9625
2	3.3625
3	3.7625
4	4.1625

Table 4.3: Radial distances of each VXD2 layer from the beam line

with respect to the x-axis; θ is the angle with respect to the positive z-axis,

4.2.1 The Vertex Detector: VXD2 and VXD3

The small SLC beam pipe allows detectors to be placed within a radius of 25 mm from the beam axis. This unique feature offers the opportunity to detect heavy hadrons particles efficiently.

Two vertex detectors have been used in data-taking at SLD: VXD2 (92-95) and VXD3 (96-98). Both VXD2 and VXD3 are Charged-Coupled Devices (CCD) based vertex detectors designed to provide the high tracking and vertexing resolutions needed by SLD physics analyses. An introduction to the CCD can be found in, for example, Ref. [75]. Based on the experience and lessons learned from VXD2, VXD3 is a major upgrade to match the needs of SLD physics objectives, which would have been out of reach just using VXD2. VXD2 is only briefly described here because data taken using VXD2 were not used in this analysis. VXD3 and its comparison with VXD2 is described in more detail in the next chapter.

The VXD2

The VXD2, shown in Figure 4-7, is a novel CCD vertex detector. The VXD2 is constructed from sixty 9.2 cm-long ladders arranged into four concentric cylinders which are held in place by a beryllium shell [75]. Radius of each cylinder is listed in Table 4.3. CCDs are used as the medium for detecting the deposition of ionization

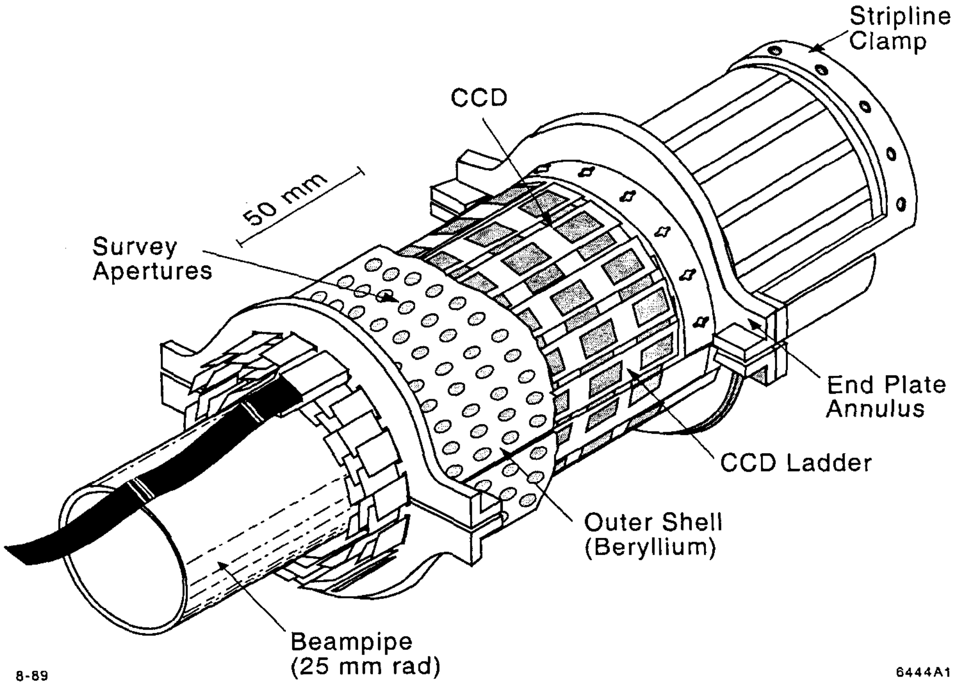

Figure 4-7: The SLD VXD vertex detector.

from charged particles passing through the devices. Eight CCDs are mounted on each ladder with four on each side to maintain symmetric polar angle. CCDs are attached to a ceramic substrate motherboard using thermoplastic adhesive. The overall thickness of each layer is 1.15% X_0 (radiation length) [1]. Electrical contact to the CCDs are made by wire-bonds to the motherboard, and to the end of the ladders by custom made micro-connectors.

The two inner layers are made up from 13 ladders and the two outer layers consist of 17 ladders. Since each layer only covers $\sim$ 60% of the azimuthal angle (ϕ), layer two is oriented to cover the gaps in layer one and similarly for the outer layers. Inside the inner-most CCD layer is the VXD cooling jacket and the thin beryllium cylinder which serves as the beampipe. The total radiation thickness of the material between the IP and the first CCD layer is .71% X_0.

[1] 1 radiation length (X_0) is the mean distance over which a high energy electron retains only a fraction of $1/e$ of its original energy by bremsstrahlung [76].

Each CCD is $\sim$ 1 cm square which contains 222,530 (385 $\times$ 578) 22 $\times$ 22 μm^2 square pixels. The depletion depth of each pixel is 5 μm. Charge collection occurs over the whole depth of the epitaxial layer ($\sim$ 15 μm) which allows excellent position resolution even for tracks passing through the detector at large dip angles.

VXD2 is operated at low temperature ($\sim$ 190K) to suppress dark current and the loss of charge transfer efficiency due to radiation damage [77]. Housed in a very low mass cryostat, the VXD2 is cooled with nitrogen evaporated from liquid, which is piped to and from the detector by means of vacuum jacketed pipes.

The vertex detector and the cryostat make up the R20 module which is clamped to each end of the CDC, by means of a pair of aluminum support cones. The R20 module is shown in Figure 4-8.

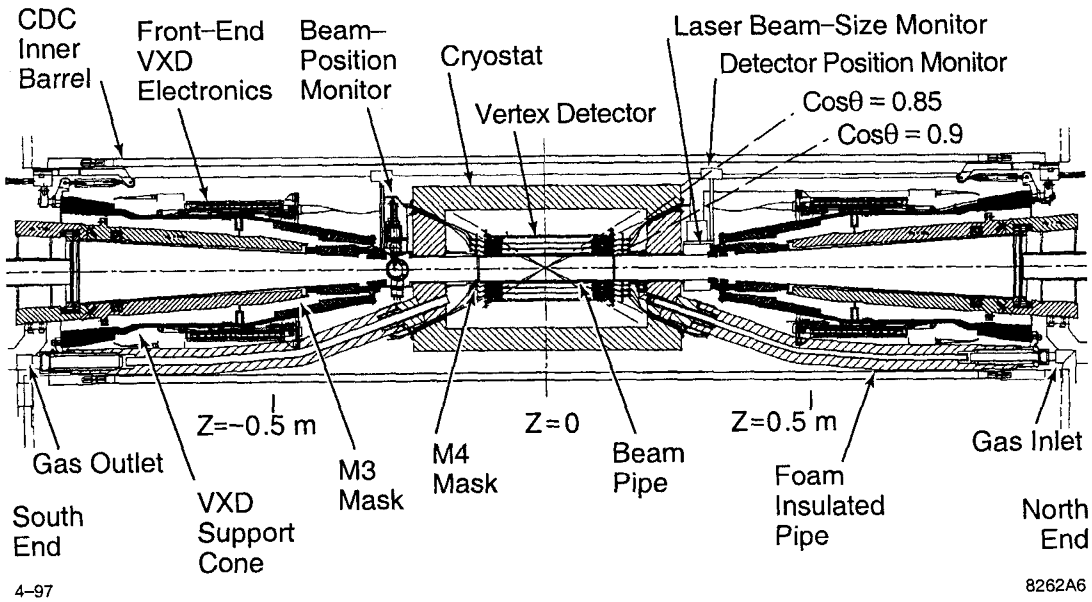

Figure 4-8: The R20 Module.

The readout rate of VXD2 is 2 MHz, the shaping time of approximately 300 ns giving a noise performance of < 100 e^-(rms). The VXD2 analog output is read out on strip-lines to local electronics which transmit the data via twisted pairs to analog-to-digital converters on top of SLD.

On the average, 2.3 VXD (pixel) hits are obtained for each charged track passing through the detector. At least two hits are possible for any track within $|\cos\theta| < 0.75$. Due to the poor lever-arm between measurements, the impact parameter resolution at the IP for a track of momentum p and polar angle θ w.r.t. the z-axis (beam direction) was limited to

$$\begin{aligned} \sigma_{r\phi} &= 11 \oplus 70/(p\sin^{3/2}\theta)\mu m, \\ \sigma_{rz} &= 38 \oplus 70/(p\sin^{3/2}\theta)\mu m, \end{aligned} \tag{4.3}$$

similar to that of a silicon micro-strip vertex detector at LEP [79].

We will discuss the upgraded VXD3 in the next Chapter.

4.2.2 The Drift Chamber

The SLD Drift Chamber (CDC) is designed to provide high resolution momentum and position measurements of charged particles [78]. It consists of one Central Drift Chamber (CDC) and four end-cap drift chambers (EDC).

The Mechanical Design

The CDC is a cylindrical annulus which occupies the volume radii from 0.2 m to 1.0 m with a length of 2.0 m centered about the interaction point, a region where the magnetic field is almost uniform (0.6 Tesla), which is suitable for the tracking of charged particles. Two end plates are supported by the inner and outer cylindrical walls. The drift chamber is filled with drift gas which is a mixture of 75% CO_2, 21% Argon, 4% Isobutane and 0.2% H_2O. 6500 25 μm-diameter tungsten sense and dummy sense wires and 31360 field and guard wires are strung between the two end-plates to a tension of approximately 100 g for sense wires and 400 g for field and guard wires. The wires are radially grouped into 10 "superlayers" of drift cells. The orientation of wires in the 10 superlayers alternate among axial layers (A), U-layer (U) and V-layer (V), resulting the following pattern AUVAUVAUVA for the ten layers (Figure 4-9).

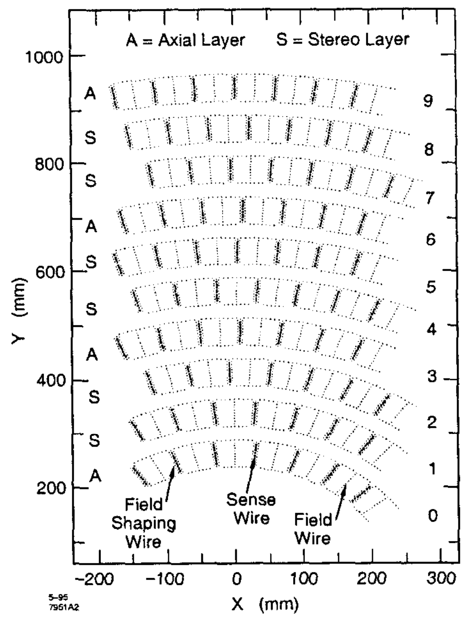

Figure 4-9: SLD's Central Drift Chamber (CDC).

The wires in an axial layer are parallel to the beam axis, while the wires in stereo layers are tilted at an angle of 42 mrad and -42 mrad for U and V layers, respectively.

The cell design is chosen to satisfy the requirement that a single track is measured by each sense wire to better than 100 μm. This resolution permits an overall detector resolution of $\sigma_p/p = 0.0015p$ (p in GeV/c) for high momentum tracks. Each cell is about 5 cm along the radius and 5.9 cm wide at the midpoint, and contains a set of 8 sense wires immediately surrounded by 24 guard wires and 27 field shaping wires which defines the cell boundaries. Two additional guard wires (dummy sense wires) are placed at the top and bottom of a cell to help shape the electrostatic fields of the cell. The entire cell is tilted by 5° away from the radial direction.

Voltages applied on the guard wires is approximately -3.4 kV, while those on the field wires may run up to -7 kV. The field wires establish precise electrostatic fields that cause the electrons from ionizing particles to drift onto the sense wires where they undergo amplification in the gas via the avalanche mechanism (Figure 4-10). The drift speed in CO_2-Isobutane is 8 μm/ns at the expected field values and is proportional to the field strength in the drift region. Changes in voltage or gas

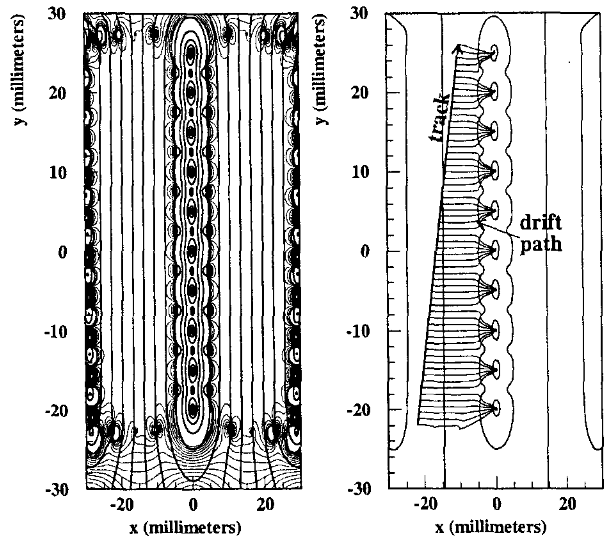

Figure 4-10: The field map for a drift cell of the CDC. The left figure shows lines of constant potential (bold) and lines of constant field strength(thin) within a CDC cell. The right figure shows a drift path of charges caused by the passing of a charged track through the cell.

density can change the drift velocity seriously degrading the position resolution. The transverse distance of a track from an individual sense wire is measured to an intrinsic resolution of 70 μm, but the uncertainties in the wire locations and changes in the drift speed degrade the resolution to approximately 100 μm.

The CDC Readout

Both ends of each sense wires are instrumented with electronics so that *charge division* can be used to measure the z coordinate of a hit. Since more than one hit can contribute to the total integrated charge emerging from the two ends of a wire, to distinguish between different hits, waveform sampler modules are used to record the pulse shapes at each end of the wire as a function of the time. Hits whose drift distances are different by more than 2 mm can be separated by the integrated charges alone. But for hits whose drift distance difference is less than 1 mm, the measurement of the z-coordinate is degraded.

Good $z-$position resolution improves the measurement of the track polar angle and thus improves the ability to link tracks from the drift chamber with the vertex detector hits. The resolution on $z-$position improves as the stereo angle increases, but the resolution on the position of the projected hit in the mid-plane of the chamber (the x-y plane at $z = 0$) becomes worse. These two criteria limit the stereo angle to lie between 35 and 50 mrad. The stereo angle chosen provides adequate resolution in the x-y plane for efficient linking.

Pattern Recognition

The track-finding process begins at the superlayer level. Straight lines are fit to drift chamber hits within a given superlayer. Hits within a superlayer which lie on a straight line (or an origin-constrained circle) form a track segment called vectored hit (VH). A minimum of 3 hits must be present in a superlayer to reconstruct a vectored hit. The positional accuracy in the drift direction is about 40 μm, and the pointing accuracy is about 3.5 mrad, both of which scale as the inverse square-root of the number of hits within the vectored hit.

Charge division is used for pattern recognition only after vectored hits have been found and projected onto the mid-plane of the chamber. If the z-position of a hit is found, vectored hits from the stereo superlayers are projected onto the mid-plane of the chamber. These stereo vectored hits can be used along with those originating from the axial layers in linking these vectored hits.

Pattern recognition then link these track-segments or vectored hits together to form candidate tracks. Combinations of 10 consistent axial vector hits are considered first. The combination with the best χ^2 is taken as a candidate track and all involved vectored hits in this combination are removed from the list of the input vectored hits. Then this track-finding process is repeated. Once all 10-VH combinations are exhausted, 9-VH combinations are considered. The number of VHs decrease by one each time all tracks in the current number of VHs are exhausted. This search procedure continues until all tracks with at least 3 VHs are found.

Track Fitting

Once all tracks are found by the pattern recognition, a track-fitting procedure is applied. Starting with the estimated track parameters from the pattern recognition, the track-fitter swims a helical trajectory through the detector, modifying the helical parameters according to the effects of multiple scattering, energy loss, and local variations in the magnet field. A χ^2 is formed by comparing the proposed trajectory with the current parameter and their errors. The error on the helical parameters are estimated from the derivatives of the χ^2 with respect to each parameter. The complete correlation matrix (error matrix) of these parameters is formed. Local minimum χ^2 is sought iteratively using these parameters, the their errors, and their correlations.

Momentum Resolution

Both the intrinsic hit resolution and multiple scattering contribute to the total momentum resolution of the CDC, in which the two contributions are added in quadrature because they are not correlated. The momentum resolution can be estimated *either* from the resolution on the hits *or* from the resolution on the reconstructed track momentum. Since the multiple scattering term is negligible for high momentum tracks, muon tracks in $Z^0 \to \mu^+\mu^-$ decays can be used to determine the term that is due to the intrinsic hit resolution. In the absence of hard photon radiation, muon tracks are nearly back to back and have identical momenta of 45.6 GeV/c. In addition, muon tracks in the central region of the CDC ($|\cos\theta| < 0.75$) leave hits in essentially all layers and are expected to have better resolution than those which do not leave hits in all layers. A Gaussian fit to the Q/P distribution for muons, where Q is the charge and P is the momentum, provides the intrinsic resolution on the curvature measurement.

Cosmic ray tracks with varying momenta which pass through the central part of the CDC can be used to measure the multiple scattering term. The two halves of cosmic rays in the CDC have almost identical momenta and thus allows the measurement of the resolution as a function of the momentum of cosmic track. The measured CDC track resolution is

$$\sigma_{1/p_\perp} = \frac{\sigma_{p_\perp}}{p_\perp^2} = \sqrt{\frac{0.0095^2}{p_\perp^2} + 0.0049^2}. \tag{4.4}$$

The momentum resolution on the CDC + VTX track is [80]

$$\sigma_{1/p_\perp} = \frac{\sigma_{p_\perp}}{p_\perp^2} = \sqrt{\frac{0.0095^2}{p_\perp^2} + 0.0026^2}. \tag{4.5}$$

The momentum resolution used in the Monte Carlo can be cross-checked by comparing the distribution of invariant mass of long-lived particles such as K_s^0s for Monte Carlo and for the data. Any discrepancy between the widths of the mass peaks indicates inaccurate estimate of momentum resolution in the Monte Carlo.

The End-cap Chambers

The End-cap Drift Chambers (EDC) are made of two sets of end-cap detectors located in the forward region ($\theta > 45°$). The SLD reconstruction code has not been tuned to reconstruct tracks in the EDC.

4.2.3 The Cerenkov Ring Imaging Detector (CRID)

Particle identification (ID) is very important for the study of heavy quark decays. Combined with high resolution tracking and vertexing, the particle ID further improves the capability for tagging heavy hadrons and their flavors. At SLD, this is achieved by the Cerenkov Ring Imaging Detector (CRID) [74, 81]. The CRID provides separations of π/e up to 6 GeV/c and $\pi/K/p$ up to 30 GeV/c [82].

A charged particle emits cones of Cerenkov light in a medium at a specific angle

(Cerenkov angle) with respect to the momentum of the particle when the speed of the particle exceeds the speed of the light in the medium. The Cerenkov angle θ_C is given by $\cos\theta_C = 1/(\beta n)$, where n is the refractive index of the medium and β is the speed of the particle. Measurement of the Cerenkov angle determines the velocity of the particle and therefore the mass of the particle, using the momentum information provided by the CDC. The mass of the particle almost uniquely determines the type of the particle. Particle ID is therefore achieved.

Barrel CRID

The Barrel CRID is a cylindrical annulus which contain 40 modules installed azimuthally around the CDC to provide complete coverage for the barrel region. Each module is divided into two independent longitudinal sections, each of which is readout at its outer end.

Shown in Figure 4-11, a barrel CRID module consists mainly of three parts: the radiator, the mirrors, and the drift box. The radiator is a medium in which charged particles radiate Cerenkov light. A set of 400 mirrors are used to reflect and focus the light back onto the 40 TPCs. The drift box shown in Figure 4-12, is a quartz box, which contains drift gas C_2H_6, which provides good ultraviolet transparency, and 1% of a photo-sensitive medium called TMAE (Tetrakis diMethyl Amino Ethylene), which provides good quantum efficiency for converting Cerenkov photons into photo-electrons. Under a uniform electric field of 400 V/cm, the photo-electrons are drifted in parallel to the magnetic field towards the multi-wire proportional chamber (MWPC) detectors located at the end of the drift box furthest from the IP, where charges are read out. The original coordinate location of a photo-electron in the TMAE, also called a hit, is obtained from the drift time (z), the wire address (ϕ), and the charge division along the thickness dimension of the box (r). A ring is then fitted to the these 'hits'. A full ring typically contains 8-10 hits in the Gas or 13-16 hits in the Liquid. In order to obtain particle ID over a wide momentum range, the

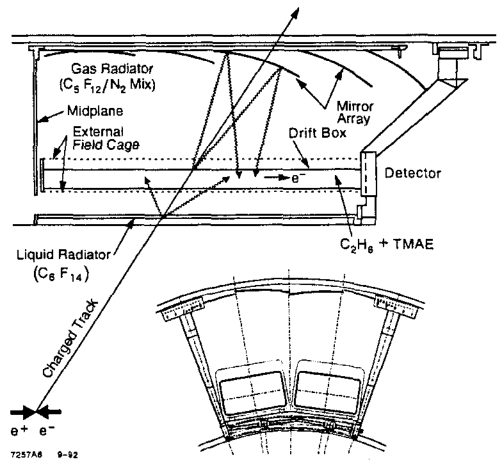

Figure 4-11: The Barrel CRID.

barrel CRID has two separate radiators, a liquid radiator (C_6F_{14} with refractive index of $n = 1.277$) and a gas radiator (C_5F_{12} with $n = 1.001725$). The cones of Cerenkov light from the liquid radiator, which is only 1 cm in thickness, can be focused directly on the TMAE by proximity. However, the light from the gas radiator which is 45 cm in thickness are reflected and focused back onto the TMAE by spherical mirrors. A more important distinction between the two radiators is that the thresholds for generating Cerenkov light are very different, owing to their very different refractive indices. The threshold in the gas is significantly higher than that in the liquid. For pions, the threshold $\gamma = 1.61$ in the liquid (corresponding to a momentum of 0.23 GeV/c), but $\gamma = 17.05$ in the gas (corresponding to a momentum of 2.6 GeV/c), where $\gamma = p/(\beta m)$. The choice of material for the liquid and gas are significantly restricted in order to close up the gap between the upper limit for the liquid and the threshold for the gas.

CRID Performance

The resolution on the measurement of the Cerenkov angle θ_C is determined by individual contributions from five separate sources of error. Variation of index of refraction of the radiator causes error in the measured Cerenkov angle. For liquid, the chromatic error is about ± 5 mrad. For the gas, it is about ± 0.3 mrad. Granularity of

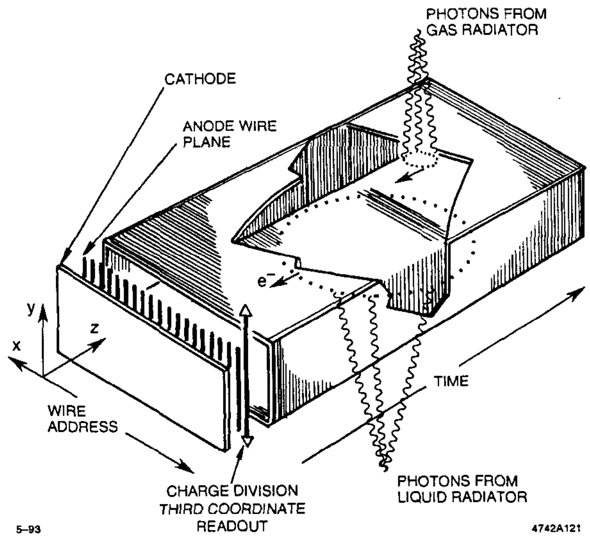

Figure 4-12: A CRID Drift Box, or TPC.

the photo-electron detector, diffusion, and non-uniformities in the detector cause the measurement errors to be about 3 mrad for liquid and 1.7 mrad for the gas. Multiple scattering leads to a momentum dependent error of $1.4/p$ mrad for the liquid and $0.4/p$ mrad for the gas. A geometric error is caused by the aberrations of the image of the Cerenkov ring due to the optical focusing method: proximity or reflection. This error is around 7 mrad for the liquid and 0.5 mrad for the gas. Finally, momentum smearing due to the change in flight direction as the particle passes through the radiator volume under the influence of the magnetic field contribute an error of $0.4/p$ mrad for the thin liquid radiator and $15/p$ mrad for the much thicker gas radiator because of longer trajectory of the particle.

The total uncertainty on angle of each photo-electron is $\pm$ 10 mrad for the liquid radiator. Using all 14 photo-electrons, the resolution on the Cerenkov angle is about 3 mrad. The angular resolution for the gas radiator is momentum dependent and is on the order of 3 mrad for a 5 GeV/c particle. The Cerenkov angle resolution for a track is better than 1 mrad.

End-cap CRID

The end-cap CRID installed between the end-cap drift chambers were designed to extend the particle ID coverage in the forward region. However, the lacking of a forward tracking makes it impossible for the end-cap CRID to provide particle ID.

4.2.4 The Liquid Argon Calorimeter (LAC)

Function of Calorimetry

The main objective of calorimetry is to detect the energy of a particle. When a high energy particle enters high-density medium such as lead plates, it interacts with the medium and generates either an electromagnetic (EM), or a hadronic (HAD) shower. Neutral particles, which escape the detection of the tracking system, will deposit energy after entering the calorimeter (except for the neutrinos), providing crucial measurements of their energy. For a charged particle, since the momentum is well measured, the measurement of its energy in the calorimeter provides little further energy information[2]. However, due to the different showering characteristics (such as EM vs HAD deposition, transverse spread or longitudinal depth) the energy deposition in the calorimeter can be used to provide particle identification such as electron or muon ID. Moreover, spatial and angular information provided by the calorimeter, combined with energy and momentum information, is very useful for determining important event variables such as the thrust axis, the event-shape and the jet axes. Another important function of the calorimeter is to provide the measurement of the total (observed) event energy to help extract the missing energy such as the energy of the neutrino. For this reason, the calorimeter should as hermetic as possible to minimize leakage of particles.

Calorimeter plays a very important role in the clean high energy e^+e^- environment.

[2]In principle, very precise measurement of a particle's momentum and energy can provide particle identification, using $m = \sqrt{E^2 - P^2}$. But achieving such a high resolution is very difficult.

Full knowledge of the initial state and precise measurement of the final state can be a powerful tool for uncovering new physics. [74].

SLD employs two calorimetry systems: the Liquid Argon Calorimeter (LAC), which is a high resolution, hermetic calorimeter, and the Warm Iron Calorimeter (WIC) which provides the flux return and muon ID. WIC will be described in the next section. The LAC is also divided into the Barrel region and the End-cap region.

The Barrel LAC

The barrel LAC is a 6-meter-long cylindrical annulus just outside the CRID, with an inner radius of 1.8 m to an outer radius of 2.9 m. The barrel LAC is the outermost detector subsystem which resides inside the magnet coil. It provides continuous coverage between $\theta = 35°$ and $\theta = 145°$ with respective to the beam direction.

The LAC is composed of long modules (Figure 4-13) which are stacked around the barrel CRID in the azimuthal plane (ϕ). The modules themselves are made of planes of lead radiator separated from each other by non-conducting spacers and immersed in a liquid argon bath several mm in thickness. The modules are radially divided into four sections: two inner EM sections and two outer HAD sections. These sections are further segmented into readout towers that project back to the beam intersection point, both azimuthally (ϕ) and along the beam axis (z). The solid angle made by each tower with respect to the IP is fixed. In ϕ, the towers have a fixed angular width of 33 mrad and 66 mrad for the EM and HAD sections respectively. Each module spans 4 EM towers and 2 HAD towers in width, matching the edges of the EM and HAD towers. In z, the towers have a fixed angular size of 36 mrad for the EM section and 72 mrad for the HAD section. The actual size of the tower pads increases with z. Tower sizes in the EM section were chosen to provide best efficiency for isolating electrons, lowest possible π/γ overlap background, and good position resolution within economic constraints [74].

The LAC is a conventional lead-liquid argon *sampling* calorimeter. Particles

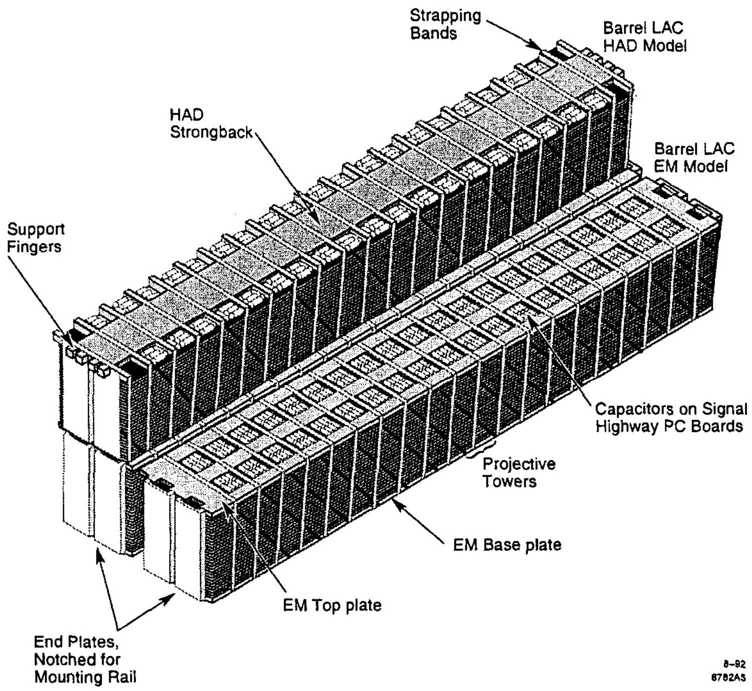

Figure 4-13: View of a LAC module, showing the inner EM and outer HAD sections.

entering the LAC interact with the lead and produce a secondary shower of low energy particles which then ionize the argon. The lead plates are held alternately at ground and high voltage, producing a field to collect the liberated charge in the argon. Since the argon supplies no charge amplification, the charge observed is proportional to the energy deposited. Approximately 10-15% of the shower energy is deposited in the argon and half of the ionized electrons are collected by the readout electrodes [74]. Each tower is connected to a low-noise, charge sensitive pre-amplifier to measure the charge deposited. In sum, the energy deposition in the calorimeter is converted into an electronic signal, which is read out and converted back to units in energy.

The two EM sections are thin and are designed primarily to measure the energy from EM showers due to the interaction of electrons or photons. The two outer HAD sections are denser in composition, and are designed to measure the energy in hadronic showers due to the interaction of neutral or charged hadrons. Overall, there are 22 X_0 of material in the EM sections of the LAC, and 2 absorption lengths[3] in the hadronic (HAD) sections. In total, there are $2.8\lambda_0$ of material in the LAC. The segmentation of the LAC modules allows for spatial determination of the energy shower. The segmentation and module thicknesses were chosen to maximize the amount of particle energy sampled, and to be able to differentiate between EM and HAD particles. The energy resolution of the LAC has been shown to be $\sim 15\%/\sqrt{E}$ GeV for EM showers and $\sim 60\%/\sqrt{E}$ GeV for hadronic showers [83].

The End-cap LAC

The two end-cap LAC, with sampling plates perpendicular to the beam axis, provide coverage between 8° and 35° with respect to the beampipe.

4.2.5 The Warm Iron Calorimeter (WIC)

The Warm Iron Calorimeter (WIC) is the outermost subsystem of SLD, providing the structural support for the rest of the detector components. Installed just outside the magnetic coil, the WIC uses the large iron structure needed for the flux return for the solenoid; As the LAC is thick enough to contain 95% of the energy from hadronic Z^0 decays, the WIC measures the remaining 5% energy and provides muon identification.

The WIC is also divided into the barrel and the end-cap regions, covering almost all the solid angle.

The Barrel WIC

The barrel is 6.8 m long and runs from 3.3 m to 4.5 m in radius. It contains eight long azimuthal sections (octants). Each of the octants is made of alternating layers of tubes and steel, as shown in Figure. 4-14. In the central and the outermost layers,

[3] 1 absorption length (λ_0) is the mean distance over which a high energy hadron loses all but 1/e of its energy due to nuclear interactions [76].

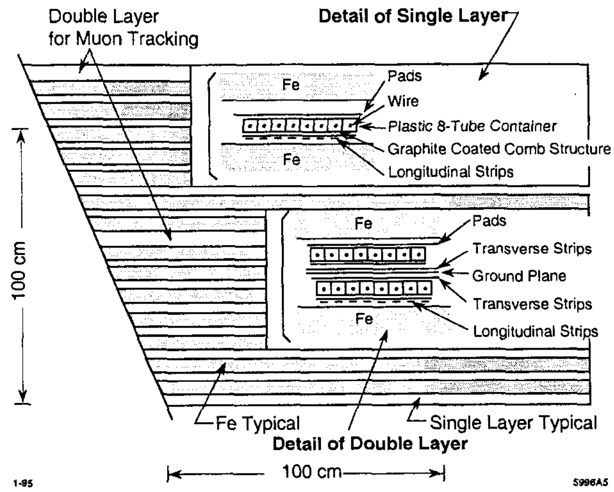

Figure 4-14: Cut-away view of the WIC.

double layers of tubes are used. Hence, there are 14 iron plates and 17 (15 + 2) planes of tubes. The total thickness of the iron is 71 cm at $\theta = 90°$, corresponding to about 4 absorption lengths. The active length of the tubes is 6.55 m. In order to avoid radial cracks in the WIC, the octants are arranged in an interlocking geometry. Each octant is made of two pieces, an inner and an outer one.

The iron layers are 5 cm thick each, separated by 3.2 cm thick gaps instrumented with a system of plastic tubes operated in the limited streamer mode. The tubes are made in modules of eight. The number of eight-tube modules in each layer of the barrel octants varies from 31 to 42, increasing with the radius of the layer. There are a total of about 40,000 tubes in the barrel region.

The tubes are filled with gas, which is a mixture of 2.5% argon, 9.5% iC_4H_10 and 88% CO_2. Each tube has an active section of 9×9 mm^2. At the center of each tube is a 100 μm Be-Cu wire. A voltage of 4.4–4.7 kV is applied to the wire. The enclosures of the eight-tube modules are placed between the three Glasteel sheets, one for the strips, one for the pads, and one as a ground plane, as is shown in Figure 4-14. Several modules are glued together to form a *chamber*, which contains at most 14 modules and is about 1 to 4 pads in width. Each layer contains 3 or 4 such chambers. Since the tower geometry is to fix solid angle coverage relative to the beam intersection point, the geometry of each chamber is unique.

The strips are made using a 1.6 mm thick Glasteel sheet laminated with 25 μm copper on both sides, glued under the plastic modules. On the top side, strip electrodes are made by removing copper strips 2 mm wide. At the end opposite to where the high voltage is supplied, each set of 8 strips is brought together to fit in an 8-pin connector which picks up the signal. The ground is provided by the copper on the bottom side of the Glasteel sheet. The strips are read out digitally.

The pads are glued on top of the plastic module with the copper side up. The pad plane is divided into two parts along the beam axis. Signals are picked up at both ends. The pad signals from several layers are added according to the tower assignment. Each tower is segmented into two parts. The inner one contains the first seven layers which are connected together to measure the energy flux in the front part. The remaining seven layers are connected together to make the back tower.

To provide muon identification, the strip signals are read out. Except for two special layers, all layers are instrumented with strips running parallel to the tube wires. This allows muon tracking the in $r - \phi$ plane in the entire barrel region. The central tube layer (8 and 9) and the outside layer (16 and 17) are double layers which are instrumented with two planes of streamer tubes, one with both longitudinal and perpendicular strips and the other with perpendicular strips and pads. This design scheme provides two space points (midpoint and outermost point). Track angles can be calculated for particles that penetrate all eight interaction lengths of the calorimeter.

The advantage of streamer tube system is high granularity, long-term reliability, simplicity of construction and the low cost of the raw materials and of readout electronics [74].

4.2.6 The Luminosity Monitor

LUM is used primarily to detect e^+e^- pairs that have undergone Bhabha scattering at the SLC IP and measure the rate of small-angle Bhabha scattering. Since the cross-section for Bhabha scattering is precisely calculable in QED, and because it occurs much more often than Z^0 production, the measurement of the rate of Bhabha scattering provides the most precise measurement of delivered luminosity at IP by the Linear Collider.

The LAC covers almost 98% of the solid angle. However, at small angles to the beam axis, the luminosity calorimetry was designed to: [84]

- provide a high precision measurement of the absolute luminosity
- provide a measure of the luminosity difference between left- and right-handed polarized electron beams
- extend the electromagnetic calorimetry coverage down to small angles
- tag electrons

To achieve these goals, the two SLD Luminosity Monitor (LUM), the small angle calorimeters, were constructed. The LUM, shown in Figure 4-15, consists of two silicon-Tungsten calorimeters which are arranged in projective towers with a high degree of segmentation and located 1 m downstream along the beam axis from the IP. Each calorimeter contains two separate modules: Luminosity Monitor/Small Angle Tagger (LMSAT) and the Medium Angle Silicon Calorimeter (MASiC). LMSATs were mounted directly on the Superconducting Final Focus triplet assembly. LUM provides coverage between 28 and 68 mrad. MASiC mounts onto the R20 assembly, providing coverage from 68 mrad to 200 mrad. The total depth of the calorimeter is 21 X_0, containing 99.5% of the 45.6 GeV electromagnetic shower. The measured energy resolution is 6% at 50 GeV.

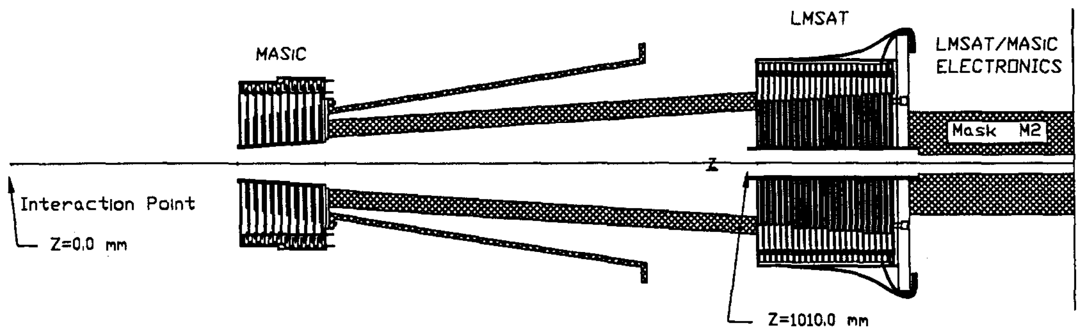

Figure 4-15: The SLD LUM, showing the LMSAT and the MASiC.

4.2.7 Data Acquisition

The SLD data acquisition design takes full advantage of the relatively long time (8.3 msec) between the SLC beam crossings. Little dedicated hardware is needed. For example, the entire calorimeter is read out and energy sums are calculated in software, all within the 8 msec time window.

Data acquisition is done through the FASTBUS. There is a network of 18 FASTBUS crates located on the top deck of the SLD. The work of assembling events is done in ALEPH Event Builder (AEB) modules. The AEBs pool data from various slave modules, whose type depends on the subsystem being read out. The calorimetric systems are processed in the Calorimeter Data Modules (CDMs), while the drift chamber and CRID systems in Waveform Sampling Modules (WSMs), The VXD in Vertex Data Acquisition (VDA) modules and the WIC Strip data in WIC Digital Readout Modules (DRMs). All of these slave modules contain some number of 68020 CPUs and connected to their respective systems via fiber optics.

Triggering is determined by a dedicated trigger AEB. Several conditions, when met, causes the detector to be read out. For hadronic events, three main triggers are used: an Energy trigger based on a sum of LAC tower response, a Track trigger based on some fast readout of the CDC cells and the existence of two tracks at large angles relative to each other, and a "hadron" trigger which combines the preceding two types of information, but with a lower energy threshold and only one track required.

A dedicated trigger is reserved for small-angle Bhabhas ($e^+e^- \to e^+e^-$) in the LUM, and a Random Trigger is used to read out the detector every 20±0.5 seconds.

An average SLD events is 250-300 kilobytes in size, 25% of which coming from the drift chamber and VXD subsystems. Event size is strongly affected by background conditions, which is related to the tuning of the SLC. Typical trigger rates during low background running condition are $\sim$ 0.2 Hz, while Z^0 luminosity was typically $\sim$ 50 Z^0 per hour for the 1996-97 run and was 100 Z^0 per hour for the 1997-98 run.

4.2.8 Detector Simulation

Most data analysis of high energy physics experiments strongly rely on Monte Carlo simulation in order to interpret and unfold the raw data. The design of the detector relies on details detector simulations. The SLD detector simulation is based on the standard GEANT 3.21 package [85]. GEANT's main function is to generate detector volumes and track particles through the detector materials and the magnetic field and simulates multiple scattering and energy loss. For showering in the calorimeters, SLD uses a hybrid scheme of a parameterized shower shape for the electromagnetic portion of the showers and the GEANT GHEISHA package for the hadronic interactions.

To make the comparison between Monte Carlo and data collected by the SLD more straightforward, simulated events and the raw data are generated in same output format.

To simulate the beam-induced backgrounds and noisy electronics channels, raw data from random triggers is overlaid with the results of the simulation. These random triggers are sampled in a luminosity-weighted fashion to reproduce the conditions corresponding to the raw data. Once the random trigger "data" is merged with simulated "data", the events are processed with the standard SLD reconstruction package.

One input to the simulation is one of several QCD event generators. For the current data set, the JETSET 7.4 parton shower model was used to supply hadronic particles as input to the detector simulation. The parameters of JETSET have been tuned by the SLD collaboration to fit available world data, and the decays of charm and bottom hadrons have been parameterized with the CLEO decay package.

Chapter 5

The VXD3

Advances in CCD technology permitted an upgrade vertex detector design (VXD3) (Figure 5-1) with the following main advantages with respect to VXD2:

- extended polar angle coverage.
- full azimuthal coverage in each of three barrel CCD layers, creating the possibility of VXD3 self-tracking.
- stretched radial level-arm and reduced material in each layer for significantly improved impact parameter resolution.

5.1 Design of VXD3

Layer Number	Number of CCD-ladders	Radius from the beam line
1	12	28.0 mm
2	16	38.2 mm
3	20	48.3 mm

Table 5.1: Number of CCD-ladders and Radius of each CCD-layer of VXD3.

Detailed discussion of VXD3 design can be found in Ref. [79] and Ref. [75]. Here we only briefly describe the features. VXD3 is made of 48 CCD-ladders which form

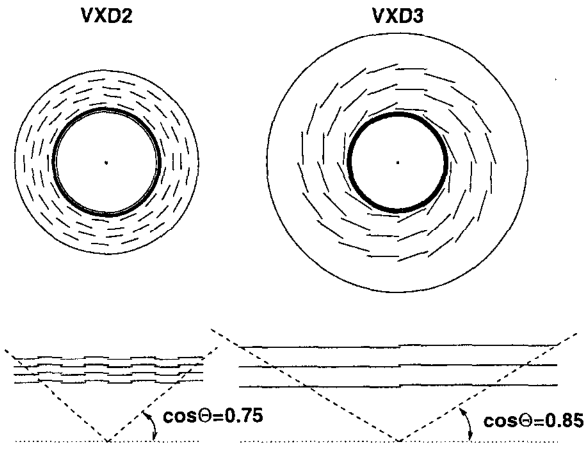

Figure 5-1: VXD2 vs VXD3

three layers of CCDs. The radius of each layer is shown in Table 5.1. Each CCD-

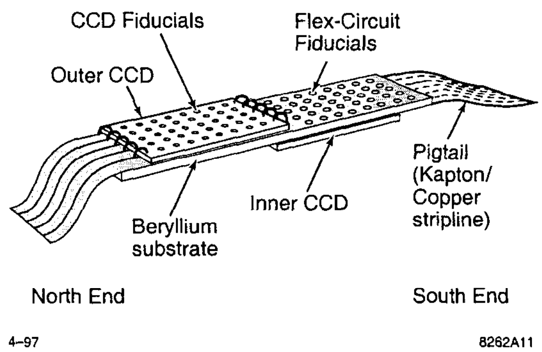

Figure 5-2: A VXD3 ladder with one CCD on each side.

ladder contains two CCDs which are mounted on a beryllium substrate. One CCD is mounted on the outer side of the substrate at the North End (positive z) and the other CCD on the inner side of the substrate at the South End (negative z), shown in Figure 5-2. The ladder thickness is only 0.4% X_0 in the active volume of the detector, which reduces multiple scattering and improves track impact parameter resolutions.

5.2 VXD3 Geometry

The VXD3 is a micron-sized CCD-pixel vertex detector which is designed to measure the track impact parameters and other spatial quantities down to micron precision, thus providing the necessary data for high quality physics analyses. In order to achieve this precision, several problems concerning the geometry of the VXD3 had to be solved.

The basic problem can be phrased as follows: after VXD3 has been installed onto the beampipe, the detector doors have been closed and e^+e^- beams are colliding, how much confidence do we have in the *global* position of each active CCD-pixel within the vertex detector? Here *global* means relative to other SLD subsystems, for example, the Central Drift Chamber.

The above question can be broken down to two separate questions. One is how well we know the global position of the VXD3 as a rigid body, assuming VXD3 being rigid is not far from the truth; the other is how well we know the *internal* position of each CCD pixel. Here *internal* means positions relative to the rigid VXD3 coordinate system.

The global location of the VXD3 can be found by applying a standard procedure called **global alignment**, which will be discussed in more detail. The internal geometry of CCDs are determined in two phases: starting from the ideal design geometry, we first find the 'first-pass' approximation to the true internal geometry by conducting the **optical survey**. This geometry must be sufficiently precise to allow reasonably good track-linking to VXD3 clusters, which is necessary for making improvements over this first-pass internal geometry by a procedure called **internal alignment** [86].

Since slight change in position or orientation of one CCD will necessarily cause changes in the global VXD3 position, it is clear that the rigidity of VXD3 is only an approximation, and internal and global alignments cannot fully decouple from each other. In practice, two global-internal alignment iterations are usually reasonably sufficient.

We do not use the VXD3 design geometry as the first-pass geometry for track-linking for the following reasons. Mechanical design geometry can be relied upon only if all of the components are highly rigid themselves as well as with respect to each other, in which case the only uncertainty in the position of each component comes from the resolutions of manufacture and installation of parts and components. In many applications, very high precision can be achieved mechanically. Unfortunately, the CCD ladders that make up the core of VXD3 do not satisfy these criteria. The design of a ladder is such that the CCDs and the ladder themselves are not rigid and can bend to take fairly complicated shapes as well as can sag under gravity. Furthermore, one end of the ladder is allowed to move slightly to relieve mechanical strain from thermal contractions, which introduces another source of uncertainty in the position of the actual CCD pixels. These factors, especially the shape of the CCD and the gravitation sag, must be measured. From this point of view, the ideal design geometry in which CCDs and ladders are flat surfaces is certainly not a good first-pass description of the VXD3 geometry.

5.3 Optical Survey

5.3.1 Goal of the Survey

An optical survey of VXD3 was performed in order to determine the internal geometry of the device to an accuracy sufficient for beam-related tracks to be used for final alignment. A secondary goal of the survey was to measure aspects of the geometry which would be difficult to determine accurately from tracks, such as the complex shape of the CCDs themselves and the gravitation sag of the ladders. These two aspects of the geometry were important factors in achieving the overall precision required.

All ladders (48) and all layers (3) were surveyed. The ladder survey determined the relation of two CCDs to each other and the barrel survey fixed the position of the ladders to each other. The precision requirement of the survey was to determine the geometry to ~ 20 μm (1 pixel) rms. At this level of alignment the finding of tracks is straightforward. However, in order to achieve the performance required for the physics objectives, the ultimate spatial precision must be of order 5 μm rms. Track alignment data was used to achieve this final level of precision.

5.3.2 The Coordinate Measuring Machine

The OMIS II programmable optical coordinate measuring machine (CMM) [87] was used for the survey. The CMM had an aperture of $12 \times 6 \times 7$ inches, which easily accommodated both the ladder and barrel surveys, and had a nominal precision of a few microns in x and y (horizontal plane of the CMM) and approximately 15 microns in z (vertical coordinate of CMM). The $x - y$ scale calibration of the CMM was monitored throughout the survey process by means of a precision glass scale and a precision stepper gauge was used for the z calibration. Both standards were NIST-traceable and were cross checked with other standards.

Objects could be illuminated in the CMM by axial lighting, ring lighting, or back lighting. It was determined that axial lighting yielded the best results and was therefore used for the measurement of most features. Back lighting was used for the profile measurement of the ladders. A variety of survey algorithms were available to measure different aspect of features. For example, an area tool was used to determine the z-coordinate and a line-scan tool was used to precisely determine the edges of sharply defined features. Simple geometric constructions, such as the intersection of two lines and circle fitting were available.

Programs were written to measure the ladders and the barrel. The initialization of each program was done on representative features requiring the most precision. In this way only 4 programs were needed for the ladder survey, one for each view defined by rotations of $N\pi/2$ about the long axis of the ladder. Symmetry was employed in the barrel survey so that only 19 programs were needed for the 48 ladders.

5.3.3 The Ladder Survey

Ladders were surveyed at room temperature in enclosed survey boxes which supported them in the same manner as in the beryllium super structure. The survey jig was outfitted with 6 precision tooling balls which defined an internal coordinate system. Figure 5-3 shows the View One configuration. Four views of each ladder were measured. The ladder geometry was reconstructed by relating 3 of the views to the standard view defined by the ladder orientation where the north CCD was visible and approximately in the CMM $x - y$ plane. Roughly 6 hours were needed to measure a ladder.

Since the survey was performed outside a clean room the CCDs had to be protected by enclosing the survey jig in a high quality optical glass window which had to be coated to reduce reflections when the axial illumination was used. In all, 4 survey boxes were fabricated although only 3 were used for production surveying.

A survey box was located on the CMM by means of 3 tooling balls mounted on the surface of each side of the box corresponding to each of the 4 views of the ladder survey. These tooling balls mated to grooves milled in an aluminum support plate which was rigidly attached to the $x - y$ table of the CMM.

A number of features were measured in the ladder survey in addition to the 6 tooling balls used to define the ladder local coordinate system.

CCD Fiducials: Each CCD had 186 fiducials which were quite accurately placed in the CCD gate structure by the same photo-etching process used in the CCD fabrication. The fiducials were arranged in 6 columns every 3.000 mm along the 16 mm dimension of the CCD and by 31 rows every 2.500 mm along the 80 mm dimension. The fiducials were 60×60 μm^2 pads 1 μm thick and located 12 μm above the mid-plane of the epitaxial layer. However, given the OMIS II lighting and edge finding tool, the edge of the polyimide layer coating of the fiducials was actually measured. It had a dimension of 80×80 μm^2 but was still quite accurately determined. All of the columns of fiducials and every other row of fiducials were measured for a total of

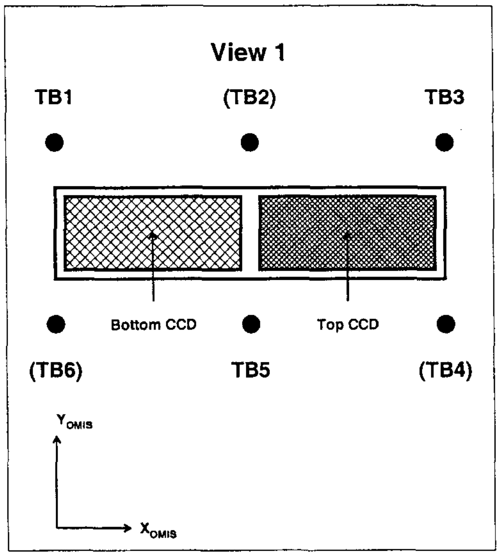

Figure 5-3: The ladder and tooling balls in View One. Tooling balls with lower z coordinate are labeled in parenthesis. The z-axis is pointing out of the page.

96 features.

Flex-strip Fiducials: All fiducials (3 columns $\times$ 14 rows) were measured on the copper-kapton flex-strips, albeit with less precision than those on the CCD surfaces.

Physical Corners of Silicon Chip: In addition to the fiducials mentioned above, the physical corners of the CCDs were measured. Although less precise than the fiducials, the physical corners of the silicon provided helpful navigation points.

Profiles of CCDs: Finally, the profiles of each CCD were measured with back lighting. These data provided useful cross checks to the face-on views and allowed the gravitation sag to be measured.

5.3.4 The Barrel Survey

After the ladders of a given barrel layer were measured they were assembled in the Be support structure in their final position and surveyed to determine the barrel geometry. A set of 32 precision tooling balls mounted on the precision Be super structure, 16 to an end defined the barrel survey coordinate system. ScotchLite was placed under each tooling ball to allow axial lighting to illuminate the circumference of the tooling ball. The Be super structure was mounted kinematically on a dummy beam pipe which was rotated inside the barrel survey box to allow the ladders of a layer to be surveyed. As in the ladder survey, the barrel survey was conducted outside a clean room and at room temperature. The window of the barrel survey box was made of optical glass which was coated in order to reduce the reflections of the axial lighting needed for the survey.

The outside surface of each ladder of a layer was measured with each ladder approximately positioned in the CMM $x-y$ plane. There were 12, 16, and 20 configurations measured for layers 1, 2, and 3, respectively. Associated with each ladder configuration was a measurement of the concomitant set of visible tooling balls. There were typically 4 to 6 balls on each end for each configuration, with at least 3 balls on each end overlapping between adjacent configurations. The barrel geometry was assembled by making the sets of overlapping tooling balls congruent.

Only about 50% of the fiducials on the outside (north CCD face up) were visible in the barrel survey since the survey had to be conducted through the beryllium cylinder which holds the two ends together. Thus all visible fiducials on the CCD and flex strips were measured as well as one of the physical corners of the silicon which served as a navigational aid. Given that a smaller number of fiducials were measured than in the ladder survey, each z-coordinate of the visible fiducials was measured 4 times resulting in an improvement in the z resolution. The complete barrel survey was executed in 10 days (not including programming time). Figure 5-4 and Figure 5-5 show the end and side views of the barrel survey, respectively.

5.3.5 Survey Data Analysis

A number of analysis steps were conducted after the geometry assemblies of the ladder and barrel data.

Calibration of Optical Distortions of Ladder Survey Boxes:

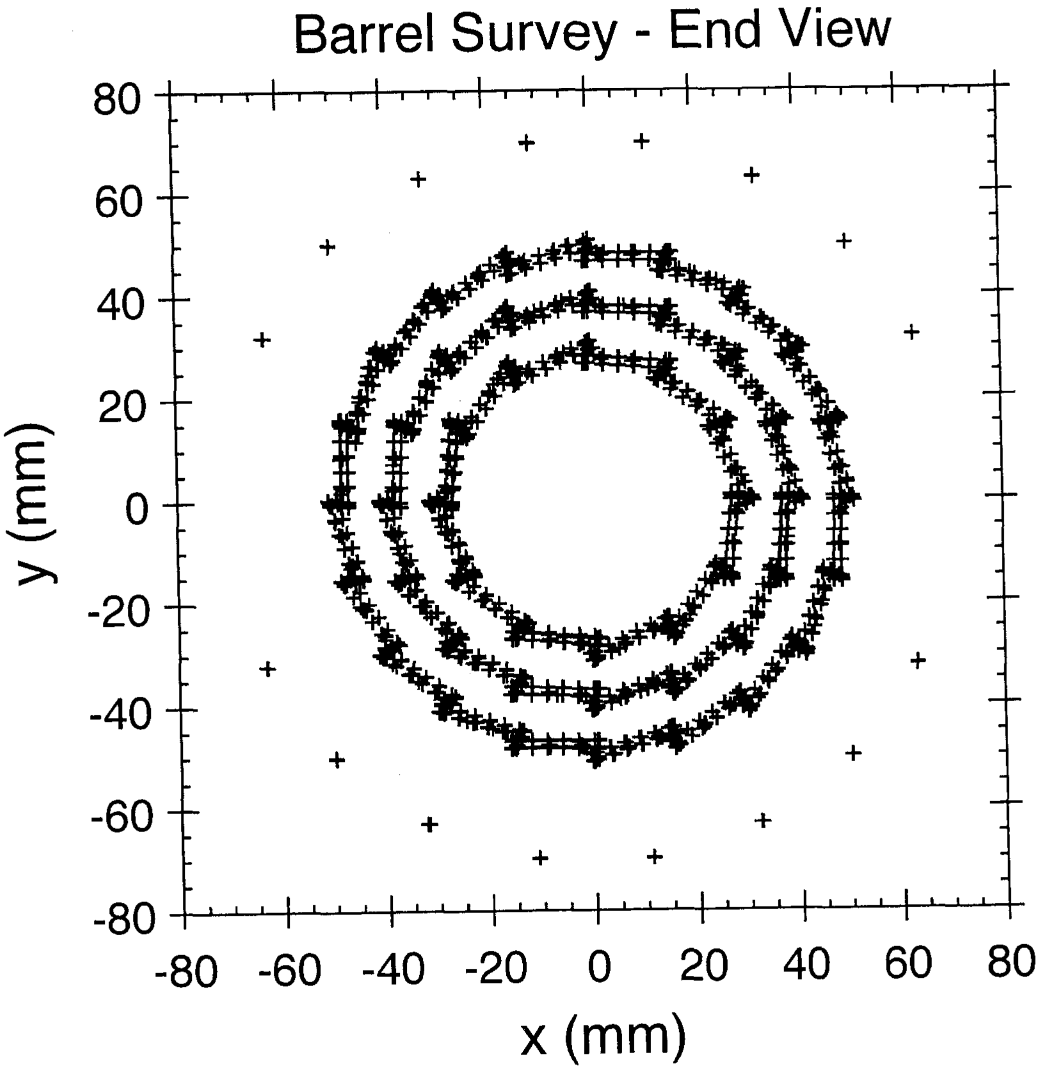

Figure 5-4: The end view of the barrel assembly. Note the 32 tooling balls which define the barrel survey coordinate system.

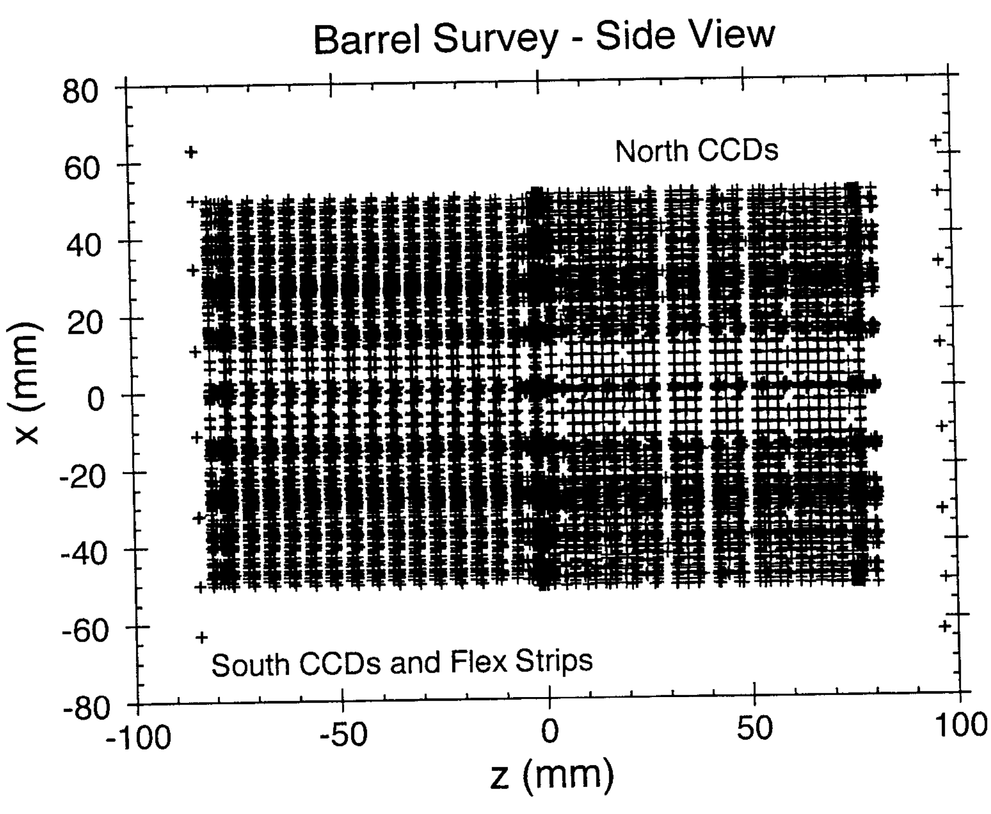

Figure 5-5: The side view of the barrel assembly. Note the 32 tooling balls which define the barrel survey coordinate system.

The 3-dimensional distances of all combinations of the 6 tooling balls were used to determine the distortions of the ladder survey box windows in a χ^2 fitting procedure. In some cases the CMM scales had to be changed by as much as 10^{-3} mm/mm although the net effect was small owing to the small distances involved.

Calibration of Optical Distortions of Barrel Survey Boxes:
The optical distortion of the barrel survey box was determined by measuring the glass scale standard and the stepper gauge through the glass window. Distortions of order 3.5×10^{-4} mm/mm were observed. These corrections were verified in the data by using the well-defined fiducial separations of the CCD fiducials.

Attaching Ladder to Barrel Data:
Since only the outer radius surface of the ladders was measured in the barrel survey, the position of the south CCD had to be derived from mating the ladder data with the barrel data which served as the backbone. This was accomplished by making the common surfaces of the ladder and barrel surveys congruent. Roughly 20 to 30 features were in common in the ladder-barrel mating. The CCD fiducials were given higher weight in the χ^2 fitting because they were much better determined than the flex strip fiducials.

Determination of the Gravity Sag and Z-Constraint:
The planes of the north and south CCDs were measured face up on the CMM. Hence the gravitation sags for the north and south CCDs were of opposite sign and had to be corrected. By comparing the profile to the end views of the CCD survey the gravitation sag of the ladders could be determined. It was found that average sagitta of the sag was roughly 30 μm but with considerable variation ladder-to-ladder. Having corrected for the gravitation sag the south CCD was constrained to the north by using the well-measured separation in the ladder profile views. Typically adjustments of 10 to 20 μm had to be made thereby improving the precision of the z-measurements of the face up view. Hence, the average correction for the south CCD was 60 m to correct to the north CCD convention. The measured gravitation sag was then

projected by a cosϕ factor to compute the sag of a ladder in its final configuration in the assembled vertex detector.

Thermal Contraction:
VXD3 was surveyed at room temperature, about 123 °K warmer than the operating point. Hence the survey data had to be contracted to correspond to the lower operating temperature by integrating the nonlinear coefficients of thermal expansion (CTE) for Be and Si. A simple model of differential thermal contraction of Be (the ladder substrate) versus Si was used which assumed that the Si contracted uniformly about its geometric center with the geometric center contracting by the Be CTE. Overall, the beryllium contracted by a factor -7×10^{-4} mm/mm and the differential contraction between Si and Be was only -20μm over the 80 mm of the CCD.

As a check of the shape of the ladder with thermal contraction the position of the CCD with respect to the Be substrate was measured at Brunel University. It was found that the CCD does not distort under cool down and only the average distance of the CCD from the substrate contracts by -10μm.

5.3.6 CCD Shape Corrections

The track fitting using the CCDs takes a simple model of the CCD position and surface which are modified by a series of corrections listed below.

Pixel (1,1) and Average CCD Plane: The lowest order description of the location of a given CCD in VXD3 was determined by the position of pixel (1,1) and the average CCD plane. Pixel (1,1) was defined by either the north-most (south CCD) or south-most (north CCD) pixel on the low $r\phi$ side. The average plane of the CCD was computed and described by unit vectors.

Shape of the CCDs: The shapes of the CCDs are complex. It was found that the short dimension (16 mm) is concave upward with a shape described by a quadratic. The long dimension (80 mm) is quartic. In order to describe the shapes a fit to the CCD surface was performed with these functional forms and all cross terms. These shapes were used to compute the perturbation of the surface from the average plane. The CCD shape description was an important correction at small polar angle, θ, varying as $\cotan(\theta)$.

5.3.7 Summary of VXD3 Optical Survey

The optical survey of VXD3 established its initial geometry to an accuracy within roughly 1 pixel, estimated by the redundancy of the measurements. Further refinements of the geometry came from tracks. There are several known distortions beyond the optical survey geometry. One was the fitting of the Be halves around the SLC beam pipe, following the optical survey at MIT. The magnitude of the distortion was estimated. During the optical survey VXD3 was assembled-disassembled-reassembled around the dummy beam pipe and resurveyed to find distortions of order 20 to 30 μm. Hence it is likely that the final geometry has such distortions. These can be accommodated in the data by moving the CCDs in order to minimize the track residuals in the internal alignment procedure. Perhaps the most important contribution of the survey is the determination of the gravitation sag and the CCD shapes. These effects would be difficult to untangle using data.

5.4 VXD3 Global Alignment

The VXD3 global alignment determines the relative position of the VXD3 with respect to the Central Drift Chamber (CDC) assuming VXD3 is a rigid body that can only change its position by the three translations (dx, dy, and dz) and its orientation by the three rotations (α, β, and γ). A rigid internal geometry of the VXD3 is needed as input to the global alignment procedure. When the internal geometry is modified, the global alignment must in principle be repeated as well.

To determine the global position of the detector to a precision of a few microns, we must make use of the precise CCD hits made by charged tracks reconstructed in the

CDC. First, we hypothesize that the VXD3 is at a particular global position parameterized by the six variables dx, dy, and dz, and α, β, and γ. High quality CDC tracks are extrapolated inward towards the IP until they intersect with the hypothesized locations of CCD surfaces at all possible layers. The position of the intersecting point is taken as an 'extrapolated hit'. These tracks actually make real hits on the CCDs. We call these the 'actual hits' and their locations are purely registered as local CCD readout coordinates. The location of the extrapolated hit, measured in CCD local coordinates, changes with the hypothesized VXD global position but the location of the actual CCD hit does not change. A hit residual is defined as the difference in locations measured in the local CCD coordinates between the extrapolated hit and the actual hit. These hit residuals are directly determined by the hypothesized global position of the detector. Figure 5-6 illustrates how the residuals are generated when a track is extrapolated to a position different from the position of the readout hit.

When a large number of tracks are extrapolated, a large number of residuals can be calculated for each hypothesized VXD global position. The optimal detector global position is found by minimizing the χ^2 formed using these residuals and the hit resolutions. Note that the resolutions of extrapolated hits are typically substantially worse than the intrinsic resolutions of CCD hits.

If the exact internal geometry and the global alignment were known, the location of extrapolated hit would coincide with that of the actual hit on the CCD to within the hit resolutions. If the internal geometry were very well known but not the global alignment, the residuals between the two hits would be non-vanishing. In this case, the detector could be precisely aligned through global movements of the detector (translation or rotation) until all pairs of extrapolated hit and actual hit would match each other to within hit resolutions. If the internal geometry were not very well known, there would be internal inconsistencies between hit-residuals on one CCD and those on another. No global movements of the detector could eliminate these inconsistencies altogether and therefore global alignment would not be quite optimal. In reality, it

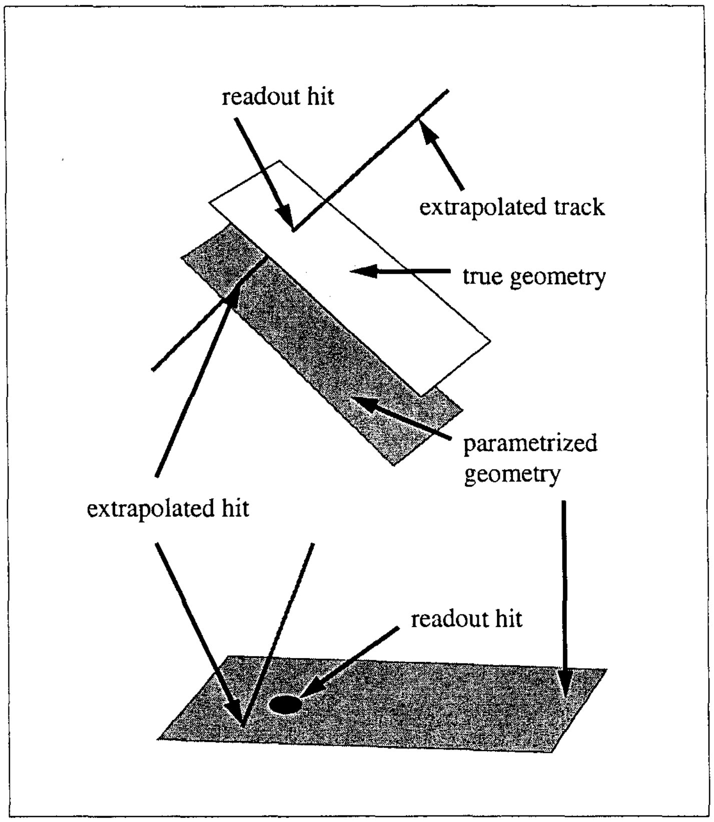

Figure 5-6: Illustration of the track extrapolation to the CCD surface, generating the 'extrapolated hit', which typically is at a different location from the readout hit.

is often the true internal geometry that is hardest to find. The precision in global alignment is typically sufficiently good for track-linking purposes even if it is not optimal.

Specifically, the global alignment is achieved through a minimization of the χ^2 of all the hit-residuals. The total χ^2 can be minimized by varying the six parameters dx, dy, dz and α, β, and γ. The outputs of the alignment procedure are precisely these three translations and three rotations of VXD3.

The global alignment is performed for the entire data set taken during the 1997-1998 run in order to 1) Monitor any small changes in global positions; 2) Minimize the statistical uncertainty on the alignment results. Every time VXD3 is known or expected to have moved, for example during a controlled R20 movement, a triplet movement, door opening, any unexpected movements indicated by the capacitive wire position monitor. Even a change in the running temperature of the VXD3 may lead to alignment changes. We now proceed to describe briefly the specifics of the alignment procedure and present the alignment results for 1997-1998. For global alignment results for run 1996, see Ref [75].

5.4.1 Global Alignment: Track Selection

The alignment procedure requires good quality tracks from the CDC which have been linked to clusters in the VXD3. The cuts placed on the tracks and the clusters are shown in Table 5.2. Figure. 5-7 shows an event, where only the clusters linked to tracks extrapolated from the CDC are plotted.

Tracks with momentum below 0.5 GeV/c are rejected because these undergo significant multiple scattering. The CDC track length and the number of hit requirements selects tracks that have gone through a large volume of the drift chamber, while the χ^2 requirement eliminates tracks that have been reconstructed poorly. Demanding that the track must come from the Interaction Point (IP) ensures that tracks similar to the one on the right of Fig. 5-7 are rejected. The CDC tracks are then extrapolated

Minimum Momentum (GeV)	0.5
Maximum $tan(\lambda)$	1.58
Minimum CDC Track Length (cm)	50
Minimum Number of CDC Hits	50
Maximum CDC Track χ^2	10
Minimum Cluster Pulse Height	20
Minimum Number of Pixels per Clusters	1
Minimum Number of Clusters	2
Track must come from the IP	YES

Table 5.2: Quality track cuts.

inwards and the point at which the track intersects the surface of a CCD is recorded.

5.4.2 Global Alignment: Residual Calculation

The residuals are formed by calculating the difference, in the x and z direction, between the track intercept point and the cluster center (Figure. 5-8). Fig. 5-9 shows plots of the residuals before the alignment is performed [75]. Notice the double peak in the Dη residuals, indicating a misalignment of the VXD3 with respect to the CDC.

5.4.3 Global Alignment: χ^2 Minimization Fit

The following function (Equation 5.1) is then calculated and fed into MINUIT [88] for a χ^2 minimization fit.

$$\chi^2 = \sum_{i=1}^{Num} \left[\left(\frac{D\eta_i}{\sigma_{\eta_i}} \right)^2 + \left(\frac{Dz_i}{\sigma_{z_i}} \right)^2 \right], \tag{5.1}$$

where Num is the number of hits used, $D\eta$ is the residual in $r\phi$, Dz is the residual in z, σ_η is the error on dη , and σ_z is the error on Dz. The parameters of the fit are the three translations and three rotations:

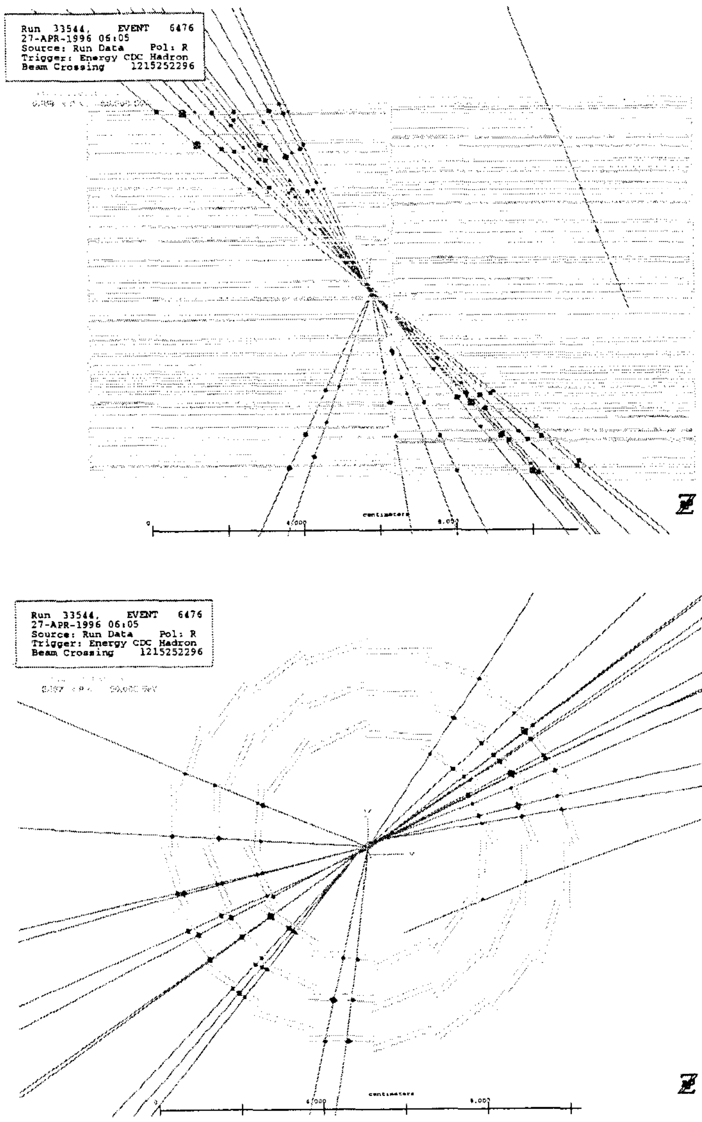

Figure 5-7: Side view (top) and front view (bottom) of VXD3. The lines are tracks extrapolated from the CDC, plotted with their associated VXD3 clusters.

- α : Roll about the beam pipe (rotation about z)
- β : Horizontal yaw (rotation about y)
- γ : Vertical pitch (rotation about x)
- dx : Translation in x
- dy : Translation in y
- dz : Translation in z

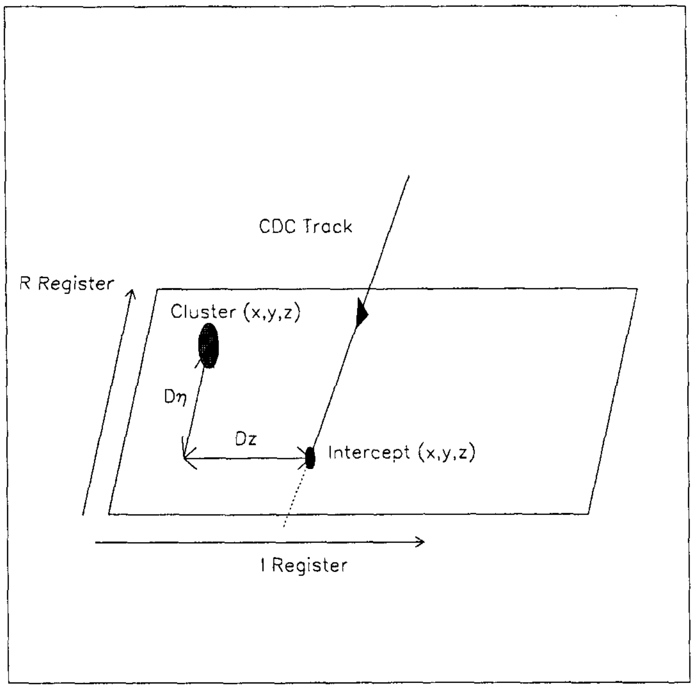

Figure 5-8: A CDC track extrapolated back onto the hypothesized surface of a CCD, plotted along with the intercept point and the residuals between that point and the associated VXD cluster. The residual Dz is along the CCD I register (z) and Dη is the residual along the CCD R register ($r\phi$).

5.4.4 Global Alignment: Results

A series of VXD3 running operations was performed during the 1997 run. For example, the VXD3 running temperature was lowered a couple of times from the original VXD2 running temperature of 190°K to reduce effects of radiation damage. Movements of the R20 module also directly affected the global position of the VXD3 relative to the CDC. The global alignment procedure described above is applied to data from each run period separated by such activities. Table 5.3 lists the alignment results for the six parameters for each of these periods. We monitored the change in alignment constants over the entire run period for 1997-98. All events are used in the

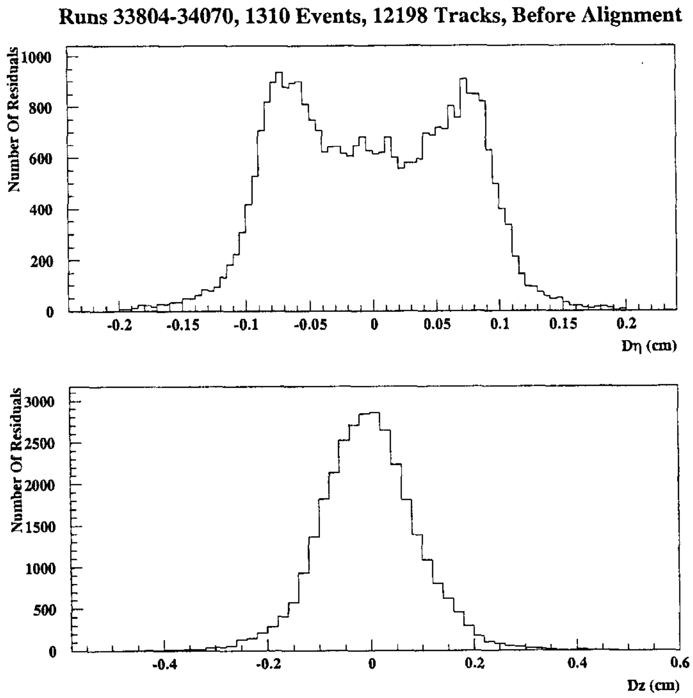

Figure 5-9: Residual plots for the whole detector, before the alignment is carried out.

alignment. Figure 5-10 shows the alignment results as a function of data set for data reconstruction 15 (R15). After we generated the alignment constants for 1998, we did a cross check by performing the alignment procedure again using the *aligned* R16 geometry. Except for dz translation, the other five constants are almost consistent with being zero, which should be the case for a well-aligned detector. The results are listed in Table 5.4. Since uncertainty in CDC dip angle is much larger than the sixty-micron shift in z, this poses essentially no problem for linking CDC tracks to VXD3. Alignment results for the latest data reconstruction (R16) are shown in Figure 5-11.

Since the VXD3 global alignment procedure minimizes χ^2 of hit residuals calculated based on an imperfect internal geometry, the precision of alignment results is partly limited by this internal geometry. Using track miss-distance in $Z^0 \to \mu^+\mu^-$ events, the global alignment constants, especially the rotations, have been

Run Period	dx (μm)	dy (μm)	dz (μm)	α (mrad)	β (mrad)	γ (mrad)	Description
37418-38639	-81.8	-66.8	153.8	-0.92	0.27	-0.27	T = 188 K
38685-38761	-73.3	-66.1	160.4	-0.88	0.25	-0.30	T = 183 K
39493-39644	-74.0	-72.2	117.0	-1.14	0.38	0.05	Pre R20 Move
39645-39781	183.3	23.7	173.4	-1.08	0.29	-0.52	Pre 2nd R20 Move
39782-40366	431.6	-211.5	105.8	-0.97	0.40	-0.62	Post 2nd R20 Move

Table 5.3: Results of VXD3 global alignment for 1997 run.

dx	5.24±0.79	μm
dy	1.52±0.76	μm
dz	-64.9 ± 5.2	μm
α	0.004±0.007	mrad
β	0.015±0.025	mrad
γ	-0.046 ± 0.025	mrad

Table 5.4: VXD3 global alignment constants for 1998 run based on R16 geometry.

slightly tuned by hand to further improve the VXD3 geometry and therefore track spatial resolutions.

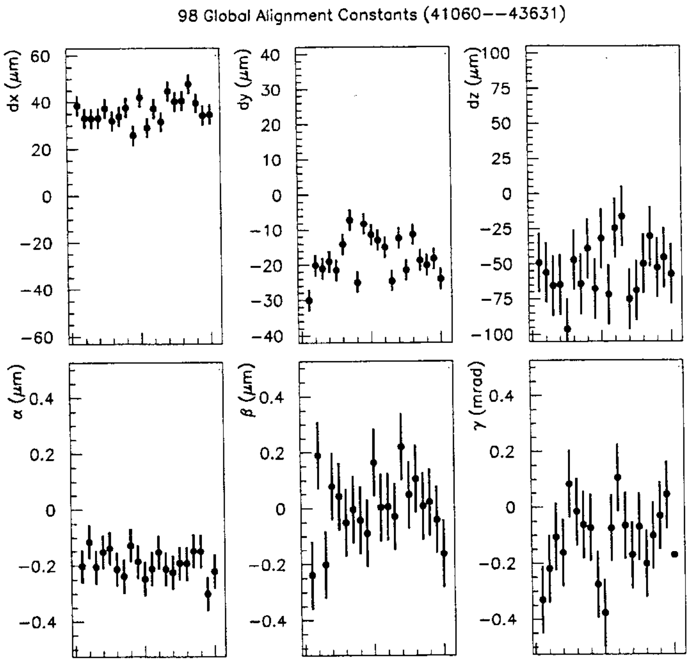

Figure 5-10: VXD3 global alignment constants vs data sets for 1998.

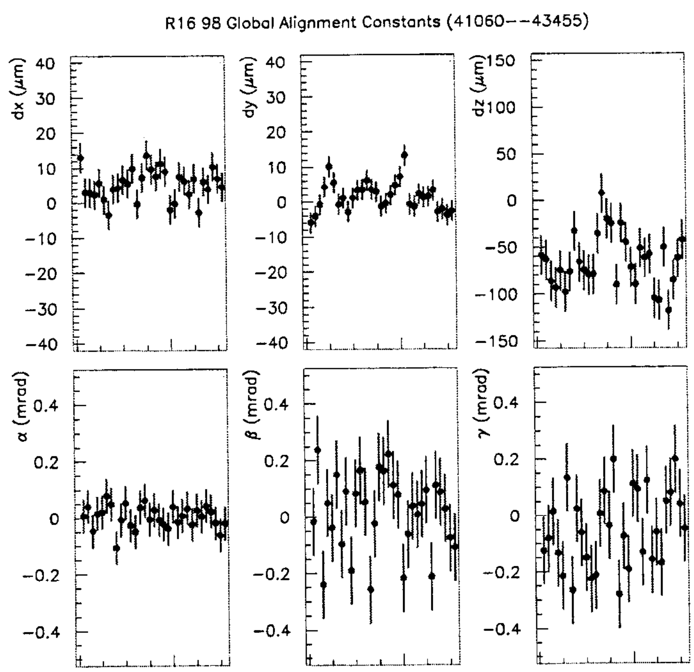

Figure 5-11: VXD3 global alignment constants vs data sets for 1998 (R16).

5.5 VXD3 Performance

The doublet and triplet (see below) resolutions for R16 1998 data (the latest version of data reconstruction) are shown in Figure 5-12 and 5-13 [89]. These plots demonstrate the current spatial resolutions from hadronic event tracks. Doublets residual is one in which a track hitting both north and south CCDs on the same CCD-ladder. Since the relative positions of 2 CCDs on the same ladder is better determined than the ladder-ladder alignment, doublets more closely reflect the intrinsic spatial resolution. Triplets are track hitting 3 ladders in 3 different layers and is sensitive to the ladder-ladder alignment precision. The doublet/triplet residuals are calculated by fixing the track to 2 of the hits on the track then look at the residual of the fixed track to the remaining hit. The single hit spatial resolution can be derived from doublet (triplet) residual divided by an average lever-arm factor of $\sqrt{2}$ ($\sqrt{1.5}$). With our current R15A 1997 alignment of Feb-03, 1998:

- Doublet $r\phi$ single hit resolution $= 5.82/\sqrt{2} = 4.1$ μm.
- Doublet z single hit resolution $= 5.88/\sqrt{2} = 4.2$ μm.
- Triplet $r\phi$ single hit resolution $= 4.68/\sqrt{1.5} = 3.8$ μm.
- Triplet z single hit resolution $= 5.15/\sqrt{1.5} = 4.2$ μm.

where we have taken doublets for all tracks with $p > 1$ GeV and triplet for all track with $p > 8$ GeV and within $\cos(\theta) < 0.7$.

The impact parameter resolution of tracks in hadronic Z^0 decays as well as in $Z^0 \to \mu^+\mu^-$ and $Z^0 \to e^+e^-$ events are studied for individual momentum and cosθ regions [79]. The expected impact parameter resolutions based on Monte Carlo for tracks at cos$\theta = 0$ with VXD3 are shown in Figure 5-14 in comparison to VXD2 Monte Carlo and data. The VXD2 Monte Carlo describes the data remarkably well. The same Monte Carlo framework applied to VXD3 results in a factor of two improvement from VXD2 in the entire rz view impact parameter resolution. Improvement in the

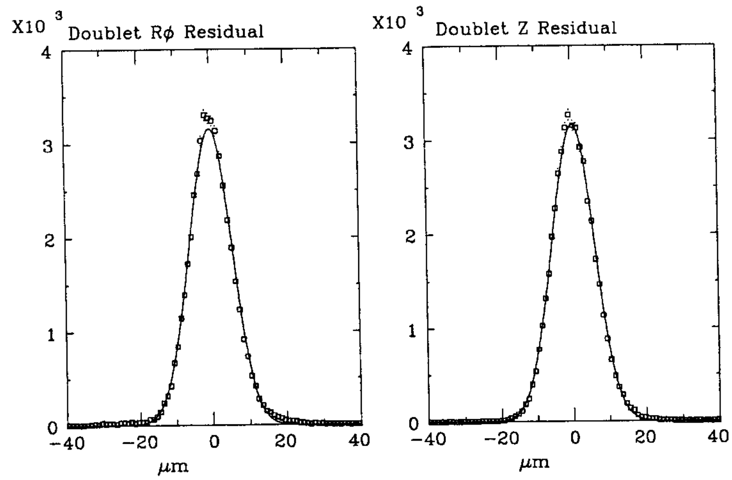

Figure 5-12: VXD3 doublet resolution (R16). The derived single hit resolutions are 4.1 μm ($r\phi$) and 4.2 μm (rz).

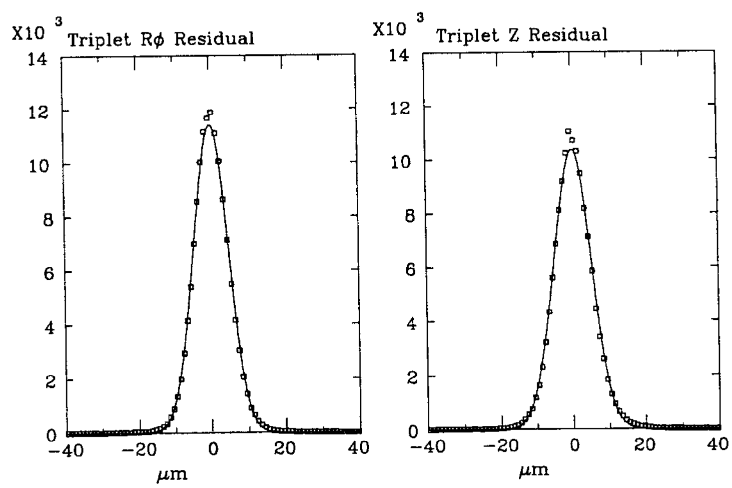

Figure 5-13: VXD3 triplet resolution (R16). The derived single hit resolutions are 3.8 μm ($r\phi$) and 4.2 μm (rz).

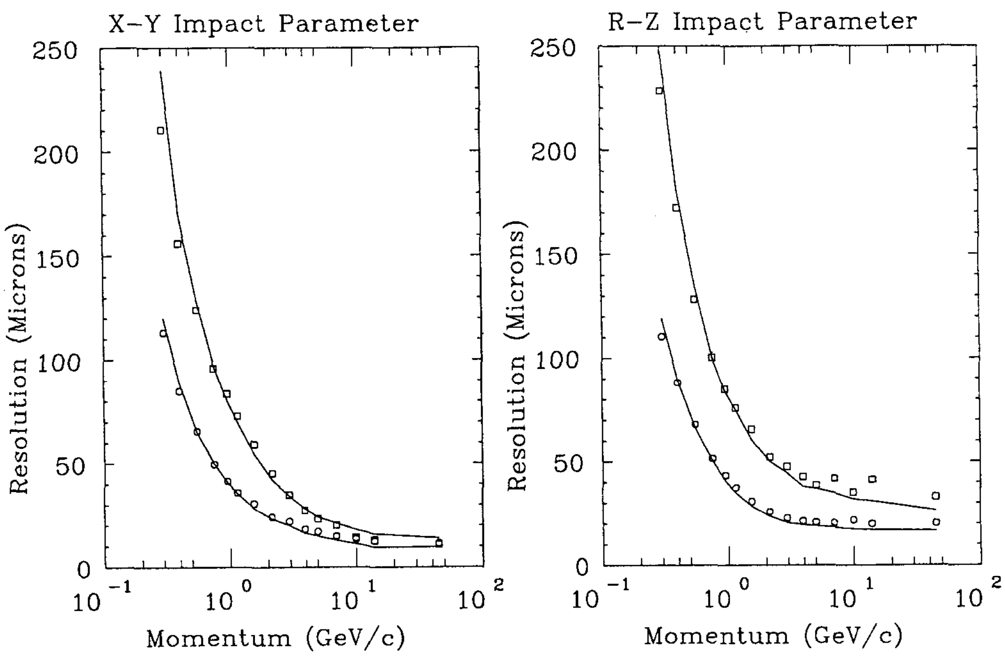

Figure 5-14: VXD3 impact parameter resolutions in comparison to VXD2 resolutions.

$r\phi$ view is also a factor of two at low momentum, while somewhat less at very high momentum. The measured VXD3 impact parameter resolution is

$$\begin{aligned} \sigma_{r\phi} &= 9 \oplus \frac{33}{(p \sin^{3/2}\theta)} \mu m, \\ \sigma_{rz} &= 17 \oplus \frac{33}{(p \sin^{3/2}\theta)} \mu m. \end{aligned} \tag{5.2}$$

In the next Chapter, we will begin to describe the physics analysis of this thesis, which has benefited tremendously from the excellent spatial resolutions provided by VXD3.

Chapter 6

Hadronic Event Selection and B Tagging

This analysis is based on roughly 150,000 hadronic events produced in e^+e^- annihilations at a mean center-of-mass energy of $\sqrt{s} = 91.28$ GeV at the SLAC Linear Collider (SLC), and recorded in the SLC Large Detector (SLD) in 1996 and 1997.

6.1 Hadronic Event Selection

The data collected by the SLD detector contains hadronic events ($e^+e^- \to q\bar{q}$) as well as leptonic events ($e^+e^- \to e^+e^-$, $e^+e^- \to Z^0 \to \mu^+\mu^-$ or $\tau^+\tau^-$). To study the B hadron energy distribution, the very first step is to select hadronic events (Z^0 decays into $q\bar{q}$).

There are several phases in selecting hadronic events. The first phase is the triggering of the SLD. The trigger decides whether events are to be read out to tapes or not. The Hadronic event filter rejects most of the background related to beam- beampipe interactions. The Hadronic event selection cuts are designed to select efficiently a highly pure sample of $Z^0 \to q\bar{q}$ events for which the simulation and the data are consistent.

6.1.1 The SLD Trigger

The SLD triggers are described in detail in Ref. [91]. We mentioned the SLD trigger briefly in the description of SLD data acquisition.

6.1.2 The Hadronic Event Filter

The triggers are designed to reduce the acquisition rate to a manageable level. The thresholds are kept as low as possible so that the triggers accepted many events that are not Z^0 events, most of which are beam-gas or beam-wall events caused by beams interacting with beampipe materials.

The pass-1 EIT filter is used to eliminate a large fraction of such background events. The filter selects events using calorimetry information only, which is processed much faster than tracking information. EIT pass-1 cuts are based on three LAC quantities, whose names are simplified by the bold-font capital letters):

- NEMHI, **N**umber of LAC **EM** towers with signals above the **HI**gh threshold of 60 ADC counts. This is equivalent to $\sim$ 250 MeV from minimum ionizing particles (min-I).

- EHI, the sum of the **E**nergy deposited in all EM (HAD) towers with signals greater than the **HI**gh thresholds of 60 (120) ADC counts. This is equivalent to 250 MeV (1.3 GeV) min-I.

- ELO, the sum of **E**nergy deposited in all EM (HAD) towers with signals greater than **LO**w thresholds of 8 (12) ADC counts. (This is equivalent to 33 MeV (130 MeV) min-I)

The filter requires that each event satisfy

1. NEMHI $\geq$ 10
2. EHI $>$ 15 GeV min-I
3. ELO $<$ 140 GeV min-I

4. $2 \times$ EHI $> 3\times$ (ELO-70)
5. NEMHI > 0 for both North and South hemispheres.

The first and second cuts are similar to the trigger requirements. Cuts three and five insure that the event had not satisfied the first two cuts by depositing a large amount of background energy and therefore remove most beam-wall events.

6.1.3 The Hadronic Event Selection Cuts

Motivation

The goal of hadronic event selection is to provide a maximal sample of hadronic events that are well contained within sensitive detector region. Most of the backgrounds should be rejected. In addition, a general requirement for hadronic event selection is to insure that, most, if not all, basic and well-understood distributions (such as event visible energy) in the data are reproduced by the Monte Carlo simulated events. Monte Carlo and the data are not usually consistent with each other before hadronic event selection.

The determination of the SLD IP, track impact parameter resolutions, the thrust axis and the selection of well-measured tracks are briefly described so we can conveniently discuss hadronic event selection.

The SLD Interaction Point and Impact Parameter Resolution

The SLD IP and the resolution of track impact parameters including the IP error must be determined before we apply the hadronic event selection cuts.

The centroid of the micron-sized SLC IP is reconstructed from tracks in sets of approximately thirty sequential hadronic Z^0 decays to a precision of $\sigma^{r\phi} \simeq 7 \pm 2$ μm (1996) and $\sigma^{r\phi} \simeq 4 \pm 2$ μm (1997). The IP position along the beam axis is determined event by event using charged tracks with a resolution of $\sigma^{z} \simeq 35$ μm (1996) and $\sigma^{z} \simeq 30$ μm (1997).

Including the uncertainty on the IP position, the resolution on the charged-track impact parameter (d) projected in the plane perpendicular to the beam-line is $\sigma_d^{r\phi}$ $= 14 \oplus 33/(p \sin^{3/2}\theta)$ μm (1996) and $\sigma_d^{r\phi} = 11 \oplus 33/(p \sin^{3/2}\theta)$ μm (1997), and the resolution in the plane containing the beam axis is $\sigma_d^z = 27 \oplus 33/(p \sin^{3/2}\theta)$ μm (1996) and $\sigma_d^z = 24 \oplus 33/(p \sin^{3/2}\theta)$ μm (1997), where θ is the track polar angle with respect to the beam-line.

The Thrust Axis

The event thrust axis [92] is calculated using energy clusters measured in the Liquid Argon Calorimeter.

"Well-measured" Charged Tracks

This analysis is mostly based on charged tracks measured in the Central Drift Chamber (CDC) [93] and in the upgraded Vertex Detector (VXD3) [79]. Since the CDC efficiency drops beyond $|cos\theta| = 0.87$, only hadronic events in this barrel region of the detector are selected. Energy flow such as energy in jets should also be largely contained in the barrel region and not lost in the end-caps (software for end-caps are not reliable enough to be used in this analysis). Most of the cuts, however, are based on quantities related to "well-measured" charged tracks. A well-measured track must satisfy

- $|cos\theta| < 0.80$ (θ is the polar angle of the track). This insures the track is contained in the barrel region of the detector.
- Distance of closest approach ($DOCA$) to the interaction point (IP) in the $r\phi$-plane, which is transverse to the beam-axis, satisfies: $DOCA_{r\phi}^{IP} < 5$ cm.
- $DOCA$ to the IP in the rz-plane, which is perpendicular to the beam-axis, satisfies: $DOCA_z^{IP} < 10$ cm. The above two cuts insures the track does not originate far from the IP.

- Transverse momentum relative to the beam axis $p_\perp > 150$ MeV/c.

The second and third cuts insure that the track comes from Z^0 decays (near the SLD IP), rather than from beam interactions.

The Hadronic Event Selection Cuts

An event is selected as a candidate hadronic event if it satisfies:

- ≥ 5 well-measured charged tracks. This cut is used to reject nearly all leptonic Z^0-decay events, which have low multiplicities except for $Z^0 \to \tau^+\tau^-$ which can have a maximum of 6 tracks.

- $|cos(\theta_{thrust})| < 0.71$. θ_{thrust} is the angle between the thrust axis determined from calorimeter clusters and the beam-axis. This rejects events in which a significant fraction of the energy may be lost in the end-caps, which are poorly instrumented.

- $E_{vis} > 20$ GeV. The visible energy, E_{vis}, is calculated by summing the energy of all well-measured charged tracks, assuming each charged track has the charged pion mass of 139.57 MeV. This cut rejects $\gamma\gamma$ events and leptonic Z^0 events, especially $Z^0 \to \tau^+\tau^-$ events.

- VXD3 fully operational. This ensures that tracks in the selected events have good spatial resolutions (such as impact parameter resolutions) which are critical for finding secondary heavy hadron decay-vertices, an important ingredient of this analysis.

Performance

Table 6.1 shows the efficiency for the different event flavors to pass all hadronic event selection cuts for each period of data used in this analysis. The selection efficiencies for uds, c, and b are almost consistent with each other within the same

Run Period	*uds* Efficiency (%)	*c* Efficiency (%)	*b* Efficiency (%)
1996	61.46±0.37	61.55±0.70	62.02±0.63
1997 Summer	67.30±0.24	67.53±0.45	68.37±0.40
1997 Fall	67.04±0.18	67.36±0.35	68.26±0.31

Table 6.1: The efficiencies for hadronic events of different primary quark flavors to pass the hadronic event selection cuts. All numbers are determined from the simulation.

Run Period	No. of events on tape	No. of selected events
1996	102,696	37,694
1997	176,814	73,875
Total	279,510	111,569

Table 6.2: Number of selected hadronic events in 1996-97 data.

period. Although the b efficiency is slightly larger, the bias is rather small. The efficiencies for 1997 simulations are about 6% higher than those in 1996. Table 6.2 lists the number of selected hadronic events in 1996 and 1997 data.

The efficiency for selecting a well-contained $Z^0 \to q\bar{q}(g)$ event is estimated to be above 96% and independent of quark flavor. The selected sample comprised 111,569 events, with an estimated $0.10 \pm 0.05\%$ background contribution dominated by $Z^0 \to \tau^+\tau^-$ events.

Inclusive distributions of single-particle and event-topology observables in hadronic events are found to be well described by the simulation [90]. Uncertainties in the simulation are taken into account in the systematic errors. Figure 6-1 the transverse momentum and momentum distributions as well as $DOCA_{r\phi}$ and $DOCA_{rz}$ for well-measured tracks in selected hadronic events. Figure 6-2 shows the distribution of the event variables for selected hadronic events. In all plots, data are represented by points and Monte Carlo by histograms.

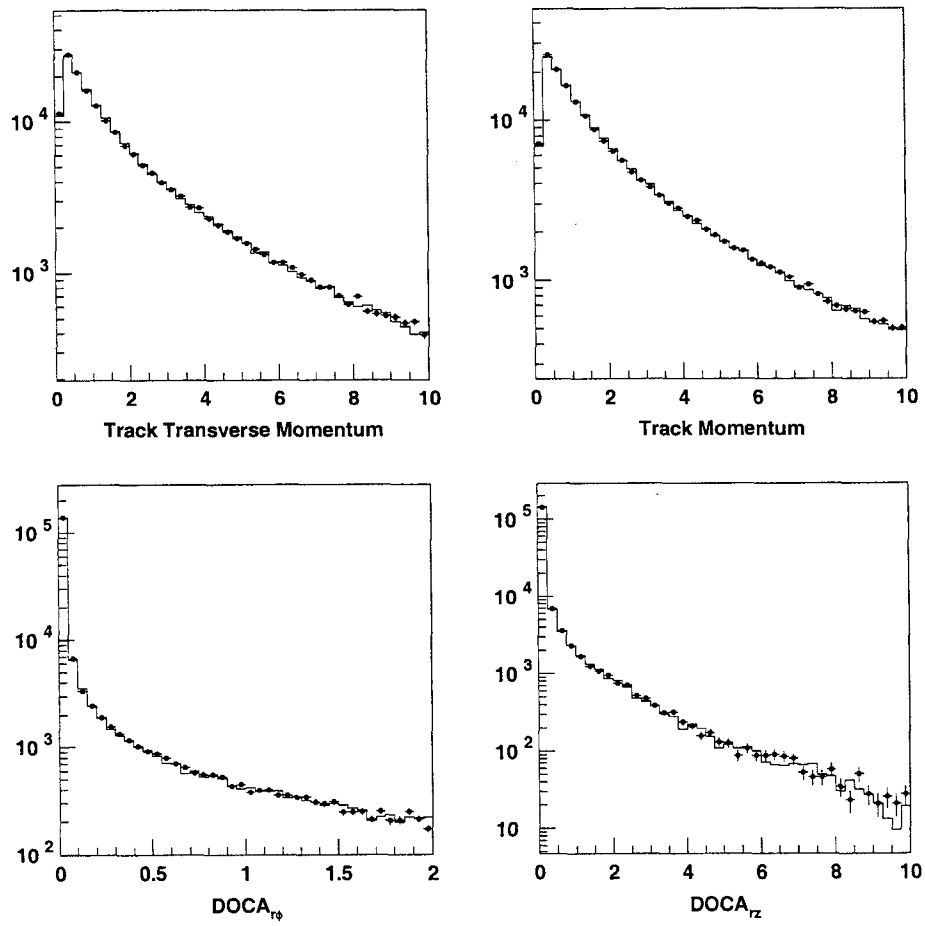

Figure 6-1: Distributions of transverse momentum, momentum, $DOCA_{r\phi}$, and $DOCA_{rz}$ for well-measured charged tracks for selected hadronic events in data (points) and Monte Carlo (histograms).

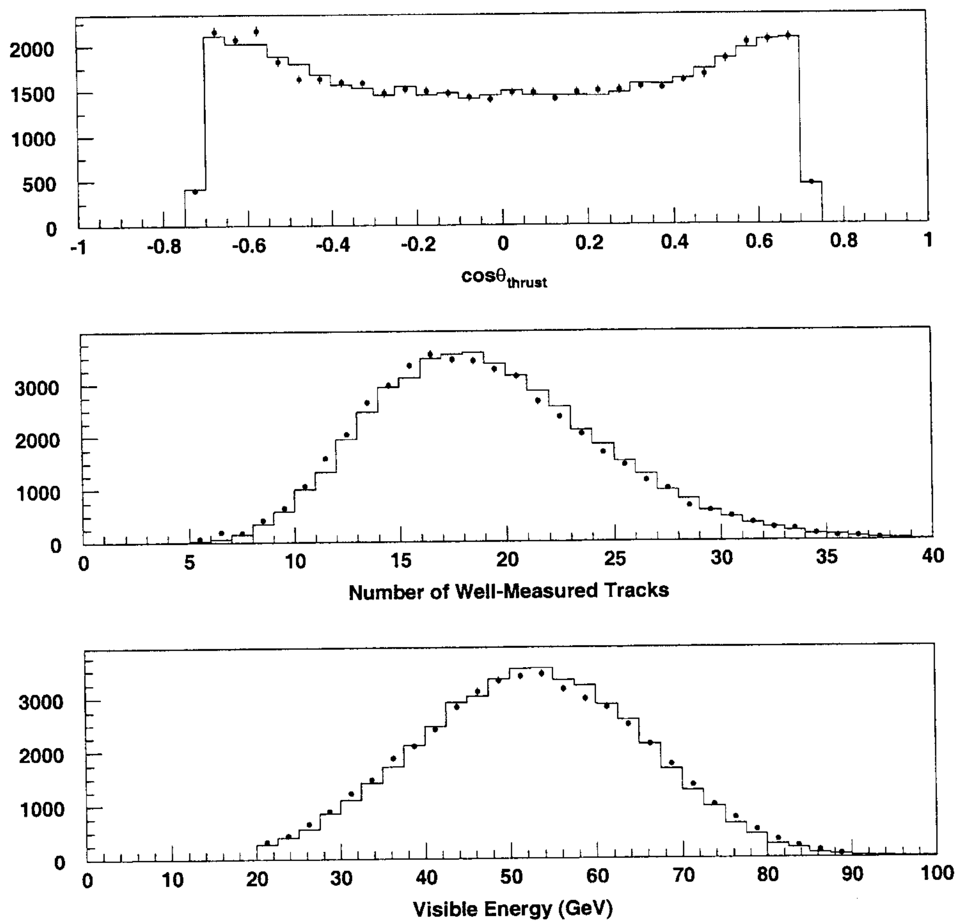

Figure 6-2: Distributions of $\cos\theta_{thrust}$, the number of well-measured tracks , and the visible energy for selected hadronic events in data (points) and Monte Carlo (histograms).

6.2 B Hadron Selection

Figure 6-3 shows a typical reconstructed B hadron decay hemisphere. In the figure shown, the B meson decayed into a D hadron and other tracks (neutral particles do not appear in the diagram). The D hadron subsequently decays into three visible tracks and invisible neutral particles.

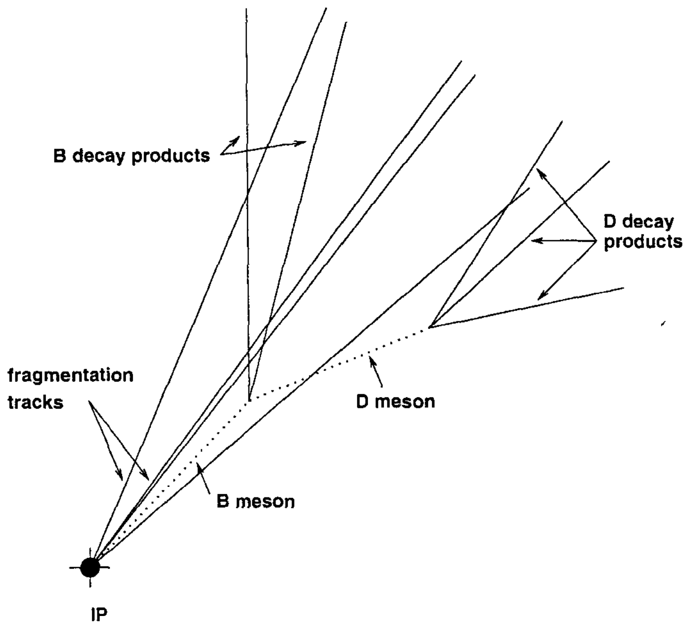

Figure 6-3: Tracks in a typical B-decay hemisphere.

6.2.1 Quality Track Selection

In order to tag B hadrons and find the locations of their decay vertices precisely, we must make use of the charged tracks of good quality. However, when we select a hadronic event, there is no guarantee that every track in this event will be a well-measured track (a hadronic event only needs to have five well-measured tracks). In fact, the set of requirements for selecting well-measured tracks does not contain any item that requires the track to be of particularly good quality (the transverse momentum cut of 150 MeV/c is very loose). To select tracks suitable for B-tagging, we must apply a more stringent set of cuts to select what are commonly referred to as 'quality' or 'flavor-tagging' tracks. A quality track satisfies the following conditions:

- $|cos\theta| < 0.87$ (θ is the polar angle of the track),
- at least 2 hits in VXD3 and 23 hits in the CDC,
- a combined CDC and VXD3 track fit quality of $\chi^2/N_{dof} < 8$,
- a momentum in the range $0.25 < p < 55$ GeV/c,
- an impact parameter of less than 0.3 cm in the $r\phi$ plane, and less than 1.5 cm along the z axis,
- a transverse impact parameter error of less than 250 μm.

Figure 6-4 and 6-5 show distributions for selected quality tracks. The agreement between data and Monte Carlo is reasonably good. We have applied a standard tracking efficiency correction and track impact parameter smearing. This is a common procedure for optimizing the Monte Carlo performance in describing the data. Effects of these corrections will be taken into account when we study the systematic uncertainties of the results in a later Chapter.

6.2.2 B Tagging

In order to find B hadrons from $Z^0 \to b\bar{b}$ decays[1], we must find B decay vertices as well as identifying the flavor of the hadron as b, rather than uds or c. We proceed as follows:

- divide each event into two hemispheres using the thrust axis.
- select quality tracks within each hemisphere;

[1] $b\bar{b}$ from gluon splitting in Z^0 $q\bar{q}$ events are very rare.

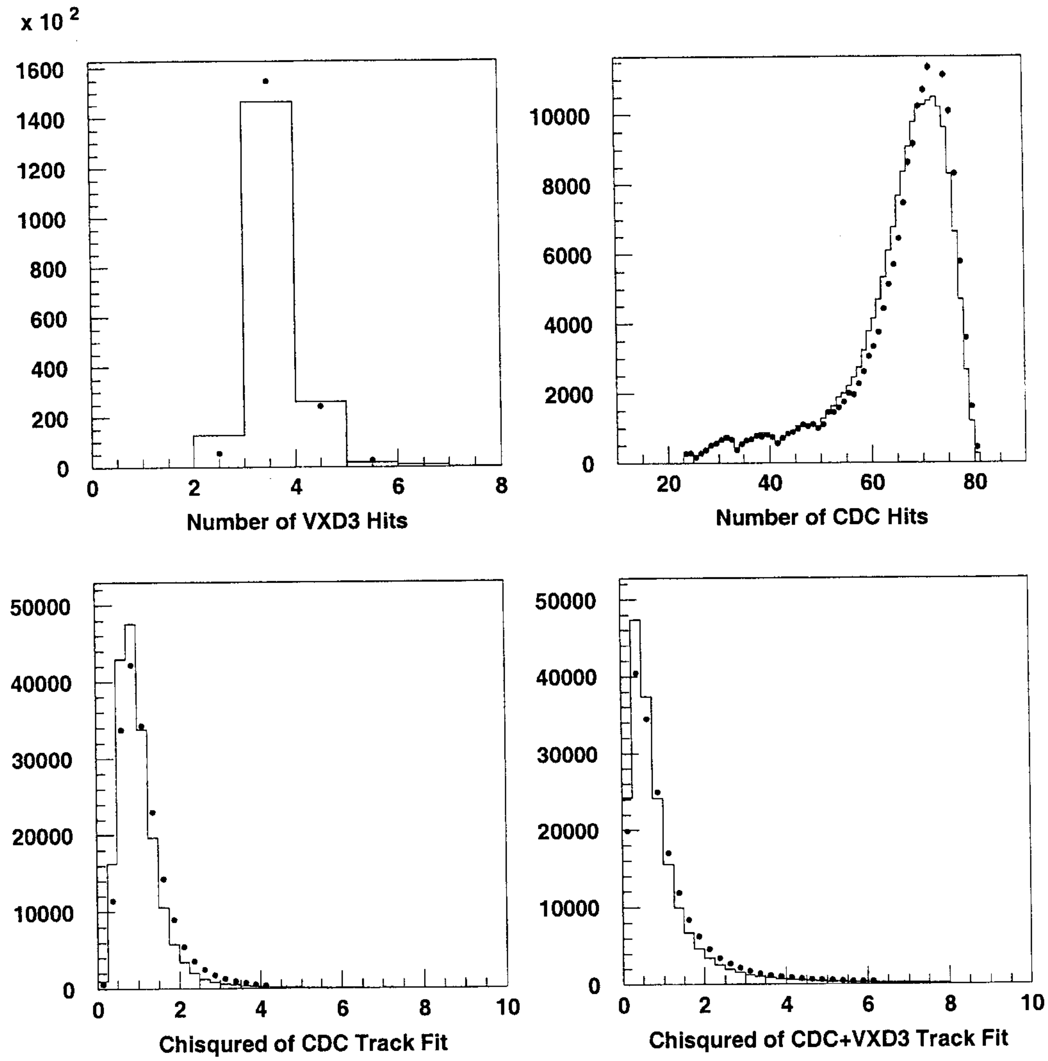

Figure 6-4: Parameters for selected quality tracks in hadronic events. MC (histogram) vs Data (points).

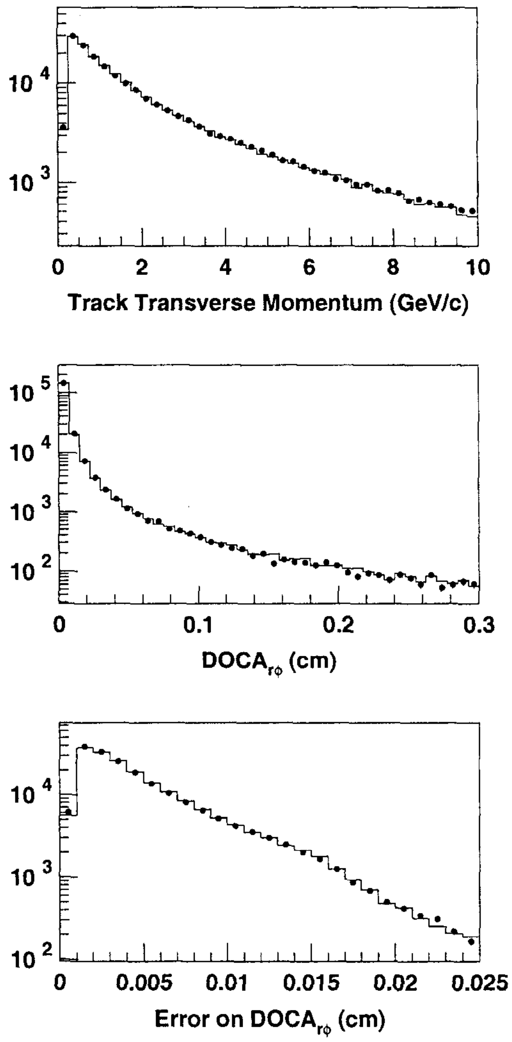

Figure 6-5: Parameters for selected quality tracks in hadronic events. MC (histogram) vs Data (points).

- search for (reconstruct) secondary decay vertices using quality tracks within each hemisphere. The topological vertexing algorithm [94] is employed here;
- associate and attach quality tracks to reconstructed vertices. [94];
- determine whether a vertex is a B hadron decay-vertex using the mass tagging technique [95]. This is a procedure called B-tagging.

Figure 6-6 shows the distribution of the number of selected quality tracks in each hemisphere.

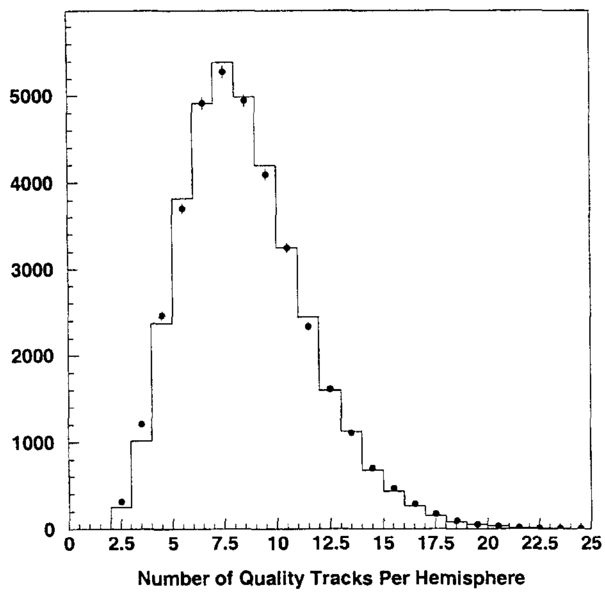

Figure 6-6: Distribution of the number of selected quality tracks in each hemisphere for 1996-97 data (points) and Monte Carlo (histogram).

Topological Vertexing Algorithm

The B sample for this analysis is selected using a topological vertexing technique based on the detection and measurement of charged tracks, which is described in detail in Ref. [94].

Each hadronic event is divided into two hemispheres by a plane perpendicular to the thrust axis. In each hemisphere the topological vertexing algorithm is applied to the set of quality tracks. By a **vertex** we mean a spatial point where a final state particle such as a B hadron has decayed. Charged tracks of daughter particles of this decay will appear to have originated from this vertex. By **vertexing** we mean to find all decay vertices from a set of charged tracks. Various different algorithms of vertexing have been used by different analyses. The topological vertexing algorithm finds vertices inclusively with excellent performance, having high efficiency and high purity.

Here is a very brief description of the vertexing algorithm. The vertices are reconstructed in 3D coordinate space by defining a vertex function $V(\vec{r})$ at each position $\vec{r}$. The helix parameters for each quality track i are used to describe the 3D track trajectory by a Gaussian probability tube $f_i(\vec{r})$, where the width of the tube is the uncertainty[2] in the measured track location close to the IP. $V(\vec{r})$ is defined as a function of the $f_i(\vec{r})$ such that it is small in regions where fewer than two tracks (required for a vertex) have significant $f_i(\vec{r})$, and large in regions of high track multiplicity. Maxima are found in $V(\vec{r})$ and clustered into resolved spatial regions. Tracks are associated with these regions to form a set of topological vertices.

The efficiency for reconstructing at least one secondary vertex in a b hemisphere is $\sim 67\%$ using VXD3. For hemispheres containing secondary vertices, the 'seed' vertex is chosen to be the one with the highest $V(\vec{r})$ value. The reconstructed vertices are ordered according to their distance to the IP as the primary, secondary, and tertiary vertices. The closest is the primary vertex, which is the IP. Very rarely will there be four vertices in one hemisphere.

In hemispheres containing at least one found vertex the vertex furthest from the IP is retained as the 'seed' vertex. Those events are retained which contain a seed vertex separated from the IP by between 0.1 cm and 2.3 cm. The lower bound reduces contamination from non-B-decay tracks and backgrounds from light-flavor

[2] A recent improvement is introduced by parameterizing this uncertainty as a function of track length.

events, and the upper bound reduces the background from particle interactions with the beam pipe.

Track Attachment to Candidate B Decay Vertices

For each hemisphere containing an accepted seed vertex, a vertex axis is formed by the straight line joining the IP to the seed vertex, which is located at a distance D from the IP. For each quality track not directly associated with the vertex, the distance of closest approach to the vertex axis, T, and the distance from the IP along the vertex axis to the point of closest approach, L, are calculated. Tracks satisfying T$<$ 1 mm and L/D$>$ 0.3 are added to the vertex. These T and L cuts are chosen to minimize false track associations to the seed vertex, since typically the addition of a false track has a much greater kinematic effect than the omission of a genuine B-decay track, and hence has more effect on the reconstructed B hadron energy resolution. Our Monte Carlo studies show that, on average, this procedure attaches 0.85 tracks to each seed vertex, 91.9% of the tracks from tagged true B decays are associated with the resulting vertices, and 98.0% of the vertex tracks are from true B decays.

Mass Tag of the B Hadrons

In this analysis, we describe how the individual B hadron energies are reconstructed. In order to select a clean B hadron sample, we must select only secondary vertices found by the vertexing algorithm that are most likely B hadron decay vertices. The large masses of B hadrons relative to light-flavor hadrons make it possible to distinguish B hadron decay vertices from those vertices found in events of light flavors using the vertex invariant mass, M. Unfortunately, a fraction of B hadrons decay products cannot be reconstructed as charged tracks, which include neutrinos which escape direct detection, and neutral decay particles that cannot be directly reconstructed as tracks. Because of these missing particles, M cannot be fully determined.

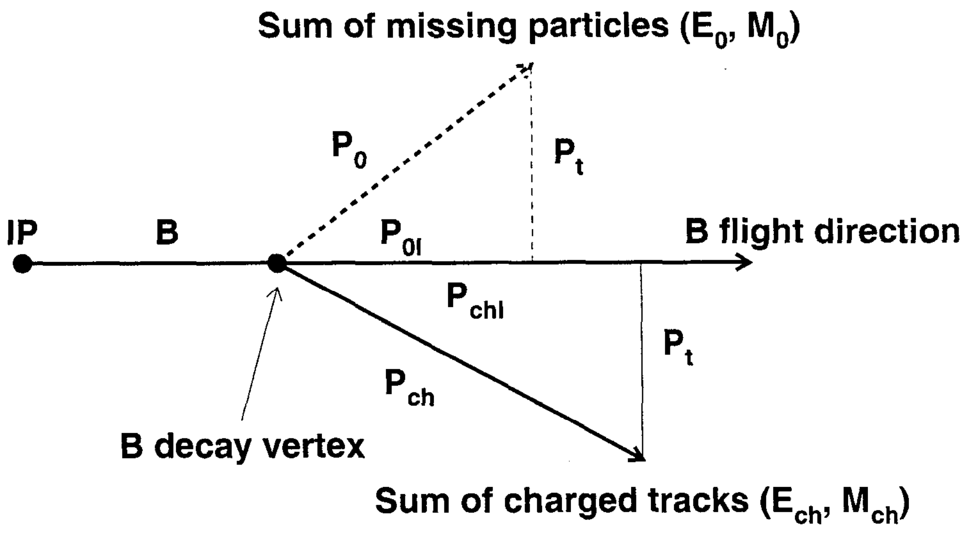

Figure 6-7: B decay kinematics: charged tracks vs missing particles

In the *rest* frame of the decaying hadron, M can be written as

$$M = \sqrt{M_{ch}^2 + P_t^2 + P_{chl}^2} + \sqrt{M_0^2 + P_t^2 + P_{0l}^2}, \tag{6.1}$$

where M_{ch} and M_0 are the total invariant masses of the set of vertex-associated tracks and the set of missing particles, respectively. P_t is the total charged track momentum transverse to the B flight direction, which is identical to the transverse momentum of the set of missing particles by momentum conservation. P_{chl} and P_{0l} are the respective momenta along the B flight direction, which is the line joining the IP and the B vertex. In the B *rest* frame, $|P_{chl}| = |P_{0l}|$. Using the set of vertex-associated charged tracks, we calculate the total momentum vector $\vec{P}_{ch}$, the total energy E_{ch} and the invariant mass M_{ch}, assuming the charged pion mass for each track.

Most B hadrons from Z^0 decays are highly energetic and their relative long lifetimes allow them to decay significantly far away from the IP. The average B decay length is about 3 mm. Given this long B decay length, the very small SLC beam spot (0.8 μm $\times$ 1.5 μm $\times$ 700 μm in xyz) and the excellent vertex resolution provided by

VXD3 the vertexing algorithm provides a precise measurement of the B flight direction (the B vertex direction relative to the IP) very well. This is one advantage SLD has compared with experiments at LEP. The well-measured B flight direction allows

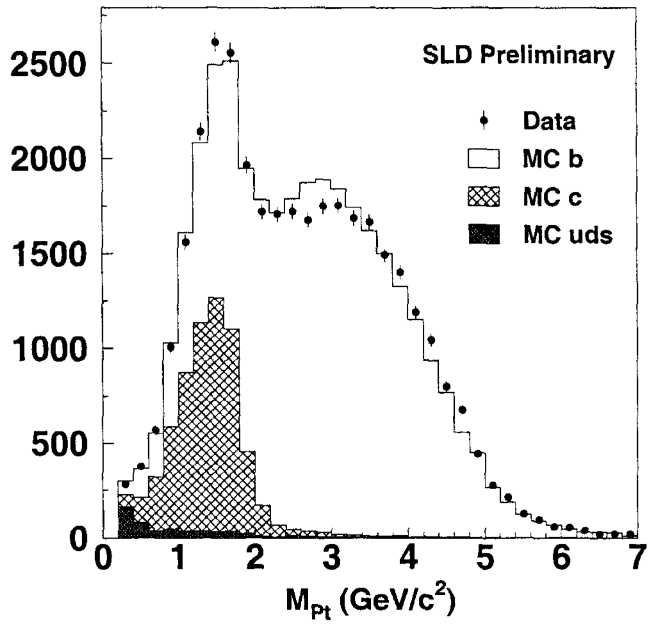

Figure 6-8: Distribution of the reconstructed P_t-corrected vertex mass in the 1996-97 data (points). Also shown is the prediction of the Monte Carlo simulation, for which the flavor composition is indicated.

the precise determination of transverse momentum P_t (See Figure 6-7), which enables us to employ the lower bound for the mass of the decaying hadron, the 'P_t-corrected vertex mass',

$$M_{Pt} = \sqrt{M_{ch}^2 + P_t^2} + |P_t|, \tag{6.2}$$

as the variable for selecting B hadrons. The majority of non-B vertices have M_{Pt} less than 2.0 GeV/c^2. However, occasionally the measured P_t may fluctuate to a much larger value than the true P_t, causing some charm vertices to have a M_{Pt}

larger than 2.0 GeV/c^2. To reduce this contamination, we calculate the 'minimum P_t' by allowing the locations of the IP and the vertex to float to any pair of locations within the respective one sigma error-ellipsoids, We substitute the minimum P_t in Equation (6.2) and use the modified M_{Pt} as the variable for selecting B hadrons [96].

Figure 6-8 shows the distribution of the M_{Pt} for the 32,492 hemispheres in the data sample with a found secondary vertex, and the corresponding simulated distribution (histogram). B hadron candidates are selected by requiring $M_{Pt} > 2.0$ GeV/c^2 and, in addition, $M_{Pt} \leq 2 \times M_{ch}$ to reduce the contamination from fake vertices in light quark events [96]. A total of 19,404 hemispheres are selected. Table 6.3 lists the number of selected B hadron candidates for 1996 and 1997 data.

Run Period	Hadronic Events	B expected	B selected	Efficiency (%)
1996	37,694	16,380	6,171	37.7±0.5
1997	73,875	32,100	13,233	41.2±0.4
Total	111,569	48,480	19,404	40.0±0.3

Table 6.3: Number of selected B hemispheres in 1996-97 data. The selection criteria are: 1) delay length> 1.0 mm) 2) $M_{Pt} > 2$ GeV and 3) $2M_{ch} > M_{Pt}$.

The estimated efficiency for selecting a true B-hadron is about 36.6% for 1996 and 39.8% for 1997, with a sample b-purity of about 98% for both 1996 and 1997. The higher efficiency for 1997 data is mainly due to the improved alignment of the vertex detector for 1997 data. The contributions from light-flavor events in the sample, shown in Figure 6.4, are 0.3% for primary light flavor (uds) events and 1.5% for charm events.

Table 6.5 lists the efficiency and purity estimated from Monte Carlo simulations. The B selection efficiencies estimated from data are slightly higher than from Monte Carlo. The effects of this small discrepancy on our final results can be treated as systematic uncertainties by comparing results obtained from Monte Carlo events in which track parameters are smeared with those in which no smearing is applied.

	Run Period	Probability %	Fraction %
uds	1996	0.05	0.3
	1997	0.05	0.3
c	1996	0.8	1.7
	1997	0.8	1.5

Table 6.4: Probability for selecting background light flavor (uds and c) events; and fraction of uds and c events in the selected B sample estimated using 1996-97 Monte Carlo.

Run Period	b Efficiency %	b Purity %
1996	36.6	97.9
1997	39.8	98.2

Table 6.5: The efficiency for selecting b hadrons and the purity for B hadrons in the selected B sample estimated using 1996-97 Monte Carlo.

Chapter 7

The B Hadron Energy Distribution

7.1 The Missing Mass Technique

The energy of each B hadron, E_B, can be expressed as the sum of the reconstructed charged track energy associated with the vertex, E_{ch}, and the energy of the missing particles (those particles not associated with the vertex), E_0. We can write E_0 as

$$\begin{aligned} E_0^2 &= M_0^2 + |\vec{P}_0|^2 \\ &= M_0^2 + P_t^2 + P_{0l}^2. \end{aligned} \tag{7.1}$$

As mentioned in the last Chapter, transverse momentum, P_t, is well-measured at SLD because of the very small SLC beam spot and the high resolution on secondary vertex locations. The two unknowns, the missing mass M_0 and the missing longitudinal momentum, P_{0l}, must be found in order to obtain E_0 (see Figure 6-7).

7.1.1 The Missing Mass Upper Bound M_{0max}

One kinematic constraint can be obtained by imposing the B hadron mass on the vertex, $M_B^2 = E_B^2 - P_B^2$, where $P_B = P_{chl} + P_{0l}$ is the total momentum of the B hadron, and P_{chl} is the momentum component of the vertex-associated tracks along the vertex axis, i.e., the B flight direction. This constraint reduces the number of unknowns from two to one, i.e., P_{0l} can be solved if the missing mass is known (see Appendix B for derivation of the formula).

We try to look for further constraints on the value of missing mass M_0. From Equation (6.1) we derive the following inequality,

$$\sqrt{M_{ch}^2 + P_t^2} + \sqrt{M_0^2 + P_t^2} \leq M_B, \tag{7.2}$$

where equality holds in the limit where both P_{0l} and P_{chl} vanish in the B hadron *rest* frame. Equation (7.2) effectively sets an upper bound on M_0, and a lower bound is given by zero:

$$0 \leq M_0^2 \leq M_{0max}^2, \tag{7.3}$$

where

$$M_{0max}^2 = M_B^2 - 2M_B\sqrt{M_{ch}^2 + P_t^2} + M_{ch}^2. \tag{7.4}$$

7.1.2 The Strong Correlation between M_0 and M_{0max}

Since M_0 is bounded from both above and below, when M_{0max}^2 is small, we expect to obtain a good estimate of M_0 and a good estimate of the B hadron energy as well.

We have used our simulation to study this issue. Assuming $M_B = 5.28$ GeV/c^2, the true value of M_0 **tends to cluster near its maximum value** M_{0max}. Figure 7-1 shows the relative deviation of M_{0max} from M_{0true} for all B hadrons. Although approximately 20% of the B hadrons are B_s^0 and Λ_b which have larger masses, the values of M_{0max} obtained using $M_B = 5.28$ GeV/c^2 in Equation (7.4) are typically within about 10% of M_0. The distribution of the reconstructed M_{0max}^2 for vertices in the selected B hadron sample is shown in Figure 7-2. The simulation indicates that the non-$b\bar{b}$ background is concentrated at high M_{0max}^2; this because most of the light flavor vertices have a small M_{Pt}. Due to the strong negative correlation between M_{Pt} and M_{0max} (Figure 7-3), a large value of M_{0max} corresponds to a small value of M_{Pt}

and vice versa. The negative tail in Figure 7-2 is an effect of detector resolution, and the Monte Carlo simulation shows good agreement with the data.

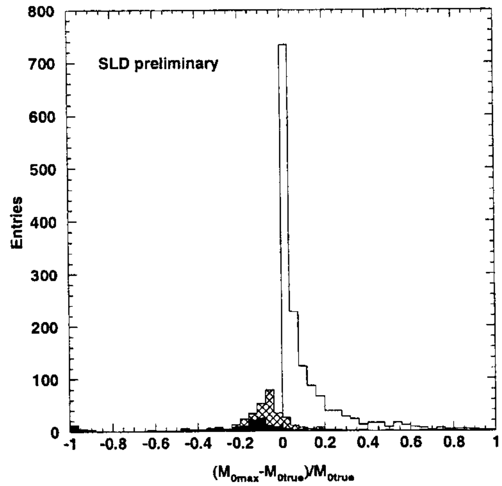

Figure 7-1: The relative deviation of the maximum missing mass from the true missing mass for Monte Carlo simulated B hadron decays, which is divided into three categories: B^0 and $B^{\pm}$ (open), B_s^0 (cross-hatched), and Λ_b (dark filled).

7.1.3 Solving for P_{0l} and E_0

Because M_0 peaks near M_{0max}, we set $M_0^2 = M_{0max}^2$ if $M_{0max}^2 \geq 0$, and $M_0^2 = 0$ if $M_{0max}^2 < 0$. We then calculate P_{0l}:

$$\begin{aligned} P_{0l} &= \frac{M_B^2 - (M_{ch}^2 + P_t^2) - (M_0^2 + P_t^2)}{2(M_{ch}^2 + P_t^2)} P_{chl} \\ &= \frac{M_B - M_{ch\perp}}{M_{ch\perp}} P_{chl}, \end{aligned} \tag{7.5}$$

where $M_{ch\perp} = \sqrt{M_{ch}^2 + P_t^2}$ is the observable, boost-invariant transverse-mass of the charged tracks, and hence determine the value of E_0 (Equation (7.1)). For a detailed derivation of equation (7.5) and a discussion of this technique, see **Appendix B.** We then divide the reconstructed B hadron energy, $E_B^{rec} = E_0 + E_{ch}$, by the beam energy, $E_{beam} = \sqrt{s}/2 \simeq 45.6$ GeV, to obtain the reconstructed scaled B hadron energy, $x_B^{rec} = E_B^{rec}/E_{beam}$.

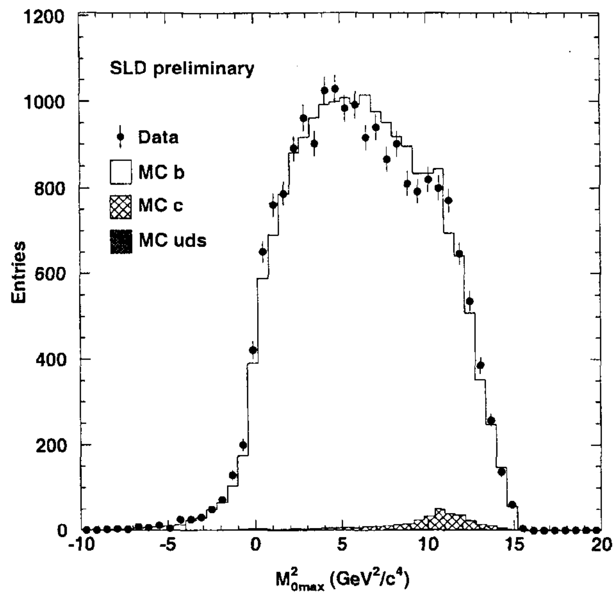

Figure 7-2: Distribution of the reconstructed M^2_{0max} for the selected vertices in the 1996-97 data (points). Also shown is the prediction of the Monte Carlo simulation.

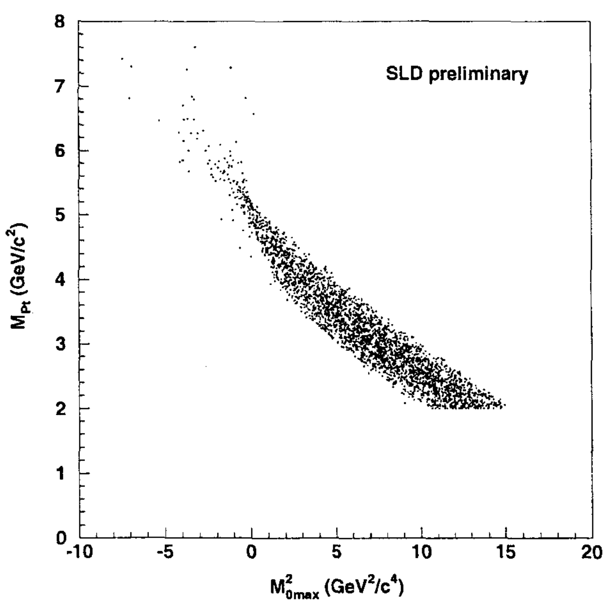

Figure 7-3: Correlation between M_{Pt} and M^2_{0max} for reconstructed B hadron vertices in the Monte Carlo simulation.

7.2 The B Energy Resolution

Figure 7-4 shows the distributions of the relative energy residuals, $(x_B^{rec} - x_B^{true})/x_B^{true}$, for the four different B flavors $B^{\pm}$, B^0, B_s and B baryons (mainly Λ_b) for our Monte Carlo. For all four flavors, we have selected only those B hadrons with small missing mass upper bounds (we used $-1 < M_{0max}^2 < 1.5$ $(\mathrm{GeV}/c^2)^2$ for illustration purpose only). These distributions are all rather **symmetric** and **centered around zero**, with a small positive shift for $B^{\pm}$ and B^0 hadrons. Since we have assumed the B^0 mass for each vertex which is slightly smaller than the B_s and B baryon masses, the reconstructed energy for the B_s and B baryons is hence slightly lower than those for $B^{\pm}$ and B^0 hadrons. In Chapter 10 we will study the systematic effects of the uncertainty on the fraction of each B flavor.

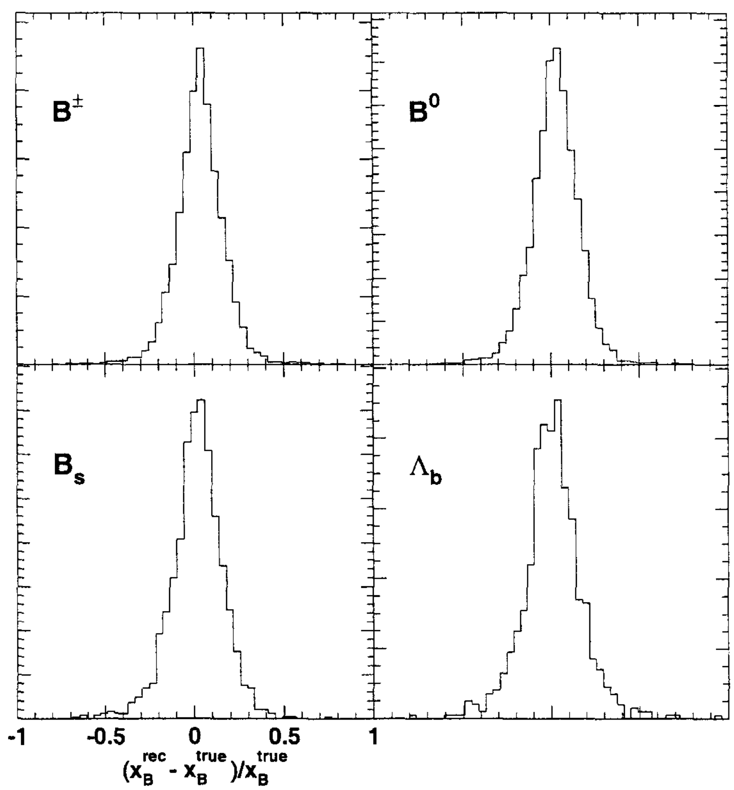

Figure 7-4: Distributions of relative B energy residual, $(x_B^{rec} - x_B^{true})/x_B^{true}$, for different flavored B hadrons. in our simulation.

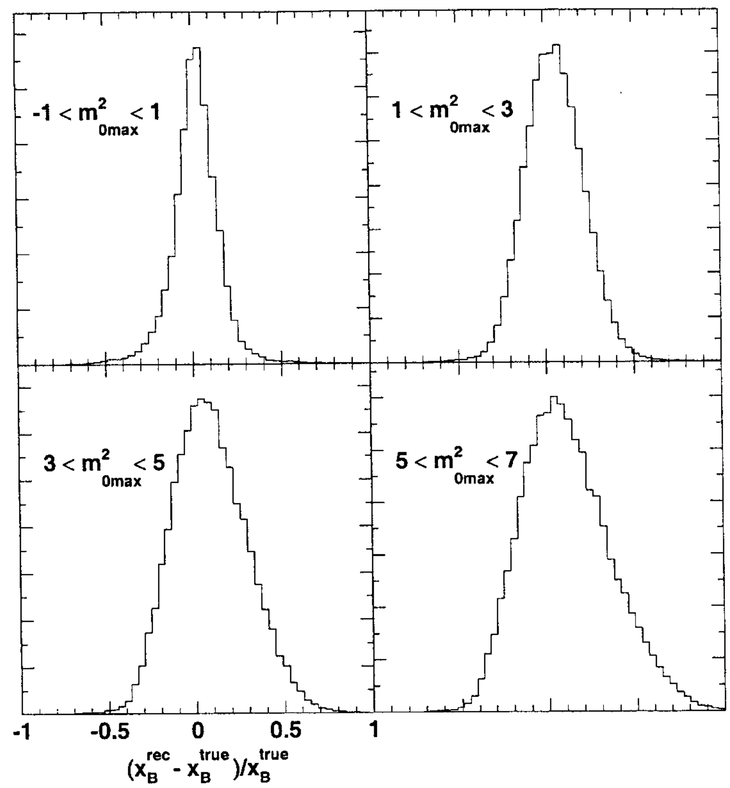

Figure 7-5: Distributions of $(x_B^{rec} - x_B^{true})/x_B^{true}$ for four M^2_{0max} ranges. The resolution is better for B hadrons with smaller M^2_{0max}.

The resolution of x_B^{rec}, or the **width** of the residual distribution, depends on M^2_{0max}. Figure 7-5 shows the relative residual distributions for four different M^2_{0max} ranges. The resolution is rather **good** only for B hadrons with **small** missing mass upper bounds. However, as M^2_{0max} increases, which corresponds to relaxing the kinematic constraint, the resolution degrades and the energy residuals are no longer symmetric and centered around zero. For B hadrons with large M^2_{0max}, the reconstructed B energy is more often larger than the true B energy. Therefore, we only select B hadrons with small missing mass upper bounds as our final B sample in order to achieve good energy resolution.

The resolution of x_B^{rec} may also depend on the true x_B, x_B^{true}. Figure 7-6 shows the distributions of the relative B energy residual for four true B energy ranges with

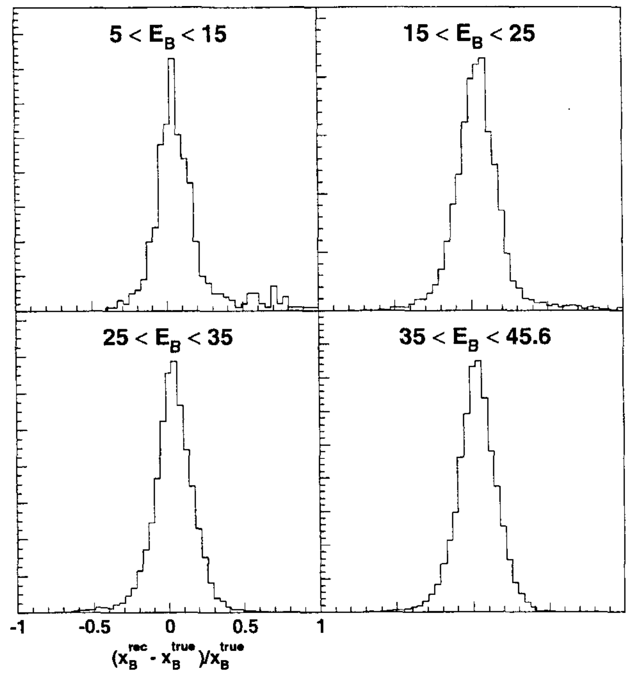

Figure 7-6: Distributions of $(x_B^{rec} - x_B^{true})/x_B^{true}$ for four different x_{true} ranges, but with $-1 < M_{0max}^2 < 1.5$. The resolutions are almost the same for all B energies.

$-1 < M_{0max}^2 < 1.5$. The resolutions are essentially the same for all B energies.

Vertices in the negative tail of the M_{0max}^2 distribution that have $M_{0max}^2 < -1.0$ $(\mathrm{GeV}/c^2)^2$ (Figure 7-2) are often poorly reconstructed and are not used in further analysis. Vertices with small values of $|M_{0max}^2|$ are typically reconstructed with better resolution and an upper cut on M_{0max}^2 is hence applied.

7.3 The Final B Sample

7.3.1 Efficiency Consideration and M_{0max}^2 Cut

For an x_B-independent cut on M_{0max}^2, the efficiency for selecting B hadrons increases almost linearly with x_B^{true}. In order to obtain an approximately x_B-**independent selection efficiency** we choose the following empirical upper cut to select our final

B sample:

$$M^2_{0max} < \{1.1 + 0.006(E_{beam} - E_B^{rec}) + 3.5exp[-(E_B^{rec} - 5.5)/3.5]\}^2, \tag{7.6}$$

where energies are measured in GeV. The two terms that depend on the reconstructed energy E_B^{rec} increase the efficiency at lower B hadron energy.

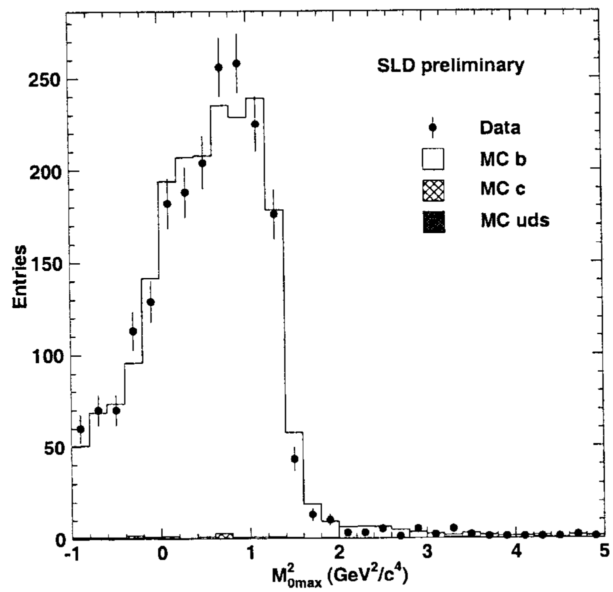

Figure 7-7: Distribution of the reconstructed M^2_{0max} for the final selected B sample (see text). Also shown is the prediction of the Monte Carlo simulation.

7.3.2 The Non-$b\bar{b}$ Background

Only about 0.7% of the selected vertices are from light-flavor events, which are concentrated in the lowest energy bin. To further remove this background, a vertex is required to contain at least 3 quality tracks with a normalized impact parameter greater than 2. This eliminates almost all of the uds-event background and cuts the charm background by about 20% overall and 43% in the few lowest energy bins. This cut helps to reduce the dependence of the reconstructed B hadron energy distribution on the light flavor simulation in the low energy region, which is a key step towards finding the correct shape of the B hadron energy distribution at low energies.

7.3.3 The Final B Sample: Efficiency and Purity

A total of 1920 vertices in the data for 1996-97 satisfy all these selection cuts. Figure 7-7 shows the distribution of M^2_{0max} after all these cuts; the data and Monte Carlo simulation are in good agreement.

The overall efficiency for selecting B hadrons is 3.9% and the estimated B hadron purity is 99.5%. The efficiency as a function of x_B^{true} is shown in Figure 7-8. The dependence is rather weak except for the lowest x_B region; the efficiency is substantial, about 1.7% even just above the kinematic threshold for B energy.

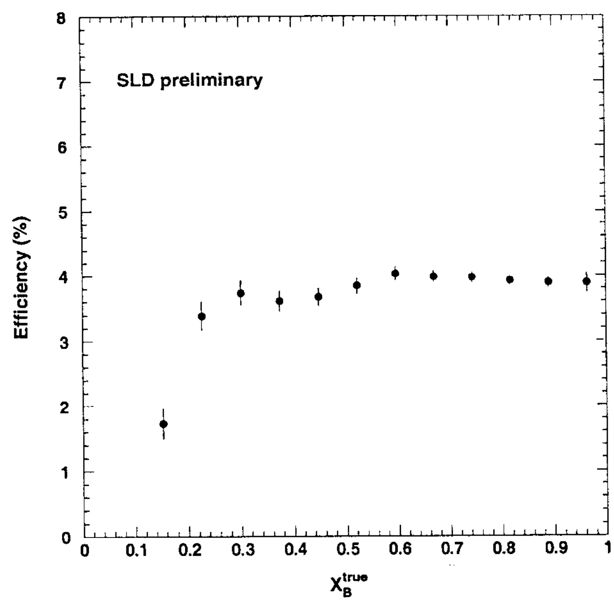

Figure 7-8: The Monte Carlo simulated efficiency for selecting B hadron decay vertices as a function of the true scaled B hadron energy, $x^{true} = E_B^{true}/E_{beam}$. The nearly energy-independent efficiency (except at very low B energy) improves the sensitivity of the measured x_B^{rec} distribution to the true underlying B energy distribution. Note the kinematic threshold of $x_B > 0.116$.

A comparison of our efficiency with those in recent B-energy measurements at LEP (1995) [97] and SLD (1997) [98] is in order here. Those previous measurements in which semileptonic B decays ($B \to Dl\nu + X$) that are suitable for a **direct** B-energy measurement[1] are selected. The overall efficiency for selecting B hadrons is only about 0.2% (LEP) and 1.1% (SLD), decreasing as the B energy decreases, and with almost no events selected for $x_B < 0.3$. In addition, non-$b\bar{b}$ backgrounds are not small and the systematic uncertainties resulting from the very low efficiency at low x_B are very substantial due to the model-dependent extrapolation to low x_B. The much higher and nearly x_B-independent B selection efficiency of this analysis represents a major improvement in the measurement technique.

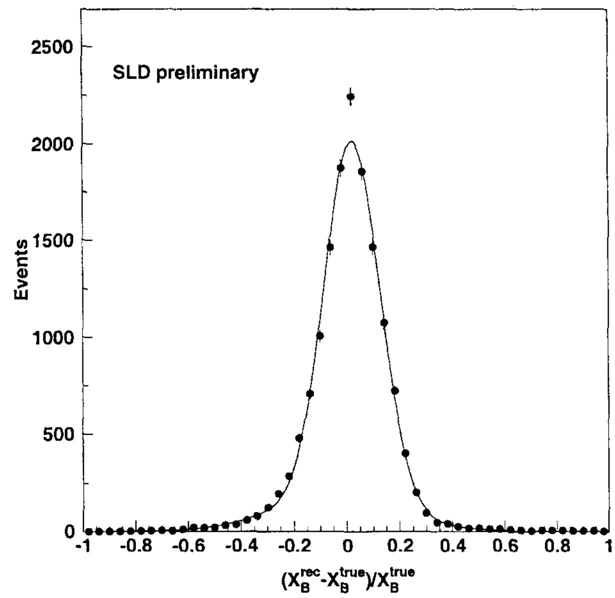

Figure 7-9: Distribution of $(x_B^{rec} - x_B^{true})/x_B^{true}$, for Monte Carlo simulated B vertices passing all cuts (points). The curve represents the result of a double Gaussian fit to the distribution.

[1]In a direct measurement [99, 97, 98, 100], each individual B hadron energy is explicitly reconstructed. This is not the case for many other **indirect** measurements[101], where the average B energy, or even the shape of the B energy distribution, are inferred from distributions of other kinematic variables rather than the reconstructed B energy distribution.

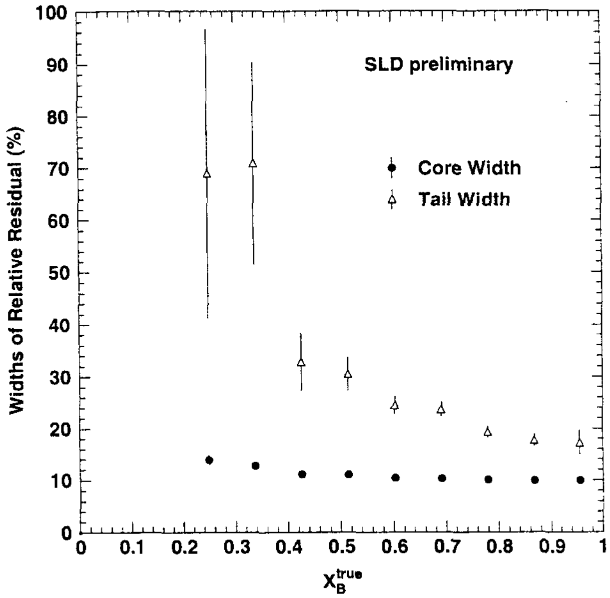

Figure 7-10: The fitted core and tail widths of the B energy resolution as a function of the true scaled B hadron energy. The ratio of the amplitude of the inner Gaussian (core) to that of the outer Gaussian (tail) is 83:17. The dependence of the core resolution on the true B energy is small. The very good resolution for low energy B hadrons improves the sensitivity of the measured x_B^{rec} distribution to the true underlying B energy distribution.

7.3.4 The Final B Sample: Resolution

We examine the B-energy resolution of our technique. The distribution of the normalized difference between the true and reconstructed B hadron energies, $(x_B^{rec} - x_B^{true})/x_B^{true}$, for Monte Carlo events, is fitted by a double Gaussian, resulting in a core width (the width of the narrower Gaussian) of 10.4% and a tail width (the width of the wider Gaussian) of 23.6% with a core fraction of 83% (Figure 7-9). The core and tail widths as a function of x_B^{true} is shown in Figure 7-10. In order to compare the widths from different x_B bins, we fix the ratio between core and tail fractions to that obtained in the overall fit above.

The **relative** resolution depends weakly on the true x_B. However, the **absolute** resolution, $x_B^{rec} - x_B^{true}$, does depend on x_B^{true} and is very good at low x_B (Figure 7-11). This is a crucial advantage of this energy reconstruction technique. In previous measurements, the energy resolution for $x_B < 0.5$ is poor: $\sigma(x_B) > 3$ GeV/($\sqrt{s}/2$). In this analysis, the $\sigma(x_B) \sim 2.5$ GeV/($\sqrt{s}/2$) for $x_B \sim 0.5$ and $\sigma(x_B) \sim 1.0$ GeV/($\sqrt{s}/2$) for x_B as low as 0.2. Figure 7-12 shows the distribution of

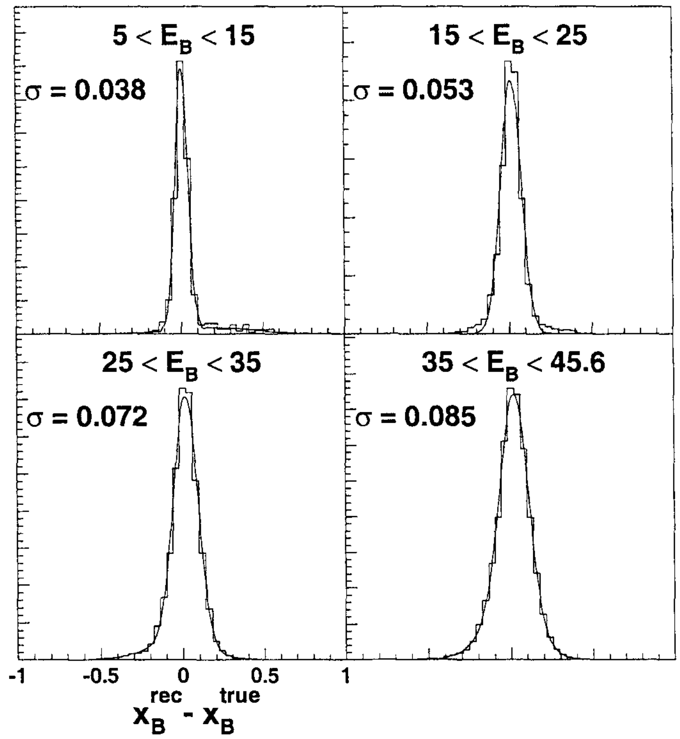

Figure 7-11: Distribution of $x_B^{rec} - x_B^{true}$ for four B energy ranges for Monte Carlo simulation. The core resolution, σ, is shown in each figure with core fraction fixed at 83%.

the reconstructed scaled B hadron energy for the data, $D^{data}(x_B^{rec})$, and for the Monte Carlo simulation, $D^{MC}(x_B^{rec})$. The small non-$b\bar{b}$ background reduces the systematic dependence of this measurement on light flavors, especially charm fragmentation and production. The full kinematic coverage, most importantly at low x_B where other measurements have not been able to probe, is critical for constraining the shape of the true underlying energy distribution. As a result of the symmetric resolution over the full range, there is a natural and small resolution tail at large x_B^{rec} that is potentially sensitive to the x_B-dependence in that region. Had we applied the beam energy constraint to gain in energy resolution, we would have, in the meantime, lost this advantage. We chose not to apply the beam energy constraint throughout this analysis for this particular reason.

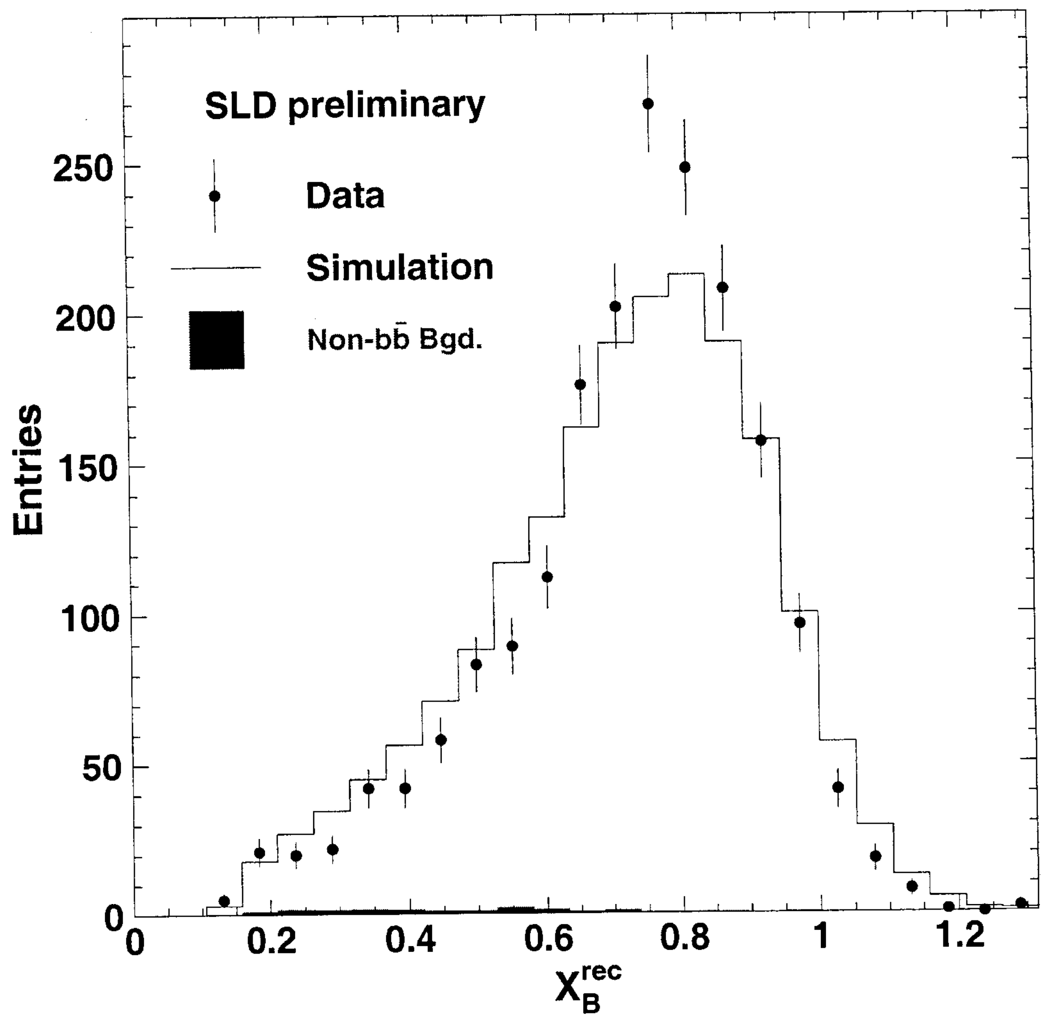

Figure 7-12: Distribution of the reconstructed scaled B hadron energy for 1996-97 data (points) and the default Monte Carlo simulation (histogram). The solid histogram shows the non-$b\bar{b}$ background.

7.3.5 Summary

We have taken the advantages present at SLC and SLD to develop a novel energy reconstruction technique which allows us to improve the B energy measurement significantly. The high B selection efficiency over the full kinematic coverage, the small non-$b\bar{b}$ background, and the good energy resolution are the most important characteristics of this analysis. No other analysis contains all of these features. As we will see in the next Chapter, these features combined give a much improved sensitivity of our data to the underlying true *shape* of the B energy distribution.

In the next Chapter we will test various fragmentation models using our measured B energy distribution. An important issue arises here which we did not discuss earlier. The event generator used in our simulation is based on a perturbative QCD 'parton shower' for production of quarks and gluons, together with the phenomenological Peterson function [48] (Table 8.1) to account for the fragmentation of b and c quarks into B and D hadrons, respectively, within the iterative Lund string hadronization mechanism [15]; this simulation yields a 'generator-level' primary B hadron energy distribution with $< x_B > = 0.693$[2]. It is apparent that this simulation does not reproduce the data well (Figure 7-12); the χ^2 for the comparison is 62 for 16 bins[3].

The distribution of the non-$b\bar{b}$ background, $S(x_B^{rec})$, is also shown in Figure 7-12. The background is subtracted bin-by-bin from the reconstructed x_B distribution.

[2]We used a value of the Peterson function parameter $\epsilon_b = 0.006$ [95].

[3]We exclude several bins with very few events in the comparison. For details see Section 8.1 for details.

Chapter 8

Tests of Fragmentation Models

Given the raw reconstructed B energy distribution in the data shown in Figure 7-12, there are several ways of estimating the true underlying B energy distribution. Here we take two approaches, each described in a subsection.

In the first part, we test several b fragmentation models, $f(z, \beta)$ embedded within Monte Carlo generators, where z is an internal, experimentally inaccessible variable, corresponding roughly to the fraction of the momentum of the fragmenting b quark carried by the resulting B hadron, and β is the set of parameters associated with the model in question. In the second part, we test several functional parameterizations for the distribution of x_B itself, $f(x_B, \lambda)$, where λ represents the set of parameters associated with each functional form.

8.1 Tests of b Quark Fragmentation Models $f(z, \beta)$

We first consider testing models of b quark fragmentation. Since the fragmentation functions for various models are usually functions of an experimentally inaccessible variable (e.g. $z = (E + p_{\|})_H/(E + p_{\|})_Q$ or $z = p_{\|H}/p_{\|Q}$), it is necessary to use a Monte Carlo generator to generate events according to a given input heavy quark fragmentation function $f(z, \beta)$, where β represents the set of parameters. Figure 8-1

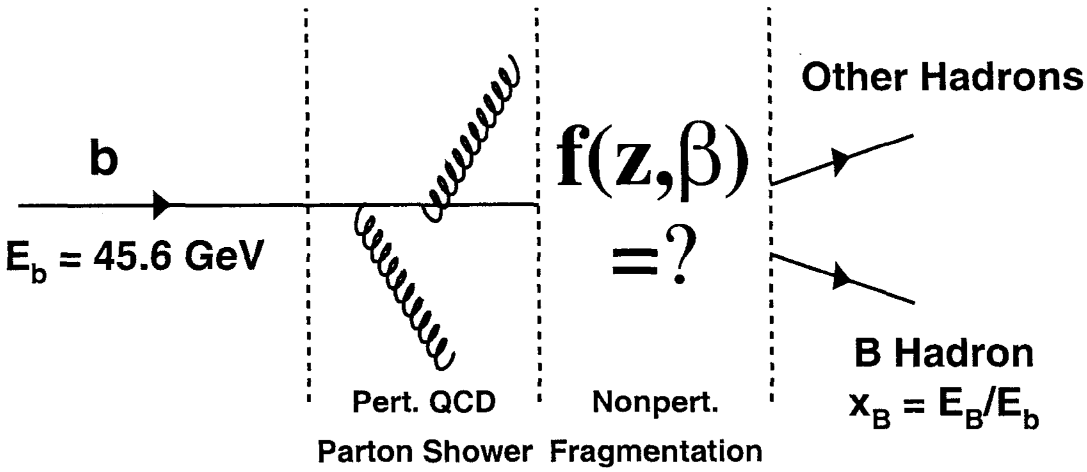

Figure 8-1: A schematic diagram showing how the non-perturbative fragmentation function $f(z,\beta)$ is tested. $f(z,\beta)$ is invoked *after* hard gluon radiation and perturbative shower evolution, which is simulated by JETSET Parton Shower Monte Carlo. The parameters β are varied in order to obtain different resulting B hadron energy distributions.

shows a schematic illustration of the situation. We consider the phenomenological models of the Lund group [102], Bowler [37], Peterson *et al.* [48] and Kartvelishvili *et al.* [49], as well as the perturbative QCD calculations of Braaten *et al.*(BCFY) [58], and of Collins and Spiller (CS) [51]. We use the JETSET [15] parton shower Monte Carlo and each fragmentation model in question to generate the simulated events without detector simulation. Table 8.1 is a list of the models considered. In addition, we test the UCLA [39] fragmentation model with fixed parameters. For b fragmentation, we also test the HERWIG [41] event-generator using both possible values of the parameter $cldir = 0$ and 1[1].

[1]The meaning of this *cldir* parameter is as follows. After the parton shower, HERWIG produces a leading 'cluster' containing the b quark and a light (u or d) quark. This may have a reasonable energy distribution, but it also has a random mass. So it is decayed into a B hadron and another hadron, $\pi^{\pm}$, K, ρ, and so on. In the old versions where $cldir = 0$ this decay is isotropic so that the B hadron acquires a rather random fraction of the energy of the leading cluster. The average B hadron energy is too soft on average. For $cldir = 1$ (default in newer versions) the B hadron is always produced forward along the cluster flight direction, thus getting the maximum energy it can, and giving a much harder spectrum.

Model	$f(z,\beta)$	Reference
BCFY	$\frac{z(1-z)^2}{[1-(1-r)z]^6}[3+\Sigma_{i=1}^4(-z)^i f_i(r)]$	[58]
Bowler	$\frac{1}{z^{(1+r_b b m_\perp^2)}}(1-z)^a exp(-bm_\perp^2/z)$	[37]
CS	$(\frac{1-z}{z}+\frac{(2-z)\epsilon_b}{1-z})(1+z^2)(1-\frac{1}{z}-\frac{\epsilon_b}{1-z})^{-2}$	[51]
Kart.	$z^{\alpha_b}(1-z)$	[49]
Lund	$\frac{1}{z}(1-z)^a exp(-bm_\perp^2/z)$	[102]
Peterson	$\frac{1}{z}(1-\frac{1}{z}-\frac{\epsilon_b}{1-z})^{-2}$	[48]

Table 8.1: b quark fragmentation models used in comparison with data. For the BCFY model, $f_1(r) = 3(3-4r)$, $f_2(r) = 12-23r+26r^2$, $f_3(r) = (1-r)(9-11r+12r^2)$, and $f_4(r) = 3(1-r)^2(1-r+r^2)$, where $r = (m_H - m_Q)/m_H$ where m_H is the mass of the heavy hadron and m_Q is the mass of the heavy quark. For a heavy-light meson, r can be interpreted as the ratio of the constitute mass of the light quark to the meson mass.

In order to make a consistent comparison of each model with the data we adopt the following procedure. For each model, starting values of the arbitrary parameters, β, are assigned and the corresponding fragmentation function $f(z,\beta)$ is used along with the JETSET Monte Carlo to produce the scaled primary B hadron energy distribution, $D^{MC}(x_B^{true})$ in the MC-generated $b\bar{b}$ event sample, *before* simulation of the detector. Then each simulated B hadron is weighted according to its true B hadron energy, x_B^{true}; the weight is determined by the ratio of the generated B hadron energy distribution, $D^{MC}(x_B^{true})$, to that of our default simulation $D^{default}(x_B^{true})$. After simulation of the detector, application of the analysis cuts and background subtraction, the resulting weighted distribution of reconstructed B hadron energies, $D^{MC}(x_B^{rec})$, is then compared with the background-subtracted data distribution and the χ^2 value, defined as

$$\chi^2 = \sum_{i=1}^{N}\left(\frac{N_i^{data} - RN_i^{MC}}{\sigma_i}\right)^2, \tag{8.1}$$

is calculated, where N is the number of bins to be used in the comparison, N_i^{data} is the number of entries in bin i in the data distribution, and N_i^{MC} is the number of entries in bin i in the simulated distribution[2]. σ_i is the statistical error on the deviation of the observed number of entries for the data from the expected number of entries in bin i, which can be expressed as

$$\sigma_i^2 = \left(\sqrt{RN_i^{MC}}\right)^2 + \left(R\sqrt{N_i^{MC}}\right)^2, \tag{8.2}$$

where $\left(\sqrt{RN_i^{MC}}\right)^2$ is the expected statistical variance on the observed data number of entries in bin i, assuming the model being tested is correct, and $\left(R\sqrt{N_i^{MC}}\right)^2$ is the statistical variance on the expected number of entries in bin i. Since the χ^2-test is not a statistically effective test for bins with a very small number of entries, the third, the fourth, and the last three bins in Figure 7-12 are excluded from the comparison.

We vary the values of the set of parameters β and repeat the above procedure. The minimum χ^2 is found by scanning through the input parameter space, yielding a set of parameters which give an optimal description of the reconstructed data by the fragmentation model in question. Each of the nine plots in Figure 8-2 shows the background-subtracted distribution of reconstructed B hadron energy for the data (points) and the respective B energy distribution (histogram) resulting *either* from the optimized input fragmentation function $f(z)$ embedded within the JETSET parton shower simulation, *or* from the predictions of the HERWIG event-generator and the UCLA fragmentation model. Data points excluded from the fit are represented in Figure 8-2 by open circles.

We conclude that with our resolution and our current data sample, we are able to distinguish between several fragmentation models. Within the context of the JETSET Monte Carlo, the Lund and Bowler models are consistent with the data with χ^2

[2] R is the factor by which the total number of entries in the simulated distribution is scaled to the number of entries in the data distribution; $R \simeq 1/12$.

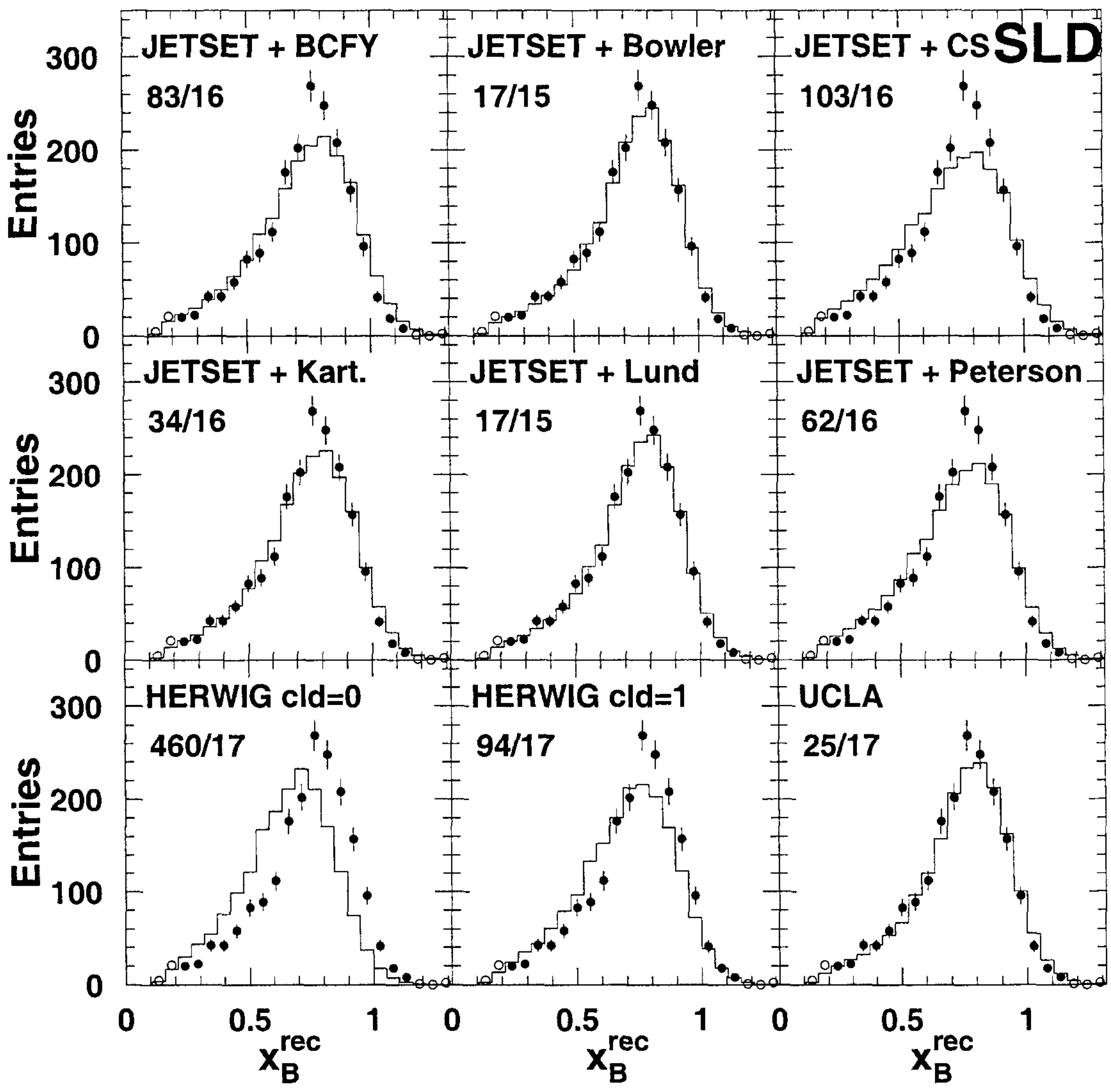

Figure 8-2: Each figure shows the background-subtracted distribution of reconstructed B hadron energy for the data (points) and for the Monte Carlo (histogram) based on the respective optimized input fragmentation function within the JETSET parton shower simulation, as well as based on the HERWIG ($cld = 0$ and $cld = 1$) and the UCLA fragmentation models. The χ^2 and the number of degrees of freedom are indicated.

probability of 32% for each, the Kartvelishvili model is marginally consistent with the data, while the Peterson, the BCFY and the CS models are found to be inconsistent with the data. The UCLA model is consistent with the data to a level of 10% χ^2 probability. The HERWIG model with *cldir* $= 0$ is confirmed to be much too soft. Using *cldir* $= 1$ results in a substantial improvement, but it is still inconsistent with the data. Table 8.2 lists the results of the comparisons.

Model	χ^2/dof	Parameters	$\langle x_B \rangle$
JETSET + BCFY	83/16	$r = (8.5 \pm 0.7) \times 10^{-2}$	0.694 ± 0.005
JETSET + Bowler*	17/15	$a = 1.5, b = 1.5, (r_b = 1)$	0.714
JETSET + Collins and Spiller	103/16	$\epsilon_b = (3.0 \pm 0.8) \times 10^{-3}$	0.691 ± 0.005
JETSET + Kartvelishvili* *et al.*	34/16	$\alpha_b = 10.4 \pm 0.5$	0.711 ± 0.004
JETSET + Lund*	17/15	$a = 2.0, b = 0.5$	0.712
JETSET + Peterson *et al.*	62/16	$\epsilon_b = (6.0^{+0.9}_{-0.8}) \times 10^{-3}$	0.697 ± 0.005
HERWIG cldir=0	460/17	–	0.632
HERWIG cldir=1	94/17	–	0.676
UCLA*	25/17	–	0.718

Table 8.2: Results of fragmentation model tests for JETSET + fragmentation models, the HERWIG model and the UCLA model. Minimum χ^2, number of degrees of freedom, corresponding parameter values, and the mean value of the corresponding B energy distribution are listed. * indicates models used to correct the data in Chapter 9.

8.2 Tests of Functional Forms $f(x_B, \lambda)$

We now consider the more general question of what functional forms of the B energy distribution, $f(x_B, \lambda)$, can be used as estimates of the true underlying B energy distribution. In particular, we would like to test a wide variety of functional forms and ask how many different forms are consistent with the data. Each consistent functional form will add to the list of our estimates of the true underlying B energy distribution. Figure 8-3 shows an illustration of how the functional forms are tested.

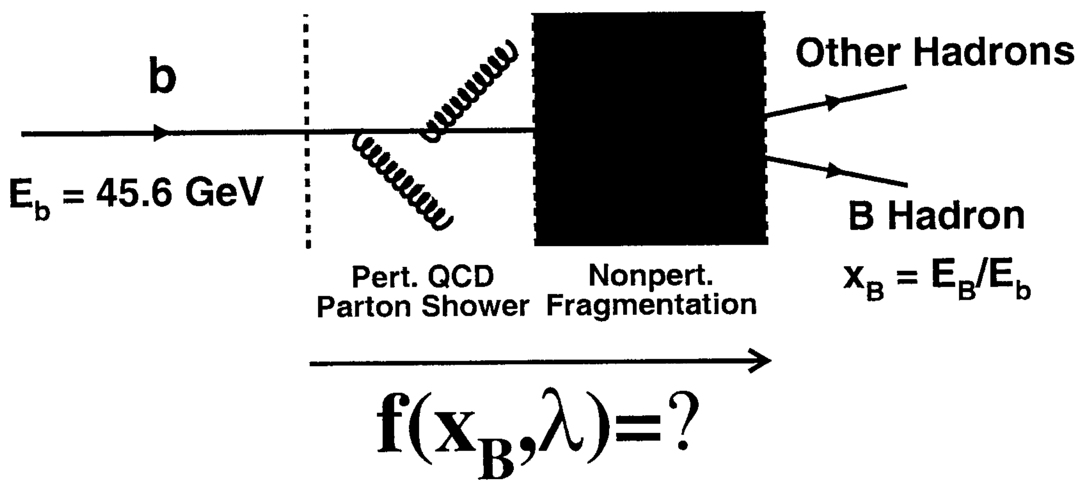

Figure 8-3: A schematic diagram showing how B energy functional forms $f(x_B, \lambda)$ are tested. $f(x_B, \lambda)$ treats everything from the initial b quark in Z^0 to $b\bar{b}$ to the B hadron in one package, which includes hard gluon radiation and perturbative shower evolution which is simulated by JETSET Parton Shower Monte Carlo, and the non-perturbative fragmentation process represented by a dark blob that signifies the fact that it is not very well understood. The parameters λ are varied in order to obtain different B hadron energy distributions.

For convenience we consider the functional forms of the BCFY, Collins and Spiller, Kartvelishvili, Lund, and Peterson groups in the variable x_B. In addition we consider *ad hoc* generalizations of the Peterson function (F), an 8th-order polynomial and a 'power' function. These functions are listed in Table 8.3. Each function vanishes at $x_B = 0$ and $x_B = 1$.

Function	$f(x_B, \lambda)$	Reference
F,F1 (a=0), F2 (b=0)	$\frac{[a+b(1-x_B)]}{x_B}(1-\frac{c}{x_B}-\frac{d}{1-x_B})^{-2}$	[97]
8th-order Polynomial	$x_B(1-x_B)(x_B-x_B^0)(1+\sum_{i=1}^{5} p_i x_B^i)$	(see text)
Power	$x_B^{\alpha}(1-x_B)^{\beta}$	(see text)

Table 8.3: B energy functional forms used in comparison with the data. A polynomial function and a power function are included (see text for discussion). x_B^0 is the low kinematic threshold for B energy. For BCFY, CS, Kartvelishvili, Lund, Peterson functional forms, see Table 8.1. Function F1 is obtained by setting $a = 0$ and F2 by setting $b = 0$, see text below.

For each functional form, a testing procedure similar to that described in subsection 8.1 is applied. The optimized fitting parameters λ and the minimum χ^2 values are listed in Table 8.4. The corresponding $D^{MC}(x_B^{rec})$ are compared with the data in Figure 8-4.

Two sets of optimized parameters are found for the generalized Peterson function F to describe the data. 'F1', obtained by setting the parameter a (shown in Table 8.3) to zero and making b a constant normalization factor, behaves like x_B as $x_B \to 0$ and $(1-x_B)^3$ as $x_B \to 1$ and yields the best χ^2 probability of 53%; 'F2', obtained by setting b to zero and making a a constant normalization factor, has a χ^2 probability of 13%. A constrained polynomial of at least 8th-order is needed to obtain a χ^2 probability greater than 0.1%. The Peterson functional form marginally reproduces the data with a χ^2 probability of about 3%. The remaining functional forms are found to be inconsistent with our data. The widths of the BCFY and CS functions are too large to describe the data; Kartvelishvili, Lund and the 'power' functional form vanish too fast as x_B approaches zero.

We conclude that, within our resolution and with our current data sample, we are able to distinguish between some of these functional forms. But most importantly, consistent functional forms will help us evaluate the uncertainty on the true B energy distribution.

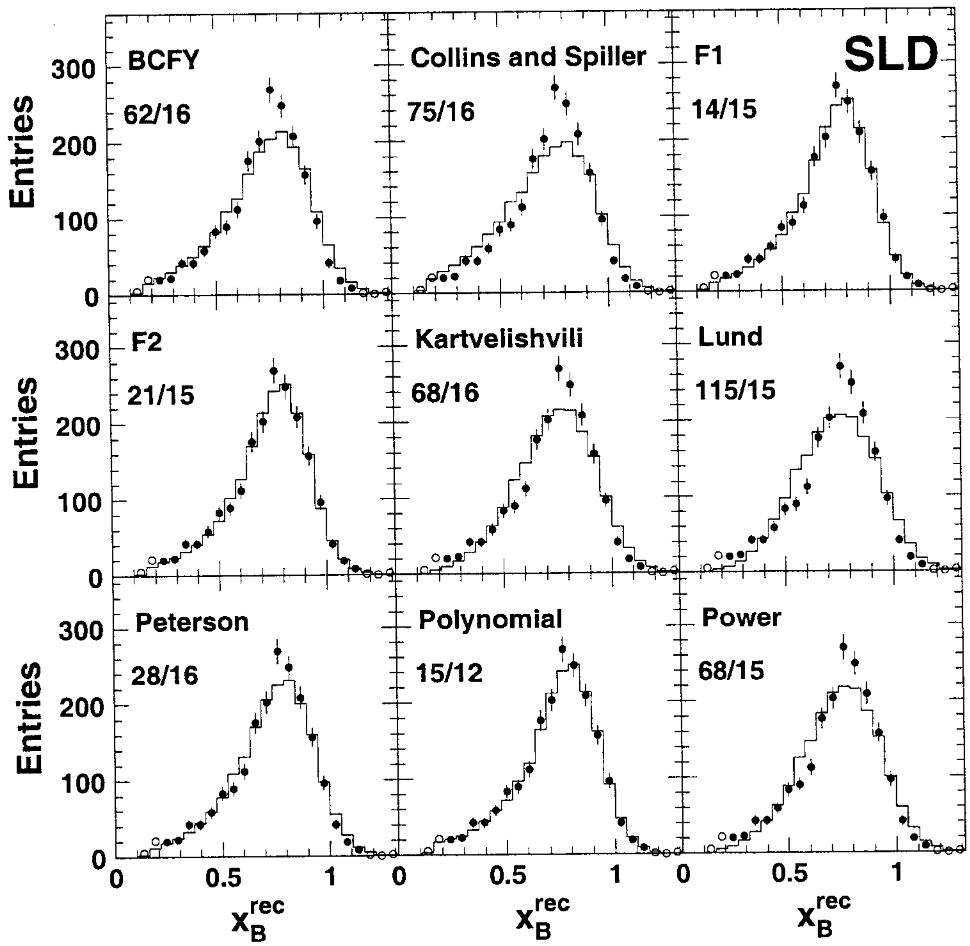

Figure 8-4: Each figure shows the background-subtracted distribution of reconstructed B hadron energy for the data (points) and for the weighted simulation (histograms) based on the respective optimized input functional form for the *true* B energy distribution. The χ^2 and the number of degrees of freedom are indicated.

Function	χ^2/dof	Parameters	$\langle x_B \rangle$
F1*	14/15	$c = 0.838 \pm 0.018$	0.714±0.005
		$d = 0.022 \pm 0.002$	
F2*	21/15	$c = 0.896 \pm 0.033$	0.717±0.005
		$d = 0.040 \pm 0.003$	
BCFY	62/16	$r = 0.240 \pm 0.009$	0.709±0.005
Collins and Spiller	75/16	$\epsilon_b = 0.043 \pm 0.005$	0.711±0.005
Kartvelishvili *et al.*	68/16	$\alpha_b = 4.16 \pm 0.11$	0.721±0.004
Lund	115/15	$a = 2.30 \pm 0.12$	0.721±0.005
		$bm_\perp^2 = 0.50 \pm 0.07$	
Peterson *et al.**	28/16	$\epsilon_b = 0.036 \pm 0.002$	0.713±0.005
Polynomial*	15/12	$p_1 = -10.76 \pm 0.16$	0.709±0.005
		$p_2 = 45.74 \pm 0.28$	
		$p_3 = -93.60 \pm 0.34$	
		$p_4 = 92.01 \pm 0.37$	
		$p_5 = -34.53 \pm 0.27$	
Power	68/15	$\alpha = 4.27 \pm 0.25$	0.720±0.005
		$\beta = 1.05 \pm 0.10$	

Table 8.4: Results of the χ^2 fit of fragmentation functions to the reconstructed B hadron energy distribution after background subtraction. The minimum χ^2 value, the number of degrees of freedom, the corresponding parameter values, and the mean value of the corresponding B energy distribution are listed. Errors are statistical only. * indicates functions used to correct the data in Chapter 9.

Chapter 9

Unfolding the B Energy Distribution

So far we have used the raw B energy distribution to test various models of the non-perturbative b quark fragmentation function and various B energy functional forms. However, in order to compare our results with those of other experiments and potential future theoretical predictions it is necessary to correct the reconstructed scaled B hadron energy distribution $D^{data}(x_B^{rec})$ for the effects of non-B backgrounds, detector acceptance, event selection and analysis bias, and initial-state radiation, as well as for bin-to-bin migration effects caused by the finite resolution of the detector and the analysis technique.

9.1 Unfolding Method

Due to the expected rapid variation of the yet-unknown true B energy distribution at large x_B, *any* correction procedure will necessarily be more or less model-dependent. We choose a method that explicitly evaluates this model-dependence and gives a very good estimate of the true energy distribution using all of the above models or functional forms that are at least marginally consistent with the data.

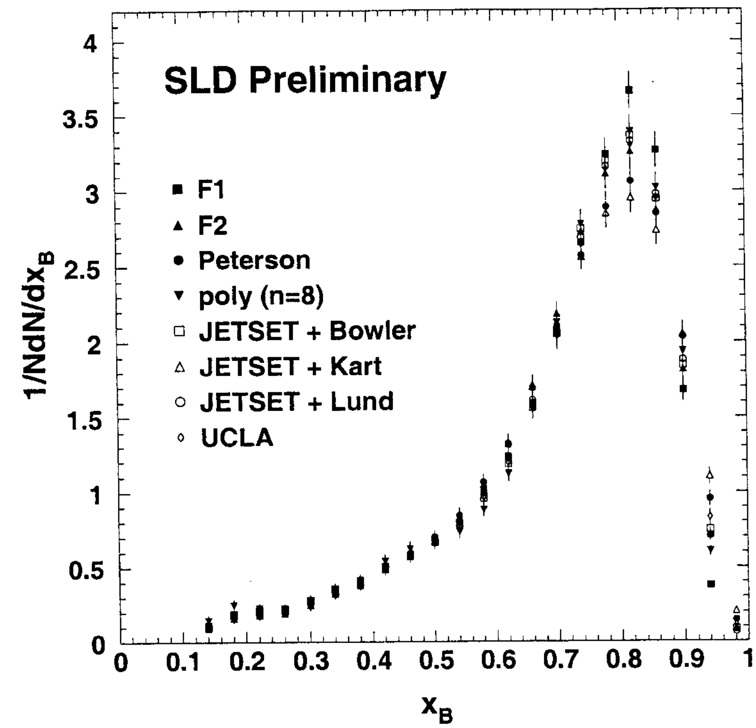

Figure 9-1: The efficiency-resolution corrected distributions of scaled weakly-decaying B hadron energies for **Case 1)** fragmentation models of the Lund, the Bowler and the Kartvelishvili within the JETSET parton shower Monte Carlo as well as for the UCLA fragmentation model; and for **Case 2)** four functional forms: F1, F2, Peterson, and the constrained 8th-order polynomial.

We apply a 25×25 matrix unfolding procedure to $D^{data}(x_B^{rec})$ to obtain an estimate of the true distribution $D^{data}(x_B^{true})$:

$$D^{data}(x_B^{true}) \quad = \quad \epsilon^{-1}(x_B^{true}) \cdot E(x_B^{true}, x_B^{rec}) \cdot (D^{data}(x_B^{rec}) - S(x_B^{rec})), \qquad (9.1)$$

where S is a vector representing the background contribution, E is a matrix to correct for bin-to-bin migrations, and ϵ is a vector representing the efficiency for selecting true B hadron decays for the analysis. The matrices S, E and ϵ are calculated from our MC simulation; the matrix E incorporates a convolution of the input fragmentation function with the resolution of the detector. $E(i,j)$ is the number of vertices with x_B^{true} in bin i and x_B^{rec} in bin j, normalized by the total number of vertices with x_B^{rec}

in bin j. Error propagation and correlation among bins of unfolded distribution are discussed in detail in **Appendix C**.

We evaluate the matrix E using the Monte Carlo simulation weighted according to an input generator-level *true* B energy distribution found to be consistent with the data in Chapter 8. We have seen that eight B energy distributions can reproduce the data: four fragmentation models $f(z)$ (JETSET+Lund, JETSET+Bowler, JETSET+Kartvelishvili, and UCLA) and four B energy functional forms $f(x_B)$ (Peterson, F1 and F2 and the 8th-order polynomial in Table 8.3. Also see text on page 170). We consider in turn each of these eight consistent distributions, using the optimized parameters listed in Table 8.2 and 8.4. The matrix E is then evaluated by examining the population migrations of true B hadrons between bins of the input scaled B energy, x_B^{true}, and the reconstructed scaled B energy, x_B^{rec}.

9.2 Unfolded Distribution

Using each $D^{MC}(x_B^{true})$, the data distribution $D^{data}(x_B^{rec})$ is then unfolded according to Equation (9.1) to yield $D^{data}(x_B^{true})$, which is shown for each input fragmentation function in Figure 9-1. For histogram bin contents, errors, and correlation matrix, see **Appendix C**.

It can be seen that the shapes of $D^{data}(x_B^{true})$ differ systematically among the input b quark fragmentation models and the assumed B energy functional forms. These differences are used to assign systematic errors. Figure 9-2 shows the final corrected x_B distribution $D(x_B)$, which is the bin-by-bin average of the eight unfolded distributions, where the inner error bar represents the statistical error and the outer error bar is the sum in quadrature of the r.m.s. of the eight unfolded distributions and the statistical error within each bin. Since two of the eight functions (the Kartvelishvili model and the Peterson functional form) are only in marginal agreement with the data, and the 8th-order polynomial has a slightly unphysical behavior near $x_B = 1$,

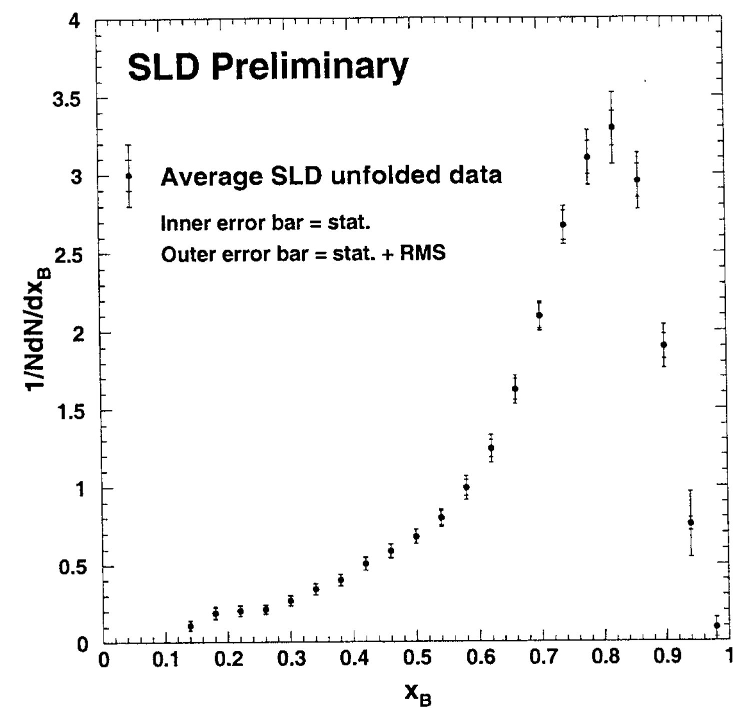

Figure 9-2: Distribution of the final corrected scaled B hadron energies. The central value is the bin-by-bin average of the eight consistent B energy distributions. In each bin the statistical error is indicated by the inner error bar, the sum in quadrature of statistical and unfolding errors from model dependence by the outer error bar. Systematic errors are small compared with the statistical and model dependence errors and are not included here. Note that the first two bins are below the kinematic limit for x_B (no point shown). For histogram bin contents, errors, and correlation matrix, see Appendix C.

this r.m.s. may be considered to be a rather reasonable envelope within which the true x_B distribution is most likely to vary. The model dependence for this analysis is significantly smaller than those of previous direct B energy measurements, indicating the enhanced sensitivity of our data to the underlying true energy distribution.

Chapter 10

Systematic Studies

We have considered sources of systematic uncertainty that potentially affect our measurement of the B hadron energy distribution. These may be divided into uncertainties in modeling the detector and uncertainties on experimental measurements serving as input parameters to the underlying physics modeling. For these studies our standard simulation, employing the Peterson fragmentation function, is used.

For each source of systematic error, the Monte Carlo distribution $D^{MC}(x_B^{true})$ is reweighted and then the resulting Monte Carlo reconstructed distribution $D^{MC}(x_B^{rec})$ is compared with the data $D^{data}(x_B^{rec})$ by repeating the fitting and unfolding procedures described in Section 4 and 5. The differences in both the shape and the mean value of the x_B^{true} distribution relative to the standard procedure with nominal values of parameters are considered. Due to the strong dependence of our energy reconstruction technique on charged tracks, the dominant systematic error is due to the discrepancy in the charged track transverse momentum resolution between the Monte Carlo and the data. We evaluate this conservatively by taking the full difference between the nominal results and results using a resolution-corrected Monte Carlo event sample. The difference between the measured and simulated charged track multiplicity as a function of $\cos\theta$ and momentum is attributed to an un-simulated tracking inefficiency correction. We use a random track-tossing procedure to evaluate the difference in our results. A large number of measured quantities relating to the production and decay of charm and bottom hadrons are used as input to our simulation. In $b\bar{b}$ events we have considered the uncertainties on: the branching fraction for $Z^0 \to b\bar{b}$; the rates of production of $B^{\pm}$, B^0 and B_s^0 mesons, and B baryons; the lifetimes of B mesons and baryons; and the average B hadron decay charged multiplicity. In $c\bar{c}$ events we have considered the uncertainties on: the branching fraction for $Z^0 \to c\bar{c}$; the charmed hadron lifetimes, the charged multiplicity of charmed hadron decays, the production of K^0 from charmed hadron decays, and the fraction of charmed hadron decays containing no π^0s. We have also considered the rate of production of $s\bar{s}$ in the jet fragmentation process, and the production of secondary $b\bar{b}$ and $c\bar{c}$ from gluon splitting. The world-average values [103, 95] of these quantities used in our simulation, as well as the respective uncertainties, are listed in Table 10.1, 10.2, and 10.3. Most of these variations have effect on normalization, but very little on the shape or the mean value. In no case do we find a variation that changes our conclusion about which functions are consistent with the data. Systematic errors of the mean value are listed in Table 10.4.

Source	Center Value	Variation	$\delta\ \langle x_B \rangle$
Monte Carlo Statistics			**0.0011**
Tracking efficiency correction	on	off	-0.0022
2d-impact parameter smearing	on	off	-0.0012
Track polar angle smearing	off	2 mrad	-0.0009
Track $1/P_{\perp}$ resolution smearing	0.0017	off	0.0054
Total Detector Systematics			**0.0060**

Table 10.1: Uncertainties in $\langle x_B \rangle$ due to Monte Carlo statistics and detector systematics.

Source	Center Value	Variation	$\delta \langle x_B \rangle$
B^0 mass effect	5.280	± 0.004	± 0.0001
B^+ lifetime	1.64 ps	± 0.04 ps	± 0.0001
B^0 lifetime	1.55 ps	± 0.04 ps	± 0.0001
B_s lifetime	1.57 ps	± 0.15 ps	± 0.0001
B baryon lifetime	1.22 ps	± 0.11 ps	± 0.0001
$B^+ \to D^0 + X$ fraction	0.632	± 0.026	<0.0001
$B^0 \to D^0 + X$ fraction	0.546	± 0.026	∓ 0.0002
$B_s \to D_s + X$ fraction	0.674	± 0.200	± 0.0006
B baryon $\to C$ baryon $+X$ fraction	0.755	± 0.100	± 0.0001
B^+ production fraction	40.67	± 10	∓ 0.0010
B^0 production fraction	40.58	± 10	<0.0001
B_s production fraction	11.49	± 4	± 0.0009
B baryon production fraction	7.26	± 4	<0.0001
B decay $\langle n_{ch} \rangle$	5.3	$+0.3$	-0.0018
		-0.3	0.0005
R_b	0.2170	± 0.0009	<0.0001

Table 10.2: Uncertainties in $\langle x_B \rangle$ due to uncertainties in physics modeling (part one).

Source	Center Value	Variation	$\delta \langle x_B \rangle$
R_c	0.1733	± 0.0048	<0.0001
D^+ lifetime	1.057 ps	± 0.015 ps	± 0.0001
D^0 lifetime	0.415 ps	± 0.004 ps	± 0.0001
D_s lifetime	0.467 ps	± 0.017 ps	<0.0001
Λ_c lifetime	0.206 ps	± 0.012 ps	± 0.0001
D^+ decay $\langle n_{ch} \rangle$	2.54	± 0.11	∓ 0.0001
D^0 decay $\langle n_{ch} \rangle$	2.50	± 0.06	∓ 0.0003
D_s decay $\langle n_{ch} \rangle$	2.65	± 0.31	∓ 0.0001
Λ_c decay $\langle n_{ch} \rangle$	2.79	± 0.45	∓ 0.0004
$D^+ \rightarrow K^0$ mult.	0.644	± 0.078	∓ 0.0003
$D^0 \rightarrow K^0$ mult.	0.402	± 0.059	∓ 0.0012
$D_s \rightarrow K^0$ mult.	0.382	± 0.057	± 0.0006
$D^+ \rightarrow$ no π^0 fraction	0.496	± 0.050	± 0.0001
$D^0 \rightarrow$ no π^0 fraction	0.370	± 0.037	∓ 0.0004
$D_s \rightarrow$ no π^0 fraction	0.348	± 0.035	∓ 0.0004
$g \rightarrow b\bar{b}$	0.31	$\pm 0.15\%$	± 0.0002
$g \rightarrow c\bar{c}$	2.38	$\pm 1.2\%$	± 0.0008
K^0 production	0.658 trks	± 0.066 trks	± 0.0009
Λ production	0.124 trks	± 0.008 trks	± 0.0002
Total Physics Modeling Syst.			**0.0029**

Table 10.3: Uncertainties in $\langle x_B \rangle$ due to uncertainties in physics modeling (part two).

Source	$\delta \langle x_B \rangle$
Monte Carlo statistics	0.0011
Detector modeling	0.0060
Physics modeling	0.0029
Total Systematics	**0.0068**

Table 10.4: Summary of systematics in $\langle x_B \rangle$.

The model-dependence of the unfolding procedure is estimated by considering the envelope of the unfolded results illustrated in Figure 9-2. Since eight functions provide an acceptable χ^2 probability in fitting to the data, in each bin of x_B we calculated the average value of these eight unfolded results as well as the r.m.s. deviation. In each bin the average value is taken as our central value and the r.m.s. value is assigned as the unfolding uncertainty.

Other relevant systematic effects such as variation of the event selection cuts and the assumed B hadron mass are also found to be very small (Table 10.5).

Source	Center Value	Variation	$\delta \langle x_B \rangle$
Visible Energy	20	-2	-0.0007
(GeV)	20	$+2$	0.0003
Number of good tracks	5	$+5$	-0.0003
$cos(\theta_{thrust})$ range	0.71	± 0.04	0.0001

Table 10.5: Uncertainties in $\langle x_B \rangle$ due to variations in hadronic event selection criteria. These changes in $\langle x_B \rangle$ are partly due to changes in the statistical sample.

In selecting the final B sample we have applied the empirical cut on M^2_{0max} in (7.6). As a cross-check of the stability of our method, we vary the M^2_{0max} cut within a wide range, repeat the analysis procedure, compare the results. Specifically we have chosen four different cuts: $-1 < M^2_{0max} < 1$, $-1 < M^2_{0max} <$ default cut, $-1 < M^2_{0max} < 3$, and $-1 < M^2_{0max} < 5$. For each cut the number of selected B vertices and the resulting statistical errors, σ_{x_B}, on $\langle x_B \rangle$ are listed in column 2 and 3 of Table 10.6, respectively.

In order to examine whether our conclusion about which functions remains valid and how the values of the average B energy change when we vary the M^2_{0max} cut, we re-test four functions F1, F2, Peterson and BCFY for each cut. If our technique is stable, functions most consistent with our data, such as F1 and F2, should still produce good fit results and the values of χ^2 should change only slightly. Functions that are only marginally consistent with our data, such as the Peterson function, can become more consistent or less consistent with our data, since our data cannot yet rule out these functions. However, functions that are significantly inconsistent with our data, such as BCFY, are expected to produce worse fits with the data as we loosen the M^2_{0max} cut. Table 10.6 lists all sixteen $\langle x_B \rangle$ values. No statistically significant variations are observed. The average energy decreases slightly when more B vertices are included in the final sample. Since B vertices with large M^2_{0max} are known to have worse energy resolutions, the stability of our technique is remarkable. Table 10.7 lists the χ^2 of the all sixteen tests. As M^2_{0max} cut is loosened, F1 remains the best fit function; however, F2 becomes marginal and Peterson turns from marginally consistent into slightly inconsistent. BCFY, as expected, remains inconsistent and is worse when we enlarge the B sample.

M^2_{0max}	Number of B	σ_{x_B}	$\langle x_B \rangle$	$\langle x_B \rangle$	$\langle x_B \rangle$	$\langle x_B \rangle$
			F1	F2	Peterson	BCFY
1.0	1438	0.0053	0.715	0.719	0.712	0.703
Default	1920	0.0046	0.713	0.716	0.713	0.708
3.0	4068	0.0037	0.710	0.714	0.712	0.706
5.0	7077	0.0029	0.707	0.710	0.709	0.705

Table 10.6: We check the stability of our $\langle x_B \rangle$ by varying the M^2_{0max} cut used in selecting our final B sample with a large range. The resulting variation in $\langle x_B \rangle$ is a result of both statistical change and systematic effects. 'Default' in the 2nd row stands for the empirical cut we have chosen in (7.6).

M^2_{0max}	χ^2	χ^2	χ^2	χ^2
	F1	F2	Peterson	BCFY
1.0	13	22	31	61
Default	16	25	32	66
3.0	10	20	28	71
5.0	17	32	43	100

Table 10.7: Values of χ^2 for four different M^2_{0max} cut and four different functions. Our conclusions about whether a function is consistent essentially remain the same.

Chapter 11

Conclusions

We have used the excellent tracking and vertexing capabilities of SLD to reconstruct the energies of B hadrons in $e^+e^- \to Z^0$ events over the full kinematic range by applying a new kinematic technique to an *inclusive* sample of topologically reconstructed B hadron decay vertices. The overall B selection efficiency of the method is 3.9%. We estimate the resolution on the B energy to be about 10.4% for roughly 83% of the reconstructed decays. The energy resolution for low energy B hadrons is significantly better than previous measurements. The overall efficiency for selecting B hadrons is about 15-20 times higher than recent direct measurements at LEP.

In order to get a good estimate of the model dependence of the unfolded distribution, the distribution of reconstructed scaled B hadron energy, $D^{data}(x_B^{rec})$, is compared **case 1)** with predictions of *either* perturbative QCD and phenomenological b quark fragmentation models in the context of the JETSET parton shower Monte Carlo, *or* HERWIG and UCLA fragmentation models, and **case 2)** with a set of functional forms for the B energy distribution. In **case 1)**, the Lund and the Bowler models are consistent with the data; the model of Kartvelishvili *et al.* is in marginal agreement with the data. The models based on the perturbative QCD calculations of Braaten *et al.*, and of Collins and Spiller, and the Peterson model are disfavored by the data. Although both versions of the HERWIG model are excluded by the data, the new version is very much improved. The UCLA model describes the data reasonably well. In **case 2)**, four functional forms, namely the two generalized Peterson functions F1 and F2, the Peterson function, and a constrained 8th-order polynomial are found to be consistent with the data.

The raw B energy distribution is then corrected for bin-to-bin migrations caused by the resolution of the method and for selection efficiency to derive the energy distribution of the weakly decaying B hadrons produced in Z^0 decays. Systematic uncertainties in the correction have been evaluated and are found to be significantly smaller than those of previous direct B energy measurements. The final corrected x_B distribution $D^{data}(x_B^{true})$ is shown in Figure 9-2. The statistical and unfolding uncertainties are indicated separately.

It is conventional to evaluate the mean of this B energy distribution, $< x_B >$. For each of the eight functions providing a reasonable description of the data (four from **case 1)** and four from **case 2)**), we evaluate $< x_B >$ from the distribution that corresponds to the optimized parameters; these are listed in Table 8.2 and Table 8.4. We take the average of the eight values of $< x_B >$ as our central value, and define the model-dependent uncertainty to be the r.m.s. deviation within each bin. All detector and physics modeling systematic errors are included. We obtain

$$< x_B > \quad = \quad 0.714 \pm 0.005(stat.) \pm 0.007(syst) \pm 0.002(model). \qquad (11.1)$$

It can be seen that $< x_B >$ is relatively insensitive to the variety of allowed forms of the shape of the fragmentation function $D(x_B)$.

Figure 11-1 shows the comparison of this result with other measurements at LEP or SLD.

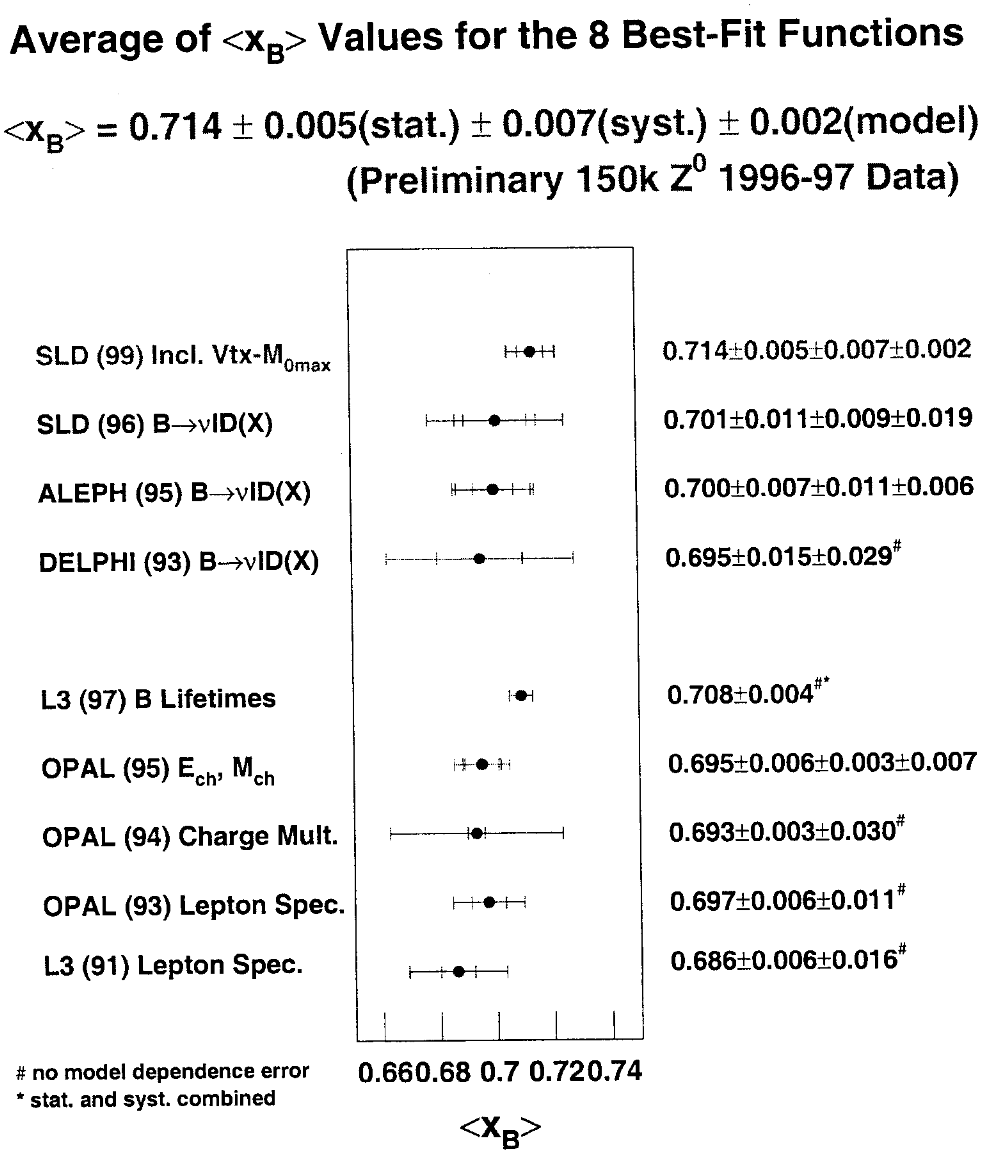

Figure 11-1: Comparison with other results of the average B hadron energy. In a *direct* measurement each individual B hadron energy is reconstructed. In *indirect* measurements [101], the average B hadron energy is inferred from distributions of other kinematic variables, such as the spectra of leptons from B semi-leptonic decays. Note that in several results the model-dependence on the average B energy were not considered.

Appendix A

Electroweak Interaction

Several key ideas were crucial to the eventual formulation of the unification of electromagnetism and the weak interaction. Local non-Abelian gauge invariance [109], spontaneous symmetry breaking [110], the Higgs mechanism [111], and the demonstration of the renormalizability of spontaneously broken gauge theories [112]. The discovery of parity violation in weak interactions [113] and other experimental observations laid the foundation in formulating the fermion structure, the Lorentz structure of the interactions, and the gauge group structure. All assumptions of the theory have been and will continue to be subject to more and more precise experimental tests. Any significant deviation from predictions of the Standard Model will have to be explained by theories beyond the Standard Model.

A.1 Local Gauge Theories

Implicit in Maxwell's unified theory of electricity and magnetism, the electromagnetism, is the U(1) local gauge invariance. It took almost a century to realize that the unification of other fundamental interactions also lay in the same direction but at a deeper level, namely, the local non-Abelian gauge invariance. The Standard Model electroweak theory was formulated based on this principle of local gauge invariance.

In Classical Electrodynamics, the electric field $\vec{E}$ and the magnetic field $\vec{B}$ are unchanged when the 4-vector potential A^μ is changed by adding the divergence of an arbitrary function,

$$A^\mu = A^\mu - \partial^\mu \Lambda. \tag{A.1}$$

The same physics is described by an infinite number of different vector potentials. This is called the local gauge invariance of classical electrodynamics.

In quantum theory, the absolute phase of a wave function cannot be measured and is chosen by convention. Under a *global* change of the phase of the wave function,

$$\psi(x) = e^{i\theta}\psi(x), \tag{A.2}$$

the expectation value of an observable,

$$\langle \mathcal{O} \rangle = \int \psi^* \mathcal{O} \psi, \tag{A.3}$$

does not change.

What happens if we make a *local* change of the phase of a wave function? Under a local phase transformation,

$$\psi(x) = e^{i\alpha(x)}\psi(x), \tag{A.4}$$

where the phase is space-time dependent, the derivative of the wave function transforms as

$$\partial_\mu \psi(x) \to \partial_\mu \psi'(x) = e^{i\alpha(x)}[\partial_\mu \psi(x) + i(\partial_\mu \alpha(x))\psi(x)], \tag{A.5}$$

which involves a translation of the original derivative. By defining a gauge-covariant derivative

$$\mathcal{D} \equiv \partial_\mu + ieA_\mu, \tag{A.6}$$

where e is the electrical charge of the particle described by $\psi(x)$ and the field $A_\mu(x)$

transforms under equation (A.4) as

$$A_\mu(x) \to A'_\mu(x) \equiv A_\mu(x) - (1/e)\partial_\mu \alpha(x), \tag{A.7}$$

then

$$\mathcal{D}_\mu \psi(x) \to e^{i\alpha(x)} \mathcal{D}_\mu \psi(x). \tag{A.8}$$

The covariant derivative of the wave function transforms just as the wave function itself. Note that the vector transformation of A_μ in equation (A.7) is in exactly the same form as that of equation (A.1). Moreover, the form of the covariant derivative suggests the form of interaction between the matter represented by charged particle ψ and the electromagnetic field.

As we have seen, imposing the local gauge invariance can be achieved by replacing the normal derivative by the gauge-covariant derivative, and shift the vector field A_μ by a divergent term.

For Dirac particles, the free-particle Lagrangian

$$\mathcal{L}_{free} = \bar{\psi}(i\gamma^\mu \partial_\mu - m)\psi \tag{A.9}$$

becomes

$$\begin{aligned} \mathcal{L}_{free} &= \bar{\psi}(i\gamma^\mu \mathcal{D}_\mu - m)\psi \\ &= \bar{\psi}(i\gamma^\mu \partial_\mu - m)\psi - qA_\mu \bar{\psi}\gamma^\mu \psi \\ &= \mathcal{L}_{free} - J^\mu A_\mu, \end{aligned} \tag{A.10}$$

where the electromagnetic current has the form

$$J^\mu = qA_\mu \bar{\psi}\gamma^\mu \psi. \tag{A.11}$$

The vector field A_μ is identified as the photon. The photon must be massless because a non-zero mass would destroy the local gauge invariance of the theory.

In sum, local gauge invariance can serve as a dynamical principle which generates interactions between matter field and gauge field (the radiation field). The gauge field, generated by the local gauge invariance, must be massless to preserve the local gauge invariance. In a Non-Abelian gauge theory, local gauge invariance leads to self interacting, massless gauge fields. The non-observation of these massless gauge bosons historically posed a great obstacle to the successful use of non-Abelian gauge theory in formulating the unified electroweak theory. The solution eventually found lies in *spontaneous symmetry breaking.*

A.2 Fermion Structure

A theory that unifies electromagnetic and weak interactions must contain a spectrum of fundamental fermions which includes, for example, the electron e and the electron-neutrino ν_e. Based on experimental observations, only left-handed neutrinos (ν_L) exist and they interact only with left-handed electrons (e_L). This indicates that neutrinos are probably massless[1]. The fact that lepton numbers are conserved suggests that ν_{eL} and e_L belong to one "lepton multiplet", similar to the relationship between the proton and the neutron from the isospin point of view. Right-handed electron (e_R) which does not have a corresponding neutrino partner should therefore be treated as a singlet. For simplicity, the Standard Model employs the "weak isospin" group $\mathrm{SU}(2)_L$ to describe the lepton multiplet. Left-handed lepton pairs form the weak-isospin doublets. For e_L and ν_{eL}, for instance, we have

$$L \equiv \begin{pmatrix} \nu_e \\ e \end{pmatrix}, \tag{A.12}$$

[1] This issue is unsettled yet.

where weak isospin $I = 1/2$ and $I_3 = \frac{1}{2}, -\frac{1}{2}$ for ν_e and e, respectively. Using the projection operator, the left-handed leptons are

$$\begin{aligned} \nu_L &= \frac{1}{2}(1-\gamma_5)\nu, \\ e_L &= \frac{1}{2}(1-\gamma_5)e. \end{aligned} \tag{A.13}$$

The group of transformation generated by weak isospin I where $I = \frac{1}{2}$ is $\mathrm{SU}(2)_L$. The right-handed lepton

$$R \equiv e_R = \frac{1}{2}(1+\gamma_5)e \tag{A.14}$$

forms a weak-isospin singlet ($I = 0$). These lepton weak-isospin multiplets determine the weak charge currents.

A.3 The $\mathrm{SU}(2)_L \otimes \mathrm{U}(1)_Y$ Gauge Theory

In order to insure the conservation of electric charge, the unified electroweak theory must preserve the $\mathrm{U}(1)_{EM}$ symmetry. The electric charge operator Q, therefore, must keep the vacuum invariant (even *after* invoking the spontaneous symmetry breaking). The empirical Gell-Mann–Nishijima formula $Q = I_3 + \frac{1}{2}Y$, which should be satisfied by the theory, suggests the use of weak-hypercharge Y to bring the electric charge Q into the theory. The group generated by the hypercharge Y is $\mathrm{U}(1)_Y$.

The Standard Model electroweak theory is thus based on the $\mathrm{SU}(2)_L \otimes \mathrm{U}(1)_Y$ local gauge symmetry group. The SU(2) weak isospin group has three generators τ_1, τ_2, and τ_3, where $I_i = \frac{1}{2}\tau_i$ ($i = 1, 2, 3$). The U(1) weak hypercharge group has only one generator Y. By construction, the commutation relation $[\tau_3, Y] = 0$ is satisfied. The vector bosons in the theory are an isovector triplet $\mathbf{b}_\mu = b^1_\mu, b^2_\mu$ and b^3_μ, corresponding to the three generators of the $\mathrm{SU}(2)_L$ group, and an isosinglet vector boson $\mathcal{A}_\mu$ corresponding to the single $\mathrm{U}(1)_Y$ generator:

$$b^1_\mu, b^2_\mu, b^3_\mu \quad \text{for} \quad SU(2)_L,$$

$$\mathcal{A}_\mu \quad \text{for} \quad U(1)_Y. \tag{A.15}$$

The Lagrangian term for the interaction between leptons and gauge bosons is

$$\mathcal{L}_{leptons} = \bar{R}i\gamma^\mu \left(\partial_\mu + \frac{ig'}{2}\mathcal{A}_\mu Y\right) R + \bar{L}i\gamma^\mu \left(\partial_\mu + \frac{ig'}{2}\mathcal{A}_\mu Y + \frac{ig}{2}\tau \cdot \mathbf{b}_\mu\right) L. \tag{A.16}$$

where the coupling constant associated with the SU$(2)_L$ and U$(1)_Y$ group are g and g′ respectively. It is evident that R only interacts via U$(1)_Y$ gauge boson and L interacts via both U$(1)_Y$ and SU$(2)_L$ gauge bosons.

A.4 Spontaneous Symmetry Breaking and the Higgs Mechanism

Given a theory which is invariant under a symmetry, if the theory contains a set of degenerate vacuum states, the observable properties of the system should not depend on any particular choice of the vacuum state because of the symmetry respected by the Lagrangian. However, once we choose *any* given vacuum state, the system will no longer be invariant under the symmetry respected by the Lagrangian. For instance, in the case of a ferromagnet, the Lagrangian respects the SO(3) symmetry and any direction can be a vacuum state. Once a certain direction is chosen, for instance, by applying a uniform magnetic field, the system is no longer invariant under SO(3), but only invariant under SO(2). The SO(3) symmetry is broken down to SO(2) symmetry. This is called spontaneous symmetry breaking.

The spontaneous breaking of a *continuous* symmetry of the Lagrangian leads to massless scalar particles called the Goldstone bosons [110]. Both the vector gauge bosons and the Goldstone bosons are massless particles and *neither* is observed in Nature (except for the massless photon). Therefore, in order to successfully apply the local gauge principle and the spontaneous symmetry breaking in formulating the unified electroweak theory, this problem must be resolved. Since we have only observed one massless gauge boson, the photon (γ), the other three gauge bosons (equation A.15) must acquire mass. The solution lies in the Higgs mechanism [111].

The Higgs mechanism states that if the spontaneously broken symmetry is a local *gauge* symmetry of the Lagrangian, then the vector gauge bosons can acquire mass by 'absorbing' the massless Goldstone boson. After spontaneous breaking of the symmetry, for each symmetry group generator under the action of which the chosen vacuum is *not* invariant (a *broken* generator), the generator's corresponding vector boson acquires mass. If the vacuum is still invariant under a generator, the corresponding vector boson will remain massless. A critical step to realize the Higgs mechanism is to gauge transform the fields into the so-called unitary gauge or U-gauge, in which the particle mass spectrum is manifest. As a result of the Higgs mechanism,

- a Higgs scalar with a mass greater than zero is introduced into the theory;
- the massless scalar Goldstone boson disappears;
- the vector gauge fields become massive.

No degrees of freedom is lost in the process: the missing Goldstone boson's degree of freedom is transformed into the longitudinal degree of freedom for the vector boson in order for it to acquire mass.

In the electroweak theory, the four vector bosons in equation (A.15) are all massless before spontaneous symmetry breaking. This is no longer a problem because of the Higgs mechanism. The problem is how charged fermions such as electrons acquire mass. A fermion mass term in the Lagrangian spoils the global SU(2) symmetry of the theory. Can the Higgs mechanism we discussed earlier, which allow the *gauge bosons* to acquire mass, also allows the *fermions* to acquire mass?

The solution is to introduce into the theory a complex doublet scalar fields

$$\phi \equiv \begin{pmatrix} \phi^+ \\ \phi^0 \end{pmatrix}, \tag{A.17}$$

which transforms as an $SU(2)_L$ doublet and has weak hypercharge of $Y = 1$. We add to the Lagrangian a term

$$\mathcal{L}_{scalar} = (\mathcal{D}^\mu \phi)^\dagger (\mathcal{D}_\mu \phi) - V(\phi^\dagger \phi), \tag{A.18}$$

where the covariant derivative, determined by the local gauge invariance, takes the form

$$\mathcal{D}_\mu = \partial_\mu + \frac{ig'}{2}\mathcal{A}_\mu Y + \frac{ig}{2}\tau \cdot \mathbf{b}_\mu \tag{A.19}$$

and the potential is

$$V(\phi^\dagger \phi) = \mu^2(\phi^\dagger \phi) + |\lambda|(\phi^\dagger \phi)^2. \tag{A.20}$$

$\mathcal{L}_{scalar}$ generates the interactions between the scalar fields and the vector gauge bosons. We also add a term

$$\mathcal{L}_{Yukawa} = -G_f[\bar{R}(\phi^\dagger L) + (\bar{L}\phi)R], \tag{A.21}$$

which is $SU(2)_L \otimes U(1)_Y$ invariant and generates the interactions between the scalar fields and the fermions f. The coupling constant is G_f.

Spontaneous symmetry breaking is then invoked to break both $SU(2)_L$ and $U(1)_Y$. After the symmetry breaking, *none* of the four generators (τ_1, τ_2, and τ_3 from $SU(2)_L$ and Y from $U(1)_Y$) leave the vacuum invariant. However, the vacuum is still invariant under the combination $I_3 + Y/2$, which is precisely the charge operator Q. This implies that the $U(1)_{EM}$ symmetry is preserved and hence the electric charge is conserved. The $SU(2)_L \otimes U(1)_Y$ symmetry group has spontaneously broken down to $U(1)_{EM}$. The vector gauge bosons corresponding to the electric charge operator Q is the photon, which remains massless in the theory. The Higgs mechanism has allowed not only the three vector gauge bosons, but also the fermion f (leptons and quarks) to acquire mass, due to the existence of the Yukawa interaction term (equation A.21) between the fermion f and scalar fields. Assuming the vacuum expectation value of the doublet scalar fields is

$$\langle\phi\rangle_0 = \begin{pmatrix} 0 \\ v/\sqrt{2} \end{pmatrix}, \tag{A.22}$$

Expanding the Lagrangian about the minimum of the Higgs potential V,

$$\phi = \begin{pmatrix} 0 \\ (v+\eta)/\sqrt{2} \end{pmatrix}, \tag{A.23}$$

where η is a scalar field, the Yukawa term becomes

$$\mathcal{L}_{Yukawa} = -G_f \frac{v+\eta}{\sqrt{2}} (\bar{f}_R f_L + \bar{f}_L f_R). \tag{A.24}$$

The charged fermion f becomes massive with $m_f = G_f v/\sqrt{2}$. The $\mathcal{L}_{scalar}$ term becomes

$$\mathcal{L}_{scalar} = \frac{1}{2}(\partial^\mu \eta)(\partial_\mu \eta) - \mu^2 \eta^2 + \frac{v^2}{8}[g^2|b^1_\mu - ib^2_\mu|^2 + (g'\mathcal{A}_\mu - g b^3_\mu)^2] + \cdots \tag{A.25}$$

plus interaction terms. The scalar η can be identified as the physical Higgs boson (H) with $M_H^2 = -2\mu^2 > 0$. By defining

$$W^\pm_\mu \equiv \frac{b^1_\mu \mp i b^2_\mu}{\sqrt{2}}, \tag{A.26}$$

we obtain two *charged* vector gauge bosons which have acquired a mass of

$$M_{W^\pm} = \frac{gv}{2}, \tag{A.27}$$

which depends only on the SU(2) coupling constant g, but not the U(1) coupling constant g'. We can also define

$$Z_\mu \equiv \frac{-g'\mathcal{A}_\mu + g b_\mu^3}{\sqrt{g^2 + g'^2}} \tag{A.28}$$

and

$$A_\mu \equiv \frac{g\mathcal{A}_\mu + g' b_\mu^3}{\sqrt{g^2 + g'^2}}. \tag{A.29}$$

The photon A_μ remains massless, but the *neutral* intermediate vector bosons Z_μ (Z^0) has acquired a mass of

$$\begin{aligned} M_{Z^0} &= \frac{v}{2}\sqrt{g^2 + g'^2} \\ &= M_W \sqrt{1 + g'^2/g^2}. \end{aligned} \tag{A.30}$$

The Z^0 mass depends on both g and g', and is always larger than the W mass. So far the Higgs has not been discovered experimentally.

A.5 The Electroweak Parameters

Comparison of the resulting $W^\pm$-lepton coupling with low-energy phenomenology allows us to relate the SU(2) coupling with the Fermi constant

$$\frac{g^2}{8} = \frac{1}{\sqrt{2}} G_F M_W^2. \tag{A.31}$$

Thus, the SU(2) coupling constant can be determined by measuring the mass of the W. The vacuum expectation value $v/\sqrt{2}$ is determined to be $\langle \phi_0 \rangle_0 = \frac{1}{\sqrt{G_F\sqrt{8}}} \sim 174$ GeV [114].

By comparing the neutral gauge boson couplings to leptons, we may identify A_μ

as the photon, if the couplings satisfy

$$gg'/\sqrt{g^2+g'^2}=e. \tag{A.32}$$

The linear combinations of $\mathrm{SU}(2)_L$ gauge bosons with $\mathrm{U}(1)_Y$ gauge bosons suggest the use of a 2-dimensional rotation by the so-called *electroweak mixing angle* θ_W. To have

$$A_\mu = \mathcal{A}_\mu \cos\theta_W + b^3_\mu \sin\theta_W, \tag{A.33}$$

$$Z_\mu = -\mathcal{A}_\mu \sin\theta_W + b^3_\mu \cos\theta_W, \tag{A.34}$$

where the electroweak mixing angle θ_W is defined as

$$\sin\theta_W = \frac{g}{\sqrt{g^2+g'^2}}. \tag{A.35}$$

The electron charge, e, is related to the coupling constants of the electroweak theory,

$$g=\frac{e}{sin\theta_W}, g'=\frac{e}{cos\theta_W}. \tag{A.36}$$

The three seemingly independent coupling constants e, g, and g' can be related by the electroweak mixing angle θ_W, and thus achieving a partial unification[2] of the electromagnetic and weak interactions.

A.6 Weak Neutral Currents

The first important prediction of the electroweak theory is the existence of the neutral weak currents, which was confirmed by experiments. The term in the electroweak

[2] A complete unification should not be based on a product group such as SU(2)⊗U(1).

Lagrangian that is responsible for the neutral current and fermion interactions is

$$\begin{aligned}\mathcal{L}_{n.c.-f\bar{f}} &= Q\bar{f}\gamma^{\mu}fA_{\mu} - \frac{1}{\sqrt{2}}\left(\frac{G_F M_Z^2}{\sqrt{2}}\right)^{1/2}\bar{\nu}\gamma^{\mu}(1-\gamma_5)\nu Z_{\mu} - \\ &\quad \frac{1}{\sqrt{2}}\left(\frac{G_F M_Z^2}{\sqrt{2}}\right)^{1/2}\bar{f}\gamma^{\mu}[2Q\sin^2\theta_W(1+\gamma_5)+ \\ &\quad (2Q\sin^2\theta_W - 2I_3)(1-\gamma_5)]fZ_{\mu}, \end{aligned} \tag{A.37}$$

where Q is the electric charge of the fermion f. The first term is the QED $\gamma f\bar{f}$ coupling; the second term the $Z^0\nu\bar{\nu}$ coupling and the third term the $Z^0 f\bar{f}$ coupling. In $e^+e^- \to f\bar{f}$, two neutral vector gauge bosons may be exchanged: the massless photon and the massive Z^0. The Born or tree-level Feynman diagram for these processes are shown in Figure A-1. The cross-section, σ, is proportional to the modulo square of the sum of the matrix elements represented by the two diagrams, $|\mathcal{M}_{\gamma} + \mathcal{M}_{Z^0}|^2$. Three terms are present in the cross section: the purely electromagnetic, the interference, and the purely weak. The existence of the interference term has been demonstrated by experiments.

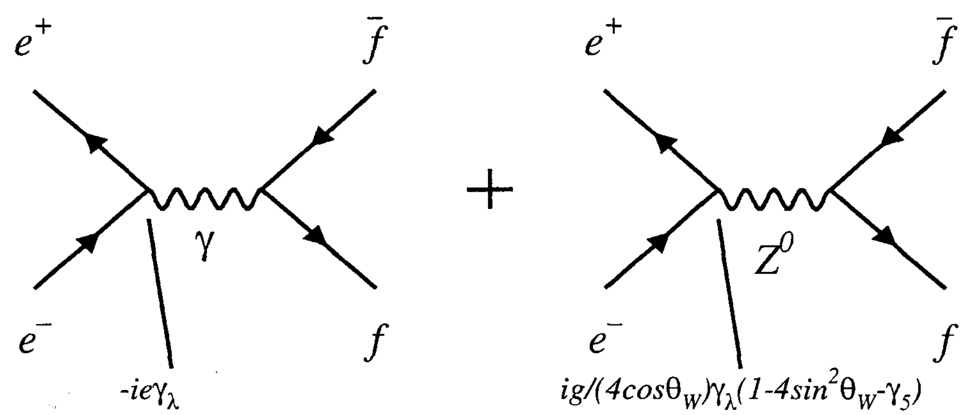

Figure A-1: Tree level Feynman diagrams representing $e^+e^- \to f\bar{f}$. Vertex factors for $e^+e^- \to \gamma$ and $e^+e^- \to Z^0$ are indicated.

One striking feature of the theory is that left-handed and right-handed fermions have different couplings to Z^0:

$$\begin{aligned} g_L &= 2I_3 - 2Q\sin^2\theta_W, \\ g_R &= -2Q\sin^2\theta_W. \end{aligned} \tag{A.38}$$

Decomposing the interaction into V−A form, we have

$$\sqrt{2}\left(\frac{G_F M_Z^2}{\sqrt{2}}\right)^{1/2} \bar{f}\gamma^\mu(c_V^f - c_A^f\gamma_5) f Z_\mu, \tag{A.39}$$

where the vector (V) and axial-vector (A) coupling coefficients are

$$\begin{aligned} c_V^f = (g_L + g_R)/2 = &\quad I_3 - 2Q\sin^2\theta_W, \\ c_A^f = (g_L - g_R)/2 = &\quad I_3. \end{aligned} \tag{A.40}$$

c_V and c_A for all Standard Model fermions are listed in Table A.1. These V- and A-

Fermion	Charge (e)	c_V	c_A
ν_e,ν_ν,ν_τ	0	$\frac{1}{2}$	$\frac{1}{2}$
e, μ, τ	$-\frac{1}{2}$	$-\frac{1}{2} + 2\sin^2\theta_W$	$-\frac{1}{2}$
u, c, t	$+\frac{2}{3}$	$+\frac{1}{2} - \frac{4}{3}\sin^2\theta_W$	$\frac{1}{2}$
d, s, b	$-\frac{1}{3}$	$-\frac{1}{2} + \frac{2}{3}\sin^2\theta_W$	$-\frac{1}{2}$

Table A.1: c_V and c_A for Standard Model fermions.

coefficients are used for determining vertex factors for $Z^0 f\bar{f}$ vertices (see Figure A-1).

A.6.1 Polarized Cross Section of $e^+e^- \to Z^0 \to f\bar{f}$

At SLC, the polarized electron beam allows precision measurements of electroweak parameters by probing the characteristics of polarized $e^+e^- \to Z^0$ production.

The electron polarization is defined as

$$\mathcal{P}_e = \frac{N_{eL} - N_{eR}}{N_{eL} + N_{eR}}, \tag{A.41}$$

where N_{eL} and N_{eR} are the number of left-handed and right-handed electrons, respectively.

At the Z-pole, ignoring the γ-exchange and $\gamma - Z^0$ interference terms, the tree-level polarization dependent cross section for $e^+e^- \to f\bar{f}$ at the Z-pole is given by

$$\begin{aligned}
\frac{d\sigma}{d\cos\theta}(e^+e^- \to f\bar{f}) &= \frac{N_c^f G_F^2 M_Z^4 s}{16\pi[(s - M_Z^2)^2 + \Gamma_Z^2 s^2/M_Z^2]} \\
&\{(1 - \mathcal{P}_z^+\mathcal{P}_z^-)[({c_V^e}^2 + {c_A^e}^2)({c_V^f}^2 + {c_A^f}^2)(1 + \cos\theta^2) - 8c_V^e c_A^e c_V^f c_A^f \cos\theta] \\
&(\mathcal{P}_z^+ - \mathcal{P}_z^-)[2c_V^e c_A^e({c_V^f}^2 + {c_A^f}^2)(1 + \cos\theta^2) + 4({c_V^e}^2 + {c_A^e}^2)c_V^f c_A^f \cos\theta] \\
&+\mathcal{P}_t^+\mathcal{P}_t^- \cos\Phi({c_V^e}^2 + {c_A^e}^2)({c_V^f}^2 + {c_A^f}^2)(1 - \cos\theta^2)\},
\end{aligned} \tag{A.42}$$

where N_c^f is the color factor ($N_c^l = 1$ for leptons and $N_c^q = 3$ for quarks), $\mathcal{P}_z$ and $\mathcal{P}_t$ are polarizations along and transverse to the momentum direction, respectively. Φ is defined by $\Phi = 2\phi - \phi^- - \phi^+$, where ϕ is the azimuthal angle of the outgoing fermion and $\phi^\pm$ the azimuthal angle of the e^- and e^+ transverse polarization direction, respectively. Ignoring transverse polarization, the polarization dependence of the differential cross-section is

$$\frac{d\sigma}{d\cos\theta} \propto (1 + \mathcal{P}_e A_e)(1 + \cos^2\theta) - 2A_f(\mathcal{P}_e + A_e)\cos\theta, \tag{A.43}$$

where θ is the angle of the final fermion with respect to the electron beam direction, and A_e is the electron left-right asymmetry which, for any fermion f, is defined as

$$A_f = \frac{(c_V^f + c_A^f)^2 - (c_V^f - c_A^f)^2}{(c_V^f + c_A^f)^2 + (c_V^f - c_A^f)^2}. \tag{A.44}$$

The A_{LR}^f at the Z^0 vertex is defined as

$$A_{LR}^f \equiv \frac{\sigma(e_R^+ e_L^- \to Z^0 \to f\bar{f}) - \sigma(e_L^+ e_R^- \to Z^0 \to f\bar{f})}{\sigma(e_R^+ e_L^- \to Z^0 \to f\bar{f}) + \sigma(e_L^+ e_R^- \to Z^0 \to f\bar{f})}. \tag{A.45}$$

For a review of recent status of experimental tests of the Electroweak Standard Model, see, for example, reference [115].

In this analysis, we measure the energy spectrum of bottom (B) hadrons in $Z^0 \to b\bar{b}$ decays[3].

Most relevant here is R_b, which is defined as the ratio of the cross section of $Z^0 \to b\bar{b}$ to the total hadronic Z^0 cross-section ($Z^0 \to q\bar{q}$)

$$R_b = \frac{\sigma(Z^0 \to b\bar{b})}{\sum_q \sigma(Z^0 \to q\bar{q})}, \tag{A.46}$$

where $q\bar{q}$ is a quark-antiquark pair and the sum is over quark flavors. At the Z-pole, five flavors, u, d, s, c, and b, are produced. The current measured value is $R_b \simeq 21.7\%$.

We use the 150,000 hadronic Z^0 events collected by the SLD detector during the 1996-1997 run. The number of $Z^0 \to b\bar{b}$ events is approximately 32,500.

[3]The rate for gluon splitting into $b\bar{b}$ is only about 0.3% so a very small number of $b\bar{b}$ come from gluon splittings.

Appendix B

Solving the Longitudinal Missing Momentum P_{0l}

Here we derive the formula for solving the longitudinal momentum of the missing particles (equation (7.5)).

The B energy is

$$E_B = E_{ch} + E_0, \tag{B.1}$$

where E_{ch} is a known, well-measured quantity. E_0 is unknown. Using the B mass constraint, we have

$$\begin{aligned} M_B^2 &= E_B^2 - |\vec{P}_B|^2 \\ &= (E_{ch} + E_0)^2 - (P_{chl} + P_{0l})^2 \\ &= E_{ch}^2 + 2E_{ch}E_0 + E_0^2 - (P_{chl} + P_{0l})^2 \\ &= E_{ch}^2 + 2E_{ch}\sqrt{M_0^2 + P_{0l}^2 + P_t^2} + (M_0^2 + P_{0l}^2 + P_t^2) - (P_{chl}^2 + P_{0l}^2 + 2P_{chl}P_{0l}), \end{aligned} \tag{B.2}$$

where we have used $E_0 = \sqrt{M_0^2 + P_{0l}^2 + P_t^2}$. Now let us denote the unknown variable

P_{0l} as x, we have

$$M_B^2 = E_{ch}^2 + 2E_{ch}\sqrt{x^2 + M_0^2 + P_t^2} + M_0^2 + P_t^2 - P_{chl}^2 - 2P_{chl}x. \tag{B.3}$$

To simplify this quadratic equation, let us define λ to be

$$\begin{aligned}
\lambda &\equiv M_B^2 - E_{ch}^2 - P_t^2 - M_0^2 + P_{chl}^2 \\
&= M_B^2 - (E_{ch}^2 - P_t^2 - P_{chl}^2) - M_0^2 - 2P_t^2 \\
&= M_B^2 - M_{ch}^2 - M_0^2 - 2P_t^2 \\
&= M_B^2 - (M_{ch}^2 + P_t^2) - (M_0^2 + P_t^2).
\end{aligned} \tag{B.4}$$

Then equation (B.3) becomes

$$\lambda = 2E_{ch}\sqrt{x^2 + P_t^2 + M_0^2} - 2P_{chl}x, \tag{B.5}$$

which can be re-written as

$$(\lambda + 2P_{chl}x)^2 = 4E_{ch}^2(x^2 + P_t^2 + M_0^2), \tag{B.6}$$

or

$$\lambda^2 + 4\lambda P_{chl}x + 4P_{chl}x^2 = 4E_{ch}^2x^2 + 4E_{ch}^2(P_t^2 + M_0^2). \tag{B.7}$$

This can be organized into a quadratic equation in x

$$4(E_{ch}^2 - P_{chl}^2)x^2 - 4\lambda P_{chl}x + 4E_{ch}^2(P_t^2 + M_0^2) - \lambda^2 = 0. \tag{B.8}$$

P_{0l} can be solved if M_0, and therefore λ, is known. There may be an ambiguity of two P_{0l} solutions. To simplify this equation, let us define

$$A = \frac{\lambda P_{chl}}{M_{ch}^2 + P_t^2}, \tag{B.9}$$

$$B = \frac{E_{ch}^2(M_0^2 + P_t^2) - \lambda^2/4}{M_{ch}^2 + P_t^2}. \tag{B.10}$$

We have $x^2 - Ax + B = 0$. The solutions of x are

$$x_{1,2} = \frac{1}{2}(A \pm \sqrt{A^2 - 4B}). \tag{B.11}$$

$A^2 - 4B \geq 0$ must hold in order to have any solutions. This means

$$(\frac{\lambda P_{chl}}{M_{ch}^2 + P_t^2})^2 - 4\frac{E_{ch}^2(M_0^2 + P_t^2) - \lambda^2/4}{M_{ch}^2 + P_t^2} \geq 0. \tag{B.12}$$

Let $C = (M_{ch}^2 + P_t^2)/P_{chl}^2$ and $D = 4E_{ch}^2(M_0^2 + P_t^2)$, we have

$$\lambda^2 \geq C(D - \lambda^2), \tag{B.13}$$

or

$$\lambda^2 \geq \frac{CD}{1+C} = 4(M_{ch}^2 + P_t^2)(M_0^2 + P_t^2). \tag{B.14}$$

By defining $\alpha = M_{ch}^2 + P_t^2$ and $\beta = M_0^2 + P_t^2$, we can rewrite the definition of λ in equation (B.4) as:

$$\lambda \equiv M_B^2 - \alpha - \beta, \tag{B.15}$$

where α is an observable quantity and β depends on the missing mass M_0. Therefore, equation (B.14) becomes

$$M_B^2 - \alpha - \beta \geq 4\alpha\beta. \tag{B.16}$$

Let $\gamma = M_B^2 - \alpha$, then $(\gamma - \beta)^2 \geq 4\alpha\beta$, so

$$\gamma^2 - 2\gamma\beta + \beta^2 - 4\alpha\beta \geq 0. \tag{B.17}$$

We now have a quadratic inequality in β:

$$\beta^2 - 2(\gamma + 2\alpha)\beta + \beta^2 + \gamma^2 \geq 0, \tag{B.18}$$

in which β depends on M_0 but the coefficients are known quantities. Since the following,

$$\Delta = [2(\gamma + 2\alpha)]^2 - 4\gamma^2 \geq 0, \tag{B.19}$$

always holds, there always exist two distinct solutions $\beta_{1,2}$:

$$\beta_{1,2} = (M_B^2 + M_{ch}^2 + P_t^2) \pm 2M_B\sqrt{M_{ch}^2 + P_t^2}. \tag{B.20}$$

In order for the inequality (B.18) to hold, β must satisfy $\beta \geq \beta_1$ or $\beta \leq \beta_2$. It is impossible to satisfy $\beta \geq \beta_1$, hence $\beta \leq \beta_2$ leads to

$$M_0^2 \leq M_B^2 + M_{ch}^2 - 2M_B\sqrt{M_{ch}^2 + P_t^2}. \tag{B.21}$$

The missing mass is found to have an upper bound M_{0max}, where

$$M_{0max}^2 \equiv M_B^2 + M_{ch}^2 - 2M_B\sqrt{M_{ch}^2 + P_t^2}. \tag{B.22}$$

This is the same formula we derived in equation (7.4) in Chapter 7. The derivation in this appendix, however, is how I originally derived this formula.

Finally we return to the question of solving the longitudinal momentum P_{0l} for the missing particles. Since M_0 is only constrained between 0 and M_{0max}, there is no unique solution of P_{0l}. Any value of M_0 in its allowed range will produce two values (solutions) of P_{0l} unless $M_0 = M_{0max}$ when there is exactly one solution. However, in the limit where M_{0max} is small, any value of M_0 we pick is not far from the true missing mass M_0^{true}. Due to the fact that, in the B rest frame, the phase-space of having $P_t \geq P_l$ is larger than the phase-space of having $P_t \leq P_l$, in most of the B

decays, the true missing mass peaks near its maximum value M_{0max}. Therefore, if we simply select a sample of B hadrons with small M_{0max} and then assume $M_0 = M_{0max}$, which is a very good estimate of M_0, we can obtain a rather good estimate of the B energy.

When $M_0 = M_{0max}$, $\sqrt{A^2 - 4B}$ in equation (B.11) vanishes. There is a unique solution:

$$\begin{aligned}
P_{0l} &= \frac{A}{2} \\
&= \frac{\lambda}{2(M_{ch}^2 + P_t^2)} P_{chl} \\
&= \frac{M_B^2 - (M_{ch}^2 + P_t^2) - (M_0^2 + P_t^2)}{2(M_{ch}^2 + P_t^2)} P_{chl} && \text{(B.23)} \\
&= \frac{M_B^2 - (M_{ch}^2 + P_t^2) - (M_B^2 + M_{ch}^2 - 2M_B\sqrt{M_{ch}^2 + P_t^2} + P_t^2)}{2(M_{ch}^2 + P_t^2)} P_{chl} && \text{(B.24)} \\
&= \frac{-2(M_{ch}^2 + P_t^2) + 2M_B\sqrt{M_{ch}^2 + P_t^2}}{2(M_{ch}^2 + P_t^2)} P_{chl} && \text{(B.25)} \\
&= \frac{(M_B - \sqrt{M_{ch}^2 + P_t^2})}{\sqrt{M_{ch}^2 + P_t^2}} P_{chl} && \text{(B.26)} \\
&= \frac{M_B - M_{ch\perp}}{M_{ch\perp}} P_{chl}. && \text{(B.27)}
\end{aligned}$$

where $M_{ch\perp} = \sqrt{M_{ch}^2 + P_t^2}$ is the observable, boost-invariant transverse-mass of the charged tracks. In going from equation (B.23) to (B.24) we replaced M_0 by M_{0max}.

The physical interpretation of this approximation is as follows. If the true missing mass is exactly equal to M_{0max}, then in the B rest frame, the *sum* of the momenta of charged particles, $\vec{P}_{ch}$, is completely transverse to the B flight direction. This means if we boost the B along its flight direction into a frame in which $\vec{P}_{ch}$ is completely transverse to the B flight direction, we will find the exact true B boost because this 'transverse frame' we have just boosted the B into is exactly the B rest frame. This is the ideal situation.

However, for the majority of B decays, M_0 is close, but not equal, to M_{0max}.

This means the 'transverse frame' above is not the B rest frame. Fortunately, for a large fraction of B decays, $M_0 \simeq M_{0max}$, making the 'transverse frame' a good approximation of the true B rest frame. The closer M_0 is to M_{0max}, the closer is this 'transverse frame' boost to the true B boost. Consequently, in the limit where $M_{0max} \to 0$, we have $M_0 \to M_{0max}$. Therefore, the 'transverse frame' approaches the true B rest frame.

It is important to stress that since the manner in which a B hadron decays has nothing to do with the B energy in the laboratory frame, our selection of B decays with small M_{0max}, which is a **boost-invariant** property of the individual B decay, should not bias the resulting B energy distribution. In fact, requiring a small missing mass M_0 is in effect selecting B decays with a large charged particle multiplicity and small neutral particle multiplicity. B-decay multiplicity is also a B decay property which should not bias the resulting B energy spectrum.

In practice, however, there exist more than one species of weakly decaying B hadrons with slightly different masses. About 80% of all weakly decaying B hadrons are $B^{\pm}$ and B^0 with $m_{B^{\pm}} \simeq m_{B^0} \simeq 5.28$ GeV/c^2. Approximately 10% are B_s^0 with $m_{B_s^0} \simeq 5.37$ GeV/c^2, and 10% are B baryons with $m_{\Lambda_b} \sim 5.65$ GeV/c^2. In our analysis, when we select a B decay vertex, we do it inclusively. We do not know what species of B hadron it is. Therefore, to apply our missing-mass technique to solve for P_{0l}, we must assume a B hadron mass. We chose the $B^{\pm}$ and B^0 mass of 5.28 GeV/c^2 because they constitute 80% of the B vertices in the sample. As a result, the energy resolution is best for $B^{\pm}$ and B^0 vertices and slightly worse for B_s^0 and B baryons. Therefore, our final energy spectrum will depend slightly on the relative fraction of these different species of B hadrons. The full effect of this is taken into account by varying fraction of each B hadron species within its uncertainty. The corresponding change in the shape is found to be almost negligible, and change in the mean of the B hadron energy distribution is also rather small

Another feature of this B boost reconstruction technique is that the resulting energy residual is almost symmetric and centered around zero, if we assumed the correct B mass. This follows from the fact that, for a sample of B hadrons with small missing mass upper bound M_{0max}, the energy residual is to first order proportional to the small longitudinal momentum of charged tracks in the B rest frame, which can be pointing either in the forward or the backward direction with *equal* probability, which results in an approximately symmetric energy residual.

Appendix C

Unfolding and Error Propagation

C.1 The Unfolding Technique

The background subtracted raw B energy distribution, $D^{data}(x_B^{rec})$ $-S(x_B^{rec})$, with x_B^{rec} ranging from 0 to 1.3158 (60 GeV/E_{beam} = 1.3158), is represented by an N-bin histogram, where $N = 25$ and S is the background. The histogram corresponds to an N-component vector $X(N)$. Similarly, the unfolded distribution, $D^{data}(x_B^{true})$, is also represented by a vector $Y(N)$.

We apply a $N \times N$ matrix unfolding procedure to X to obtain an estimate of the true distribution Y:

$$Y_i \quad = \quad \sum_{j=1}^{N} \epsilon_i^{-1} \cdot E_{ij} \cdot X_j, \tag{C.1}$$

where E is a matrix to correct for bin-to-bin migrations, and ϵ is a vector representing the efficiency for selecting true B hadron decays for the analysis. The N by N matrix E and the vector $\epsilon(N)$ are calculated from our MC simulation.

We consider the error propagation of this unfolding procedure. First, we need to get the errors and correlations of *input* variables correct.

The 25 bins of the measured distribution, vector X, are not correlated unless we are choosing to normalize the histogram to a certain total number of events. The error on the value of each bin, $X_j, j = 1, \cdots, N$, is the statistical error, given by the Poisson distribution:

$$\sigma(X_j) = \sqrt{X_j}. \tag{C.2}$$

The errors of the matrix elements E_{ij} are not negligible due to limited Monte Carlo statistics. Let us assume the number of Monte Carlo events in bin j of the measured raw distribution is M_j ($j = 1, \cdots, N$). Out of these M_j events, m_{ij} come from bin i of the true distribution. We have,

$$M_j = \sum_{i=1}^{N} m_{ij}. \tag{C.3}$$

The matrix element E_{ij}, defined as

$$E_{ij} = \frac{m_{ij}}{M_j}, \tag{C.4}$$

hence represents the probability for a measured event in bin j of the raw distribution to have come from bin i of the true distribution Because of Equation (C.3), the sum of all elements in any given column of E is exactly one. Namely, the probability for any measured raw event to have come from *some* bin of the true B energy distribution is one:

$$\sum_{i=1}^{N} E_{ij} = 1. \tag{C.5}$$

Because of this normalization to 1, all elements within one column of the matrix E are correlated. The error of each element E_{ij} is given by the multinomial distribution instead of the Poisson distribution,

$$\sigma(E_{ij}) = \sqrt{\frac{E_{ij}(1 - E_{ij})}{M_j}}. \tag{C.6}$$

The covariance of any two elements E_{ij} and E_{kl} is given by

$$\mathrm{cov}(E_{ij}, E_{kl}) = E_{ij} E_{kl} \delta_{jl}, \quad (i \neq k). \tag{C.7}$$

Elements of the raw distribution, X_j, is not correlated with any of the elements of the matrix E.

Now we consider the error propagation in applying the unfolding procedure of Equation (C.1). Let us first ignore the efficiency correction since that is straightforward. We focus our attention on the matrix E multiplying the vector X. The problem becomes

$$Y \quad = \quad E \cdot X. \tag{C.8}$$

The output vector Y, which is the unfolded distribution, has N bins. Each of these N components is calculated from the unfolding matrix E, which has N^2 number of elements, and the raw distribution X, which has N components. In other words, each of the N components of Y is a *function* of $N^2 + N$ input *variables*. Even if all of these input $N^2 + N$ variables are statistically independent, the resulting elements of Y will still be correlated because they are calculated from a common set of variables. What makes matter more complicated is that, as we have seen above, some of these input variables are correlated with one another. We must take all these correlations into account when we propagate the errors from the input variables to the output vector Y.

Because the elements of X are *not* correlated with elements of E, the variance-covariance matrix of input variables, which has dimension $(N + N^2) \times (N + N^2)$, can be written in a diagonal-block form

$$M_{X,E} = \left\{ \begin{array}{cc} M_X & \mathbf{0} \\ \mathbf{0} & M_E \end{array} \right\}, \tag{C.9}$$

where M_X is the variance-covariance matrix for the vector X, M_E is the variance-covariance matrix for the matrix E, and $\mathbf{0}$ represents zero entries. Written in explicit form, M_X is an $N \times N$, or 25×25 matrix:

$$M_X = \left\{ \begin{array}{cccc} var(X_1) & \mathrm{cov}(X_1, X_2) & \cdots & \mathrm{cov}(X_1, X_N) \\ \mathrm{cov}(X_2, X_1) & var(X_2) & \cdots & \\ \cdots & & & \\ \cdots & & & \\ \mathrm{cov}(X_N, X_1) & \cdots & \cdots & var(X_N) \end{array} \right\}, \tag{C.10}$$

where $var(X_j)$ is the variance of the X_j and $\mathrm{cov}(X_i, X_j)$ is the covariance between X_i and X_j. M_E is an $N^2 \times N^2$, or 625×625, matrix,

$$M_E = \left\{ \begin{array}{cccc} var(E_{11}) & \mathrm{cov}(E_{11}, E_{12}) & \cdots & \mathrm{cov}(E_{11}, E_{NN}) \\ \mathrm{cov}(E_{12}, E_{11}) & var(E_{12}) & \cdots & \mathrm{cov}(E_{12}, E_{NN}) \\ \cdots & & & \\ \cdots & & & \\ \mathrm{cov}(E_{NN}, E_{11}) & \cdots & \cdots & var(E_{NN}) \end{array} \right\}. \tag{C.11}$$

The propagation of errors to the error of the i^{th} element of the unfolded vector Y_i is derived as follows. Using Equation (C.8),

$$Y_i = \sum_{j=1}^{N} E_{ij} \cdot X_j = \vec{E}_i \cdot \vec{X}, \tag{C.12}$$

where $\vec{E}_i$ is the i^{th} row of the matrix E. The error of Y_i is a result of the errors of both X and $\vec{E}_i$, so

$$\delta Y_i = \vec{E}_i \cdot \delta \vec{X} + \delta \vec{E}_i \cdot \vec{X}. \tag{C.13}$$

The covariance matrix for the output vector Y can therefore be written as

$$\begin{aligned} M_{Yij} &= \delta Y_i \delta Y_j \\ &= (\vec{E}_i \cdot \delta \vec{X} + \delta \vec{E}_i \cdot \vec{X})(\vec{E}_j \cdot \delta \vec{X} + \delta \vec{E}_j \cdot \vec{X}) \\ &= \vec{E}_i \cdot \delta \vec{X} \vec{E}_j \cdot \delta \vec{X} + \delta \vec{E}_i \cdot \vec{X} \delta \vec{E}_j \cdot \vec{X}, \end{aligned} \tag{C.14}$$

where cross-terms vanish because the errors of X and E are not correlated. This allows us to write down the covariance matrix of Y in a simple form in which the contributions of errors of X and E are decoupled,

$$M_Y = EM_X E^T + KM_E K^T, \tag{C.15}$$

where the matrix K is an $N \times N^2$ matrix defined as

$$K = \left\{ \begin{array}{cccc} \vec{X}^T & 0 & \cdots & \\ 0 & \vec{X}^T & 0 & 0 \\ & \cdots & \cdots & \\ 0 & 0 & \cdots & \vec{X}^T \end{array} \right\}, \tag{C.16}$$

or written in explicit form,

$$K = \left\{ \begin{array}{cccc} X_1, X_2, \cdots, X_N & 0 & \cdots & \cdots \\ 0 & X_1, X_2, \cdots, X_N & 0 & \cdots \\ \cdots & 0 & \cdots & 0 \\ 0 & \cdots & 0 & X_1, X_2, \cdots, X_N \end{array} \right\}. \tag{C.17}$$

The elements of M_Y are greater than they would be if errors in the elements of E were ignored. Because of the large number of zero elements in the matrix K, a complete calculation of KM_EK^T is not necessary. The elements of this matrix are given by

$$(KM_EK^T)_{ij} = \sum_{k=1,l=1}^{N} \mathrm{cov}(E_{ik}, E_{jl})X_kX_l. \tag{C.18}$$

The diagonal elements of the resulting covariance matrix M_Y are the standard deviations of the N components of Y. Off-diagonal elements represent correlations between any two different bins.

C.2 Unfolding Results

We used a set of eight functions (4 models and 4 functional forms) to unfold our uncorrected data x_B distribution. Here we list results of the unfolded x_B distribution and uncertainty in each bin for each of the eight unfolded distributions as well as the average of the eight unfolded distributions. The bin-to-bin correlation matrices, discussed in Section C.1, differ only slightly for different functions used in the unfolding. To save space, we only list the correlation matrix for the UCLA model as an example.

Bin	x_B	$1/\sigma d\sigma/dx_B$	Stat. error
1	$0.00 < x_B < 0.04$	0.000	0.000
2	$0.04 < x_B < 0.08$	0.000	0.000
3	$0.08 < x_B < 0.12$	0.000	0.000
4	$0.12 < x_B < 0.16$	0.114	0.039
5	$0.16 < x_B < 0.20$	0.180	0.038
6	$0.20 < x_B < 0.24$	0.198	0.034
7	$0.24 < x_B < 0.28$	0.209	0.029
8	$0.28 < x_B < 0.32$	0.269	0.033
9	$0.32 < x_B < 0.36$	0.344	0.039
10	$0.36 < x_B < 0.40$	0.392	0.039
11	$0.40 < x_B < 0.44$	0.501	0.045
12	$0.44 < x_B < 0.48$	0.586	0.046
13	$0.48 < x_B < 0.52$	0.681	0.050
14	$0.52 < x_B < 0.56$	0.807	0.053
15	$0.56 < x_B < 0.60$	0.998	0.057
16	$0.60 < x_B < 0.64$	1.240	0.064
17	$0.64 < x_B < 0.68$	1.593	0.073
18	$0.68 < x_B < 0.72$	2.046	0.086
19	$0.72 < x_B < 0.76$	2.639	0.102
20	$0.76 < x_B < 0.80$	3.231	0.119
21	$0.80 < x_B < 0.84$	3.657	0.133
22	$0.84 < x_B < 0.88$	3.255	0.126
23	$0.88 < x_B < 0.92$	1.668	0.077
24	$0.92 < x_B < 0.96$	0.368	0.026
25	$0.96 < x_B < 1.00$	0.017	0.004

Table C.1: The fully corrected scaled B energy distribution using F1 functional form.

Bin	x_B	$1/\sigma \mathrm{d}\sigma/\mathrm{d}x_B$	Stat. error
1	$0.00 < x_B < 0.04$	0.000	0.000
2	$0.04 < x_B < 0.08$	0.000	0.000
3	$0.08 < x_B < 0.12$	0.000	0.000
4	$0.12 < x_B < 0.16$	0.096	0.035
5	$0.16 < x_B < 0.20$	0.162	0.036
6	$0.20 < x_B < 0.24$	0.184	0.033
7	$0.24 < x_B < 0.28$	0.196	0.028
8	$0.28 < x_B < 0.32$	0.254	0.032
9	$0.32 < x_B < 0.36$	0.329	0.038
10	$0.36 < x_B < 0.40$	0.378	0.038
11	$0.40 < x_B < 0.44$	0.492	0.044
12	$0.44 < x_B < 0.48$	0.583	0.046
13	$0.48 < x_B < 0.52$	0.686	0.050
14	$0.52 < x_B < 0.56$	0.830	0.054
15	$0.56 < x_B < 0.60$	1.048	0.059
16	$0.60 < x_B < 0.64$	1.323	0.067
17	$0.64 < x_B < 0.68$	1.715	0.077
18	$0.68 < x_B < 0.72$	2.180	0.091
19	$0.72 < x_B < 0.76$	2.711	0.105
20	$0.76 < x_B < 0.80$	3.106	0.115
21	$0.80 < x_B < 0.84$	3.258	0.120
22	$0.84 < x_B < 0.88$	2.861	0.112
23	$0.88 < x_B < 0.92$	1.806	0.082
24	$0.92 < x_B < 0.96$	0.705	0.044
25	$0.96 < x_B < 1.00$	0.091	0.013

Table C.2: The fully corrected scaled B energy distribution using F2 functional form.

Bin	x_B	$1/\sigma \mathrm{d}\sigma/\mathrm{d}x_B$	Stat. error
1	$0.00 < x_B < 0.04$	0.000	0.000
2	$0.04 < x_B < 0.08$	0.000	0.000
3	$0.08 < x_B < 0.12$	0.000	0.000
4	$0.12 < x_B < 0.16$	0.108	0.037
5	$0.16 < x_B < 0.20$	0.174	0.037
6	$0.20 < x_B < 0.24$	0.194	0.034
7	$0.24 < x_B < 0.28$	0.206	0.029
8	$0.28 < x_B < 0.32$	0.267	0.033
9	$0.32 < x_B < 0.36$	0.343	0.039
10	$0.36 < x_B < 0.40$	0.394	0.039
11	$0.40 < x_B < 0.44$	0.510	0.045
12	$0.44 < x_B < 0.48$	0.603	0.047
13	$0.48 < x_B < 0.52$	0.711	0.051
14	$0.52 < x_B < 0.56$	0.852	0.055
15	$0.56 < x_B < 0.60$	1.067	0.060
16	$0.60 < x_B < 0.64$	1.331	0.068
17	$0.64 < x_B < 0.68$	1.692	0.077
18	$0.68 < x_B < 0.72$	2.100	0.089
19	$0.72 < x_B < 0.76$	2.552	0.100
20	$0.76 < x_B < 0.80$	2.886	0.109
21	$0.80 < x_B < 0.84$	3.062	0.114
22	$0.84 < x_B < 0.88$	2.840	0.111
23	$0.88 < x_B < 0.92$	2.020	0.089
24	$0.92 < x_B < 0.96$	0.938	0.054
25	$0.96 < x_B < 1.00$	0.145	0.018

Table C.3: The fully corrected scaled B energy distribution using Peterson functional form.

Bin	x_B	$1/\sigma d\sigma/dx_B$	Stat. error
1	$0.00 < x_B < 0.04$	0.000	0.000
2	$0.04 < x_B < 0.08$	0.000	0.000
3	$0.08 < x_B < 0.12$	0.000	0.000
4	$0.12 < x_B < 0.16$	0.150	0.046
5	$0.16 < x_B < 0.20$	0.256	0.048
6	$0.20 < x_B < 0.24$	0.232	0.038
7	$0.24 < x_B < 0.28$	0.201	0.027
8	$0.28 < x_B < 0.32$	0.242	0.030
9	$0.32 < x_B < 0.36$	0.330	0.038
10	$0.36 < x_B < 0.40$	0.415	0.040
11	$0.40 < x_B < 0.44$	0.551	0.048
12	$0.44 < x_B < 0.48$	0.632	0.049
13	$0.48 < x_B < 0.52$	0.685	0.050
14	$0.52 < x_B < 0.56$	0.744	0.049
15	$0.56 < x_B < 0.60$	0.883	0.052
16	$0.60 < x_B < 0.64$	1.126	0.060
17	$0.64 < x_B < 0.68$	1.551	0.072
18	$0.68 < x_B < 0.72$	2.113	0.089
19	$0.72 < x_B < 0.76$	2.756	0.107
20	$0.76 < x_B < 0.80$	3.218	0.119
21	$0.80 < x_B < 0.84$	3.382	0.124
22	$0.84 < x_B < 0.88$	3.005	0.116
23	$0.88 < x_B < 0.92$	1.924	0.087
24	$0.92 < x_B < 0.96$	0.597	0.038
25	$0.96 < x_B < 1.00$	0.000	0.000

Table C.4: The fully corrected scaled B energy distribution using polynomial functional form.

Bin	x_B	$1/\sigma d\sigma/dx_B$	Stat. error
1	$0.00 < x_B < 0.04$	0.000	0.000
2	$0.04 < x_B < 0.08$	0.000	0.000
3	$0.08 < x_B < 0.12$	0.000	0.000
4	$0.12 < x_B < 0.16$	0.105	0.036
5	$0.16 < x_B < 0.20$	0.191	0.039
6	$0.20 < x_B < 0.24$	0.213	0.036
7	$0.24 < x_B < 0.28$	0.224	0.030
8	$0.28 < x_B < 0.32$	0.287	0.034
9	$0.32 < x_B < 0.36$	0.360	0.040
10	$0.36 < x_B < 0.40$	0.408	0.040
11	$0.40 < x_B < 0.44$	0.512	0.045
12	$0.44 < x_B < 0.48$	0.588	0.047
13	$0.48 < x_B < 0.52$	0.676	0.050
14	$0.52 < x_B < 0.56$	0.789	0.052
15	$0.56 < x_B < 0.60$	0.962	0.056
16	$0.60 < x_B < 0.64$	1.194	0.063
17	$0.64 < x_B < 0.68$	1.566	0.072
18	$0.68 < x_B < 0.72$	2.045	0.087
19	$0.72 < x_B < 0.76$	2.729	0.106
20	$0.76 < x_B < 0.80$	3.195	0.118
21	$0.80 < x_B < 0.84$	3.359	0.123
22	$0.84 < x_B < 0.88$	2.935	0.114
23	$0.88 < x_B < 0.92$	1.834	0.082
24	$0.92 < x_B < 0.96$	0.735	0.045
25	$0.96 < x_B < 1.00$	0.085	0.012

Table C.5: The fully corrected scaled B energy distribution using JETSET parton shower with Bowler model.

Bin	x_B	$1/\sigma \mathrm{d}\sigma/\mathrm{d}x_B$	Stat. error
1	$0.00 < x_B < 0.04$	0.000	0.000
2	$0.04 < x_B < 0.08$	0.000	0.000
3	$0.08 < x_B < 0.12$	0.000	0.000
4	$0.12 < x_B < 0.16$	0.107	0.036
5	$0.16 < x_B < 0.20$	0.189	0.038
6	$0.20 < x_B < 0.24$	0.209	0.035
7	$0.24 < x_B < 0.28$	0.222	0.030
8	$0.28 < x_B < 0.32$	0.283	0.034
9	$0.32 < x_B < 0.36$	0.355	0.039
10	$0.36 < x_B < 0.40$	0.402	0.039
11	$0.40 < x_B < 0.44$	0.509	0.045
12	$0.44 < x_B < 0.48$	0.595	0.047
13	$0.48 < x_B < 0.52$	0.700	0.050
14	$0.52 < x_B < 0.56$	0.837	0.054
15	$0.56 < x_B < 0.60$	1.055	0.060
16	$0.60 < x_B < 0.64$	1.335	0.068
17	$0.64 < x_B < 0.68$	1.700	0.078
18	$0.68 < x_B < 0.72$	2.095	0.089
19	$0.72 < x_B < 0.76$	2.543	0.100
20	$0.76 < x_B < 0.80$	2.846	0.108
21	$0.80 < x_B < 0.84$	2.952	0.111
22	$0.84 < x_B < 0.88$	2.730	0.107
23	$0.88 < x_B < 0.92$	2.039	0.089
24	$0.92 < x_B < 0.96$	1.085	0.061
25	$0.96 < x_B < 1.00$	0.204	0.024

Table C.6: The fully corrected scaled B energy distribution using JETSET parton shower with Kartvelishvili model.

Bin	x_B	$1/\sigma d\sigma/dx_B$	Stat. error
1	$0.00 < x_B < 0.04$	0.000	0.000
2	$0.04 < x_B < 0.08$	0.000	0.000
3	$0.08 < x_B < 0.12$	0.000	0.000
4	$0.12 < x_B < 0.16$	0.107	0.037
5	$0.16 < x_B < 0.20$	0.190	0.039
6	$0.20 < x_B < 0.24$	0.214	0.036
7	$0.24 < x_B < 0.28$	0.225	0.030
8	$0.28 < x_B < 0.32$	0.284	0.034
9	$0.32 < x_B < 0.36$	0.355	0.040
10	$0.36 < x_B < 0.40$	0.406	0.040
11	$0.40 < x_B < 0.44$	0.510	0.045
12	$0.44 < x_B < 0.48$	0.586	0.046
13	$0.48 < x_B < 0.52$	0.675	0.049
14	$0.52 < x_B < 0.56$	0.792	0.052
15	$0.56 < x_B < 0.60$	0.979	0.056
16	$0.60 < x_B < 0.64$	1.232	0.064
17	$0.64 < x_B < 0.68$	1.612	0.074
18	$0.68 < x_B < 0.72$	2.081	0.088
19	$0.72 < x_B < 0.76$	2.670	0.104
20	$0.76 < x_B < 0.80$	3.154	0.117
21	$0.80 < x_B < 0.84$	3.324	0.122
22	$0.84 < x_B < 0.88$	2.963	0.115
23	$0.88 < x_B < 0.92$	1.872	0.084
24	$0.92 < x_B < 0.96$	0.696	0.043
25	$0.96 < x_B < 1.00$	0.067	0.010

Table C.7: The fully corrected scaled B energy distribution using JETSET parton shower with Lund model.

Bin	x_B	$1/\sigma \mathrm{d}\sigma/\mathrm{d}x_B$	Stat. error
1	$0.00 < x_B < 0.04$	0.000	0.000
2	$0.04 < x_B < 0.08$	0.000	0.000
3	$0.08 < x_B < 0.12$	0.000	0.000
4	$0.12 < x_B < 0.16$	0.107	0.037
5	$0.16 < x_B < 0.20$	0.192	0.039
6	$0.20 < x_B < 0.24$	0.213	0.036
7	$0.24 < x_B < 0.28$	0.226	0.030
8	$0.28 < x_B < 0.32$	0.287	0.034
9	$0.32 < x_B < 0.36$	0.357	0.040
10	$0.36 < x_B < 0.40$	0.404	0.040
11	$0.40 < x_B < 0.44$	0.509	0.045
12	$0.44 < x_B < 0.48$	0.587	0.047
13	$0.48 < x_B < 0.52$	0.676	0.050
14	$0.52 < x_B < 0.56$	0.790	0.052
15	$0.56 < x_B < 0.60$	0.964	0.056
16	$0.60 < x_B < 0.64$	1.194	0.063
17	$0.64 < x_B < 0.68$	1.561	0.072
18	$0.68 < x_B < 0.72$	2.033	0.086
19	$0.72 < x_B < 0.76$	2.638	0.103
20	$0.76 < x_B < 0.80$	3.138	0.116
21	$0.80 < x_B < 0.84$	3.296	0.121
22	$0.84 < x_B < 0.88$	2.948	0.114
23	$0.88 < x_B < 0.92$	1.934	0.086
24	$0.92 < x_B < 0.96$	0.827	0.049
25	$0.96 < x_B < 1.00$	0.112	0.015

Table C.8: The fully corrected scaled B energy distribution using the UCLA model.

Bin	x_B	$1/\sigma \mathrm{d}\sigma/\mathrm{d}x_B$	Stat. error	Unfolding r.m.s	Total error
1	$0.00 < x_B < 0.04$	0.000	0.000	0.000	0.000
2	$0.04 < x_B < 0.08$	0.000	0.000	0.000	0.000
3	$0.08 < x_B < 0.12$	0.000	0.000	0.001	0.000
4	$0.12 < x_B < 0.16$	0.110	0.029	0.014	0.034
5	$0.16 < x_B < 0.20$	0.188	0.035	0.025	0.043
6	$0.20 < x_B < 0.24$	0.204	0.032	0.013	0.035
7	$0.24 < x_B < 0.28$	0.213	0.027	0.010	0.029
8	$0.28 < x_B < 0.32$	0.268	0.031	0.015	0.035
9	$0.32 < x_B < 0.36$	0.340	0.036	0.011	0.038
10	$0.36 < x_B < 0.40$	0.398	0.037	0.010	0.039
11	$0.40 < x_B < 0.44$	0.505	0.041	0.016	0.043
12	$0.44 < x_B < 0.48$	0.587	0.042	0.015	0.046
13	$0.48 < x_B < 0.52$	0.677	0.044	0.011	0.047
14	$0.52 < x_B < 0.56$	0.796	0.047	0.030	0.056
15	$0.56 < x_B < 0.60$	0.991	0.052	0.056	0.077
16	$0.60 < x_B < 0.64$	1.241	0.058	0.070	0.090
17	$0.64 < x_B < 0.68$	1.622	0.068	0.062	0.091
18	$0.68 < x_B < 0.72$	2.092	0.080	0.044	0.092
19	$0.72 < x_B < 0.76$	2.671	0.094	0.075	0.120
20	$0.76 < x_B < 0.80$	3.102	0.104	0.140	0.175
21	$0.80 < x_B < 0.84$	3.290	0.111	0.201	0.230
22	$0.84 < x_B < 0.88$	2.953	0.106	0.144	0.179
23	$0.88 < x_B < 0.92$	1.897	0.079	0.113	0.138
24	$0.92 < x_B < 0.96$	0.753	0.042	0.205	0.209
25	$0.96 < x_B < 1.00$	0.090	0.011	0.061	0.063

Table C.9: The fully corrected scaled B hadron energy distribution obtained by averaging over all eight unfolded distributions. The statistical error of each bin is obtained by averaging over the eight statistical errors, but the unfolding error is taken as the r.m.s. of entries in each bin for the eight distributions. The total error is the sum in quadrature of the statistical and unfolding errors.

N	5	6	7	8	9	10	11	12	13	14	15	16	17	18	19	20	21	22	23	24	25
4	34.8	20.7	12.3	7.2	4.3	1.3	3.4	3.1	2.3	2.5	2.7	3.9	2.7	2.7	2.1	1.1	0.8	0.6	0.4	0.2	0.1
5		55.3	30.0	4.4	9.2	4.3	5.2	3.1	1.9	1.9	1.9	3.6	2.7	3.2	2.0	0.9	0.6	0.4	0.2	0.1	0.0
6			54.7	28.6	13.8	6.8	5.7	4.3	2.7	2.5	1.9	3.0	2.3	2.8	1.3	0.7	0.4	0.3	0.2	0.1	0.0
7				55.9	32.9	17.4	10.3	7.2	4.5	4.8	4.3	4.0	3.8	3.4	1.3	0.9	0.7	0.2	0.2	0.1	0.0
8					57.0	33.7	20.5	13.2	7.1	6.6	6.4	4.6	5.1	3.4	1.9	1.3	1.1	0.5	0.6	0.3	0.0
9						50.4	35.0	22.5	11.1	8.8	8.0	5.0	5.0	2.6	2.1	1.2	0.9	0.6	0.6	0.4	0.0
10							57.5	41.9	22.7	16.2	11.9	7.2	5.8	3.8	3.3	2.1	1.4	1.2	1.1	0.7	0.1
11								57.4	38.7	28.2	18.0	11.0	7.1	4.5	3.3	2.3	1.8	1.4	1.1	0.5	0.1
12									53.8	44.0	29.6	18.7	12.2	7.6	5.2	3.7	2.8	2.3	1.4	0.6	0.1
13										57.9	43.9	29.8	19.9	12.4	8.5	5.9	4.0	3.2	1.7	0.8	0.1
14											54.2	41.3	28.9	19.3	13.6	9.2	5.9	4.3	2.2	1.1	0.2
15												54.1	42.5	31.9	23.6	16.2	10.4	7.1	3.8	2.3	0.6
16													53.7	45.6	35.4	25.5	16.7	10.7	5.6	3.4	0.8
17														57.5	49.3	38.6	27.3	18.0	10.1	6.0	1.6
18															59.2	50.6	38.8	27.4	16.7	10.0	3.1
19																62.2	53.1	40.8	27.4	16.8	6.0
20																	65.1	54.7	40.2	26.2	10.2
21																		66.5	55.0	38.8	16.5
22																			67.3	53.6	26.9
23																				62.1	32.9
24																					33.5

Table C.10: The complete correlation matrix for the UCLA model, a 25 by 25 matrix, with each element corresponding to the correlation coefficient, written in percentage, between one bin and another. For example, the correlation coefficient between bin 8 and bin 14 is 0.066 or 6.6%. Note that the first 3 rows and columns of the matrix are omitted because these bins ($0 < x_B < 0.12$) are almost entirely below the B mass-threshold of $x_B^{th} = 0.116$. Because the correlation matrix is symmetric, elements in the lower-left half of the matrix can be found in the upper-right half and is therefore omitted. The correlation coefficient of any bin with itself is 100% and is therefore omitted as well. Column 4 and Row 25 are omitted for the same reason.

Appendix D

The SLD Collaboration

K. Abe,[2] K. Abe,[19] T. Abe,[27] I.Adam,[27] T. Akagi,[27] N. J. Allen,[4] A. Arodzero,[20] W.W. Ash,[27] D. Aston,[27] K.G. Baird,[15] C. Baltay,[37] H.R. Band,[36] M.B. Barakat,[14] O. Bardon,[17] T.L. Barklow,[27] J.M. Bauer,[16] G. Bellodi,[21] R. Ben-David,[37] A.C. Benvenuti,[3] G.M. Bilei,[23] D. Bisello,[22] G. Blaylock,[15] J.R. Bogart,[27] B. Bolen,[16] G.R. Bower,[27] J. E. Brau,[20] M. Breidenbach,[27] W.M. Bugg,[30] D. Burke,[27] T.H. Burnett,[35] P.N. Burrows,[21] A. Calcaterra,[11] D.O. Caldwell,[32] D. Calloway,[27] B. Camanzi,[10] M. Carpinelli,[24] R. Cassell,[27] R. Castaldi,[24] A. Castro,[22] M. Cavalli-Sforza,[33] A. Chou,[27] E. Church,[35] H.O. Cohn,[30] J.A. Coller,[5] M.R. Convery,[27] V. Cook,[35] R. Cotton,[4] R.F. Cowan,[17] D.G. Coyne,[33] G. Crawford,[27] C.J.S. Damerell,[25] M. N. Danielson,[7] M. Daoudi,[27] N. de Groot,[27] R. Dell'Orso,[23] P.J. Dervan,[4] R. de Sangro,[11] M. Dima,[9] A. D'Oliveira,[6] D.N. Dong,[17] P.Y.C. Du,[30] R. Dubois,[27] B.I. Eisenstein,[12] V. Eschenburg,[16] E. Etzion,[36] S. Fahey,[7] D. Falciai,[11] C. Fan,[7] J.P. Fernandez,[33] M.J. Fero,[17] K.Flood,[15] R. Frey,[20] T. Gillman,[25] G. Gladding,[12] S. Gonzalez,[17] E.L. Hart,[30] J.L. Harton,[9] A. Hasan,[4] K. Hasuko,[31] S. J. Hedges,[5] S.S. Hertzbach,[15] M.D. Hildreth,[27] J. Huber,[20] M.E. Huffer,[27] E.W. Hughes,[27] X.Huynh,[27] H. Hwang,[20] M. Iwasaki,[20] D. J. Jackson,[25] P. Jacques,[26] J.A. Jaros,[27] Z.Y. Jiang,[27] A.S. Johnson,[27] J.R. Johnson,[36] R.A. Johnson,[6] T. Junk,[27] R. Kajikawa,[19] M. Kalelkar,[26] Y. Kamyshkov,[30] H.J. Kang,[26] I. Karliner,[12] H. Kawahara,[27] Y. D. Kim,[28] R. King,[27] M.E. King,[27] R.R. Kofler,[15] N.M. Krishna,[7] R.S. Kroeger,[16] M. Langston,[20] A. Lath,[17] D.W.G. Leith,[27] V. Lia,[17] C.-J. S. Lin,[27] X. Liu,[33] M.X. Liu,[37] M. Loreti,[22] A. Lu,[32] H.L. Lynch,[27] J. Ma,[35] G. Mancinelli,[26]

S. Manly,(37) G. Mantovani,(23) T.W. Markiewicz,(27) T. Maruyama,(27)
H. Masuda,(27) E. Mazzucato,(10) A.K. McKemey,(4) B.T. Meadows,(6)
G. Menegatti,(10) R. Messner,(27) P.M. Mockett,(35) K.C. Moffeit,(27) T.B. Moore,(37)
M.Morii,(27) D. Muller,(27) V.Murzin,(18) T. Nagamine,(31) S. Narita,(31)
U. Nauenberg,(7) H. Neal,(27) M. Nussbaum,(6) N.Oishi,(19) D. Onoprienko,(30)
L.S. Osborne,(17) R.S. Panvini,(34) H. Park,(20) C. H. Park,(29) T.J. Pavel,(27)
I. Peruzzi,(11) M. Piccolo,(11) L. Piemontese,(10) E. Pieroni,(24) K.T. Pitts,(20)
R.J. Plano,(26) R. Prepost,(36) C.Y. Prescott,(27) G.D. Punkar,(27) J. Quigley,(17)
B.N. Ratcliff,(27) T.W. Reeves,(34) J. Reidy,(16) P.L. Reinertsen,(33) P.E. Rensing,(27)
L.S. Rochester,(27) P.C. Rowson,(8) J.J. Russell,(27) O.H. Saxton,(27) T. Schalk,(33)
R.H. Schindler,(27) B.A. Schumm,(33) J. Schwiening,(27) S. Sen,(37) V.V. Serbo,(36)
M.H. Shaevitz,(8) J.T. Shank,(5) G. Shapiro,(13) D.J. Sherden,(27) K. D. Shmakov,(30)
C. Simopoulos,(27) N.B. Sinev,(20) S.R. Smith,(27) M. B. Smy,(9) J.A. Snyder,(37)
H. Staengle,(9) A. Stahl,(27) P. Stamer,(26) R. Steiner,(1) H. Steiner,(13)
M.G. Strauss,(15) D. Su,(27) F. Suekane,(31) A. Sugiyama,(19) S. Suzuki,(19)
M. Swartz,(27) A. Szumilo,(35) T. Takahashi,(27) F.E. Taylor,(17) J. Thom,(27)
E. Torrence,(17) N. K. Toumbas,(27) A.I. Trandafir,(15) J.D. Turk,(37) T. Usher,(27)
C. Vannini,(24) J. Va'vra,(27) E. Vella,(27) J.P. Venuti,(34) R. Verdier,(17)
P.G. Verdini,(24) S.R. Wagner,(27) D. L. Wagner,(7) A.P. Waite,(27) Walston, S.,(20)
J.Wang,(27) C. Ward,(4) S.J. Watts,(4) A.W. Weidemann,(30) E. R. Weiss,(35)
J.S. Whitaker,(5) S.L. White,(30) F.J. Wickens,(25) B. Williams,(7) D.C. Williams,(17)
S.H. Williams,(27) S. Willocq,(27) R.J. Wilson,(9) W.J. Wisniewski,(27)
J. L. Wittlin,(15) M. Woods,(27) G.B. Word,(34) T.R. Wright,(36) J. Wyss,(22)
R.K. Yamamoto,(17) J.M. Yamartino,(17) X. Yang,(20) J. Yashima,(31) S.J. Yellin,(32)
C.C. Young,(27) H. Yuta,(2) G. Zapalac,(36) R.W. Zdarko,(27) J. Zhou.(20)

(The SLD Collaboration)

(1) *Adelphi University, South Avenue- Garden City,NY 11530,*
(2) *Aomori University, 2-3-1 Kohata, Aomori City, 030 Japan,*
(3) *INFN Sezione di Bologna, Via Irnerio 46 I-40126 Bologna (Italy),*
(4) *Brunel University, Uxbridge, Middlesex - UB8 3PH United Kingdom,*
(5) *Boston University, 590 Commonwealth Ave. - Boston,MA 02215,*
(6) *University of Cincinnati, Cincinnati,OH 45221,*
(7) *University of Colorado, Campus Box 390 - Boulder,CO 80309,*
(8) *Columbia University, Nevis Laboratories P.O.Box 137 - Irvington,NY 10533,*
(9) *Colorado State University, Ft. Collins,CO 80523,*
(10) *INFN Sezione di Ferrara, Via Paradiso,12 - I-44100 Ferrara (Italy),*
(11) *Lab. Nazionali di Frascati, Casella Postale 13 I-00044 Frascati (Italy),*

[12] *University of Illinois, 1110 West Green St. Urbana,IL 61801,*
[13] *Lawrence Berkeley Laboratory, Dept.of Physics 50B-5211 University of California- Berkeley,CA 94720,*
[14] *Louisiana Technical University, ,*
[15] *University of Massachusetts, Amherst,MA 01003,*
[16] *University of Mississippi, University,MS 38677,*
[17] *Massachusetts Institute of Technology, 77 Massachussetts Avenue Cambridge,MA 02139,*
[18] *Moscow State University, Institute of Nuclear Physics 119899 Moscow Russia,*
[19] *Nagoya University, Nagoya 464 Japan,*
[20] *University of Oregon, Department of Physics Eugene,OR 97403,*
[21] *Oxford University, Oxford, OX1 3RH, United Kingdom,*
[22] *Universita di Padova, Via F. Marzolo,8 I-35100 Padova (Italy),*
[23] *Universita di Perugia, Sezione INFN, Via A. Pascoli I-06100 Perugia (Italy),*
[24] *INFN, Sezione di Pisa, Via Livornese,582/AS Piero a Grado I-56010 Pisa (Italy),*
[25] *Rutherford Appleton Laboratory, Chiton,Didcot - Oxon OX11 0QX United Kingdom,*
[26] *Rutgers University, Serin Physics Labs Piscataway,NJ 08855-0849,*
[27] *Stanford Linear Accelerator Center, 2575 Sand Hill Road Menlo Park,CA 94025,*
[28] *Sogang University, Ricci Hall Seoul, Korea,*
[29] *Soongsil University, Dongjakgu Sangdo 5 dong 1-1 Seoul, Korea 156-743,*
[30] *University of Tennessee, 401 A.H. Nielsen Physics Blg. - Knoxville,Tennessee 37996-1200,*
[31] *Tohoku University, Bubble Chamber Lab. - Aramaki - Sendai 980 (Japan),*
[32] *U.C. Santa Barbara, 3019 Broida Hall Santa Barbara,CA 93106,*
[33] *U.C. Santa Cruz, Santa Cruz,CA 95064,*
[34] *Vanderbilt University, Stevenson Center,Room 5333 P.O.Box 1807,Station B Nashville,TN 37235,*
[35] *University of Washington, Seattle,WA 98105,*
[36] *University of Wisconsin, 1150 University Avenue Madison,WS 53706,*
[37] *Yale University, 5th Floor Gibbs Lab. - P.O.Box 208121 - New Haven,CT 06520-8121.*

Bibliography

[1] H. Fritzsch, M. Gell-Mann, and H. Leutwyler, Phys. Lett. **47B** (1973) 365.
D. J. Gross and F. Wilczek, Phys. Rev. Lett. **30** (1973) 1343.
H. D. Politzer, *ibid.* **30** (1973) 1346.
S. Weinberg, Phys. Rev. Lett. **31** (1973) 494

[2] M. Gell-Mann, Phys. Rev. **125** (1962) 1067.

[3] E. C. G. Stueckelberg and A. Peterman, *Helv. Phys. Acta* **26** (1953) 499.
M. Gell-Mann and F. E. Low, *Phys. Rev.* **95** (1954) 1300.
C. Callan, Phys. Rev. **D2** (1970) 1541.
K. Symanzik, *Comm. Math. Phys.* **18** (1970) 227.

[4] J. Maldacena, Adv. Theor. Math. Phys.2 (1998) 231.

[5] J. Ellis, M. K. Gaillard, and G. G. Ross, Nucl. Phys. **B111** (1976) 253.

[6] A. Ali *et al.*, Nucl. Phys. **B167** (1980) 454.

[7] R. K. Ellis, D. A. Ross, and A. E. Terrano, Phys. Rev. Lett. **45** (1980) 1226; Nucl. Phys. **B178** (1981) 421.

[8] K. Fabricius, G. Kramer, G. Schierholz, and I. Schmitt, Phys. Lett. **B97** (1980) 431. Z. Phys. **C11** (1982) 315.

[9] K. Hagiwara and D. Zeppenfeld, Nucl. Phys. **B313** (1989) 560.

[10] F. Gutbrod, G. Kramer, and G. Schierholz, Z. Phys. **C21** (1984) 235.

[11] G. Kramer, B. Lampe, Z. Phys. **C39** (1988) 101.

[12] A. Signer, L. Dixon, Phys. Rev. Lett. **78** (1997) 811.

[13] V. N. Gribov and L. N. Lipatov, Yad. Fiz. **15** (1972) 781, 1218 [Sov. J. Nucl. Phys. **15** (1972) 438, 675].

[14] G. Altarelli, G. Pairsi, Nucl. Phys. **B126** (1977) 298.

[15] T. Sjöstrand, Comput. Phys. Commun. **82** (1994) 74.

[16] K. Kato and T. Munehisa, Mod. Phys. Lett. **A1** (1986) 345. K. Kato and T. Munehisa, Phys. Lett. **B214** (1988) 286.

[17] Yu. L. Dokshitzer, V. A. Khoze, A.H. Mueller, and S. I. Troyan, *Basics of Perturbative QCD*, Editions Frontieres, Gif-sur-Yvette Cedex, France (1991).

[18] C. L. Basham, L.S. Brown, S.D. Ellis, and S.T. Love, Phys. Rev. **D17** (1978) 2298. C. L. Basham, L.S. Brown, S.D. Ellis, and S.T. Love, Phys. Rev. Lett. **41** (1978) 1585.

[19] G. C. Fox and S. Wolfram, Nucl Phys. **B149** (1979) 413.

[20] G. 't Hooft and M. Veltman, Nucl. Phys. **B44** (1972) 189.

[21] W. J. Marciano, Phys. Rev. **D12** (1975) 3861.

[22] F. Bloch and A. Nordsieck, Phys. Rev. **52** (1937) 54.
A. Nordsieck, Phys. Rev. **52** (1937) 59.

[23] T. Kinoshita, *J. Math. Phys.* **3** (1962) 650. T. D. Lee and M. Nauenberg, *Phys. Rev.***133B** (1964) 1549.

[24] R. Marshall, Z. Phys. **C43** (1989) 595.

[25] R. D. Field, Application of Perturbative QCD, Addison-Wesley (1989).

[26] P. Nason and B. R. Webber, Nucl. Phys. **B421** (1994) 473.

[27] Yu. L. Dokshitzer, Zh. Eksp. Teor, Fiz **73** (1977) 1216 [Sov. Phys. JETP, **46** (1977) 641.]

[28] R.D. Field and R.D. Feynman, Nucl. Phys. **B136** (1978) 1.

[29] F.E. Paige and S.D. Protopopescu, in Physics of the Superconducting Supercollider-1986 (1987) 320.

[30] X. Artru and G. Mennessier, Nucl. Phys. **B70** (1974) 93.

[31] T. Sjöstrand, Comp. Phys. Commun. **43** (1987) 3.

[32] T. Sjöstrand, CERN-TH-7112/93 (1993).

[33] B. Foster, Electron-Positron Annihilation Physics, 1990.

[34] T. Sjöstrand, Comp. Phys. Comm. **39** (1986) 347.

[35] M. Bengtsson and T. Sjöstrand, Nucl. Phys. **B289** (1987) 810.

[36] D. Buskulic *et al.*(ALEPH Collab.), Z. Phys. **C55** (1992) 209. B. Adeva *et al.*(L3 Collab.), Z. Phys. **C55** (1992) 39. R. Akers *et al.*(OPAL Collab.), Z. Phys. **C63** (1994) 181.

[37] M.G. Bowler, Z. Phys. **C11** (1981) 169.

[38] S. Chun and C. Buchanan, Phys. Rev. Lett **59** (1987) 1997.

[39] S. Chun and C. Buchanan, Phys. Rep. **292** (1998) 239.

[40] G. Marchesini and B.R. Webber, Nucl. Phys. **B310** (1988) 461. w

[41] G. Marchesini *et. al.*, Comp. Phys. Comm. **67** (1992) 465.

[42] Yu L. Dokshitzer, V. A. Khoze, A. H. Mueller and S. Troyan, Basics of Perturbative QCD, Editing Frontières Publishing (1991).

[43] M. Suzuki. *Phys. Lett.* **B71** (1977) 139.

[44] J.D. Bjorken, Phys. Rev. **D17** (1978) 171.

[45] Ya. I. Azimov, Yu L. Dokshitzer and V. A. Khoze, *Sov. J. Nucl. Phys* **36** (1982) 878.

[46] V. G. Kartvelishvili, A. K. Likhoded and S. R. Slabospitskii, *Sov. J. Nucl. Phys* **38** (1983) 952.

[47] Ya. I. Azimov, Yu L. Dokshitzer, S. I. Troyan and V. A. Khoze, *Sov. J. Nucl. Phys* **40** (1984) 498.

[48] C. Peterson, D. Schlatter, I. Schmitt and P.M. Zerwas, Phys. Rev. **D27** (1983) 105.

[49] V. G. Kartvelishvili, A. K. Likhoded and V. A. Petrov, Phys. Lett. **78B** (1978) 615.

[50] S. D. Drell, D. J. Levy and T.-M. Yan, Phys. Rev. **D1** (1972) 1617. V. N. Gribov and L. N. Lipatov, Yad. Fiz. **15** (1972) 781, 1218 R. Gatto, P. manotti and I. Vendramin, Phys. Rev. **D7** (1973) 2524.

[51] P.D.B. Collins and T.P. Spiller, J. Phys. G **11** (1985) 1289.

[52] S. J. Brodsky and G. R. Farrar, Phys. Rev. Lett. **B31** (1973) 1153.

[53] D. Silvers, S. J. Brodsky, R. Blankenbecler, Phys Rep. **23** (1976) 1

[54] B. Mele and P. Nason, Phys. Lett. **B245** (1990) 635.

[55] G. Colangelo and P. Nason, Phys. Lett.**B285** (1992) 167.

[56] R.L.Jaffe, L.Randall, Nucl. Phys. **B412** (1994) 79.

[57] L. Randall, N. Rius, Nucl. Phys. **B441** (1995) 167.

[58] E. Braaten, K. Cheung, T.C. Yuan, Phys. Rev. **D48** (1993) R5049.
E. Braaten, K. Cheung, S. Fleming, T.C. Yuan, Phys. Rev. **D51** (1995) 4819.

[59] SLAC Linear Collider Conceptual Design Report, SLAC-REPORT-229 (1980). This report is somewhat outdated, but it still gives an overview of the design options of the major SLC components.

[60] M. Breidenbach *et al.*, SLAC-PUB-6313. Presented at the 2^{nd} International Workshop on Physics Experiments with Linear Colliders, Waikala, Hawaii, April, 1993.

[61] Y.-C. Chao *et al.*, SLAC-PUB-5868 (1992). Presented at the 15^{th} International Conference on High Energy Physics Accelerators, Hamburg, Germany, July 20-24, 1992.

[62] R. Prepost, Proceedings of the 21^{st} SLAC Summer Institute on Particle Physics, SLAC-REPORT-444, (1994), 54.

[63] K. Abe *et al.*, (SLD Collab.), Phys. Rev. Lett. **73** (1995) 24.

[64] A. Lath, Ph.D. Dissertation, MIT, SLAC-R-454 (1994).

[65] A.A. Sokolov and I.M. Ternov, Sov. Phys. Doklady **8** (1964) 1203.

[66] SLAC-CN-58 (1981).

[67] Simopoulos and R. L. Holtzapple, SLAC-PUB-6813 (1995)

[68] R. Koontz *et al.*, SLC-PUB-5890. Presented at Linac '92 Conference, Ottawa, Ottawa, Canada, August 1992.

[69] T. Limberg, P. Emma, and R. Rossmanith. The North Arc of the SLC as a Spin Rotator, SLAC-PUB-6210, 1993.

[70] F. Zimmermann *et al.*, SLAC-PUB-6790 (1995). Presented at the IEEE Particle Accelerator Conference (PAC 95).

[71] D. Calloway *et al.*, The Compton Polarimeter for SLC. SLAC-PUB-6026 (1992).

[72] G. Blaylock, SLC Physics Notes, 1993.

[73] K. Abe *et al.*, (SLD Collab.), Phys. Rev. Lett. **73** (1994) 25.

[74] SLD Design Report, SLAC-273, UC-34D, (1984).

[75] Paul Dervan, Ph.D. Dissertation, Brunel University, England, SLAC-R-523 (1998).

[76] The Particle Data Group, Phys. Rev. **D50**, Part I (1994).

[77] M.S. Robbins, *Radiation Damage Effects in Charged Coupled Devices*, Ph.D. Thesis, Brunel University (1992).

[78] M. Hildreth *et al.*, IEEE Trans Nucl. Sci. **NS-42** (1995) 451.

[79] C.J.S. Damerell et. al., Nucl. Instr. Meth. **A400** (1997) 287.

[80] D. Williams, Ph.D. Dissertation, MIT, SLAC-R-445 (1994).

[81] K. Abe *et al.*, Nucl. Inst. Mech. **A343** (1994) 74.

[82] Tom Pavel, Ph.D. Dissertation, Stanford, SLAC-R-491 (1997).

[83] D. Axen *et al.*, Nucl. Inst. Meth. **A328** (1993) 472.

[84] K. Pitts, Ph.D. Dissertation, University of Oregon. SLAC-R-446 (1994).

[85] R. Brun *et al.*, GEANT3, CERN-DD/EE/84-1 (1987). CERN Application Software Group, GEANT 3.21 Program, CERN Program Library (1994).

[86] A curious reader is encouraged to communicate with Dr. David Jackson for details concerning the implementation of VXD3 internal alignment.

[87] RAM Optical Instrumentation, Huntington Beach, CA.

[88] F. James and M. Roos, Comp. Phys. Comm. **10** (1975) 343.

[89] I thank Su Dong for providing the plots used here.

[90] SLD Collaboration, K. Abe *et al.*, Phys. Rev. **D51** (1995) 962.

[91] J. M. Yamartino, Ph.D. Dissertation, MIT, SLAC-R-426 (1994).

[92] S. Brandt *et al.*, Phys. Lett. **12** (1964) 57.
E. Farhi, Phys. Rev. Lett. **39** (1977) 1587.

[93] M.D. Hildreth *et al.*, IEEE Trans. Nucl. Sci. **42** (1994) 451.

[94] D. J. Jackson, Nucl. Inst. and Meth. **A388**, 247 (1997).

[95] SLD Collab., K. Abe *et al.*, Phys. Rev. **D53** (1996) 1023.

[96] SLD Collab., K. Abe *et al.*, Phys. Rev. Lett. **80** (1998) 660.

[97] ALEPH Collab., D. Buskulic *et al.*, Phys. Lett. **B357** (1995) 699.

[98] SLD Collab., K. Abe *et al.*, Phys. Rev. **D56** (1997) 5310.

[99] DELPHI Collab., P. Abreu *et al.*, Z. Phys. **C57** (1993) 181.

[100] SLD Collab., K. Abe *et al.*, SLAC-PUB-7826, (1998).

[101] ALEPH Collab., D. Buskulic *et al.*, Z. Phys. **C62** (1994) 179.
DELPHI Collab., P. Abreu *et al.*, Z. Phys. **C66** (1995) 323.
L3 Collab., O. Adeva *et al.*, Phys. Lett. **B261** (1991) 177.
OPAL Collab., P.D. Acton *et al.*, Z. Phys. **C60** (1993) 199.

[102] B. Andersson, G. Gustafson, G. Ingelman, T. Sjöstrand, Phys. Rep. **97** (1983) 32.

[103] The LEP Electroweak Working Group, D. Abbaneo *et al.*, LEPHF/96-01 (July 1996).

[104] OPAL Collab., G. Alexander *et al.*, Phys. Lett. **B364** (1995) 93.

[105] A. C. Benvenuti *et al.*, The Limited Streamer Tubes of the SLD, Nucl. Instr. Meth. **A290** (1990) 353.

[106] P. N. Burrows, Z. Phys. **C41** (1988) 375.
OPAL Collab., M.Z. Akrawy *et al.*, Z. Phys. **C47** (1990) 505.

[107] SLD Collab., K. Abe *et al.*, SLAC-PUB-7117; to appear in Phys. Rev. Lett.

[108] R. Brun *et al.*, Report No. CERN-DD/EE/84-1 (1989).

[109] C. N. Yang and R. Mills, Phys Rev. **96** (1954) 191.

[110] J. Goldstone, *Nuovo Cim* **19** (1961) 154.
J. Goldstone, A. Salam, and S. Weinberg, Phys. Rev. **127** (1962) 965.

[111] P. W. Higgs, Phys. Lett. **12** (1964) 132.

[112] G. 't Hooft, Nucl. Phys. **B33** (1971) 173; **B35** (1971) 167.

[113] T. D. Lee and C. N. Yang, Phys. Rev. **104** (1956) 254.

[114] Review of Particle Physics, The European Physics Journal, Volume 3, Number 1-4 (1998).

[115] F. E. Taylor, Talk at SLAC Summer Institute, (1998).